Light Dark Matter Constraints from a SuperCDMS Cryogenic Silicon Detector with Single-Charge Sensitivity

by

Enze Zhang

A thesis submitted in conformity with the requirements
for the degree of Doctor of Philosophy

Department of Physics
University of Toronto

© Copyright 2025 by Enze Zhang

Light Dark Matter Constraints from a SuperCDMS Cryogenic Silicon Detector with Single-Charge Sensitivity

Enze Zhang
Doctor of Philosophy
Department of Physics
University of Toronto
2025

Abstract

Astrophysical observations suggest that the universe contains a substantial amount of dark matter, likely composed of particles beyond the Standard Model. The SuperCDMS (Cryogenic Dark Matter Search) SNOLAB experiment is a next-generation direct detection effort using cryogenic germanium and silicon detectors to measure phonon and ionization signals from dark-matter recoils. It aims to improve sensitivity to dark-matter particles with masses below 10 GeV by an order of magnitude. As part of this effort, HVeV detectors (high voltage eV scale), which are gram scale with single-charge sensitivity, serve as a prototype to provide insight into detector response, calibration methods and background sources. Three prior HVeV runs have yielded competitive constraints on low-mass dark matter.

This dissertation analyzes data from the HVeV Run 4 experiment, conducted in an underground laboratory at Northwestern University. The experiment benefits significantly from the identification and elimination of the luminescence from the printed circuit boards in the detector holder used in Run 3, resulting in a lower background event rate and stronger constraints. Data from 10.80 gram-days of exposure were analyzed in a blinded study using a likelihood-based method. Limits are set on the dark matter-electron scattering cross-section in the mass range of MeV to GeV, dark photon absorption mixing parameter and axion-like particle coupling constant in the mass range of eV to tens of eV. The results turn out to be competitive and world-leading in some of the lower mass ranges. The experiment also provides information on potential background sources in the low-energy range, where future HVeV runs are expected to reduce or model them.

Acknowledgements

I would like to express my deepest gratitude to all those who supported me during my PhD journey.

First and foremost, I would like to thank my supervisor, Miriam Diamond, for her unwavering support, insightful guidance, and immense patience throughout this research project. Together with two other professors from our SuperCDMS group at the University of Toronto, Ziqing Hong and Pekka Sinervo, their expertise and encouragement were invaluable and kept me on track during the challenging times. I have greatly benefited not only from the training I received as a scientific researcher but also from their sincere advice on my career development.

Secondly, I would like to thank my friends and colleagues in the SuperCDMS collaboration. Amirata Sattari Javid and Imran Alkhatib, my peers at the University of Toronto, are the best friends I have made in the past few years. We tackled numerous discussions on physics and statistics, worked together through shared challenges, and enjoyed ourselves in casual times. Kyle Kennard and Yongqi Wang provided significant assistance with onsite data collection and readout processing in HVeV Run 4. I am also deeply thankful to the postdoctoral researchers, Stefan Zatschler, Birgit Zatschler, Matthew Wilson, and Valentina Novati, for their substantial support throughout my project. All of them played significant roles in helping me become a better researcher and a critical thinker.

Finally, I owe a great deal of gratitude to my parents. Without their cultivation and love, I would not have made it this far. They gave me immense emotional support during times of loneliness and stress, especially in the COVID-19 pandemic. Despite being separated by the vastest ocean, our bond as a family has remained strong. We share our lives, care for each other's well-being, and plan for the future together. This dissertation is dedicated to them.

Contents

List of Tables

List of Figures

Statement about Collaborative Work

The work presented in this dissertation is a collective effort from the SuperCDMS collaboration.

The main contributors of the HVeV Run 4 low-mass dark-matter search analysis include myself, Imran Alkhatib and Huanbo Sun. My own contributions include the signal shape study, continuous readout processing, quality cut development with efficiency calculations, some early work in the energy calibration (working point alignment and zeroth peak correction), and the development and validation of the likelihood-based limit setting approach. I also took remote shifts for data quality monitoring during the data collection of Nexus Run 14. Imran contributed in the noise study, the development of three of the four live time cuts (fridge temperature cut, baseline excursion cut and coincidence-type cuts), and most of the work in energy calibration and detector response modeling. Huanbo developed the elevated rate live-time cut and studied the position-dependent relative calibration.

Other key contributors to this experiment and analysis include Valentina Novita, Enectali (Tali) Figueroa-Feliciano, Ziqing Hong, Miriam Diamond, Stefan Zatschler, Matthew (Matt) Wilson, Alexander (Sasha) Zaytsev, Kyle Kennard and Yongqi Wang. Valentina and Kyle played the most significant role in terms of experimental setup and onsite data collection for HVeV Run 4. When it comes to the analysis, we analyzers benefited a lot from the guidance and suggestions from Valentina, Tali, Ziqing, Miriam, Stefan and Matt. The signal models used in HVeV Run 4 analysis are mostly inherited from HVeV Run 3, where Matt and Sasha built a well-developed Python package. Finally, Yongqi helped measure some key parameters of the LED source used in calibration, and also contributed in the maintenance of the offline processing package.

Chapter 1

Introduction to Dark Matter and SuperCDMS Experiment

This chapter gives a general introduction to dark matter and the SuperCDMS experiment. Section 1.1 reviews the historical development of the dark-matter hypothesis. Section 1.2 summarizes three major lines of evidence that support the existence of dark matter. Some key properties of the local dark matter distribution are discussed in Section 1.3. In Section 1.4, several dark-matter candidates are introduced, with more details of certain low-mass candidates presented in Chapter 4, since they are the signal models of this analysis. In the end, Sections 1.5 and 1.6 introduce the dark-matter direct detection method and provide an overview of the SuperCDMS experiment.

1.1 The History of Dark Matter

The concept of dark matter was first put forward in the early 20^{th} century, in order to explain the observations of large gravitationally bound structures, indicating that stars in galaxies orbit at speeds faster than what would be expected based on the visible matter they contain.

Lord Kelvin was one of the first physicists to make a dynamic estimation of the amount of dark matter in the Milky Way [3]. He proposed the assumption to describe stars in the Milky Way as gas of particles under the influence of gravity. A relationship is then established between the size of the system and the velocity dispersion of the stars, given by the virial theorem from thermal dynamics, as shown in Eq. 1.1:

$$\langle T \rangle = \frac{1}{2} \sum_{k=1}^{N} \langle \overline{F}_k \cdot \overline{r}_k \rangle, \tag{1.1}$$

where T is the total kinetic energy of the N particles in the system, $\overline{F}_k$ represents the force on the k_{th} particle located at position $\overline{r}_k$, and the angle brackets represent the average over time of the enclosed product. If the force $\overline{F}_k$ on the particles has an associated potential energy in the form of Eq. 1.2:

$$V(r) = \alpha r^n, \tag{1.2}$$

which is proportional to some power n of the distance r between particles. The virial theorem will be simplified as in Eq. 1.3:

$$\langle T \rangle = \frac{n}{2} \langle V_{tot} \rangle, \tag{1.3}$$

where V_{tot} is the time average of the total potential energy over all pairs of particles in the system. In the special case of gravity, $n = -1$.

Inspired by Kelvin's "theory of gases" idea, Henri Poincaré first explicitly used the word "dark matter" [4]. In 1922, Jacobus Kapteyn developed a quantitative model of the Galaxy's shape and size, describing it as a flattened distribution of stars rotating around an axis aligned with the Galactic Pole [5]. In 1932, Jan Oort published an analysis of the vertical kinematics of stars in the solar neighborhood, where he derived the most probable value for the total density of matter near the Sun as 6.3×10^{-24} g/cm^3 [6]. Astronomers at that time believed that dark matter was likely composed of faint stars instead of a completely new category of matter. All of them reached the similar conclusion that the total mass of nebulous or meteoric matter near the sun is probably less than the total mass of visible stars, or even much less [5].

In 1933, Fritz Zwicky analyzed the redshifts of various galaxy clusters and observed a significant variation in the apparent velocities of eight galaxies within the Coma Cluster, with differences exceeding 2000 km/s [7]. After applying the virial theorem to estimate the velocity dispersion and comparing it to the observed value, he came to the surprising conclusion that dark matter is present in much greater quantities than luminous matter.

Apart from the question of whether the dynamics of galaxy clusters require the existence of dark matter, the nature of dark matter has sparked increasing interest among physicists. With the development of quantum mechanics and the discoveries of more and more fundamental particles, the Standard Model of particle physics was developed throughout the latter half of the 20^{th} century, which describes all of the known elementary particles as quarks, leptons and bosons, and describes three of the four fundamental forces: electromagnetic, weak, and strong. In the early ages, dark matter was hypothesized by many scientists as gases, massive collapsed objects [8], HI (hydrogen line) snowballs [9] and M8 dwarf stars [10]. However, measurements of the primordial light element abundances eventually ruled out these possibilities, instead favoring a non-baryonic nature for dark matter. In 1985, Mark Goodman and Ed Witten proposed that if dark matter consists of particles, it might be detectable using methods similar to those used in neutrino detection [11]. This proposal marked the beginning of direct detection experiments for dark matter. The first such experiment commenced in 1986 at the Homestake Mine in South Dakota, employing a low-background germanium ionization detector [5].

1.2 Observational Evidence

There is a lot of observed astrophysical evidence that supports the presence of dark matter. In this subsection, a few major lines of evidence are introduced.

1.2.1 Galaxy Rotation Curves

Historically, galaxy rotation curves, meaning the circular speed of stars and gas in a galaxy as a function of their distance to the galactic center, played a significant role in convincing the scientific community of the existence of large amounts of dark matter in the outer regions of galaxies. The gravitational potential energy of a galaxy of stars orbiting around the center is described in Eq. 1.4:

$$V(r) = -\frac{GmM(r)}{r}, \tag{1.4}$$

where G is the gravitational constant, r is the distance from the center and M(r) is the total mass enclosed within radius r. In the simplest case of a circular orbit and a spherical potential, the object's velocity as a function of radius can be derived as in Eq. 1.5:

$$v = \sqrt{\frac{GM(r)}{r}}. \tag{1.5}$$

Despite the simplification here from the general elliptical orbit to a circular one, the velocity dependence on the radius r is similar to what we concluded in Eq. 1.5. Since the amount of stellar and gaseous matter at the outer edges of a galaxy is relatively small, the total enclosed mass should approach an asymptotic value at large radii, which yields a velocity drop $\propto r^{1/2}$, as predicted by Eq. 1.5.

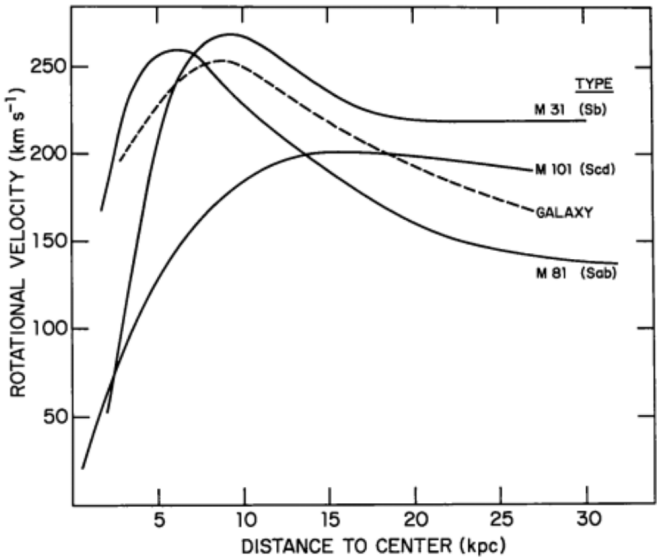

Figure 1.1: The rotation curves for the galaxies M31, M101, and M81 (solid lines) obtained by Roberts and Rots in 1973, overlaid with the curve of the Milky Way Galaxy for comparison. Plot is taken from Ref. [5].

However, this prediction of galactic rotational velocities is likely to be wrong as more and more astronomical observations provided inconsistent results. In 1970, the first explicit claims emerged, suggesting that additional mass was required in the outer regions of certain galaxies. This conclusion was drawn from comparisons between rotation curves predicted from photometry and those measured

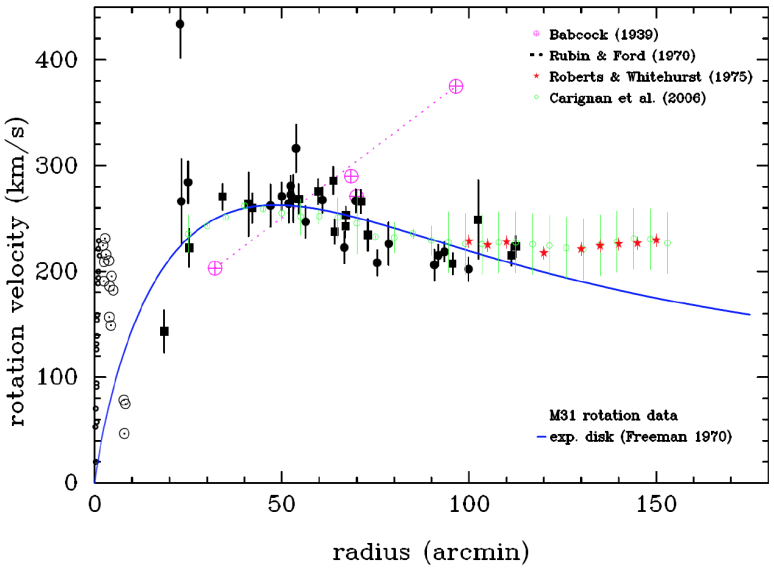

Figure 1.2: Rotation curve data for M31. The purple points are emission line data in the outer parts from Babcock 1939 [12]. The black points are from Rubin and Ford 1970 [13]. The red points are the 21-cm HI line data from Roberts and Whitehurst 1975 [14]. The green points are 21-cm HI line data from Carignan et al. [15]. The black solid line corresponds to the rotation curve of an exponential disc with a scale length according to the value given in Freeman 1970 [16], suitably scaled in velocity. 21-cm data demonstrate clearly the mass discrepancy in the outer parts. Plot is taken from Ref. [5].

from 21 cm observations. Fig. 1.1 shows the rotation curves for the galaxies M31, M101, and M81 (solid lines) obtained by Roberts and Rots in 1973 [17], where a flat tail was noticed in their outer parts. Fig. 1.2 provides more observation results for M31 from different scientists.

To explain the observed rotation curves, several hypotheses have been proposed. One path is to assume that the gravitational theory needs correction, but the more popular and widely accepted hypothesis is that the mass distribution of galaxies is not what we anticipated. For a sphere with a symmetric mass distribution in all directions, the total enclosed mass at a distance r is given by Eq. 1.6:

$$M(r) = \int 4\pi r^2 \rho(r), \tag{1.6}$$

where $\rho(r)$ is the radial mass dependence function. If we focus on the tail region of Fig. 1.2 where the rotational velocity is asymptotically constant at a speed of v_{const}, then combining with Eq. 1.5, we can derive $\rho(r)$ at large radius as Eq. 1.7:

$$\rho(r) = \frac{v_{const}^2}{4\pi G r^2}. \tag{1.7}$$

Eq. 1.7 indicates that the shape of rotation curves makes sense if the galactic mass follows a r^{-2} density distribution, which implies not only that the majority of the galactic mass is located farther from the galactic core, but also that a significant portion extends well beyond any observable objects. It is now widely accepted that galaxies contain large dark matter structures with a mass

density that follows a r^{-2} scaling relation [5].

1.2.2 Cosmic Microwave Background

The Cosmic Microwave Background (CMB), also known as relic radiation, discovered in 1965 by the American radio astronomers Arno Penzias and Robert Wilson, is microwave radiation that permeates all space in the observable universe, as shown in Fig. 1.3. Although standard optical telescopes show the background between stars and galaxies to be nearly completely dark, a sufficiently sensitive radio telescope reveals a faint, nearly uniform glow which is not linked to any star, galaxy, or other celestial object and is most prominent in the microwave region of the radio spectrum.

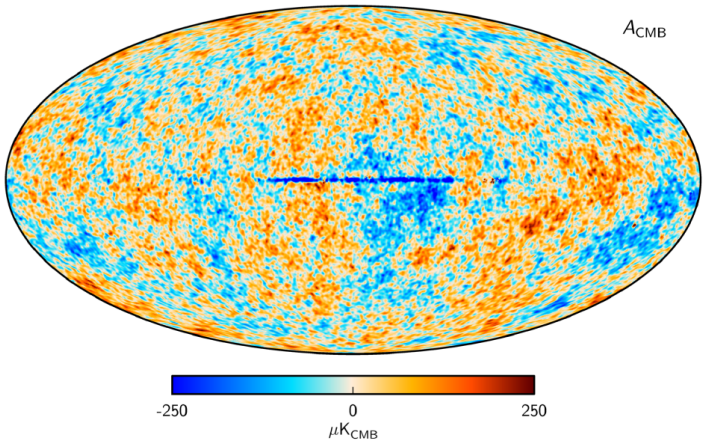

Figure 1.3: Cosmic Microwave Background temperature map derived from Planck, WMAP, and 408 MHz observations. Figure is taken from Ref. [18].

The CMB is landmark evidence of the Big Bang theory for the origin of the universe. In the Big Bang cosmological models, the early universe was hot and dense enough to produce all Standard Model particles [19], and some dark matter models, such as WIMPs, are also produced thermally. The expansion in scale R and cooling of the universe is described by the Friedmann equation, as shown in Eq. 1.8:

$$H^2 = (\dot{R}/R)^2 = \frac{8\pi G\rho_{tot}}{3} - \frac{kc^2}{R^2}, \tag{1.8}$$

where ρ_{tot} is the total energy density, k is the curvature parameter, H is defined as the Hubble parameter, G is Newton's constant, and c is the speed of light.

Cosmological measurements support a flat universe, i.e. $k = 0$ [20]. Given the Hubble constant H_0 today, the critical energy density where the universe is exactly flat is given by Eq. 1.9:

$$\rho_c = \frac{3H_0^2}{8\pi G}. \tag{1.9}$$

The energy densities of different particles such as neutrinos and photons, are typically expressed as a fraction of the critical energy density $\Omega = \rho/\rho_c$, with $H^2/H_0^2 = \sum \Omega$ for the evolution of the

universe. For non-relativitic particles, their kinetic energies are much smaller than their rest masses, and therefore $\rho \propto R^{-3}$. On the other hand, radiation including relativistic particles is red-shifted as the universe expands, and their energy density falls faster, with $\rho \propto R^{-4}$. In the early, hot universe, radiation was the dominant component. However, as the universe cooled, non-relativistic matter began to play a central role in its evolution. This shift happened when the universe was roughly 3000 times smaller than it is today [19]. Observations of the expansion of the universe indicate the presence of a third component; dark energy, which did not affect the early universe but causes the expansion of the universe to accelerate today, parameterized with a constant energy density component $\Omega_\Gamma = \Gamma$. The cosmological standard model includes cold dark matter [21] and dark energy components in addition to baryonic matter to fit the CMB and other cosmological observations.

In the earliest stages of the universe, it was shrouded in a dense, hot plasma consisting of subatomic particles. As the universe expanded, this plasma cooled, allowing protons and electrons to combine and form neutral atoms, primarily hydrogen. The recombination epoch was characterized by an extremely hot and dense primordial fluid composed of baryonic matter and radiation. These components were closely coupled through scattering processes between charged particles and photons. The radiation within this fluid exerted an outward pressure as a result of its density. In contrast, dark matter during this period was largely decoupled from the baryonic radiation fluid, though it still interacted with it via gravitational forces. The gravity of dark matter caused the fluid to compress into regions of higher density, leading to corresponding regions of lower density due to matter conservation. The pressure of the fluid acted to push it from over-dense regions into under-dense areas. These competing forces resulted in oscillatory compressions and decompressions of the fluid, similar to sound waves. At the end of the recombination, the radiation was released from the baryonic matter, and the density fluctuations of the fluid ceased. Consequently, the remaining baryonic matter was imprinted with a pattern of high-density and low-density regions. The high-density regions eventually served as seeds for the formation of the large-scale structure of the universe. Light escaping from high-density regions generally had a higher temperature than light from low-density regions. Thus, the temperature fluctuations observed in the CMB reflect the density fluctuations of the primordial fluid at the end of recombination.

Figure 1.4 displays the temperature anisotropies measured by Planck [22], a space observatory operated by the European Space Agency from 2009 to 2013. The measurements from the Planck Collaboration, as summarized in Table 1.1, are consistent with a flat universe model. This model suggests that approximately 5% of the universe is composed of baryonic matter, 26% of cold (i.e., non-relativistic) dark matter, and the remaining 69% is dark energy.

Table 1.1: Matter-energy abundances from CMB data, scaled with the reduced Hubble constant [22].

Parameter	Symbol	Value
Baryon abundance	$\Omega_b h^2$	0.2230 ± 0.00014
Dark matter abundance	$\Omega_c h^2$	0.1188 ± 0.0010
Dark energy density	$\Omega_\Gamma h^2$	0.6911 ± 0.0062
Reduced Hubble constant	$h = H_0/(100\ \mathrm{kms}^{-1}\mathrm{Mpc}^{-1})$	0.6774 ± 0.0046

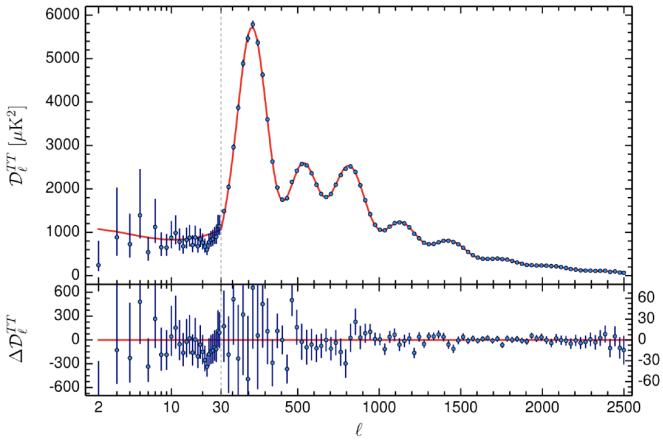

Figure 1.4: Observed CMB temperature power spectrum as a function of the multipole number l. Data points are found from observations of the CMB, and the red curve is the best-fit result of numerical models. Plot is taken from Ref. [22].

1.2.3 Gravitational Lensing

One of the consequences of general relativity is gravitational lensing. This phenomenon occurs when massive objects situated between a light source and an observer act as lenses that bend the light from the source. An illustrative example is a galaxy cluster positioned between a more distant source, such as a quasar, and the observer. The degree of lensing observed increases with the mass of the intervening object.

The angular deflection of light α due to a point-like lens with mass M is given by Eq. 1.10:

$$\alpha = \frac{4GM}{rc^2} = \frac{2r_s}{r}, \tag{1.10}$$

where G is the gravitational constant, c is the speed of light, r is the distance between the light and the lens in the plane perpendicular to the observer, and $r_s = 2\mathrm{G}M/c^2$ is the Schwarzschild radius (a physical parameter in the Schwarzschild solution to Einstein's field equations that corresponds to the radius defining the event horizon of a Schwarzschild black hole). Eq. 1.10 gives an accurate approximation of the angular deflection of light. When the background object, lens, and observer are well aligned, gravitational lensing can produce structures known as Einstein rings. Additionally, Eq. 1.10 demonstrates that the mass of the lens can be inferred from observations of gravitational lensing, even without detailed knowledge of the lens's internal composition.

When two galaxy clusters collide, the plasma, which constitutes the majority of visible matter in the cluster, will interact significantly. In contrast, most stars and galaxies will pass through the collision without experiencing substantial deceleration. Collisionless dark matter will follow a trajectory similar to that of the galaxies, remaining distinct from the plasma. The gravitational potential in these systems can be mapped by analyzing the distortions of background galaxies caused by gravitational lensing.

The most prominent example of gravitational lensing with respect to dark matter is the "Bullet Cluster". Studies of the "Bullet Cluster" [23], as shown in the optical image in Fig. 1.5, reveal that the gravitational potential of merging clusters aligns with the galaxies rather than with the plasma.

Gravitational lensing measurements indicate that the mass surrounding the visible galaxies is seven times greater than that surrounding the plasma component. Additionally, the visible mass at the peak of the plasma is twice that of the brightest galaxy. These findings suggest that the majority of the matter in the Bullet Cluster must originate from an unknown and unseen substance. It also supports the notion that dark matter is primarily collisionless, as the distinct dark matter components from the colliding clusters seem to have passed through one another, leaving the interstellar plasma unaffected.

Figure 1.5: Composite image of the "Bullet Cluster". The pink coloring shows the X-ray gas, while the blue color indicates the gravitational potential inferred with gravitational lensing in Ref. [23], on top of a visible-light image.

1.3 Local Dark Matter Properties

Based on the observational constraints, a particle dark matter candidate should have the following properties:

1. Dark matter must have mass. Its gravitational influence causes the galaxy rotation curves to deviate from theoretical predictions.

2. Dark matter is *dark*, meaning it is electrically neutral, or at least with very limited (fractional) charge. Otherwise, it will interact with ordinary matter through electromagnetic interaction, making it visible optically.

3. Dark matter is most likely to be *cold*, meaning it is non-relativistic in terms of its speed. This property is crucial for explaining the formation of structures in the universe. Cold dark matter is expected to cluster around smaller-scale objects, such as galaxies, whereas hot dark matter would cluster around larger-scale structures such as galaxy clusters or superclusters. Observations of the large-scale structure of the universe support the cold dark matter model [24].

4. Dark matter is *non-baryonic*. As mentioned in Section 1.1, strong evidence indicates that dark matter is not composed of ordinary/baryonic matter. Both observations of the CMB and

studies on the Big Bang nucleosynthesis conclude that baryonic matter cannot account for the missing dark matter. In terms of Big Bang nucleosynthesis, a greater abundance of baryonic matter in the early universe would have led to a significantly different distribution of isotopes than what we observe today.

5. Dark matter is most likely to be *stable*. The evidence of dark matter's influence on the CMB and the formation of large-scale structures in the universe indicates that dark matter has been present since the early stages of the universe. This strongly suggests that dark matter has a very long lifetime. Many theoretical models propose that dark matter particles are the lightest particles in an unknown "dark sector".

Apart from the properties mentioned above, when it comes to the local dark matter in a specific galaxy, the notion of "dark matter halo" is put forward, indicating the structures of dark matter around galaxies. It is a hypothetical region that has decoupled from cosmic expansion and contains gravitationally bound matter. Dark matter halos are expected to encompass the entire galactic disk and extend well beyond the visible matter in a galaxy. For that reason, the Earth is continuously moving through a dark matter halo. Predictive models for detecting DM from Earth rely heavily on the characteristics of dark matter in the vicinity of the Earth.

We will discuss below two most important constraints of the local dark matter: the local density ρ_{DM} and the velocity distributions.

1.3.1 Local Density of Dark Matter

The estimation of ρ_{DM} dates back to the 1920s and 1930s, when Jacobus Kapteyn, Jan Oort, and James Jeans observed stellar kinematics [5]. After that, numerous additional measurements have been conducted. Ref. [25] provides a detailed summary and analysis of these dark matter measurements on ρ_{DM}. According to Ref. [25], a population of "tracer" stars moving in a gravitational potential will obey the collisionless Boltzmann equation, as shown in Eq. 1.11:

$$\frac{df}{dt} = \frac{\partial f}{\partial t} + \nabla_x f \cdot \overrightarrow{v} - \nabla_v f \cdot \nabla_x \Phi = 0, \tag{1.11}$$

where $f(\overrightarrow{x}, \overrightarrow{v})$ is the distribution function of stars with positions $\overrightarrow{x}$ and velocities $\overrightarrow{v}$, while Φ is the gravitational potential. When the gravity field is weak, the force $\nabla_x \Phi$ is related to the total mass density ρ through Eq. 1.12 (the Poisson equation):

$$\nabla_x^2 = 4\pi G\rho, \tag{1.12}$$

where G is the gravitational constant.

Since ρ is the total mass density of all the stars, gas, and dark matter in the system, solving Eq. 1.11 for a set of tracer stars can provide an estimate of ρ_{DM}. However, it is still a challenging task to solve Eq. 1.11, and therefore several methods are developed as introduced in Ref. [25]. A summary of ρ_{DM} measurements made over time is shown in Fig. 1.6.

Currently, the widely accepted value of the local dark matter density is $\rho_{DM} \sim 0.3$ GeV/cm^3, which we choose to adopt in our signal models.

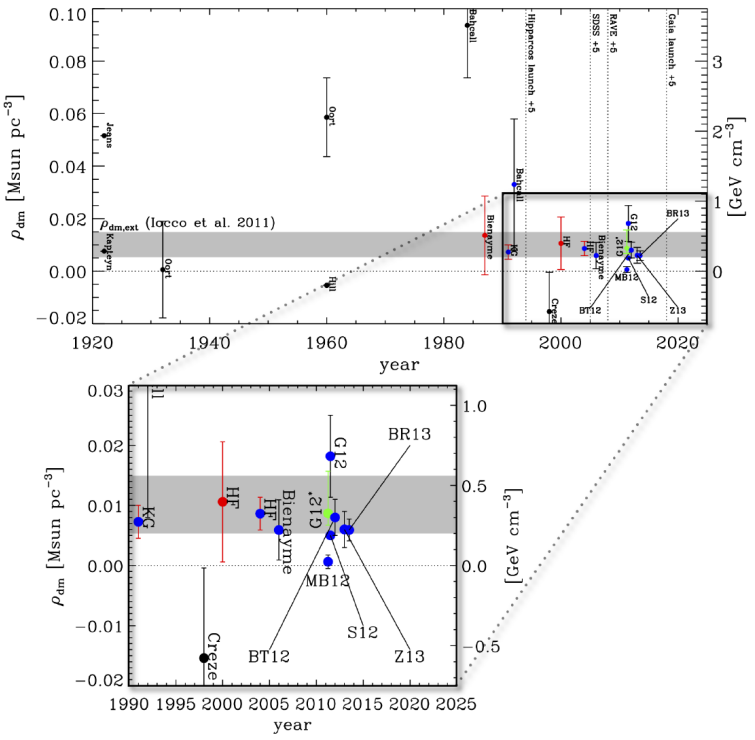

Figure 1.6: Summary of the measurements of the local dark matter density ρ_{DM} made over time. The currently accepted value of ρ_{DM} is $\rho_{DM} \sim 0.3$ GeV/cm^3. The grey band is the DM density extrapolated to the entire DM halo. Plot is taken from Ref. [25].

1.3.2 Velocity Distributions

The velocity distribution is another key property of local dark matter. The energy depositions are different when dark matter particles travel at different speeds and collide with a detector on Earth. The velocities of dark matter particles are typically modelled using the Standard Halo Model (SHM) [26], where the dark matter halo is assumed to be an isotropic and isothermal sphere with a density that scales as $\rho \propto r^{-2}$, where r is the distance to the center of the galaxy. Under such assumptions, the dark matter particles with velocities $\overrightarrow{v}$ are expected to obey a Maxwell distribution in the rest frame of the galaxy, as shown in Eq. 1.13:

$$f_{gal}(\overrightarrow{v}) = \begin{cases} \frac{N}{(2\pi\sigma_v)^{2/3}} e^{-\frac{|\overrightarrow{v}|^2}{2\sigma_v^2}} & |\overrightarrow{v}| < v_{esc} \\ 0 & |\overrightarrow{v}| \geq v_{esc} \end{cases}, \tag{1.13}$$

where N is a normalization constant, and σ_v is the one-dimensional velocity dispersion related to the local circular velocity v_c as $\sigma_v = v_c/\sqrt{2}$.

The upper threshold of the dark matter velocity is constrained by the escape velocity of the galaxy v_{esc}, since otherwise it would not be bound within the galaxy. Some other models suggest that a portion of the local dark matter could include non-galactic dark matter particles that are not gravitationally bound to the Milky Way and have velocities exceeding the galactic escape velocity [27], but we do not consider that in this analysis.

Typical values for v_c and v_{esc} are ∼220 km/s and ∼550 km/s, respectively. It is also worth noticing that for the dark matter detection experiments carried out on Earth, we also need to add the Earth's motion relative to the DM halo as a vector sum: $\overrightarrow{v} \rightarrow \overrightarrow{v} + \overrightarrow{v_E}$, where $\overrightarrow{v_E}$ is the Earth's velocity in the galaxy rest frame. Combining the orbital motion of Earth around the Sun and the orbital motion of the Sun around the center of the galaxy, $\overrightarrow{v_E}$ varies about ± 15 km/s at different times of the year [28]. This slight variation in velocity can result in an annual modulation of the expected dark matter interaction rate, which could be detectable by certain dark matter experiments.

1.4 Dark Matter Candidates

Various dark matter candidates have been proposed in the past few decades, each supported by a different particle theory to explain the astronomical observations. In general, dark matter particles are thought to exist in an unknown "dark sector" and interact with known Standard Model particles through some mediating force. This dark sector could consist of either multiple types of dark particles or just a single type. For a long time, the Weakly Interacting Massive Particles (WIMPs) have been the most popular candidate within the science community, yet in recent years, the absence of discovery forces physicists to shift interests on other potential candidates. In the next few paragraphs, we will introduce WIMPs as well as several other popular candidates, including the ones on which we will set limits in this analysis.

1.4.1 WIMPs

The argument for WIMP dark matter arises from calculating the velocity-averaged self-annihilation cross section σ_v that yields the current dark matter density observed today. As detailed in Ref. [29], the relic abundance of stable dark matter particles remaining after the freeze-out period corresponds to $\sigma_v \approx 3 \times 10^{-27}$ cm^3/s. This value is approximately comparable to the self-annihilation cross section expected for a new particle with weak-scale interactions and a mass of ∼100 GeV. Interestingly, various theories that extend beyond the Standard Model (such as several versions of the Supersymmetry model [29]) predict the existence of a new particle around this mass, which motivates physicists to take WIMPs as the primary search candidate of direct detection experiments for decades.

The WIMPs model discussed in this subsection is derived from Ref. [30][28]. Consider an interaction between a WIMP χ with mass m_χ and a nucleus of the target material. The deposited recoil energy is E_R. For a target material with a total mass of m_T and a nucleus mass m_N, the total number of target nuclei is m_T/m_N. If the cross section of the WIMP-nucleus scattering is σ, then the effective area of the target is $\sigma m_T/m_N$. The flux of dark-matter particles passing through the detector is $n_\chi \cdot \langle v \rangle$, where $n_\chi = \rho_{DM}/m_\chi$ is the number density of WIMPs and $\langle v \rangle$ is the average WIMP velocity. Putting all these together, the number of expected interactions N detected over some time t is given by Eq. 1.14:

$$N = t \cdot \sigma \cdot \frac{m_T}{m_N} \cdot \frac{\rho_{DM}}{m_\chi} \cdot \langle v \rangle. \tag{1.14}$$

Typically, interactions are described as an event rate R, measured as the number of events per unit time per unit mass of the detector. Transforming Eq. 1.14 into R gives Eq. 1.15:

$$R = \frac{\rho_{DM}}{m_N m_\chi}\sigma \cdot \langle v \rangle = \frac{\rho_{DM}}{m_N m_\chi}\int \sigma \cdot v f(\overrightarrow{v}) d^3\overrightarrow{v}, \tag{1.15}$$

where $\langle v \rangle$ is substituted by an integral over the velocity distribution of dark-matter particles. Eq. 1.15 can be further written as a differential rate over the possible recoil energies E_R, as shown in Eq. 1.16:

$$\frac{dE}{dR} = \frac{\rho_{DM}}{m_N m_\chi}\int \frac{d\sigma}{dE_R} \cdot v f(\overrightarrow{v}) d^3\overrightarrow{v}. \tag{1.16}$$

The relative speed of WIMPs and nuclei is at the order of a few hundred km/s, which implies that the scattering interactions occur in the non-relativistic scenario. For a 2-body elastic scattering collision with a nucleus initially at rest, the final velocity of the nucleus in the laboratory frame v_N is given by Eq. 1.17:

$$v_N = v\frac{2m_\chi}{m_\chi + m_N}\sin\frac{\theta^*}{2} = 2v\frac{\mu_N}{m_N}\sin\frac{\theta^*}{2}, \tag{1.17}$$

where v is still the initial WIMP velocity in the laboratory frame, θ^* is the scattering angle in the center of mass frame, and $\mu_N = m_\chi m_N/(m_\chi + m_N)$ is the WIMP-nucleus reduced mass. The recoil energy deposited by the WIMP to the nucleus is therefore given by Eq. 1.18:

$$E_R = \frac{1}{2}m_N v_N^2 = \frac{\mu_N^2 v^2}{m_N}(1 - \cos\theta^*). \tag{1.18}$$

From Eq. 1.18, one can determine the minimum WIMP speed v_{min} that can result in a recoil energy of E_R, as given in Eq. 1.19:

$$v_{min} = \sqrt{\frac{m_N E_R}{2\mu_N^2}}. \tag{1.19}$$

Eq. 1.19 provides an important relationship between v_{min} and the mass of the target nuclei. In the region where $m_\chi < m_N$, v_{min} increases with m_N, which implies that a target with heavier nuclei requires a higher minimum WIMP velocity to produce a recoil energy E_R compared to a target with lighter nuclei. For scattering events in the non-relativistic limit, the scattering cross section is approximately isotropic. This means that the cross section over all scattering angles θ^* in the center-of-mass frame is constant between 0 and 180 degrees, and therefore $d\sigma/d(\cos\theta^*) = \sigma/2$. Similarly, the differential cross section is given by Eq. 1.20:

$$\frac{dE}{dR} = \frac{d\theta}{d\cos\theta^*}\frac{d\cos\theta^*}{dE_R} = \frac{m_N}{2\mu_N^2 v^2}\sigma. \tag{1.20}$$

The interaction between a WIMP and a nucleus is highly dependent on the energy transfer involved. Deeper scatters probe the internal structure of the nucleus, whereas low-energy scatters interact primarily with the collective nuclear charge. This dependence is quantified through the form factor $F(E_R)$, as shown in Eq. 1.21:

$$\frac{d\sigma}{dE_R} = (\frac{d\sigma}{dE_R})_0 F(E_R)^2 = \frac{m_N}{2\mu_N^2 v^2}\sigma_0 F^2(E_R), \tag{1.21}$$

where σ_0 is the cross section at zero momentum transfer. The $d\sigma/dE_R$ term is the differential cross section when the nucleus is treated as a point-like target. $F(E_R)$ captures the dependence on momentum transfer and accounts for the suppression observed when considering the substructures within the target nuclei. The total WIMP-nucleus cross section can be separated into a spin-dependent (SD) and spin-independent (SI) component, as shown in Eq. 1.22:

$$\sigma_{N,0} = \sigma_{N,0}^{SD} + \sigma_{N,0}^{SI}. \tag{1.22}$$

The distinction between these contributions pertains to the specific coupling of the WIMP to the quarks within the nucleus. The terms "spin-dependent" and "spin-independent" indicate whether the coupling depends on the net spin of the target nucleus. The spin-dependent (SD) term results from an axial-vector coupling, with the cross-section expressed as in Eq. 1.23:

$$\sigma_{N,0}^{SD} = \frac{32 G_F^2 \mu_N^2}{\pi} \frac{J+1}{J} (a_p < S_p > a_N < S_N >)^2, \tag{1.23}$$

where G_F is Fermi's constant, J is the total nuclear spin, S_p, S_N are the expectation values of the proton and neutron spins, and a_p, a_N are the couplings of the WIMP to protons and neutrons. This spin-dependent contribution can only be explored using target materials with a non-zero total nuclear spin, such as fluorine. Other materials like Si and Ge, whose most naturally abundant isotope has no nuclear spin, are unable to probe this type of interaction.

The SI term primarily arises from a scalar coupling, with the cross section given by Eq. 1.24:

$$\sigma_{N,0}^{SI} = \frac{4\mu_N^2}{\pi} (Z f_p + (A - Z) f_N)^2, \tag{1.24}$$

where A is the number of nucleons, Z is the number of protons, and f_p, f_N are the couplings of the WIMP to protons and neutrons, which in most cases are similar, giving a simplified form of Eq. 1.24 as Eq. 1.25:

$$\sigma_{N,0}^{SI} = \frac{4\mu_N^2}{\pi} A^2 f^2. \tag{1.25}$$

In order to compare and combine results from experiments that use different target materials, the WIMP-nucleon cross section $\sigma_{n,0}^{SI}$ is defined as in Eq. 1.26:

$$\sigma_{n,0}^{SI} = \frac{4\mu_n^2}{\pi} f^2, \tag{1.26}$$

where μ_N is replaced by μ_n, the WIMP-nucleon reduced mass, and the A^2 dependence is removed. In this way, the SI cross section for any target nucleus containing A nucleons is given as Eq. 1.27:

$$\sigma_{N,0}^{SI} = \sigma_{n,0}^{SI} \frac{\mu_N^2}{\mu_n^2} A^2. \tag{1.27}$$

Putting all these together, the expected differential event rate for spin-independent WIMP scattering can be written as Eq. 1.28:

$$\frac{dR}{dE_R} = \frac{\rho_{DM}}{2\mu_N^2 m_\chi}\sigma_{n,0}^{SI}\frac{\mu_N^2}{\mu_n^2}A^2F^2(E_R)\int_{v_{min}}^{\infty}\frac{1}{v}f(\overrightarrow{v})d^3\overrightarrow{v}. \tag{1.28}$$

Note that the integration of the velocity term in Eq. 1.28 has an implicit maximum velocity set by the escape velocity of the galaxy, usually taken as $v_esc \approx 550km/s$ [31]. The form factor term F(ER) is typically found experimentally for various elements, as shown in Ref. [29]. In the case of lighter nuclei, it can often be approximated by unity, which results in $\sigma_N^{SI} = \sigma_{N,0}^{SI}$. Figure 1.7 shows the parameter space for the SI WIMP-nucleon cross section, along with the exclusion limits from several recent experiments.

The type of target material used in an experiment determines the mass range to which it is sensitive. A higher WIMP mass is expected to lead to a reduced interaction rate due to the lower abundance of WIMPs available to interact with the detector. Consequently, heavier target materials are more appropriate for WIMP searches at masses greater than 10 GeV. On the other hand, lighter target materials offer better sensitivity to WIMP masses below 10 GeV due to the kinematics of WIMP-nucleus scattering. Experiments such as XENON1T [32] and PandaX [33] that use liquid xenon as the target material fall into the first category, while the SuperCDMS experiment using germanium and silicon targets belongs to the latter.

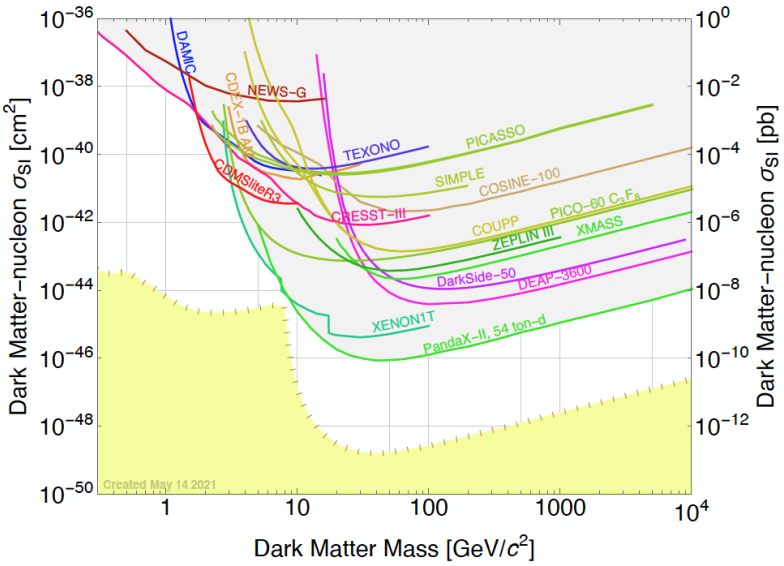

Figure 1.7: Parameter space of the spin-independent (SI) WIMP-nucleon scattering cross section σ_n^{SI} over WIMP mass. The curves shown are the exclusion limits on $\sigma_{n,0}^{SI}$ obtained by various dark matter search experiments over recent years. The yellow shaded region represents the neutrino fog [34]. The plot is taken from Ref. [28].

1.4.2 Light Dark Matter

Light dark matter (LDM) is usually motivated by production mechanisms that extend beyond the standard freeze-out process and can be found in various theoretical frameworks where the sub-GeV mass scale arises. Moreover, the origin of the dark matter relic density can be explained by several mechanisms, which propose that light dark matter interacts with Standard Model particles, for

instance, through the exchange of a light "dark photon," an axion, or via an electromagnetic dipole moment.

The masses of fermionic dark matter, such as WIMPs and light dark matter, are constrained to have masses above the keV level due to the Lyman-alpha forest astrophysical observations made of substructure formation [35]. Specifically, the number density of sub-keV fermionic dark matter would be large enough that its Fermi degeneracy pressure in the early universe would affect the formation of galactic substructure [36]. This constraint has led to a class of "Ultralight Dark Matter" comprised of bosonic dark matter candidates; bosonic dark matter would not produce Fermi degeneracy pressure and thus avoids the issue with galactic substructure formation. Two prominent bosonic dark matter candidates that are described in this subsection are dark photons and axion-like particles (ALPs).

Since light dark matter (including both sub-GeV fermionic dark matter scattering with electrons and bosonic dark matter of dark photons and ALPs) is the target signal of this analysis, we leave the details of the signal model derivations to Section 4.

1.4.3 Lightly Ionizing Particles

Free particles with fractional charges are a possibility in extensions of the Standard Model that include additional U(1) gauge symmetries [37][38]. However, they have yet to be detected in collider or astrophysical experiments. As they pass through matter, these particles would lose energy at a much slower rate than known minimum ionizing particles, leading to their classification as Lightly Ionizing Particles (LIPs), or Fractional Charged Particles (FCPs).

The lightly ionizing nature of LIPs allows for their detection in direct detection experiments, though the search strategies differ. LIPs are expected to interact primarily with electrons, losing only a small amount of energy in the process. As a result, energetic LIPs would leave straight trajectories that could be reconstructed using a stack of detectors. The modular design of the CDMS is particularly suited for this purpose. Stringent upper limits on the flux of cosmogenically produced energetic particles with an electric charge smaller than e/6 were derived from CDMS II data [39]. Using a similar approach, SuperCDMS SNOLAB could be sensitive to LIPs with a fractional charge 10 times smaller than that detected by its predecessor CDMS II. This enhanced sensitivity is attributed to SuperCDMS SNOLAB's lower background levels, thicker detectors, and improved detector resolution. Fig. 1.8 shows the projected sensitivities of SuperCDMS SNOLAB LIP searches, overlaid with the results from MACRO, the most sensitive prior search for energetic cosmogenic fractional charges greater than e/6.

1.5 Dark Matter Direct Detection

Searches for WIMP dark matter can be broadly categorized into three types: direct searches, which look for dark matter interacting with a detector target; indirect searches, which seek particles produced from dark matter decaying or annihilating in the universe; and collider experiments, where a transverse energy imbalance in the final state may indicate the presence of a non-interacting particle. Fig. 1.9 illustrates the three types of searches using Feynman diagrams, and Fig. 1.10 shows observables of an elastic WIMP interaction with matter under different detecting strategies.

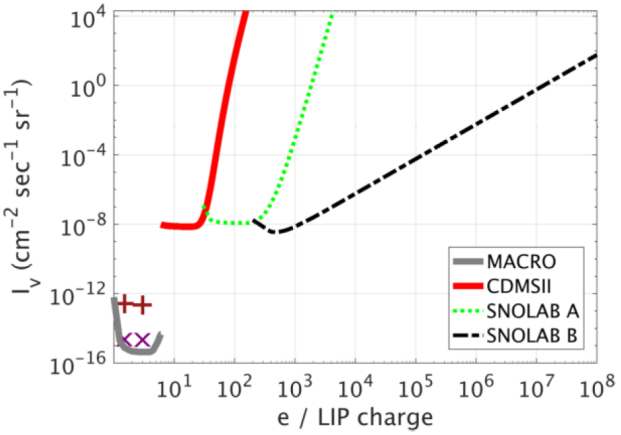

Figure 1.8: The projected sensitivity of the cosmogenic LIP searches at SNOLAB compared to prior LIP searches. The projected sensitivity of the low-background-level, one-tower search (green dots) and the higher-background-level one-detector search (black dot-dashed) is shown. Both are sensitive to fractional charges far smaller than any prior search. The most sensitive prior search for energetic, cosmogenic fractional charges greater than $e/6$ is MACRO (gray solid) [40]. The most sensitive prior search for fractional less than $e/6$ is CDMS II (red solid) [41]. Both Kamiokande-II [42](×'s) and LSD [43] (+'s) have performed searches for LIPs with fractional charges of e/3 and 2e/3.

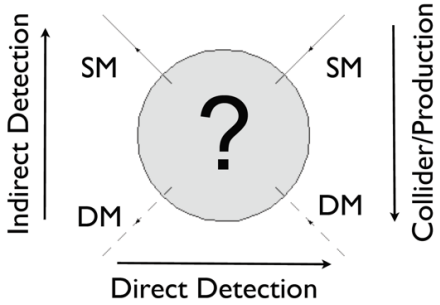

Figure 1.9: Illustration of different dark matter detection methods in terms of the Feynman diagrams.

1.5.1 Direct Detection

Direct detection experiments seek to observe dark matter particles as they interact with a target medium while passing through the Earth. The most commonly hypothesized interaction mechanism is the DM-nucleus scattering, which would result in low-energy recoils within the target medium that can be detected. This approach includes a variety of detection techniques. Cooled crystal detectors can be used to measure the ionization or heat generated by particle interactions. Noble gas detectors can measure the scintillation light produced by interactions with liquid xenon or argon. Charge-coupled devices can detect ionization across an array of pixels. In addition, bubble chambers and resonant detectors designed to probe low-mass dark matter candidates are also employed in this field.

1.5.2 Indirect Detection

Indirect detection experiments aim to identify the products generated by the self-annihilation of dark matter particles or, if dark matter is unstable, by the decay of these particles. The primary

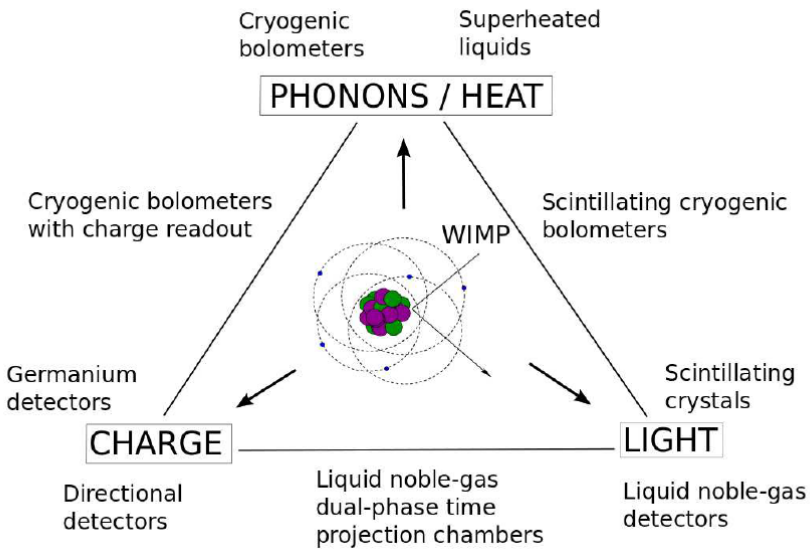

Figure 1.10: Possible signatures of direct detection WIMP experiments. Diagram taken from Ref. [44].

products of interest are high-energy gamma rays or Standard Model particle-antiparticle pairs. These experiments often search for an excess of decay products around massive objects such as stars or black holes, where the accumulation of dark matter in these regions would significantly enhance the likelihood of self-annihilation. Balloon-borne instruments and space probes are also included in this category.

1.5.3 Collider Searches

Most searches for dark matter using particle accelerators focus on detecting a significant imbalance in momentum among the products of particle collisions. This imbalance is typically caused by a non-interacting particle escaping, which results in a recoil effect against, for example, a hadronic jet [45], photons [46], or Z and W bosons [47]. Collider searches may also look for vertices and resonances, from an invisible particle decaying into multiple SM particles that leave reconstructed tracks in the detector.

1.6 The SuperCDMS SNOLAB Experiment

The Super Cryogenic Dark Matter Search (SuperCDMS) at the Sudbury Neutrino Observatory (SNOLAB) is a next-generation experiment designed to search for low-mass dark matter particles less than 10 GeV. It is the successor to previous generations of CDMS experiments including CDMS-I, CDMS-II and SuperCDMS Soudan. Projected sensitivities for the experiment suggest that it will be capable of conducting a comprehensive search for dark matter particles within this mass range. The primary scientific objective of SuperCDMS SNOLAB is to detect WIMPs with masses below 10 GeV through spin-independent dark matter-nucleus elastic scattering, utilizing complementary target nuclei (Si and Ge) and detection techniques. Additionally, secondary goals include searching

for other low-mass dark matter candidates such as solar axions and lightly ionizing particles. The detectors used in this experiment feature a lower energy threshold compared to previous CDMS detectors, enhancing sensitivity to lower dark matter masses. Moreover, the SNOLAB facility, operated in a class-2000 clean room 2 km underground as illustrated in Fig. 1.11, provides 6000 meters of water-equivalent shielding, reducing background radiation from cosmic rays by a factor of 50 million. It offers an exceptionally low-background environment, further improving sensitivity to potential dark matter interactions.

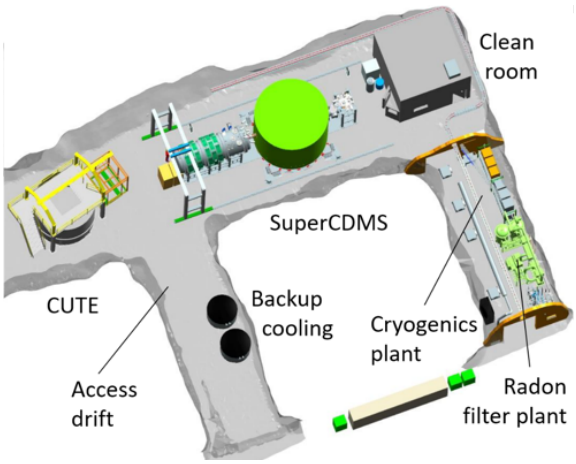

Figure 1.11: A diagram illustrating the location of the SuperCDMS facilities in SNOLAB [1].

Figure 1.12 shows a schematic diagram of the SuperCDMS SNOLAB experiment [2]. The SuperCDMS SNOLAB detectors are configured in tower arrangements and housed within a vacuum-sealed container known as the "Snobox," which is constructed from copper. A dilution refrigeration system cools both the Snobox and its internal detectors to temperatures ranging from approximately 15 to 30 mK. The Snobox is surrounded by multiple layers of shielding to protect against various sources of background radiation. The outer water tanks shield against cavern neutrons, the gamma shield mitigates external gamma rays, and the inner polyethylene layers absorb radiogenic neutrons emitted from the Snobox and gamma shield. Additionally, the entire setup is placed on a seismic platform to ensure isolation from seismic disturbances.

Although the SNOLAB facility provides a low background environment, several sources of background are still present and could influence the experiment, as shown in Fig. 1.13. Background sources are generally classified into those causing electron-recoil (ER) events and those causing nuclear-recoil (NR) events. Major contributors to ER-type backgrounds include beta decay products from cosmogenically produced tritium (^{3}H) contamination in the detectors, gamma rays and beta particles from the decay of contaminant radioisotopes in non-detector materials, and decay products from radioisotopes in non-detector materials activated by high-energy cosmic-ray secondaries. For silicon (Si) detectors, the most significant source of background events is the beta decay of the naturally occurring ^{32}Si isotope. In germanium (Ge) detectors, another significant background source is the activation lines produced by long-lived radioisotopes that decay via electron capture. The event rate from NR-type background sources is expected to be significantly lower compared to that from ER-type sources. Major contributors to the NR background rate include coherent neutrino-nucleus scattering, beta decay products from contaminant radioisotopes in non-detector

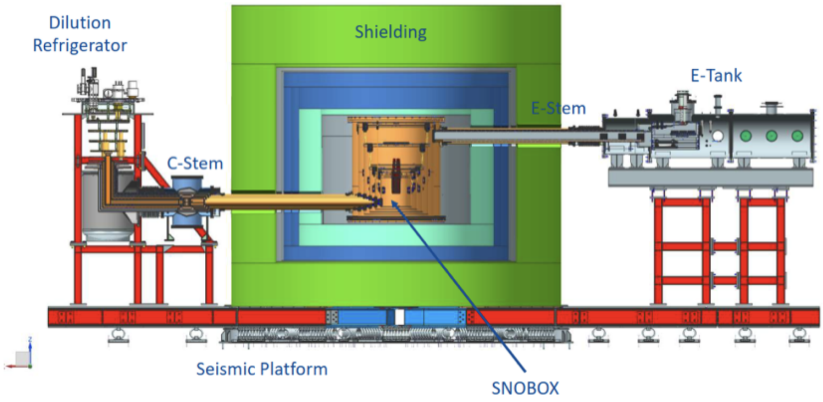

Figure 1.12: A schematic diagram of the SuperCDMS SNOLAB experiment is shown. The dark matter detectors are arranged in a tower configuration inside the Snobox. A dilution refrigeration system cools the Snobox and its contents to temperatures as low as 15 mK. Several shielding layers surround the Snobox to protect against various background sources. The entire setup is mounted on a seismic platform to isolate it from seismic activity. Diagram taken from Ref. [1].

materials, and neutrons induced cosmogenically or within the cavern environment.

Two designs of detectors, interleaved Z-sensitive ionization phonon (iZIP) detectors and high voltage (HV) detectors, are employed in the SuperCDMS SNOLAB experiment, each applied to Si and Ge materials. The details of detector physics will be discussed in Section 2. The iZIP and HV detectors employ distinct but complementary detection techniques to explore the parameter space of WIMP-nucleus scattering. The initial payload of SuperCDMS SNOLAB will feature four detector towers, which will collectively include ten Ge iZIP detectors, two Si iZIP detectors, eight Ge HV detectors, and four Si HV detectors. Together, these detectors will contribute to a total exposure of 144.4 kg-years [2]. Fig. 1.14 shows the projected limits on the spin-independent (SI) WIMP-nucleon cross section for the initial payload of the SuperCDMS SNOLAB experiment. The yellow-shaded region called "the neutrino floor" represents the background level of neutrino interactions when searching for dark matter particles.

In addition to the SNOLAB experiment, the SuperCDMS collaboration includes several other smaller scale experiments conducted at various research and development (R&D) test facilities. Among those, the HVeV experiment, initially designed as a prototype detector study but later yielding promising constraints on several dark matter models, is the primary focus of this dissertation. The details of the HVeV experiments and detector designs are introduced in Chapter 2. The experimental setup for the latest run, HVeV Run 4, which we analyze in this dissertation, is introduced in Chapter 3. Chapter 4 will focus on the signal models and detector response models of this analysis. Finally, Chapter 5 will cover all details of the HVeV Run 4 analysis effort and show the final results.

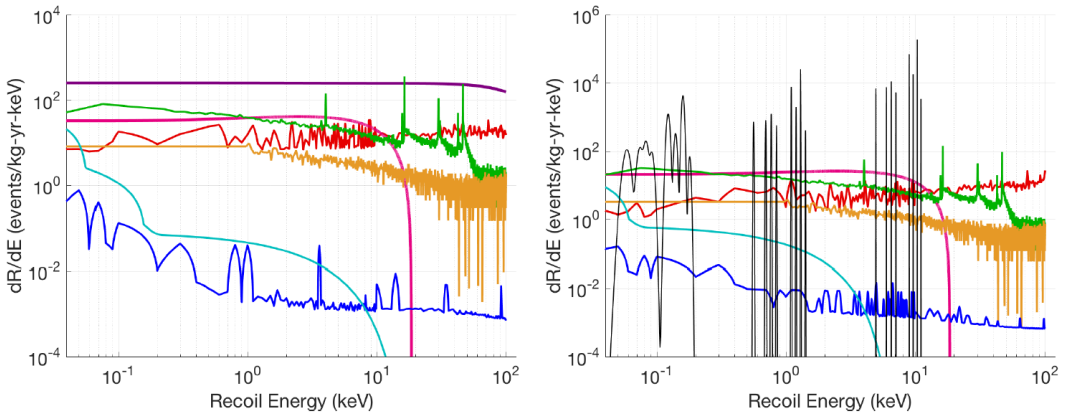

Figure 1.13: Raw background spectra of single scatter interactions in Si (left) and Ge (right) detectors, obtained from the Monte Carlo simulation [2] are presented. The spectra are categorized by components and plotted as a function of recoil energy (ER or NR, depending on the interaction). Tritium (^{3}H, pink) and silicon-32 (^{32}Si, purple) are the predominant individual contributors to the backgrounds in the Ge and Si detectors, respectively. The activation lines for Ge (black) are shown convolved with a 10 eV RMS resolution (σ_{Ph} for the Ge HV detectors) to enhance clarity in this figure. Other components include Compton scatters from gamma rays (red), surface beta particles (green), surface ^{206}Pb recoils (orange), neutrons (blue), and coherent elastic neutrino-nucleus scattering (cyan). Plot is taken from Ref. [2].

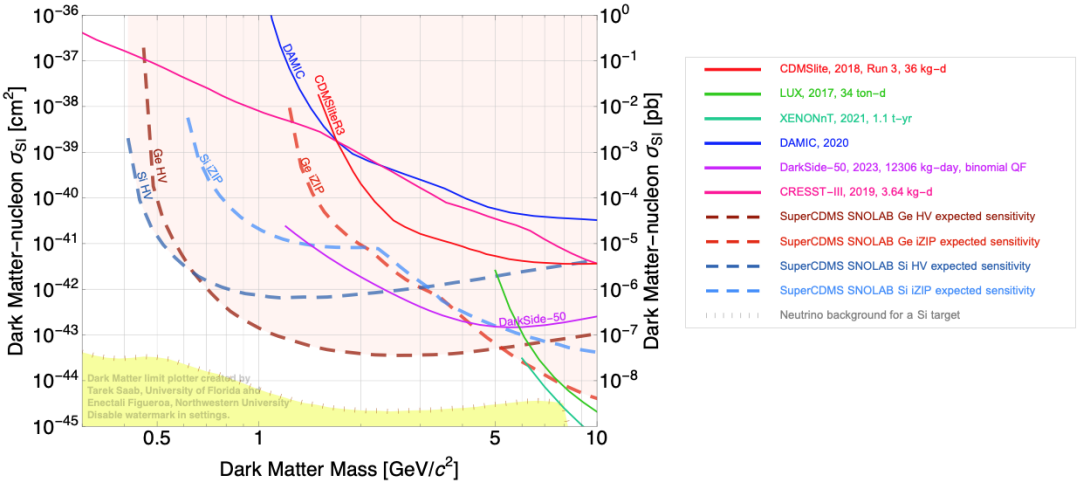

Figure 1.14: Projected limits on the spin-independent (SI) WIMP-nucleon scattering cross section σ_n^{SI} over WIMP mass for the initial payload of the SuperCDMS SNOLAB experiment. The projected limits are shown separately for the four types of detectors that will be used, overlaid with exclusion limits from other dark matter search experiments in this low-mass region [48][49][50][51][52][53]. The yellow-shaded region is the neutrino floor for a Si target [54]. This plot was produced using the SuperCDMS Limit Plotter v5.18.

Chapter 2

HVeV Runs and Detector Designs

This chapter provides an overview of the HVeV experiments and the detector designs. Section 2.1 introduces the underlying cryogenic semiconductor detector physics used in the SuperCDMS experiment. Section 2.2 discusses the HVeV detectors and their characteristic optimizations. Finally, Section 2.3 reviews previous HVeV runs.

2.1 SuperCDMS Cryogenic Semiconductor Detectors

This section discusses the physical processes in the detection of dark matter particles with cryogenic semiconductor detectors.

2.1.1 Semiconductor Crystal Ionization

The periodic lattice of a semiconductor crystal features a continuous range of electron energy levels, resulting in a complex band structure, as illustrated in Fig. 2.1 for silicon and germanium. A narrow energy gap divides the filled valence bands from the empty conduction bands. When electrons are excited across this gap, mobile electron-hole pairs are generated, which can then be manipulated and detected. The energy difference between the conduction and valence bands is known as the band gap energy E_g. Electrons will occupy energy states with energy E according to the Fermi-Dirac distribution f(E), as shown in Eq. 2.1:

$$f(E) = \frac{1}{e^(E - E_F)/k_b T} + 1, \tag{2.1}$$

where k_b is the Boltzmann constant, T is the temperature of the system, and E_F is the Fermi constant, which is halfway between the valence and conduction bands. Methods such as doping can change the value of E_F to make it harder or easier for a semiconductor to carry a current, as illustrated in Fig. 2.2. Here, p-type means a semiconductor doped with Group V elements, while n-type means one doped with Group III elements. However, for semiconductor detectors, only intrinsic semiconductors without doping are widely used.

When the temperature is high, electrons in the valence band have a certain probability of moving to a state in the conduction band above E_F, leaving a "hole" in the valence band. This pairing of

an electron and a corresponding hole is usually referred to as an electron-hole pair (e^-h^+). The electrons in the conduction band and the holes in the valence band can move around in the crystals, providing conductivity to the semiconductor.

However, if the temperature is very low as we operate cryogenic semiconductor detectors, almost all electrons occupy states in the valence band, with negligible probability of appearing in the conduction band at equilibrium. Electrons will only move into the conduction band if there is an external energy deposition larger than the band gap energy, which allows us to take advantage of such features to detect interactions between dark matter and Standard Model particles.

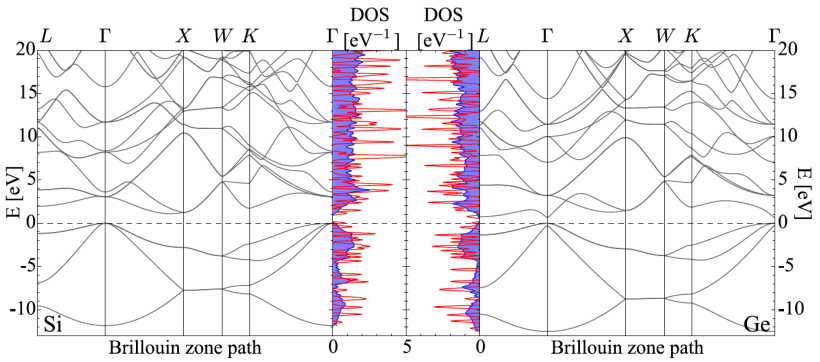

Figure 2.1: Scissor corrected [55][56] band structure for silicon (left) and germanium (right) as calculated with Quantum ESPRESSO [57] with a very fine k-point mesh. The horizontal dashed line indicates the top of the highest valence band. The four bands below the horizontal dashed line are the valence bands while the bands above the dashed line are the conduction bands. The density-of-states (DOS) are shown as a function of the energy for a very fine k-point mesh [58] (blue) and for the 243 k-point mesh (red). A Gaussian smearing of 0.15 eV was used to generate a smooth function. Plot is taken from Ref. [58].

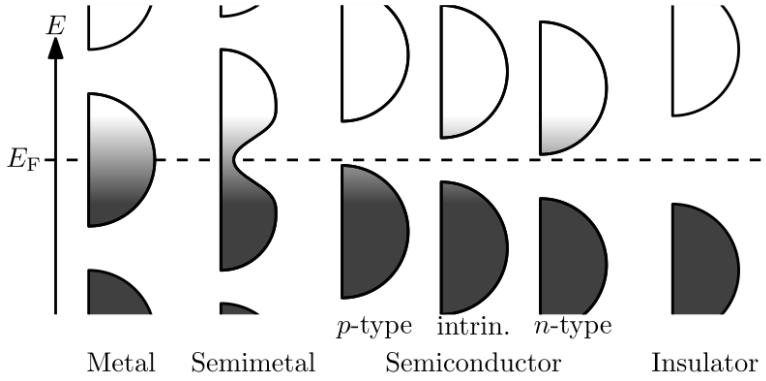

Figure 2.2: Filling of the electronic states in various types of materials at equilibrium. Here, height is energy while width is the density of available states for a certain energy in the material listed. The shade follows the Fermi–Dirac distribution. Plot is taken from Ref. [59]

2.1.2 Neganov-Trofimov-Luke Effect and Phonon Amplification

There are two types of phonons in the semiconductor crystal, thermal phonons and athermal phonons. Phonons as quantized vibrations of atoms in a solid are often treated as particles in the

study of heat and sound conduction. Typically, phonons in a material are in thermal equilibrium, which means that their distribution follows the Bose-Einstein distribution at a given temperature, as shown in Eq. 2.2:

$$\langle n_i \rangle = \frac{1}{e^(E-\mu)/k_b T} - 1, \tag{2.2}$$

where $\langle n_i \langle$ is the average number of particles in the energy state E_i, μ is the chemical potential, k_b is the Boltzmann constant and T is the temperature. Such phonons are referred to as thermal phonons and will have energies of $\sim 1\mu eV$ for a detector operated at the temperature of 10 mK. Meanwhile, athermal phonons occur in situations where the thermal equilibrium is disturbed. It can happen, for example, when a material is subjected to a sudden, non-equilibrium process such as the scattering of a dark matter particle with either the nucleus or the electron, depositing recoil energy in the crystal. Moreover, when the electron-hole pairs ionized from the scattering drift across the detector under an external electric field, secondary phonons will be generated due to the phonon amplification caused by the Neganov-Trofimov-Luke (NTL) effect [60][61]. Both the prompt phonons from the primary recoil and the secondary NTL phonons are athermal phonons, with an average energy in silicon or germanium crystals ≥ 0.4 meV at 10 mK [62], discriminating themselves from thermal phonons.

The superCDMS cryogenic semiconductor detector technology exploits the interconnected charge and phonon systems in Si and Ge to make ultra-low-energy measurements free from the dark current. At cryogenic temperatures, the crystal lacks free charge carriers, so no current flows when a voltage is applied, and only a small population of low-energy thermal phonons is present. When a particle interacts with a nucleus or electron in a semiconductor, the resulting recoil generates both free charge carriers (electron-hole pairs) and athermal phonons, both with energies significantly higher than thermal energies. By applying an electric field to drift the charges to the surface for collection and by detecting the produced phonons, the energy, position, and type of the recoil can be reconstructed.

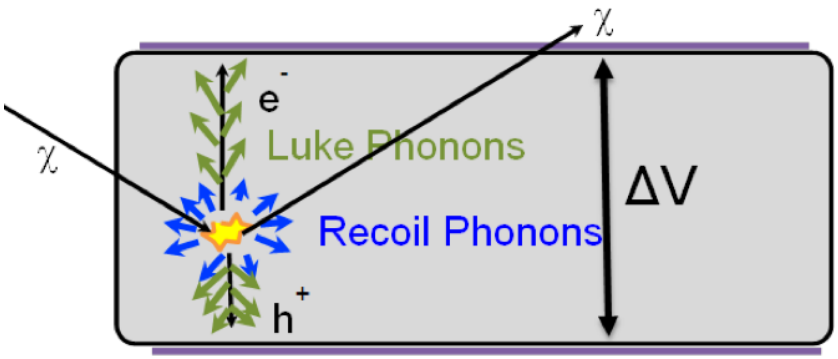

Figure 2.3: Illustration of emission of primary phonons from the interaction site and generation of Neganov-Trofimov-Luke phonons along the ionization drift path [2].

For an electron recoil in germanium, an electron-hole pair is generated for every 3.0 eV of recoil energy (3.8 eV in silicon [63]). Nuclear recoils are less efficient, with efficiency reduced by a factor of 2 to 10 above 1 keV recoil energy ($\mathrm{keV_r}$), as well described by the Lindhard yield model (which will be discussed later) at higher energies. Most of the energy not used in electron-hole pair production is instead released as athermal phonons. The generated electron-hole pairs quickly relax to the

material's band gap, releasing their excess energy as athermal phonons. When these charge carriers recombine with partners, they release the remaining band gap energy in the form of phonons. While a small portion of the recoil energy, potentially more than 50 eV_r, may become trapped in states with long lifetimes (such as crystal defects like Frenkel pairs) and thus be lost from the athermal phonon signal, the majority of the energy, especially for recoils exceeding keV_r, is deposited in the athermal phonon system, leading to the production and collection of electron-hole pairs.

2.1.3 Athermal Phonon Sensors

SuperCDMS utilizes Quasiparticle-trapping-assisted Electrothermal-feedback Transition-Edge Sensors (QETs) to measure athermal phonon energies. The overall phonon detection architecture is illustrated in Fig. 2.4 [2]. When an event occurs in the detector substrate, it generates athermal phonons that propagate to the detector surface and are absorbed by superconducting aluminum (Al) collection fins. These absorbed phonons break Cooper pairs, producing quasiparticle excitations (essentially free electrons) within the Al. The quasiparticles then diffuse through the Al, with the majority ideally becoming trapped in the attached tungsten (W) Transition Edge Sensors (TESs). Their energy is deposited there, causing the TESs to heat up. The tungsten is voltage-biased within its narrow superconducting transition, and the slight increase in electron temperature due to the deposited energy results in a significant (and measurable) change in electrical resistance. The geometry of the QET used for the SuperCDMS SNOLAB CDMS-HV detector design is shown in Fig. 2.5.

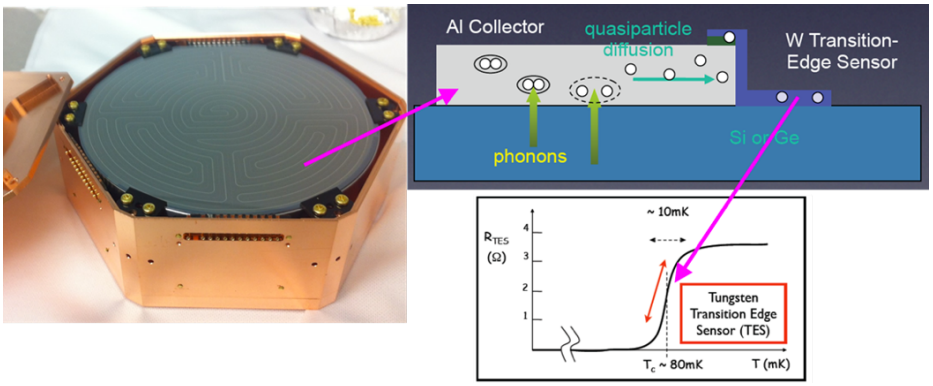

Figure 2.4: Illustration of athermal phonon collection and signal generation in SuperCDMS detectors [2].

By substantially increasing the surface area for the athermal phonon collection compared to designs that rely solely on TESs, such as those used in experiments like CRESST [64][65][66], superconducting aluminum fins significantly reduce the signal collection time, which in turn provides position information. Additionally, the increased signal bandwidth better aligns with the TES bandwidth, improving energy resolution and further enhancing position information. Since a phonon must possess sufficient energy to break a Cooper pair into quasiparticles ($\sim 340\mu eV$), only athermal phonons are collected.

The use of athermal phonons in the SuperCDMS detector design significantly decouples sensor performance from the heat capacity of the crystal. This decoupling enables an increase in individual detector mass compared to thermal phonon calorimeters, thereby enhancing the exposure per detector day of live time. Moreover, it allows for improved detector energy resolution through the

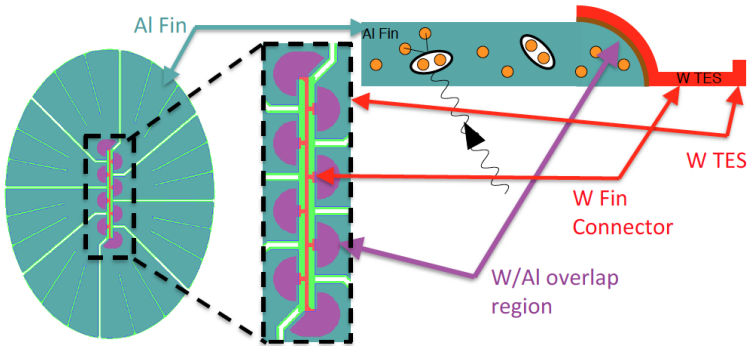

Figure 2.5: (Left) Diagram of the SuperCDMS HV athermal phonon sensor design. (Middle) Closeup of the W TES and its connections to the Al phonon collection fins. (Right top) Heuristic cross-sectional view of the athermal phonon sensor. Plot is taken from Ref. [2].

refinement of QET design parameters. The energy resolution can be estimated as a function of key device parameters [67][68], as given in Eq. 2.3:

$$\sigma^2(E) = \left[4\int_0^\infty \frac{|S(f)|^2}{N^2(f)}df\right]^{-1}, \tag{2.3}$$

where $S(f)$ is the energy-integral-normalized signal template Fourier transform and $N^2(f)$ is the noise power spectral density in power units.

2.1.4 TES SQUID Circuit and Thermal Feedback System

Resistance changes in the TES are converted to a measurement signal using superconducting quantum interference devices (SQUIDs). SQUIDs operate using superconducting loops containing Josephson junctions to measure extremely small magnetic fields. If the current through a SQUID exceeds a critical current, a voltage will appear across the SQUID with a periodic dependence on the magnetic flux through the SQUID. This voltage dependence on magnetic flux is illustrated in Fig. 2.6, with the period of oscillation equal to one flux quantum Φ_0. Fig. 2.7 shows a simplified schematic of the TES-SQUID readout circuit.

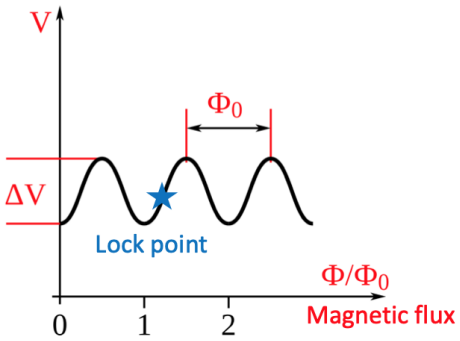

Figure 2.6: Periodic voltage response due to flux through a SQUID. The periodicity is equal to one flux quantum, Φ_0.

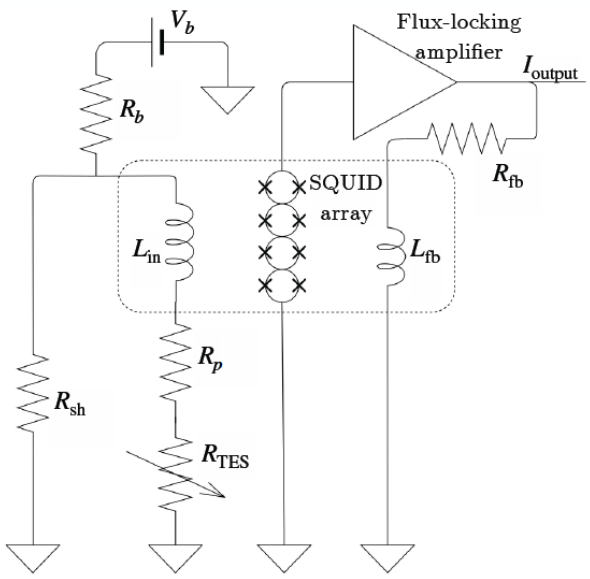

Figure 2.7: Simplified schematic of the TES-SQUID circuit used for HVeV detectors [62]. Plot is taken from Ref. [28].

An array of TESs in parallel is held at a temperature T_0 near the critical temperature by providing a voltage bias V_b with a bias resistance R_b that keeps a constant current I_s through the TESs. Because the TESs are thermally coupled with the detector substrate that has a bath temperature of T_b, the TESs exhibit thermal power loss described in Eq. 2.4:

$$P = K(T_0^5 - T_b^5), \tag{2.4}$$

where K is the thermal conductivity between the TESs and the thermal bath of the detector substrate and $T_b < T_0$. When there is no heat deposition in the TESs, this thermal power loss is equal to the Joule power provided by the bias voltage and current through the TESs, described by Eq. 2.5:

$$P = I_s^2 R_{\mathrm{TES}} = \frac{V_b^2}{R_{\mathrm{TES}}}, \tag{2.5}$$

where R_{TES} is the TES resistance. The shunt resistor R_{sh} in the TES-SQUID circuit ensures that the voltage across the TESs remains relatively constant. Therefore, the Joule power can be expressed solely as $P = V_b^2/R_{\mathrm{TES}}$, which provides the necessary negative feedback system referred to as electrothermal feedback. As the resistance of the TESs increases, the Joule power provided to the TESs will decrease and become less than the thermal power loss. This power inequality returns the TESs to their original operating temperature and resistance.

The array of TESs are also in series with a coil that has an input inductance L_{in} as seen in the circuit diagram in Fig. 2.7. The SQUIDs are connected to a flux-locking amplifier which serves multiple purposes, one of which is to provide a bias current through the SQUIDs to lock them at some point on the periodic voltage-magnetic flux curve. Fig. 2.6 shows an example of a lock point. The magnetic flux from L_{in} induces a voltage across each of the SQUIDs, and the total voltage

signal across the SQUID array is amplified by the flux-locking amplifier. Let the amplified output voltage signal from the SQUID array be denoted as V_{SQ}. A feedback voltage V_{fb} is provided to supply a current through a feedback resistor R_{fb} and an additional coil that provides a feedback inductance L_{fb} to the array of SQUIDs.

The purpose of this feedback inductance is to continuously counteract the magnetic flux through the SQUIDs supplied by Lin by supplying an opposing magnetic flux. Through a negative-feedback loop gain circuit, V_{fb} provides the voltage required to keep the net magnetic flux through the SQUIDs, and thus V_{SQ}, constant at all times. This remains true when the TES-SQUID circuit is in steady state and there is no heat deposition in the TESs. When a heat deposition does occur, the current through the input coil will decrease, and V_{fb} will adjust to the necessary voltage to keep V_{SQ} constant. The actual signal taken as a measurement is V_{fb} recorded over time and later digitized and converted to current through the TESs.

The flux-locking feedback system is a critical component to measure heat depositions in the TESs. Keeping the SQUIDs locked at one point on the periodic voltage-magnetic flux curve ensures a linear relationship between the current through the input coil and V_{fb}. Additionally, the lock point determines the amount of direct current (DC) offset that signals are subject to; the baseline current of signals measured at different lock points will be offset by different amounts. Although this flux locking mechanism is very robust, there are rare instances in which the lock point can spontaneously and unintentionally jump to a new position during data acquisition.

2.1.5 Ionization Yield and Charge Measurement

The number of electron-hole pairs produced per unit recoil energy depends on the recoil type, electron or nuclear. The ionization production efficiency of nuclear recoils relative to that of electron recoils is well described at higher energies by the Lindhard nuclear screening model [69], but begins to fail at lower recoil energies of ∼1 keV. Multiple measurements were performed in this range to obtain empirical values as shown in Fig. 2.8, taken from Ref. [70] where the HVeV detectors are used in that measurement.

The total amount of phonon energy measured by the detector for a single particle interaction, E_{ph}, is the sum of the recoil energy E_r of the interaction and the energy produced from the drifting electron-hole pairs, as shown in Eq. 2.6:

$$E_{ph} = E_r + n_{eh} e V_{bias}, \tag{2.6}$$

where $n_e h$ is the number of electron-hole pairs produced in the event. Although some of the recoil energy is required to excite the $n_e h$ electron-hole pairs, the energy is recovered as the charges recombine with the semiconductor crystal on the surface. Moreover, Eq. 2.6 makes it clear how the NTL effect is able to amplify phonon signals. The signals from small recoil energies can be amplified by applying a strong voltage bias and increasing the amount of NTL phonons produced.

The number of electron-hole pairs produced in an interaction is proportional to the recoil energy. Although an initial ionized electron may receive a surplus of energy above the band gap, a cascading process occurs that distributes the energy of the initial electron to create additional electron-hole pairs [78]. The mean number of electron-hole pairs produced for a given energy deposition of E_r is

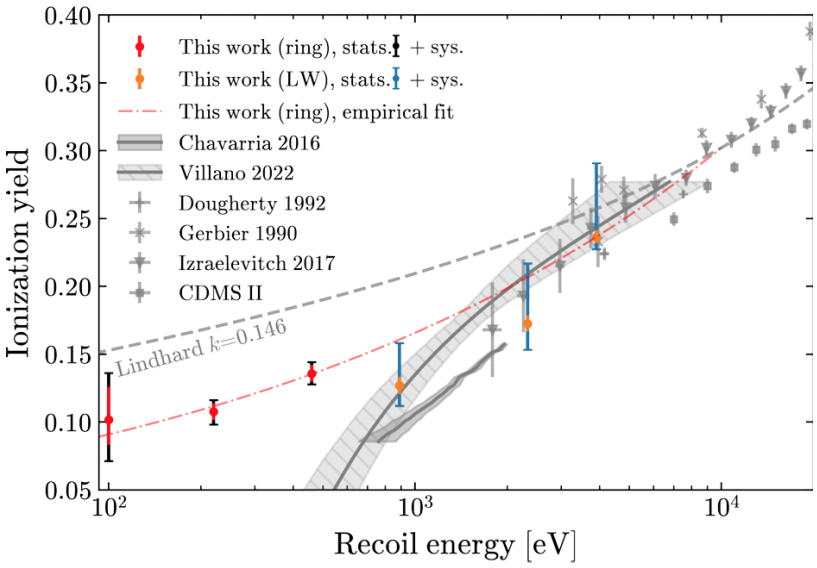

Figure 2.8: The measured ionization yields, along with their statistical and total uncertainties and a fit with a power-law function. Also shown are data points from previous measurements [71][72][73][74][75][76]. The dashed line shows the Lindhard model with k=0.146 [77]. Plot is taken from Ref. [70], and the red and orange points and lines labeled as "this work" refer to the measurements in that paper.

given by Eq. 2.7:

$$\langle n_{eh} \rangle = Y(E_r) \frac{E_r}{\varepsilon_{eh}}, \tag{2.7}$$

where ε_{eh} is the average energy to produce a single electron-hole pair (3.0 eV in Ge and 3.8 eV in Si).

Y(E_r) is the ionization yield that describes how much of the recoil energy is converted to produce electron-hole pairs. For electron-recoil (ER) interactions, $Y(E_r) \approx 1$ in average in the high E_r limit. For nuclear-recoil (NR) interactions, $Y(E_r) < 1$ and is described by Lindhard theory as well as empirical fits to data for low recoil energies where Lindhard theory is known to become inaccurate. For two recoil types above ~100 eV E_r, the averaged phonon energy $\langle E_{ph} \rangle$ can be expressed as in Eq. 2.8:

$$\langle E_{ph} \rangle = \begin{cases} E_r(1 + Y(E_r) eV_{bias}/\varepsilon_{eh}) & \text{Nuclear recoil} \\ E_r(1 + eV_{bias}/\varepsilon_{eh}) & \text{Electron recoil} \end{cases}. \tag{2.8}$$

.

2.1.6 SuperCDMS HV and iZIP detectors

The SuperCDMS Collaboration employs various types of solid-state detectors for DM search experiments. Four types of detectors will be used for the SuperCDMS experiment at SNOLAB as mentioned in Section 1: interleaved Z-sensitive ionization phonon (iZIP) detectors made of either Si

or Ge, and high voltage (HV) detectors made of either Si or Ge [2]. Each of these detectors consists of a cylindrical crystal that is 100 mm in diameter and 33.3 mm thick. Si and Ge detectors have a mass of 0.61 and 1.39 kg, respectively. iZIP and HV detectors are fabricated identically, but utilize a different combination and layout of either ionization (charge) sensing channels or phonon sensing channels in order to optimize the detectors for separate purposes. The charge channels consist of high-electron-mobility transistors (HEMTs) that measure the amount of charge and energy produced by an event. The phonon channels use aluminum fins to absorb phonons and tungsten transition edge sensors (TESs) to measure the amount of phonon energy.

iZIP detectors (as shown in Fig. 2.10a) operate using a combination of phonon and charge channels. Both the top and bottom surfaces of the detector are fitted with six phonon channels interleaved with two charge channels. A small voltage bias of $\sim 5 - 10V$ is applied to allow electron-hole pairs to drift to either surface. The bottom image of Fig. 2.9 shows the channel layout of the iZIP detectors. By separately measuring phonon and charge signals, iZIP detectors can discriminate between nuclear recoil (NR) and electron recoil (ER) interactions with the detector. On average, the measured charge signal E_{ch} as defined in Eq. 2.9:

$$E_{ch} = n_{eh}\varepsilon_{eh} \sim Y(E_r)E_r, \tag{2.9}$$

is equal to the amount of energy from ionization produced for a given event.

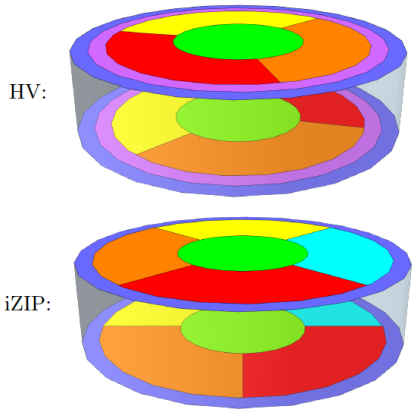

Figure 2.9: Channel layout for the HV (top) and iZIP (bottom) detectors. Both have six phonon channels on each side. For HV detectors, the wedge channels on the bottom surface are rotated by 60° with respect to those on the top, while for iZIP detectors it is 45°. Diagrams are taken from Ref. [2].

This charge energy can be compared to the measured phonon energy E_{ph}, which has an average value given in Eq. 2.8. Isolating for E_r and substituting in Eq. 2.9, the measured charge and phonon signals are related by Eq. 2.10:

$$E_{ch}/E_{ph} \sim \left[\frac{1}{Y(E_r)} + \frac{eV_{bias}}{\varepsilon_{eh}}\right]^{-1}, \tag{2.10}$$

which shows that the relationship between E_{ch} and E_{ph} can be approximated as a line with a slope

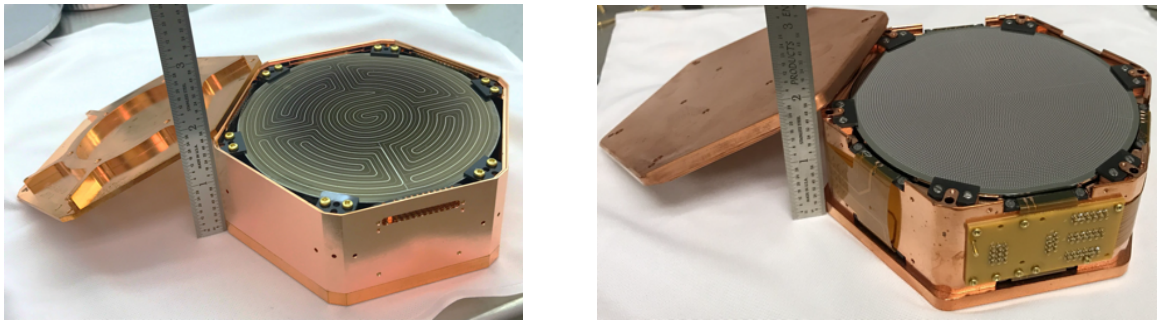

(a) CDMS-iZIP (b) CDMS-HV

Figure 2.10: A photograph of CDMS-iZIP detector (left) and CDMS-HV detector (right) inside the detector housing. The size of each detectors is 100 mm × 33 mm. Diagrams are taken from Ref. [2].

of $[1/Y(E_r) + eV_{bias}\varepsilon_{eh}]^{-1}$.

For ER events with $Y(E_r) = 1$, the slope of E_{ch} versus E_{ph} is greater than that of NR events with $Y(E_r) < 1$. By plotting the E_{ch} and E_{ph} data of events, ER and NR interactions can be distinguished based on which slope they follow. This remains true as long as the resolution is high enough and the applied voltage bias remains relatively small; if $eV_{bias}/\varepsilon_{eh} \gg 1/Y(E_r)$ in Eq. 2.10, the distinction between ER and NR events becomes less apparent. iZIP detectors can utilize this ER/NR discrimination to identify events resulting from ER interactions. From the perspective of NR DM searches, this discrimination can be used to remove ER backgrounds that interact with the bulk of the detector.

HV detectors (as shown in Fig. 2.10b) consist of only phonon channels, with six channels arranged on both the top and bottom surfaces. The top image in Fig. 2.9 shows the channel layout of the HV detectors. HV detectors have more phonon sensors compared to iZIP detectors, allowing for better phonon collection and therefore better phonon energy resolution and a lower energy threshold. Furthermore, the HV detectors will be operated with a bias voltage of up to $\sim 100V$. The high operating voltage allows for a greater amplification of the phonon signal due to NTL production, and allows the HV detectors to be sensitive to much lower recoil energies. Table 2.1 summarizes the properties for each detector type for the SuperCDMS SNOLAB experiment [2]. The listed values for the phonon and charge energy resolution depend on the properties of the sensor designs that are not discussed here.

Table 2.1: Summary of the properties for iZIP and HV detectors expected for the SuperCDMS SNOLAB experiment. All values in the table are from Ref. [1].

	Ge-iZIP	Si-iZIP	Ge-HV	Si-HV
Phonon energy resolution [eV]	33	19	34	13
Charge energy resolution [eV]	160	180	-	-
Voltage bias [V]	6	8	100	100
Number of detectors	10	2	8	4
Exposure [kg-year]	56	4.8	44	9.6

The differences between the detectors can be used to explain the differences in the projected sensitivities for WIMP-nucleon scattering for each detector type. The iZIP detectors have a better

projected sensitivity for WIMP masses $\sim$ 5 GeV due to the ability of the iZIP detectors to remove the vast majority of expected background events [2] using ER/NR discrimination. This means that iZIP detectors are expected to operate in a nearly background-free mode where the sensitivity is only limited by the amount of exposure. The projected sensitivity for Ge iZIP detectors is better than that of Si because of the greater exposure of Ge iZIPs expected in the initial payload for the SNOLAB experiment. Conversely, HV detectors have better sensitivity for WIMP masses below $\sim$ 5 GeV because they are sensitive to lower nuclear recoil energies. However, because HV detectors cannot distinguish between ER and NR events, the projected sensitivities are limited by the background rate. The projected sensitivity for Si HV detectors is worse than that of Ge due to the additional background rate of beta particles caused by the decay of Si^{32}. However, Si HV detectors are sensitive to slightly lower WIMP masses compared to Ge. This is due to the kinematics of NR interactions and the fact that Si detectors contain lighter isotopes than Ge detectors.

The detectors described for the SNOLAB experiment are not the only detectors employed by the SuperCDMS collaboration. Other detectors with similar technologies have been developed in test facilities for the purposes of R&D and, in some cases, are used to perform DM search experiments. This includes a class of detectors known as high-voltage eV-scale (HVeV) detectors that are small, 0.93 g devices made of Si that utilize the same concepts as the SNOLAB HV detectors but have extremely high energy resolution, which we will introduce in Section 2.2.

2.1.7 Detector Leakage

When a high voltage is applied to the crystal detector, individual charge carriers could tunnel through the electrode into the crystal bulk [1], generating events in a similar way as single electron-hole pairs. In rare cases, such events could also pile up to produce multi-electron-hole pair events. These leakage events are different from the cosmic-ray-induced external events since they are from the detector itself.

2.2 Gram-Scale Prototype Detector

A SuperCDMS high-voltage eV resolution (HVeV) detector has a gram-scale crystal mass and single charge sensitivity. These detectors measure interactions of dark matter or background particles with the target material using cryogenic athermal phonon sensor technology similar to that of CDMS-HV detectors, as we discussed in Section 1.6.

Figure 2.11 shows the photo of a test Si detector before the first HVeV run, which employs a $1 \times 1 \times 0.4$ cm^3 thick Si crystal (0.93 gram) operated at $\sim$ 35mK [79]. Individual electron-hole pairs were resolved under 160 V bias voltage when a fiber optic provides photons of wavelength 650 nm (1.9eV) that each produce an electron-hole pair in the crystal near the grid. The energy resolution measured is $\sim$ 0.09 electron-hole pair [79].

2.3 Previous Iterations of HVeV Runs

So far, four separate HVeV Runs have taken place with improving detector designs and decreasing background event rate, resulting in stronger dark matter constraints after each iteration.

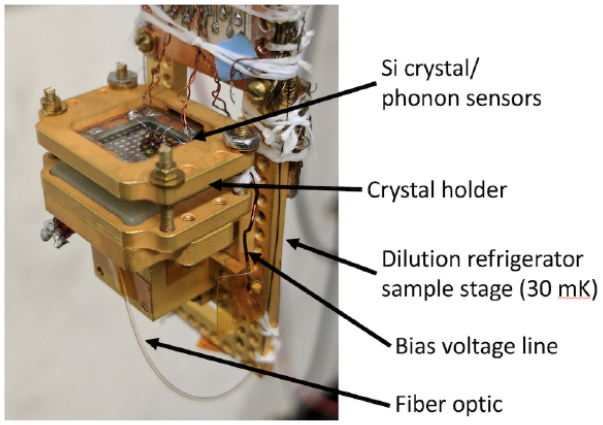

Figure 2.11: Photograph of Si detector mounted on mixing chamber stage of KelvinOx 15 dilution refrigerator with phonon sensors on top and bias grid below. A fiber optic illuminates the device from below with 650 nm photons. Plot is taken from Ref. [79].

2.3.1 HVeV Run 1

The first generation experiment employs a $1 \times 1 \times 0.4$ cm^3 high-purity Si crystal with mass 0.93 gram instrumented on one side with two channels of TES biased at -42 mV, and on the other side with a 20 % coverage electrode consisting of an aluminum/amorphous silicon bilayer biased relative to ground [79][80]. The QETs, which measure the total energy of the phonons produced in the substrate, had an energy resolution of $\sigma_{ph} \sim 14eV$ at the nominal base temperature of 33-36 mK. The single charge resolution was achieved by drifting electron hole pairs across 140V external voltage, resulting in an effective charge resolution of ~ 0.1 electron-hole pairs. A pulsed monochromatic 650 nm laser (~ 1.91 eV photons) provided periodic in-run calibrations. Data were acquired over 6 days with 36 hours of raw exposure (among which 27 hours of data with negative voltage [80] are used for the analysis). The acquired spectrum along with the cut efficiencies are shown in Fig. 2.12. One of the major achievements in HVeV Run 1 is the confirmation of the visibility of electron-hole peaks in the spectrum.

2.3.2 HVeV Run 2

The second-generation HVeV detector uses the same size of substrate as in HVeV Run 1. As in previous versions of HVeV detectors, QETs are arranged on one face of the detector substrate and are held at ground potential, while the opposing face contains an Al grid that is biased to induce an electric field of $0 - 625$ V/cm across the detector. The layout and geometry of the QETs on the detector substrate is referred to as the mask design, where in HVeV Run 2 it is named NFC, as shown in Fig. 2.13a, with the top view of the detector shown in Fig. 2.13b. The chosen parameters for the NFC design are TES length $l_{\mathrm{TES}} = 150\mu m$ and Al fin length$l_{fin} = 60\mu m$. In order to obtain positional information about events, the NFC mask design implements two separate channels of QET arrays. The inner channel is a square centered on the detector face, and the outer channel is a surrounding frame of equal area. Based on the chosen values of l_{TES} and l_{fin}, the number of QETs in each channel is 536 and 504 for the inner and outer channels, respectively. Each channel is connected to a separate TES-SQUID circuit, and thus energy depositions in each channel are

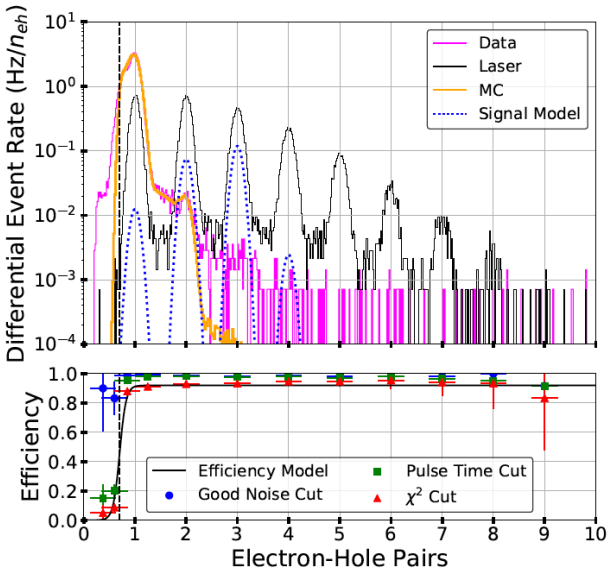

Figure 2.12: Top: HVeV Run 1 Event rate for calibration (black) and science exposure (magenta) with live time and quality cuts applied. Also shown are an impact ionization background Monte Carlo model (orange), and the signal distribution for an excluded dark photon model (dotted line). Bottom: Measured cut efficiency as a function of number of electron-hole pairs along with the efficiency model used in sensitivity estimates. Plot is taken from Ref. [80].

measured separately.

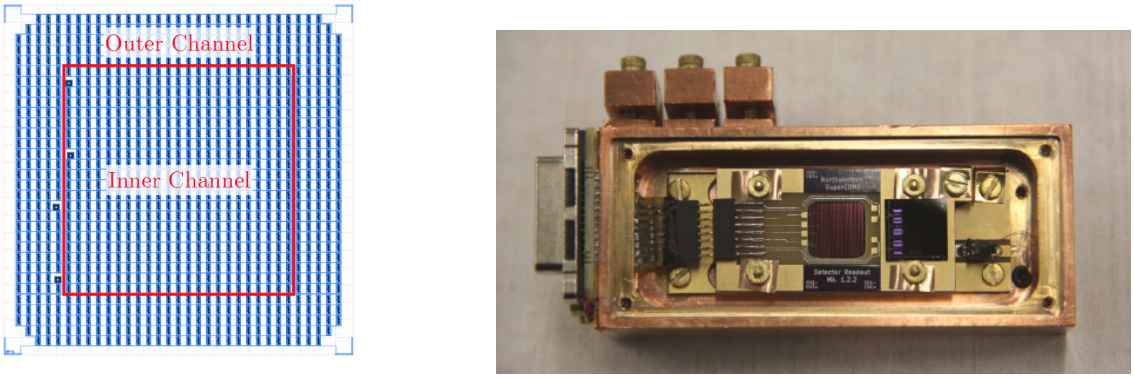

(a) (b)

Figure 2.13: (Left) Illustration of the QET pattern used in the NFC mask design. The red line divides the inner and outer channel of this design, where each channel is comprised of an array of QETs connected in parallel. The four filled squares on the left side are contacts used for wire bonding to the readout electronics. (Right) Top view of the second-generation Si HVeV detector and the adjacent veto detector inside the copper housing. The HVeV detector is at the center of the housing surrounded by the black frame, and the veto detector is to the right. Diagram and photo are taken from Ref. [81].

There are several notable differences between the first and second generation HVeV detectors. Firstly, the first generation detector has a 40 nm thick amorphous Si layer sitting between the detector substrate and QET array, added as an attempt to insulate the detector substrate from

potential leakage at the metal-substrate interfaces, yet proved by various tests that it makes no significant impact on the amount of detector leakage. Therefore, the HVeV Run 2 detector removes the amorphous layer. Secondly, the NFC design has an Al coverage fraction increased to $\sim 50\%$, with an expected energy efficiency of $\sim 27\%$, corresponding to an improvement in efficiency by a factor of ~ 4.4. Finally, the second-generation detector operates with an inner and outer channel. With the additional channel, the positional information of events can be analyzed by comparing the energy deposition measured in each channel.

A raw exposure of 3.0 gram-days was collected over 7 days in a surface laboratory at Northwestern University (Evanston, IL), with a 635 nm laser source used for energy calibration. Fig. 2.14 shows the HVeV Run 2 spectrum along with the cut efficiencies.

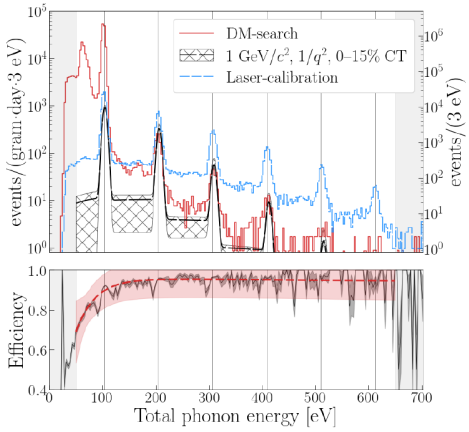

Figure 2.14: HVeV Run 2 spectrum in event rate unit along with the cut efficiency [81].

2.3.3 HVeV Run 3

HVeV Run 3 is the third electron-recoil and absorption dark-matter search using the SuperCDMS HVeV detector design. The first HVeV run showed the power of the cryogenic calorimeters for the detection of sub-GeV dark matter by setting a world-leading limit in electron-recoil dark matter searches. The second run implemented the second generation detector chip design, which improved the energy resolution from ∼14 eV to ∼3 eV. Run 2 saw success in improving detector performance, but the limit did not improve because the underlying background was the same.

HVeV Run 3 is the first HVeV Run operating underground. 13.14 days of DM search data were acquired at the Northwestern Experimental Underground Site (NEXUS) at Fermilab, where the facility provides 225 meters of water-equivalent rock overburden. It turns out that low energy background events with energies less than one electron-hole pair seen in Run 1 and 2 are a major barrier towards an improved sensitivity, and by studying these events observed in Run 2 we find a category of "burst events" [82]. A hypothesis was put forward that these events are due to scintillation from the printed circuit board holder clamping the detectors in place. Therefore, HVeV Run 3 aims to determine whether the main background in the HVeV detectors originates internally within the detector chips, such as from spontaneous electron-hole pair production, or externally, such as from scintillation off the detector housing. This was investigated by analyzing coincidences between detectors.

The payload includes four separate silicon detector chips, each of the same dimensions and mass as the detectors in HVeV Run 1 and Run 2. These detector chips were placed in pairs on two sides of two separate detector holders with all four along the same central axis, as shown in Fig. 2.15. This allows for discrimination of events based on close-time occurrence of signals seen in multiple detectors creating a signal veto for events of this type (DM particles in our signal models would not produce hits in multiple detectors), introducing a very powerful live-time cut not previously possible in HVeV Run 1 or Run 2. Additionally, Run 3 analysis implements several improvements, including better pile-up event identification and improved detector response modeling.

Figure 2.16 shows the spectrum acquired in HVeV Run 3 compared to Run 2. The coincidence study through comparing data taken at 0V, 60V and 100V separately indicates that the dominant contribution to the excess is consistent with a hypothesized luminescence from the printed circuit boards used in the detector holder [83].

This chapter summarizes the underlying detector physics of a cryogenic semiconductor detector, and how HVeV detectors are designed with similar principles but much smaller size. We also reviewed the experiments and results of three previous HVeV runs. In the next chapter, we will introduce the experimental setup of HVeV Run 4.

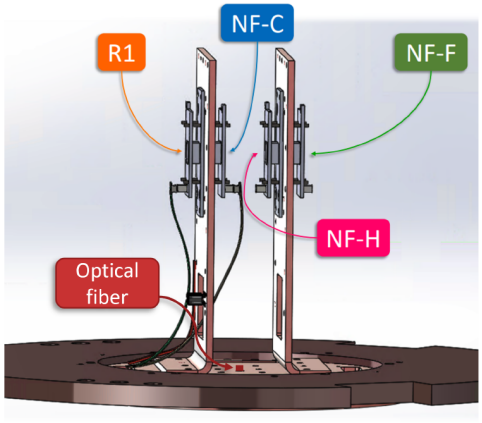

Figure 2.15: Illustration of the detector setup for Run 3. Four HVeV detectors were mounted on two copper holders that were thermally anchored to the mixing chamber of a dilution refrigerator. Each detector was clamped between two printed circuit boards. An optical fiber coupled to the laser was inserted between the detector holders. Diagram is taken from Ref. [83].

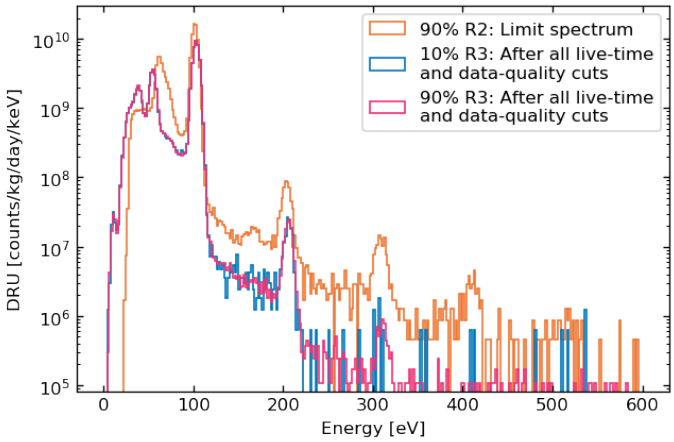

Figure 2.16: Calibrated 10% and 90% data spectrum of HVeV Run 3, post all live-time and data-quality cuts, converted to DRU for comparison to the spectrum used for the R2 limit setting. Plot is taken from Ref. [83].

Chapter 3

HVeV Run 4 Experimental Setup

HVeV Run 4 is conducted in the clean room at the Northwestern Experimental Underground Site (NEXUS) within the Fermi National Accelerator Laboratory in Batavia, Illinois. This facility is located 107 meters underground, which is equivalent to a 300-meter water overburden, helping to reduce the impact of cosmic rays. As shown in Fig. 3.1a, the CryoConcepts dilution refrigeration system is incorporated into the experiment. The payloads are placed inside a copper cavity (Figure 3.1b) within the dilution refrigerator, which can maintain their temperature at 10.5 mK. During operation, a metglas blanket is wrapped around the refrigerator to provide magnetic shielding. Additionally, a lead shield (Figure 3.1c) is positioned around the dilution fridge to minimize background environmental interference.

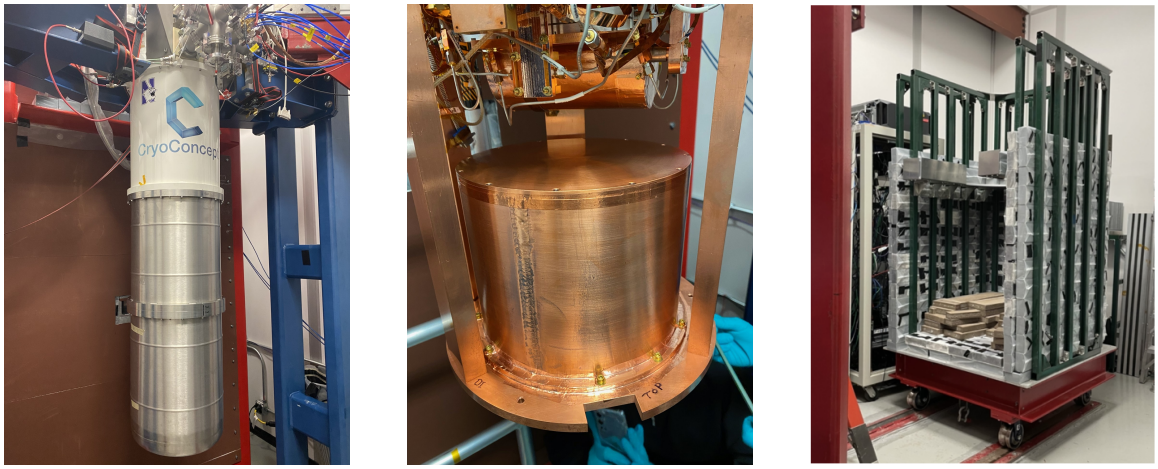

(a) (b) (c)

Figure 3.1: Left: Dilution fridge system used in the HVeV Run 4. Middle: Copper cavity which contains HVeV detectors. When the detectors are operated, it is regulated at 10 mK. Right: Lead shield used to reduce local environment backgrounds. Photos are provided by the SuperCDMS Collaboration.

There are two data taking periods in HVeV Run 4, Nexus Run 13 and Nexus Run 14, named in time order in the Nexus facility (the previous 12 Nexus runs correspond to previous HVeV runs). In HVeV Run 4, four detectors are used, each employing a silicon base with dimensions of 10 mm x 10

mm x 4 mm and a mass of 0.93 g, to interact with dark matter particles. The bottom surface of the silicon base features an aluminum grid with a parquet pattern covering 5% of the area, used to apply the voltage bias for NTL amplification. QETs are connected in parallel to form two channels, known as inner and outer channels, as illustrated in Fig. 2.13a and Fig. 3.2. These channels cover the top surface of each silicon base and detect phonon signals generated by scattering processes within the silicon absorber. Both channels are wire-bonded to two separate SQUID systems, which amplify the changes in current within the TES circuits. The amplified current is then digitized and recorded by the SuperCDMS Detector Control and Readout Card (DCRC).

The detectors used in HVeV Run 4 are designated as follows: two NFC detectors (labeled as NFC1 and NFC2 separately), one NFH detector and one NFE detector. The detector mask design is a joint optimization of several factors, including the geometry and normal state resistance (R_n) of the QETs, to target different requirements of detector resolution and dynamic range. More details on this optimization can be found in Ref. [62]. The design parameters for HVeV Run 4 detectors are listed in Table 3.1. Although the NFC detector is designed to maximize the dynamic range while maintaining a decent level of detector resolution, it did show the best resolution compared to NFE and NFH detectors, as we will see in Chapter 5. The reason for this could be the thermal fluctuation noise not dominating over the electronic noise in the cases of NFE and NFH detectors, causing the measured detector resolution to deviate from the intrinsic energy resolution predicted from Ref. [62]. As a result, in this analysis, we only used the NFC1 detector for limit setting, while the other detectors employed contributed to the coincidence veto (will be discussed in Section 5.3.4). They also played roles in other analyses of HVeV Run 4 (e.g. the Compton step analysis) and in the characterization studies of different detectors.

Table 3.1: Mask design of HVeV Run 4 detectors.

Detector Type	QET R_n (mOhm)	TES Length (μm)	Al Fin Length (μm)
NFC	300	150	60
NFE	300	25	100
NFH	900	100	125

To eliminate luminescence from the PCB material surrounding the detectors in previous experiments, we mounted all detectors in newly designed copper housings. The configuration of the detectors is shown in Fig. 3.3. This configuration remained unchanged through NEXUS Run 13 and NEXUS Run 14, with the exception that LED boxes were added to the top and bottom of the copper housing during NEXUS Run 14.

3.1 Nexus Run 13

The science data collection for NEXUS Run 13 (NR14) spanned approximately 11 days of live time within a 66-day period, which also involved measuring IV curves, comparing NTL bias voltages, and testing shield performance, among other activities. The primary objective of this run was to evaluate the performance of the newly designed copper holder and to release new DM search results. Fig. 3.4a and Fig. 3.4b illustrate the detectors housed within the copper holder, while Fig. 3.4c presents the final configuration of the NEXUS Run 13 payload.

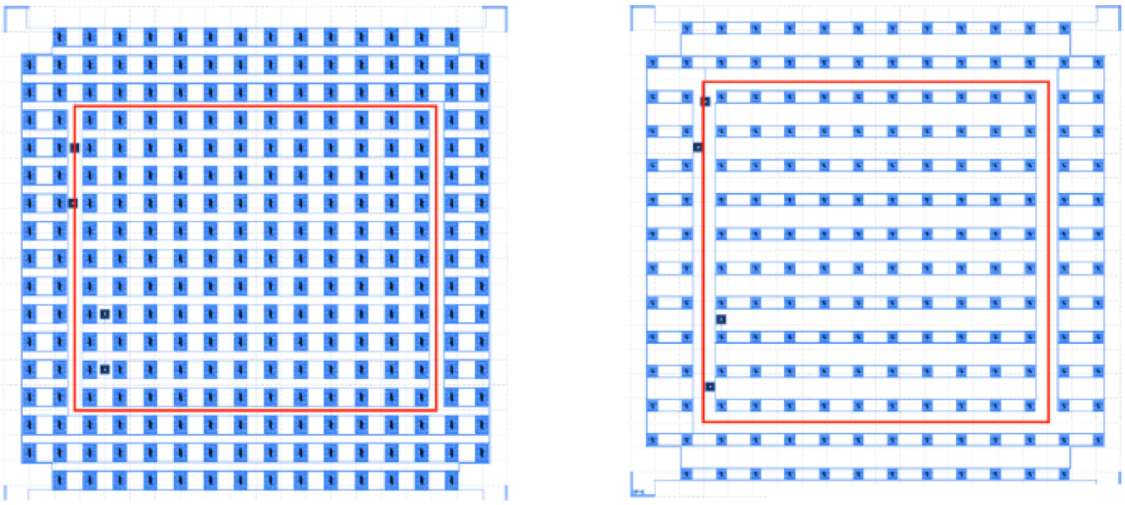

(a) (b)

Figure 3.2: Layout of QET channels on the HVeV detector (Left: NFH. Right: NFE). The added red square labels the boundary of inner and outer channels. The layout of NFC detector is shown in Fig. 2.13a.

3.2 Nexus Run 14

The primary objective of NEXUS Run 14 (NR14) was to establish a low energy calibration utilizing the LED system to generate low energy photons of known energy. The detectors and the LED system were configured as illustrated in Fig. 3.5a. Each HVeV detector was paired with an LED that illuminated it through a pinhole. An infrared (IR) filter was placed over the pinhole in the LED box to minimize the leakage of background photons from the LED box to the detectors. The pinhole and IR filters are depicted in Fig. 3.5b. Fig. 3.5c provides details on the voltage settings of the LED control system. A function generator was used in conjunction with a battery. The battery provided a constant voltage offset that was insufficient to activate the LED. The function generator was then configured to generate a burst of a triangle wave at a specified frequency to intermittently flash the LED.

An LED identical to those used in Nexus Run 14 was used to measure the wavelength of LED photons. This was done using a Thorlabs CCS100 spectrometer, and the LED was tested at various temperatures, as summarized in Table 3.2.

Table 3.2: Measurements of LED peak wavelength and corresponding energy of photons using spectrometer at different temperatures.

Temperature	296 K	Liquid N_2 (77 K)	Liquid He (4 K)
Measured Wavelength (nm)	630.3	607.3	605.7
Photon Energy (eV)	1.97	2.04	2.05

In Chapter 3, we introduced the experimental setup of HVeV Run 4, including two data taking periods for dark matter search and energy calibration separately. Four gram-scale silicon detectors of three different mask designs are employed in our experiment. In Nexus Run 14, an LED source

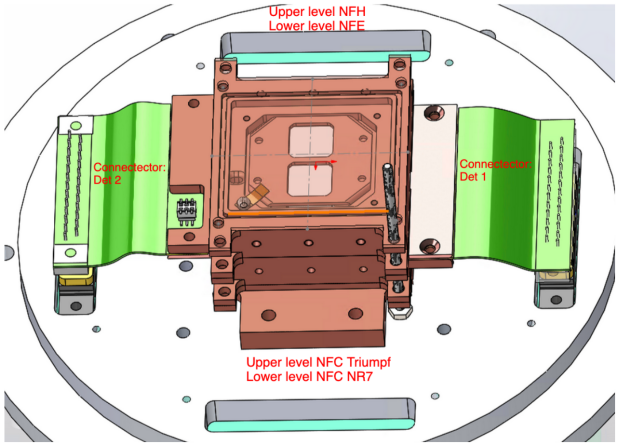

Figure 3.3: Detectors setup during Nexus Run 13 including detector labels. Diagram is provided by the SuperCDMS Collaboration.

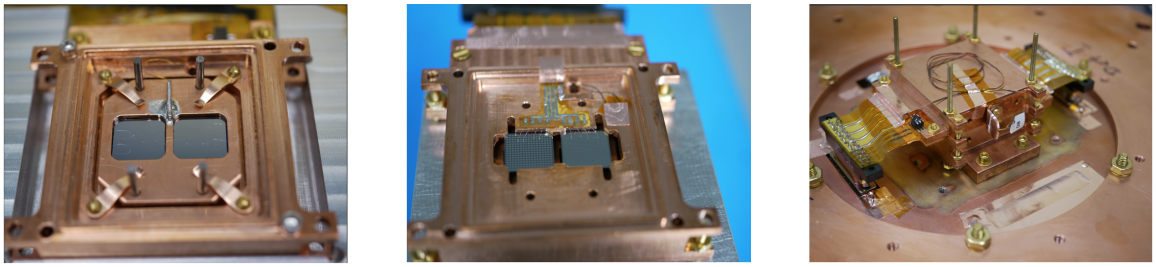

(a) (b) (c)

Figure 3.4: Left: NEXUS Run 13 back side of HVeV detectors mounted on the bottom holder with NFC1 on the left and NFE on the Right. Middle: Front side of HVeV detectors in upper box with NFH on the left and NFC2 on the right. Right: Final look of detector tower mounted on the mixing chamber plate. Photos are provided by the SuperCDMS Collaboration.

of photon energy around 2 eV is used as the calibration source. In the next chapter, we will discuss in detail the signal models of four dark matter candidates, the electron-hole pair ionization model and two major detector response effects considered in this analysis.

(a) (b) (c)

Figure 3.5: (Left) Final detector tower mounted on the mixing chamber. Uppermost layer in the tower: LED box. Each detector has a corresponding LED shining at the centre of the HV electrode side through pinholes covered with infrared filters. Each of the LEDs is wired up independently to be pulsed independently via BNC breakouts on the 300K air side. (Middle) LED calibration box - Filter side. Pinholes can be seen through filters. The black material is a sheet of metal velvet foil to eliminate light reflection. (Right) Input voltage signal from a pulse generator in yellow (4V pp ramp with 1s period) Voltage signal on a ∼50 Ohm resistor in series with the LED in green, showing a very distinct change from room temperature operation with the appearance of a saturation current of the LED circuit of ∼2mA at 77K.

Chapter 4

Signal Models, Ionization and Detector Response Effects

This chapter discusses low mass dark matter signal models that are used in this analysis, as well as the ionization model and detector response effects. Section 4.1 introduces the two fermionic low mass dark matter signal models, while Section 4.2 and Section 4.3 introduce the two bosonic ones. Section 4.4 discusses the ionization model, and Section 4.5 introduces the modeling of charge trapping and impact ionization effects.

4.1 Dark-Matter Electron Scattering

As introduced in Section 1, light dark matter particles of mass keV to GeV range have received increasing attention in recent years due to the absence of a WIMP dark matter discovery. For lower masses, both the total kinetic energy of the dark matter particle and the fraction of energy transferred to the nucleus are significantly reduced. Therefore, light dark matter primarily interacts with target materials through electron scattering instead of through nuclear scattering as in the WIMPs case.

In this analysis, we consider a model where light dark matter particles χ with mass m_χ interact with SM particles through a new force mediator, taking the form of a gauge boson A' with mass $m_{A'}$ in some dark sector that includes a $U(1)_D$ gauge group that kinetically mix with the Standard Model hypercharge $U(1)_Y$ gauge group, as illustrated in Fig. 4.1 with the mixing term in Lagrangian shown in Eq. 4.1:

$$\mathcal{L} \supset \frac{\epsilon}{2} F_Y^{\mu\nu} F^{'}_{\mu\nu}. \tag{4.1}$$

The mathematical derivation presented below follows Ref. [58][28].

A' can therefore mediate interactions between dark matter particles and electromagnetically charged SM particles, including electrons. The underlying DM-electron scattering cross section $\overline{\sigma}_e$ can be parameterized as in Eq. 4.2 [58]:

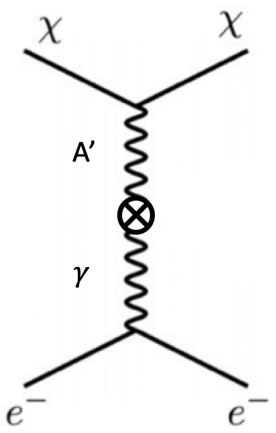

Figure 4.1: Feynman diagram of DM-electron scattering, with time axis to the right.

$$\overline{\sigma}_e = \frac{\mu_{\chi e}^2 \overline{|\mathcal{M}_{\chi e}(q = \alpha m_e)|^2}}{16\pi m_\chi^2 m_e^2}, \tag{4.2}$$

where $\alpha \approx 1/137$ is the fine structure constant, m_e is the electron mass, and $\mu_{\chi e}^2$ is the DM-electron reduced mass. Note that $\overline{|\mathcal{M}_{\chi e}(q = \alpha m_e)^2|}$ represents the squared matrix element for DM-electron scattering with the initial spins of the particles and summed over the final ones under a momentum transfer of αm_e.

If we define a dark matter form factor that provides the momentum-transfer dependence of the interaction as in Eq. 4.3:

$$F_{DM}(q) = \frac{m_{A'}^2 + \alpha^2 m_e^2}{m_{A'}^2 + q^2}. \tag{4.3}$$

Eq. 4.2 can be generalized to find the matrix element for any momentum transfer, as shown in Eq. 4.4:

$$\overline{|\mathcal{M}_{\chi e}(\vec{q})|^2} = \overline{|\mathcal{M}_{\chi e}(q = \alpha m_e)|^2} F_{DM}(\vec{q}). \tag{4.4}$$

Now we consider two extreme cases where the interaction is mediated by either a heavy mediator where $m_{A'} \gg \alpha m_e$, leading to a point-like interaction, or by a very light mediator where $m_{A'} \ll \alpha m_e$. In such cases, the form faction Eq. 4.3 can be simplified as Eq. 4.5:

$$F_{DM}(q) \cong \begin{cases} 1 & m_{A'} \gg \alpha m_e \\ \alpha^2 m_e^2 / q^2 & m_{A'} \ll \alpha m_e \end{cases}. \tag{4.5}$$

Theoretically, light dark matter particles can scatter off either a nucleus or an electron. However, the two processes differ significantly in the amount of energy deposited. If the DM particle is light, the momentum transfer q between dark matter and the target nucleus is small and may not provide enough energy for the recoil of the nucleus to be detected. For this reason, only energy depositions from electron recoils are considered in our signal models, and the event rate is calculated only with

the DM-electron scattering cross section.

The differential event rate for this process in a crystal target is given by Eq. 4.6 [58]:

$$\frac{dR}{dlnE_r} = \frac{\rho_{DM}}{m_\chi} N_{cell} \overline{\sigma}_e \alpha \frac{m_e^2}{\mu_{\chi e}^2} \int d\ln q \left(\frac{E_r}{q} \eta(v_{min}(q, E_r))\right) F_{DM}(q^2) |f_{crystal}(q, E_r)|^2, \tag{4.6}$$

where $N_{cell} = m_T/m_{cell}$ is the number of unit cells in the target with total mass m_T($m_{cell} = 2m_N$ for silicon and germanium), and the DM velocity distribution is contained in $\eta(v_{min}(q, E_r))$, defined as Eq. 4.7:

$$\eta(v_{min}) = \int_{v_{min}}^{\infty} f(\vec{v})/v d^3\vec{v}, \tag{4.7}$$

with v_{min} given by Eq. 4.8:

$$v_{min}(q, E_r) = E_r/q + q/2m_\chi. \tag{4.8}$$

Here, the maximum velocity is constrained by the escape velocity of the galaxy. The crystal form factor $|f_{crystal}(q, E_r)|$ in Eq. 4.6 contains all the details of the target's electronic structure and the momentum states of the electron. In contrast to DM-nucleus scattering, DM-electron scattering does not have a straightforward relationship between recoil energy and momentum transfer. Therefore, the total event rate is found by integrating over E_r and q separately.

The analysis presented in Chapter 5 uses the publicly available electron recoil spectra for light dark matter masses between 0.1 MeV to 10 GeV for different forms of F_{DM} [84], which have been numerically calculated using a package called "QEdark" [85]. The recoil spectra themselves are binned across E_r using a bin size of 0.1 eV. Fig. 4.2 shows the total event rate as a function of light dark matter mass for a silicon target with $F_{DM} = 1$ and $F_{DM} \propto 1/q^2$, assuming a DM-electron cross section of $\overline{\sigma}_e = 10^{-37}\text{cm}^2$.

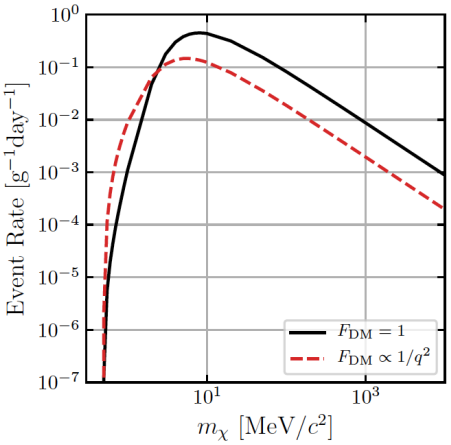

Figure 4.2: Expected event rate for DM-electron scattering as a function of DM mass m_χ for a Si target assuming a DM-electron cross section of $\overline{\sigma}_e = 10^{-37}\text{cm}^2$. Plot is taken from Ref. [28]

4.2 Dark Photon Absorption

The dark photon A' is a hypothetical massive vector boson of a dark sector $U(1)_D$ gauge group with mass $m_{A'}$ and kinetically mixes with the SM hypercharge $U(1)_Y$ gauge group [86]. The dominant mixing channel at low energies is between dark photons and the SM photons, characterized by the DM-SM kinetic mixing parameter ϵ, as shown in Eq. 4.9:

$$\mathcal{L} \supset -\frac{1}{4}F'^{\mu\nu}F'_{\mu\nu} - \frac{\epsilon}{2}F'^{\mu\nu}F_{\mu\nu} + \frac{1}{2}m^2_{A'}A'^{\mu}A'_{\mu}, \tag{4.9}$$

where $F^{\mu\nu}$ is the field strength of the SM photons. If ϵ is small enough and $m_{A'}$ is less than twice the electron mass, dark photons can have decay lifetimes exceeding the age of the Universe. This makes them potential candidates to constitute all of the relic dark matter. One possible interaction mechanism for dark photons is an absorption process similar to the photoelectric absorption of SM photons [86, 87].

The mathematical derivation presented below follows Ref. [87][28]. For a target material with mass m_T and density ρ, the number of target electrons is given by $m_T n_e/\rho$, where n_e is the electron number density. The expected event rate, as illustrated in Fig. 4.3 and shown in Eq. 4.10:

$$R = \frac{1}{\rho}\frac{\rho_{DM}}{m_{A'}}\langle n_e \sigma_{abs} v_{rel}\rangle_{A'}, \tag{4.10}$$

depends on the absorption cross section $\sigma_{\rm abs}$. The average cross section, $\langle n_e\sigma_{\rm abs}v_{\rm rel}\rangle_{A'}$, describes the DM-electron absorption rate based on dark photon velocities $v_{\rm rel}$. For photon absorption, the equivalent rate $\langle n_e\sigma_{\rm abs}v_{\rm rel}\rangle_{\gamma}$ is equal to the real part of the complex conductivity, σ_1, which relates to the SM photoelectric cross section $\sigma_{\rm p.e.}$ via $\sigma_1 = n\sigma_{\rm p.e.}$, where n is the index of refraction of the target material [87].

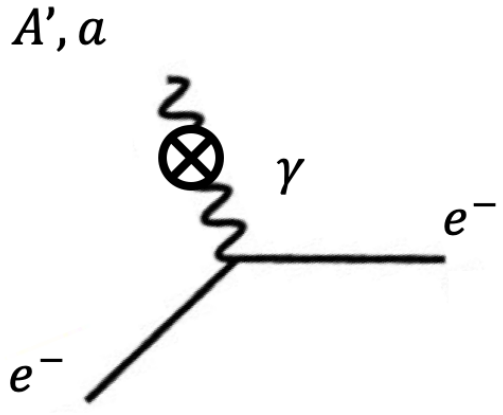

Figure 4.3: Feynman diagram of dark photon or axion like particle absorption, with time axis pointing to the right.

Dark photon absorption (DPA) is modeled as the absorption of a massive particle that deposits an energy of $E_{A'}$, with an effective coupling of ϵe to electrons. The matrix elements for dark and SM photons are related by the expression $|\mathcal{M}|^2_{A'} = \epsilon^2_{\rm eff}|\mathcal{M}|^2_{\gamma}$, which leads to the relation shown in

Eq. 4.11:

$$< n_e \sigma_{abs}(E_{A'} v_{rel}) >_{A'} = \varepsilon_{eff}^2 < n_e \sigma_{abs}(E_{A'} v_{rel}) >_{\gamma} = \varepsilon_{eff}^2 \frac{n \sigma_{p.e.}(E_{A'})}{\hbar}, \tag{4.11}$$

where $\sigma_{\text{p.e.}}$ is in unit eV, and $\hbar$ is the reduced Planck constant. The parameter ϵ_{eff}^2 represents the effective kinetic mixing, accounting for in-medium effects that can significantly change ϵ if the kinetic mixing does not occur in vacuum. This effective mixing depends on the dark photon mass and both the real and imaginary parts of the complex conductivity, σ_1 and σ_2, as shown in Eq. 4.12:

$$\varepsilon_{eff}^2 = \frac{\epsilon^2 m_{A'}^2}{m_{A'}^2 - 2 m_{A'} \sigma_2 + \sigma_1^2 + \sigma_2^2}. \tag{4.12}$$

When the dark photon masses are greater than 100 eV, ε_{eff} closely matches ε for most target materials. However, for masses below 100 eV, ε_{eff} can differ from ε by more than an order of magnitude, especially for materials like silicon and germanium. For non-relativistic cold dark matter, the absorption energy is approximately equal to the dark photon's mass energy, $E_{A'} \sim m_{A'} c^2$. This implies that the mass range accessible to an experiment searching for dark photons corresponds to the energy range to which the experiment is sensitive. For semiconductor detectors like silicon and germanium, this sets a lower limit on the dark photon masses, which is determined by the band gap energy of the detector material. Combining all these factors, Eq. 4.10 can be rewritten as Eq. 4.13:

$$R = \frac{1}{\rho \hbar} \frac{\rho_{DM}}{m_{A'}} n \sigma_{p.e.}(m_{A'} c^2). \tag{4.13}$$

The expected signal for dark photon absorption is a delta function at $m_{A'}$, with the event rate given by Eq. 4.13. The signal deviates from the delta function only due to the detector resolution or other effects related to the detector. Fig. 4.4 shows the predicted rate of dark photon absorption in silicon, assuming $\varepsilon = 5 \times 10^{-13}$, for dark photon masses below 1 keV. The rate is presented both with and without considering the in-medium effects for comparison.

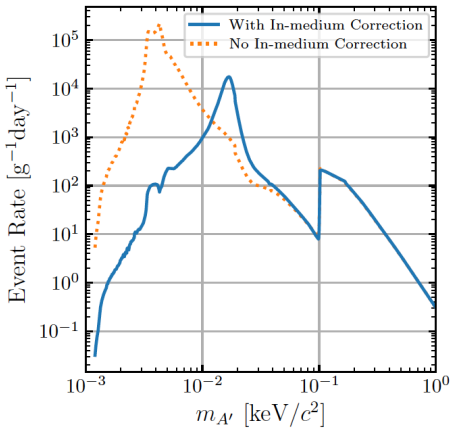

Figure 4.4: Expected event rate of dark photon absorption in Si over the dark photon mass $m_{A'}$ assuming a dark photon kinetic mixing parameter of $\varepsilon = 5 \times 10^{13}$. The event rate is computed with (blue, solid) and without (orange, dotted) accounting for the in-medium correction. Plot is taken from Ref. [28].

4.3 Axion-Like Particle Absorption

The axion is a hypothetical particle introduced to address the strong Charge-Parity (CP) problem in quantum chromodynamics [88]. They are bosons that result from the spontaneous breaking of a U(1) symmetry, with masses constrained between 10^{-5} and 10^{-3} eV [89]. While the axion could potentially explain the dark matter abundance, its mass-coupling relationship limits the parameter space for axion searches. Axion-like particles (ALPs), which have the independent relationship between mass and coupling, enable experiments to probe a broader and more flexible parameter space [20].

We make the assumption that axion-like particles (ALPs) with mass m_a as the sole constituent of dark matter relic abundance, interacting with SM particles through the axioelectric effect [90][91]. The axioelectric effect resembles the photoelectric absorption of an SM photon, where an ALP is absorbed by an atom's bound electron, leading to the release of an electron. This process is governed by the axioelectric coupling constant g_{ae} between the ALP and the electron. The expected event rate is determined by the effective area of the target material and the flux of dark matter particles, as shown in Eq. 4.14:

$$R = \frac{\rho_{DM}}{m_N m_a}\sigma_a(E_a)\langle v_a\rangle = \frac{\rho_{DM}}{m_N m_a}\sigma_a(E_a)\beta_a/c. \tag{4.14}$$

Here, m_N represents the mass of the target material's nucleus, $\sigma_a(E_a)$ is the absorption cross section for an ALP with energy E_a, v_a is the axion velocity, c is the speed of light, and $\beta_a = \langle v_a/c\rangle$ is the relativistic beta factor. The axioelectric absorption cross section is proportional to the SM photoelectric absorption cross section $\sigma_{p.e}$ of the target material, given by Eq. 4.15:

$$\sigma_a(E_a) = \sigma_{p.e.}(E_a)\frac{g_{ae}^2}{\beta_a^2}\frac{3E_a^2}{16\pi\alpha m_e^2 c^4}(1 - \frac{\beta_a^{2/3}}{3}), \tag{4.15}$$

where m_e is the electron mass and α is the fine structure constant.

For non-relativistic, cold dark matter, the energy of the ALP is approximately equal to its mass energy, i.e., $E_a \sim m_a c^2$, and $\beta_a \ll 1$. Under these conditions, Eq. 4.15 simplifies to Eq. 4.16:

$$\sigma_a(m_a c^2) = \sigma_{p.e.}(m_a c^2)\frac{g_{ae}^2}{\beta_a^2}\frac{3m_a^2}{16\pi\alpha m_e^2}, \tag{4.16}$$

leading to an event rate for ALP absorption given by Eq. 4.17:

$$R = \frac{\rho_{DM}}{m_N}\sigma_{p.e.}(m_a c^2)\frac{3g_{ae}^2}{16\pi\alpha}\frac{m_a}{m_e^2}c. \tag{4.17}$$

Similar to the DPA model, the expected signal for ALP absorption is a delta function centered at m_a, with an event rate given by Eq. 4.17. Fig. 4.5 illustrates the expected event rate for ALP absorption in silicon, assuming $g_{ae} = 5 \times 10^{-11}$, for ALP masses below 1 keV.

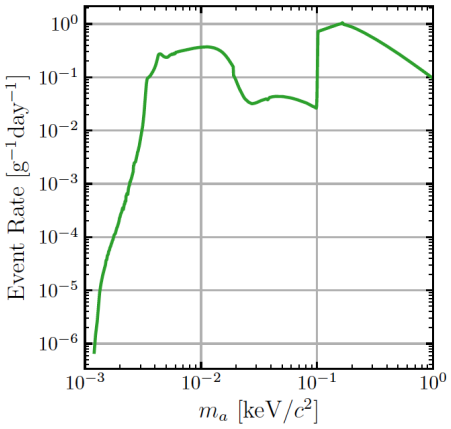

Figure 4.5: Expected event rate of axion-like particle (ALP) absorption in Si over the ALP mass m_a assuming an axioelectric coupling constant $g_{ae} = 5 \times 10^{-11}$. Plot is taken from Ref. [28].

4.4 Ionization model and Charge Quantization

In this analysis, we use the charge quantization model developed by Ramanathan and Kurinsky [78], where they conducted measurements of the ionization yield in silicon for gap energies between 1.12 and 1.170 eV to produce a phenomenological ionization model.

When a particle, DM or otherwise, interacts with an electron in the crystal (either through a scattering or absorption process), the electron will ionize and create $e^- h^+$ pairs if the amount of recoil/absorption energy E_r transferred to the electron is above the band gap energy E_g of the crystal material. The mean number of $e^- h^+$ pairs $< n_{eh} >$ produced in the high energy limit $E_r \gg E_g$ for electron interactions is given by Eq. 4.18:

$$n_{eh} = E_r / \varepsilon_{eh}, \tag{4.18}$$

where E_r is either the recoil or absorption energy of the dark matter particle and ε_{eh} is the average energy per electron hole pair. However, this relationship breaks down as E_r approaches E_g. Near the band gap energy, the average energy per electron hole pair ε_{eh} will be described by a piecewise function according to the model, as shown in Eq. 4.19:

$$\varepsilon_{eh}(Er) = \begin{cases} \infty & E_r < E_g \\ E_r & E_g \leq E_r < 2E_g \\ \varepsilon_{imp}(E_r) & E_r \geq 2E_g \\ \varepsilon_{eh,\infty} & E_r \to \infty \end{cases}, \tag{4.19}$$

where E_g is the band gap energy, $\varepsilon_{imp}(E_r)$ is a functional form of ε_{eh} extracted from simulation and literature data, and $\varepsilon_{eh,\infty}$ is the asymptotic value $\varepsilon_{imp}(E_r)$ for E_r above 50 eV.

The variation in n_{eh} is determined by the Fano factor F, which this model also describes in a piecewise and energy-dependent way, as shown in Eq. 4.20:

$$F(Er) = \begin{cases} 0 & E_r < 2E_g \\ F_{imp}(E_r) & E_r \geq 2E_g \\ F_\infty & E_r \to \infty \end{cases}, \tag{4.20}$$

where $F_{imp}(E_r)$ is a functional form for F extracted from simulation and literature data, and F_∞ is the asymptotic value of $F_{imp}(E_r)$ for E_r above 50 eV (analogous to $\varepsilon_{imp}(E_r)$ and $\varepsilon_{eh,\infty}$ respectively). Below E_g, ionization is never produced. Therefore, the variation in n_{eh} and the Fano factor are both zero. Between E_g and two times of E_g, an ionization will always be produced, but neither the generated electron nor the hole can have sufficient kinetic energy to produce further ionization. Therefore, the Fano factor is still zero. For two times of E_g and above, the generated hole or electron may have sufficient energy for further ionization, which depends on how the kinetic energy is split between the two charge carriers. This is where the Fano factor becomes non-zero.

The supplementary materials of Ranmanathan and Kurinsky's paper include the simulation-generated ionization probabilities for E_r between 0 and 50 eV. The included probabilities are for three specific temperatures (0, 100, and 300 K) which correspond to three specific values of E_g in silicon (1.1692, 1.1627, and 1.1230 eV). In order to use this model with a different E_g (specifically, the value from the photoelectric cross-section model, 1.131 eV), we can interpolate Ranmanathan and Kurinsky's results as a function of E_g. This interpolation method has been validated with additional data provided by K. Ramanathan using $E_g = 1.134eV$ (a previous value of interest). The result agreed closely with the interpolation for the same value, as shown in Fig. 4.6.

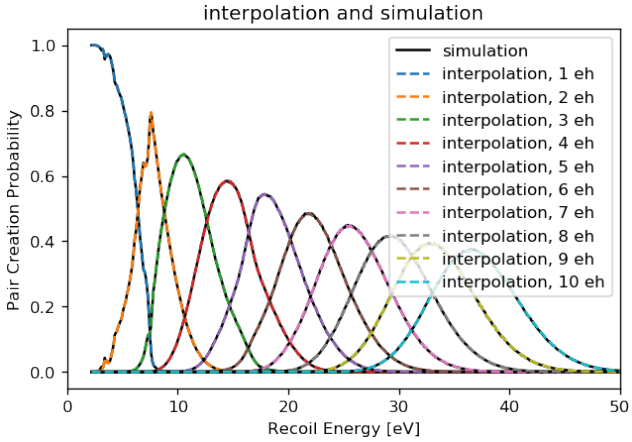

Figure 4.6: Pair creation probabilities for electron-holnumbers 1-10 and energy up to 50 eV. The simulation was generated by K. Ramanathan for $E_g = 1.134$ eV. The interpolation was calculated using the supplementary materials from Ranmanathan and Kurinsky's paper [78].

Above 50 eV, the model provides a functional form for the ionization probabilities using $\varepsilon_{eh,\infty}$ and F_∞, as shown in Eq. 4.21, 4.22, and 4.23 [78]:

$$P_n(E_r) = \frac{1}{\sqrt{2\pi n F_\infty}} \exp\left[-\frac{1}{2}\left(\frac{(n_{eh,\infty} - E_r)/[\text{eV}]}{\sqrt{n}F_\infty}\varepsilon_{eh,\infty}/[\text{eV}]\right)^2\right], \tag{4.21}$$

$$F_\infty = -0.0281E_g/[\text{eV}] + 0.0015A/[\text{eV}]^2 + 0.1383, \tag{4.22}$$

$$\varepsilon_{eh,\infty} = 1.6989E_g + 0.0843A/[\text{eV}] + 1.2972[\text{eV}], \tag{4.23}$$

which can be calculated using a fit to the simulation results. P_n is the pair creation probability for n electron-hole pairs, and A = 5.2 eV^2 from the literature review in Ranmanathan and Kurinsky's paper is the ratio of phonon-carrier to carrier-carrier scattering.

4.5 Charge Trapping and Impact Ionization Effects

With impurities in the crystal, a non-quantized amount of NTL energy may be generated during an event. Two categories of effects are considered in this analysis which could produce energy deposition between quantized electron-hole pair peaks: the charge trapping (CT) and impact ionization (II) effects. Charge trapping occurs when a moving electron or hole gets trapped in a vacancy within the crystal, reducing the number of charges that pass through the detector. Meanwhile, impact ionization occurs when a moving charge frees another loosely bound charge in the crystal, increasing the number of electrons or holes passing through the detector. Both trapped charge carriers and unpaired charge carriers generated will either terminate or initiate their trajectories within the detector. Consequently, they traverse only a portion of the voltage bias, leading to the production of a non-quantized amount of NTL energy. Fig. 4.7 illustrates the effects of CT and II inside the crystal for a single electron-hole pair.

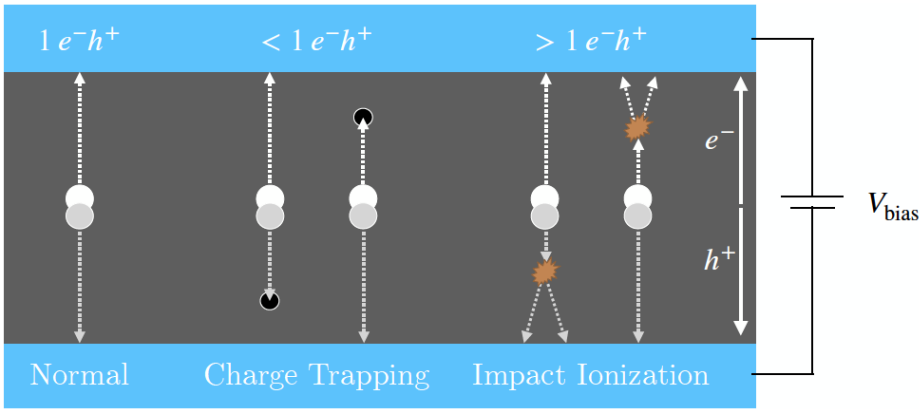

Figure 4.7: Illustration of the effects of charge trapping (CT) and impact ionization (II) for a single electron-holpair. Diagram is taken from Ref.[28].

The modelling of these detector response effects is essential for the dark matter analysis. In HVeV Run 2 and Run 3, a "flat model" was used as described in Ref. [92]. However, in this analysis, an improved model (called the "exponential CTII model") summarized in Ref. [93] was developed to take into consideration the distribution of locations where the CT and II processes occur. The model assumes there are three types of processes when a charge carrier transverses the detector crystal with an external electrical field applied:

1. It gets trapped in an impurity state.

2. It creates a single free electron from an impurity state by promoting it into the conduction band.

3. It promotes an electron from the valence band to an impurity state, creating a single hole in the valence band.

Considering that there are two types of charge carriers (electrons and holes), a total of six different processes need to be handled separately. They are electron trapping (CTe), hole trapping (CTh), hole creation by an electron (IIeh), electron creation by an electron (IIee), electron creation by a hole (IIhe) and hole creation by a hole (IIhh). The model assumes each of these six processes has a constant probability independent of the location of the charge carrier in the crystal, the length it has drifted through and the amount of charge carriers surrounding it.

Assume the impurities are distributed uniformly throughout the crystal, and p_i is the probability for a charge carrier to experience process i (among the six ones mentioned above) per unit distance travelled along the z-axis which denotes the direction of the electrical field applied. Then considering infinite small steps, the total probability of the charge carrier not experiencing process i is given by Eq. 4.24:

$$\overline{C}_i(\Delta z) = \lim_{n\to\infty}(1 - p_i\frac{\Delta z}{n})^n = e^{-\Delta z/\tau_i}, \tag{4.24}$$

where the p_i term is replaced by the characteristic length τ_i of each specific process.

To obtain the probability density function (PDF) of a charge carrier traveling a distance Δz before running into any of the CT and II processes, one simply takes the derivative of $\overline{C}_i(\Delta z)$ with respect to Δz, as given by Eq. 4.25:

$$P_i(\Delta z) = \frac{d}{d\Delta z}(1 - \overline{C}_i(\Delta z)) = \frac{1}{\tau}e^{-\Delta z/\tau_i}. \tag{4.25}$$

For simplicity, the thickness of the crystal along the z direction is denoted as 1, which equivalently replaces z with a fractional distance of the total length. The boundary condition gives that at the surfaces of the crystal, i.e. $z = 0$ and $z = 1$, the charge carries always terminate. The six characteristic lengths τ_i measured in fractions of the crystal thickness are the only fundamental input parameters of the model. The probability of a particular process occurring when a charge carrier goes through the entire length of the detector f_i is given by Eq. 4.26:

$$f_i = 1 - \overline{C}_i(\Delta z = 1) = 1 - e^{-1/\tau_i}, \tag{4.26}$$

which makes up the fundamental building blocks of the exponential CTII model.

Eventually, the output of the model is a PDF of the NTL energy produced by an event, and therefore the distance traveled must be converted in the z direction to the NTL energy, as given by the second term of Eq. 2.6 where we replace the total bias voltage with a fractional one depending on the distance z traveled. For simplicity, an energy scale E_{neh} is adopted so that a unit energy is produced by a charge that travels a distance equal to the thickness of the crystal. For example, a pair of electrons and holes that initially sit at $z = 0.5$ will produce a total energy of $E_{neh} = 1$.

Three distinct classes of events are relevant in this model:

1. Surface events. A single charge is created on one surface of the crystal and moves to the other. They usually originate from the laser or LED source used for calibration or the charge leakage at the surface of the crystal.

2. Single charges produced throughout the crystal. These events correspond to some charge leakage process that occurs throughout the detector bulk.

3. Electron-hole pair production events in the detector bulk. They are potential candidates of the dark matter signals.

For each type of events, various combinations of CT and II processes are solved for the probabilities of measuring an energy of E_{neh}. However, a challenge arises when multiple II processes are modelled in a single event. Each II process introduces a new charge carrier, causing the number of possible combinations of CT and II processes to grow exponentially, significantly increasing the complexity of each new solution. The core idea of the exponential CTII model is that we limit the number of solutions to a certain "order" of processes. For processes of order N, charge carries that participated or were produced in a primary II process can take part in no more than $(N-1)$ additional II processes. For surface and bulk single charge events, the solutions for processes up to the second order are found, resulting in 28 unique solutions for each event type. For bulk electron-hole pair events, the solutions for processes up to the first order are found, resulting in 16 unique solutions. When solving for these analytical solutions, it is assumed that any charge carriers present after the order limit is reached will propagate to the crystal surface with 100 % probability. A detailed description of the analytical solutions of the model is provided in Ref. [93] and we will not cover the full content here. Fig. 4.8 shows some analytical solutions in the E_{neh} energy space of the exponential CTII model for single electron-hole pair events.

So far we have only considered the analytical solutions for only one single charge or electron-hole pair. Large energy depositions in the crystal will usually generate multiple charges or electron-hole pairs for a single event. Denote $F^{(1)}_{type}(E_{neh})$ as the PDF for one charge or electron-hole pair in the energy space. Here, the type refers to the three distinct classes of events as mentioned above. $F^{(1)}_{type}(E_{neh})$ is found by summing the analytical solutions for the given event type, as shown by the black dashed curves in Fig. 4.8. Without any additional detector response, the PDF for j electron-hole pairs $F^{(j)}_{type}(E_{neh})$ is calculated by convolving $F^{(1)}_{type}(E_{neh})$ with itself $(j-1)$ times, as shown in Eq. 4.27:

$$F^{(j)}_{type}(E_{neh}) = F^{(j-1)}_{type}(E_{neh}) * F^{(1)}_{type}(E_{neh}). \tag{4.27}$$

The PDF $H(E_{neh})$ for events that generate multiple electron-hole pairs up to j is then given by Eq. 4.28:

$$H(E_{neh}) = \sum_{j=1}^{J} a_j \cdot F^{(j)}_{type}(E_{neh}), \tag{4.28}$$

where a_j are the weights associated with producing j electron-hole pairs.

Figure 4.9 shows a few PDF examples for the exponential CTII model. From the plot, we notice that although higher-order processes are important for single electron-hole pair solutions, they become less significant, or even negligible, for multiple electron-hole pair solutions. Furthermore, the type of events matters, which was not differentiated by the previous "flat CTII model".

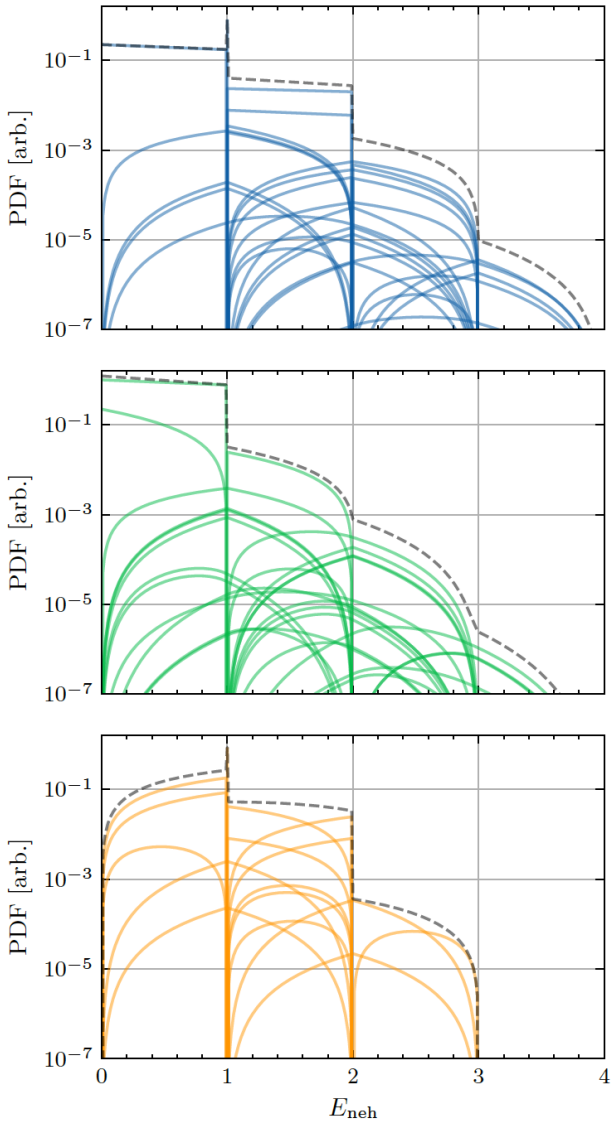

Figure 4.8: Analytical solutions in the E_{neh} energy space of the exponential CTII model for single electron-hole pair events. The unique solutions represented by the solid, coloured curves are found for surface events (top), bulk-single-charge events (middle), and bulk electron-hole pair events (bottom), with CTII input parameters $f_{CTe} = 0.2$, $f_{CTh} = 0.1$, $f_{IIee} = 0.01$, $f_{IIeh} = 0.03$, $f_{IIhe} = 0.01$ and $f_{IIhh} = 0.05$. Top and middle plots assume that the initial charge is an electron. The black dashed curves in each plot are the sums of the analytical solutions for each event type. Plot is taken from Ref. [93].

Finally, the exponential CTII model needs to be put together with other considerations to form a complete detector response model. Those other considerations include the following.

1. The ionization model. With a specific ionization model (e.g. the one we introduced in Section 4.4), the generic weights a_j can be replaced with the probability mass function (PMF) describing the probability of a given amount of ionization.

2. The conversion to the total phonon energy E_{ph}. According to Eq. 2.6, the energy conversion from E_{neh} space to E_{ph} space can be achieved through Eq. 4.29:

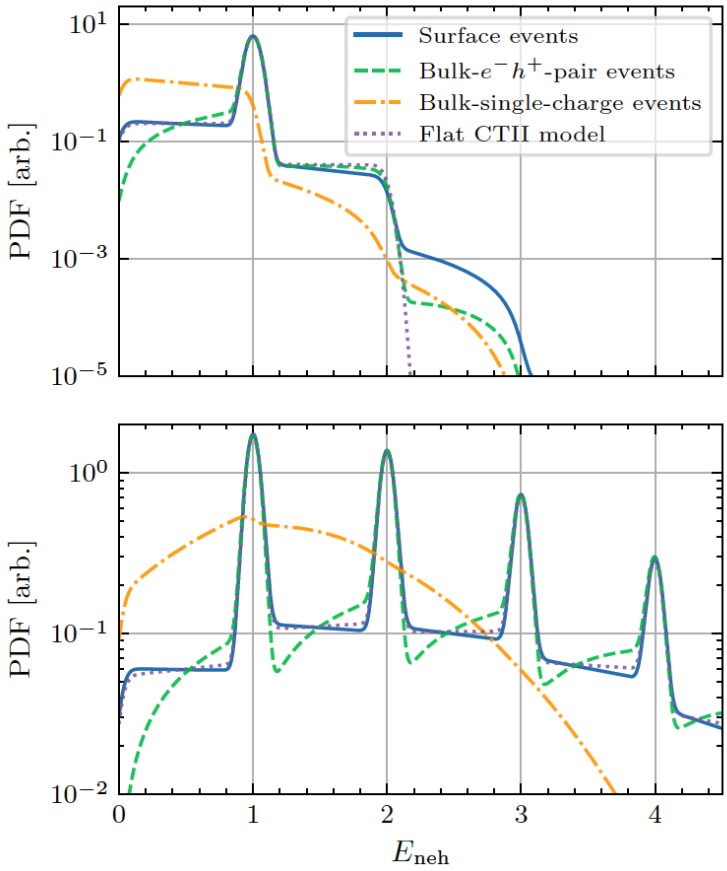

Figure 4.9: Example PDFs found for single electron-hole pair events $F^{(1)}_{type}(E_{neh})$ (top) and multiple electron-hole pair events $H(E_{neh})$ (bot). The PDFs are computed for all three types of events using the exponential CTII model. For comparison, the PDFs computed using the flat CTII model from Ref. [92] are shown by the dotted purple curves. The input CTII parameters are $f_{CTe} = f_{CTh} = 0.2$ and $f_{IIee} = f_{IIeh} = f_{IIhe} = f_{IIhh} = 0.02$ for the exponential CTII model, while $f_{CT} = 0.2$ and $f_{II} = 0.04$ for the flat CTII model. The a_j terms follow a Poisson distribution with a mean of two electron-hole pairs. For illustrative purposes, the PDFs are convolved with a Gaussian function with a width of $E_{neh} = 0.05$ to emulate the detector energy resolution. Plot is taken from Ref. [93].

$$E_{neh} = \frac{E_{ph} - E_{dep}}{eV_{bias}}, \tag{4.29}$$

where E_{dep} is the primary energy deposition in the detector.

3. The detector energy resolution σ_{res}. In this model, σ_{res} is assumed to be constant over different E_{ph}. Therefore, incorporating σ_{res} only needs to be convolved with a Gaussian function with a width of σ_{res}.

4. Non-ionizing energy deposition. For the calibration data with an external LED source, non-ionizing energy deposition may occur either due to some proportion of photons being absorbed directly into the aluminum fins of the phonon sensors, or the surface trapping effect that elec-

trons or holes happen to recombine at the nearest detector surface, as illustrated in Fig. 4.10. The surface trapping effect can be included by introducing a probability α for created electron-hole pairs to get surface-trapped. For photons that encounter surface trapping, the deposited energy will only be the absorption energy of the photon E_γ. Fig. 4.11 shows the modeling of the surface trapping effect with different λ, which characterize the Poisson distribution of the number of photons generated by the LED source. The exponential model with non-ionizing energy deposition included is also sometimes referred to as the "constant shift model".

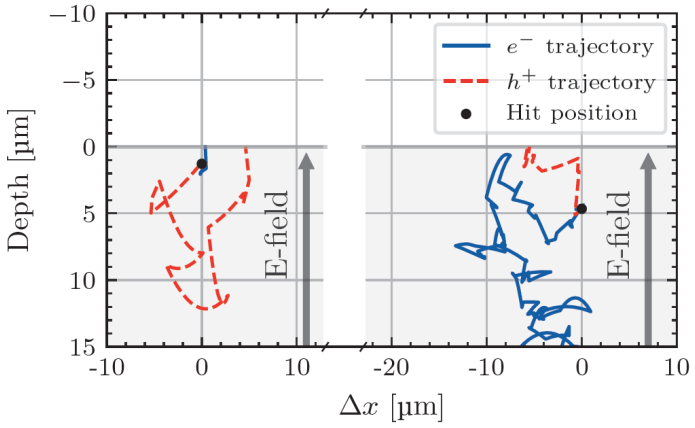

Figure 4.10: Illustration of the hypothesized surface trapping effect as observed from simulation data using G4CMP [94]. Two examples are shown of the trajectory of an ionized electron-hole pair in terms of the depth below the detector surface and the perpendicular x-coordinate relative to the hit position of the absorbed photon. The right example shows a typical event, where the electron eventually travels in the direction opposing the electric field. The left example shows a surface-trapped event, where the electron recombines with the detector surface before it can turn around. Plot is taken from Ref. [93].

With all these considerations included, the extended exponential CTII model wrap up as a python package which is used in the energy calibration of HVeV Run 4 data, as we will discuss in Chapter 5.

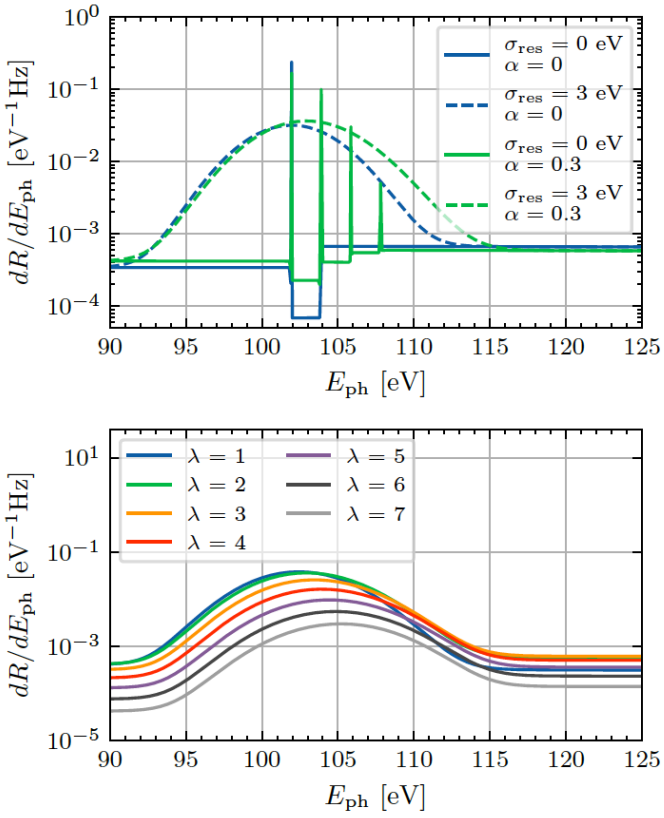

Figure 4.11: Examples of modelling the surface trapping effect with $V_{bias} = 100V$, $E_\gamma = 1.95eV$ and $\alpha = 0.3$. The additional spikes observed in the middle plot demonstrate the contribution of non-ionizing energy deposition when $\alpha > 0$ which, when smeared by the energy resolution, widen and shift the electron-hole pair peaks. Plot is taken from Ref. [93].

Chapter 5

Data Analysis of HVeV Run 4 Low Mass Dark Matter Search

In this chapter, the full analysis of HVeV Run 4 is presented. Section 5.1 discusses continuous readout processing, including triggering and event reconstruction algorithms. Section 5.2 introduces in detail the energy calibration with the Nexus Run 14 LED calibration data. Four live-time cuts are applied, as covered in Section 5.3, while one quality cut is discussed in Section 5.4, with the cut efficiencies estimated. A likelihood-based limit setting approach is explained in Section 5.5, and an overburden attenuation study is discussed in Section 5.6. Finally, Sections 5.7 and 5.8 present the limit setting results for the 30 % unblinded data and the 70 % blinded data separately.

5.1 Continuous Readout Processing

Generally, the continuous readout processing includes two parts, the triggering algorithm and the event reconstruction method. They will be discussed in detail in the following subsections.

5.1.1 Data Acquisition and Blinding Scheme

Two extensive periods of data collection comprise HVeV Run 4. The first period, from February to April 2022 (Nexus Run 13), included science data collection for a DM search, with each detector achieving 11.1 gram-days of raw exposure over 13 days. Nexus Run 13 also involved high-energy calibration for a separate Compton step study using a Caesium-137 source of X-rays at 0V and 100V HV bias. Although the Caesium data were not used for the calibration of electron recoil DM search, they played a role in the definition and efficiency calculation of the energy dependent χ^2 cut.

The second period of data collection started a few months later, from June to August 2022 (Nexus Run 14), where the major goal was to take the LED energy calibration data for our electron recoil DM search.

To avoid any bias in the analysis, it was decided to make 70 % of the DM search science data blinded to the analyzers. The blinding scheme was implemented by allowing only the first three of every 10 data files (each file corresponding to a 5-minute period) to be accessible to analyzers before approval of unblinding. This 30 % fraction was chosen to make the unblinded exposure of

HVeV Run 4 comparable to its counterpart in HVeV Run 3, so that there are enough data for us to conduct all necessary studies, especially on live-time and quality selections.

Data were collected as current amplitudes (in microamperes) using a continuous streaming data acquisition (DAQ) system called the Maximum Integrated Data Acquisition System (MIDAS) on an analog-to-digital converter (ADC) card named the SuperCDMS Detector Control and Readout Card (DCRC), producing 0.5-second raw readout traces.

5.1.2 Threshold Triggering

In HVeV Run 4, an offline triggering algorithm was applied to the 0.5 second raw traces collected from the continuous readout with a sampling frequency of 156,250 Hz. A threshold triggering is applied after convolution of the raw trace with a Gaussian derivative kernel. In the analysis of previous HVeV runs, both Gaussian Derivative Filtering (GF) and Optimal Filtering (OF) before triggering have been studied. The OF trigger has a more straightforward connection to the reconstructed amplitude since they share the same fundamental algorithm, as we will introduce later. However, it suffers more from "echos", meaning non-zero OF amplitudes at time-shift values that are far from the true pulse. Fig. 5.1 shows a raw sample trace before and after both GF and OF, and Fig. 5.2 shows the shape of the kernel that was used in HVeV Run 4. The kernel is the first derivative of a Gaussian function with a standard deviation of 6 samples (38.4 μs) truncated at 4 times the kernel width, as recommended by previous HVeV studies. The recorded trigger point is further shifted to the location of the maximum filtered amplitude, rather than sitting at the rising edge. An additional trigger hold-off feature is adopted so that no consecutive triggers will take place within six samples to avoid unnecessary computational load during processing.

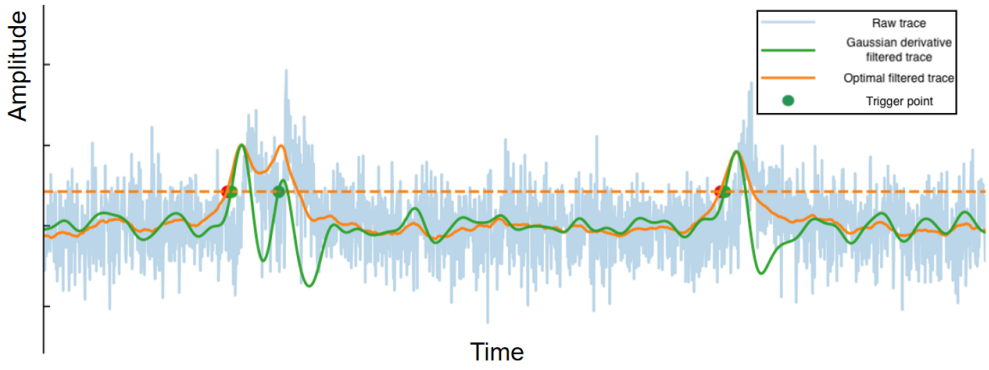

Figure 5.1: Illustration of a raw trace convoluted by a Gaussian derivative filter (green) or an optimal filter (orange).

After locating the trigger points, for each of them, a 2048-sample (∼13 ms) pulse slice is cut from the 0.5 s raw trace with the trigger point at the center (the trigger point is always the first sample of the 1024-sample post-trigger trace). During processing, whenever one detector is triggered, the truncation procedure will be performed for all four detectors to save those pulse slices for event reconstruction.

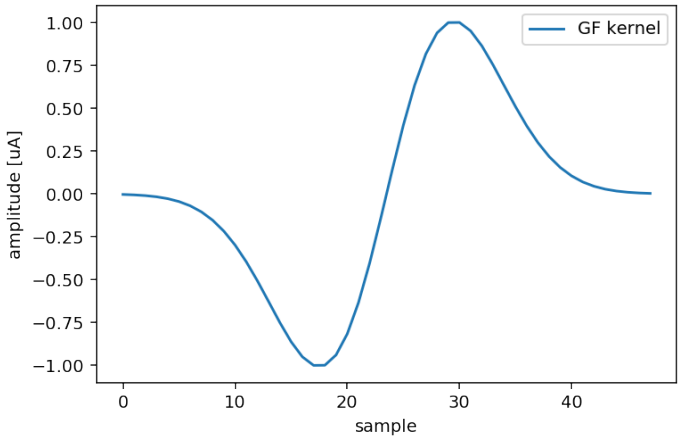

Figure 5.2: Gaussian derivative kernel used in HVeV Run 4 processing. The kernel is the first derivative of a Gaussian function with a standard deviation of 6 samples (38.4 μs) truncated at 4 times the kernel width.

5.1.3 Trigger Efficiency

Trigger efficiency describes the ratio of events that get triggered by a specific trigger algorithm to the total number of events that occur. Usually it is presented as a function of the measured physical quantity (e.g. deposited energy in our case) in the experiment. For HVeV Run 4, the trigger thresholds for the four detectors are given in Table 5.1. The corresponding trigger efficiency curve has been studied with the Nexus Run 14 calibration dataset, as shown in Figs. 5.3 and 5.4. Here, the energy calibration has been applied to covert the current amplitude into the energy deposited in the detector. More details of this will be covered in Section 5.2.

Unlike the OF trigger, where the threshold is directly related to the amplitude of the pulse, which is further related to the energy deposited, the GF trigger threshold does not have a one-by-one mapping into the energy deposited. Therefore, there is a wider transitional energy region where the triggering efficiency is between zero and one. The trigger thresholds adopted in Table 5.1 are tuned so that they are neither too low to include unnecessary noise triggers to overload the processing, nor too high to miss any potential DM signal event with an energy in our analysis range. From Fig. 5.4, we can safely conclude that the current triggering threshold yields an efficiency of 1 above 85 eV for the NFC1 detector, which means that in our whole analysis range, dark matter signal events are always triggered.

Table 5.1: Gaussian derivative filtering trigger thresholds for different detectors in HVeV Run 4

Detector	NFC1	NFC2	NFE	NFH
GF Trigger Thresholds [μA/sample]	0.273	0.198	0.273	0.0922

5.1.4 Event Reconstruction

As in the previous HVeV runs, the event reconstruction in our processing is based on the optimal filter (OF) method [95][96]. The most basic OF algorithm requires a signal template, s(t) in the time domain or s(f) in the frequency domain, and a noise PSD function J(f) that describes the amount of

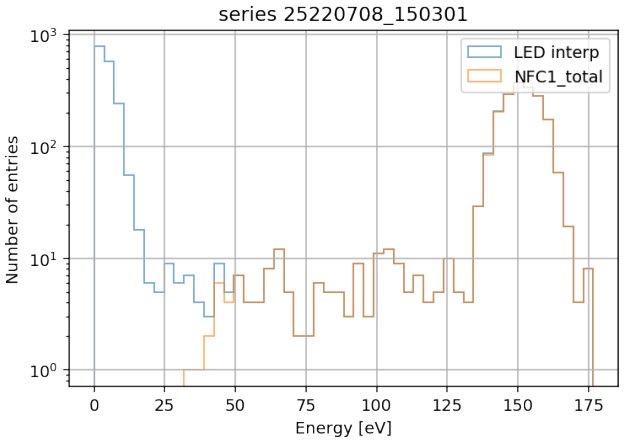

Figure 5.3: Trigger efficiency study of the Gaussian derivative filtering threshold for the NFC1 detector using Nexus Run 14 LED pulses. X-axis is the total phonon energy calibrated from the OF amplitude through the calibration discussed in Section 5.2.

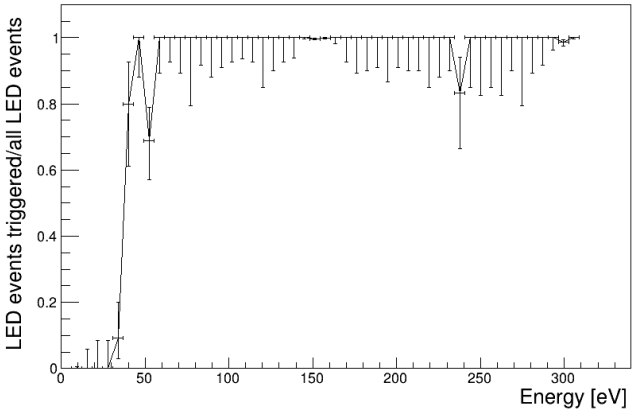

Figure 5.4: Trigger efficiency curve as a function of energy deposition from LED pulses. X-axis is the total phonon energy calibrated from the OF amplitude through the calibration discussed in Section 5.2.

power at different frequencies. The best-fit pulse amplitude A is found by minimizing the frequency domain χ^2 of the fit defined as

$$\chi^2(A) = \int_{-\infty}^{\infty} \frac{|v(f) - As(f)|^2}{J(f)} df. \tag{5.1}$$

The best fit χ^2 describes the goodness of the fit. The larger its value, the more inconsistency exists between the signal template and the pulse we are looking at under the assumed level of noise indicated by J(f). A χ^2 close to one represents a potential DM signal-like pulse.

The basic OF algorithm (Eq. 5.1) only works in the case when we are confident that the alignment of the pulse and the template in the time domain is accurate. However, this is not guaranteed considering that the trigger point location is discrete in samples (neighbouring samples are separated by 0.64 microseconds). Therefore, we extend the basic algorithm to a more complicated version where a time offset is allowed, either globally or within a certain range.

$$\chi^2(A, t_0) = \int_{-\infty}^{\infty} \frac{|v(f) - Ae^{-i\omega t_0} s(f)|^2}{J(f)} df. \tag{5.2}$$

Here, the exponential term $e^{-i\omega t_0}$ accounts for the Fourier transform of the signal shifted by amount t_0 in time to the frequency domain, where $\omega = 2\pi f$.

In our analysis, the basic OF method (Eq. 5.1) and the extended OF method (Eq. 5.2) are both applied in event reconstruction to produce similar, but slightly different energy indicators, OF0 ("0" stands for $t_0 = 0$) and OFL ("L" stands for "Limited", which in our case is [-6, 6] samples), respectively. Their corresponding best fit χ^2 values, χ^2_{OF0} and χ^2_{OFL}, are also saved as reduced quantities (RQs) included in the processing output.

Table 5.2: Major reduced quantities (RQs) generated in the HVeV Run 4 event reconstruction.

Name	Unit	Description
OF0	uA	No time offset
χ^2_{OF0}	None	Best fit χ^2 with no time offset
OFL	uA	Limited (6 samples) time offset
χ^2_{OFL}	None	Best fit χ^2 with limited time offset
MeanBase	uA	Average of first half truncated trace
BaselineSlope	uA/sample	Slope of the baseline
Slope	uA/sample	Slope of the full truncated trace
Max-Min	uA	Maximum subtracting minimum of a trace
Integral	uA	Integral of the trace after baseline subtraction
FallTime1	sample	Fall time from 50% to 30% maximum
FallTime2	sample	Fall time from 90% to 50% maximum
FallTime3	sample	Fall time from 100% to 90% maximum
...	...	...

Table 5.2 lists some of the most important RQs that are used in this analysis. In our experiment, the OF amplitudes are the indicators of the energy deposition in the detector for each event. The relation between the OF amplitude and the deposited energy is approximately linear but not exactly due to the saturation of pulses at high energy. The complete mapping between the two quantities will be discussed in detail in Section 5.2.

5.1.5 Signal Shape Study and Templates Generation

The event reconstruction step in the HVeV processing workflow requires both a signal template and noise power spectra densities (PSDs), as we discussed in Section 5.1.4. The signal templates used for processing are calculated from the time domain average of the 1200 pulse slices from the unblinded science data, both in the total channel and its corresponding sub-channels (inner and outer channels). The idea behind pulse averaging is that the noise components of the pulses will cancel out with each other with the number of pulses involved increasing, as their phases are random and independent of each other, while the signal components remain intact. These 1200 pulse slices

are chosen by applying preliminary selections of shape and amplitude after pre-processing with the pre-templates that were derived from a previous HVeV run. Their trigger points are aligned with each other based on the best-fit position in time axis of the OF pre-template. Fig. 5.5 demonstrates the trigger point alignment during the averaging procedure, Fig. 5.6 shows the shape of the average pulse in comparison with the pre-template, and Fig. 5.7 compares the frequency domain spectra with the typical noise level in the experiment.

In principle, we could build the signal templates from the LED data which we assume to be DM signal-like, but the LED data are taken in a separate run (Nexus Run 14) so we have to be careful with the differences in experimental setups, as we faced in energy calibration in Section 5.2. However, from the 30% unblinded data, after some pre-selection of DM-like pulses, we already have good enough statistics to build a 1eh signal template.

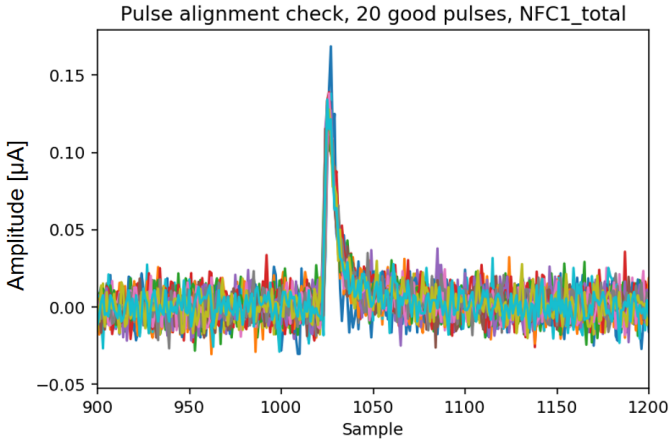

Figure 5.5: A demonstration of pulse averaging of 20 selected pulses. The pulses in the plot are already aligned by their best-fit positions in time axis of the OF pre-template, instead of having their original trigger point at the exact center of the 13ms window. The plot is zoomed in around the rising edge.

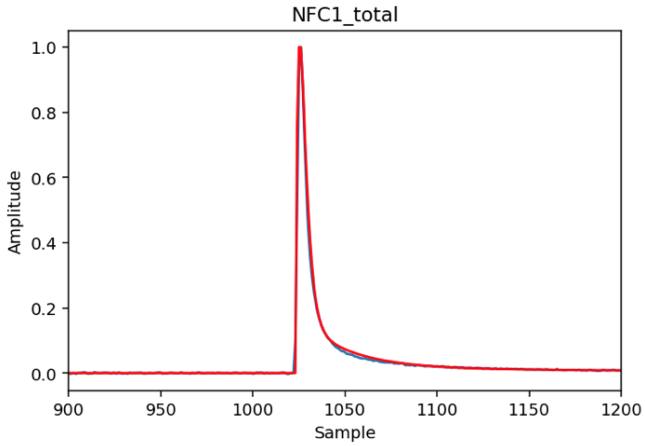

Figure 5.6: The averaged pulse for NFC1 detector in the time domain, with the maximum amplitude normalized to one. The blue curve is the averaged pulse over 1200 selected 1eh pulses. The red curve is the pre-template derived from a previous HVeV run.

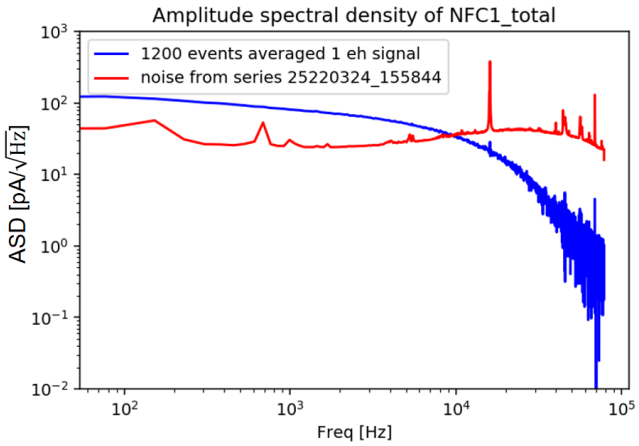

Figure 5.7: The averaged pulse for NFC1 detector in the frequency domain.

5.1.6 Noise Study and Power Spectra Density Generation

To prepare the noise power spectra densities for reconstruction, we randomly trigger in the raw traces where there are no signal events. Pulse rejection is realized through an auto-cut algorithm based on four parameters of the truncated trace: average (mean amplitude), slope, skewness and range (max-min), where the 3-σ outliers corresponding to signal events are removed. The remaining trace slices without pulses are saved and averaged in the frequency domain for each series of data to make its own noise PSD file during processing. Fig. 5.8 shows the day-by-day variation of the noise spectra throughout the science data, where the spikes in the high frequency ($> 10k$Hz) regions might arise from electronic noise. The noise level in general remains stable for all four detectors, especially for the NFC1 detector. We take the noise PSD of March 24 as our noise template for event reconstruction, since it is closest to the average noise level of the whole 13 days. We avoid using series-by-series noise templates for reconstruction because it would require recalibrating the energy each time we switch to a new series, which is unnecessary given that the noise variation is not significant.

5.2 Energy Calibration and Detector Response Modeling

Energy calibration is an essential step in this analysis to convert the energy estimator OF amplitude to the total phonon energy deposition.

5.2.1 Identification and Interpolation of LED Pulses

In Nexus Run 13 when our science data were taken, despite the Caesium-137 calibration data we have for high energy calibrations, a low energy calibration source is absent, as a laser or LED apparatus may add luminescence backgrounds from the low radio-purity plastic materials involved (for example the IR filters described in Section 3). To enable the low energy calibration, a separate run of data taking, Nexus Run 14, was conducted with an external LED source shining on one of the four detectors used in Nexus Run 13.

The LED pulses are expected to occur periodically since we generate them at a known burst

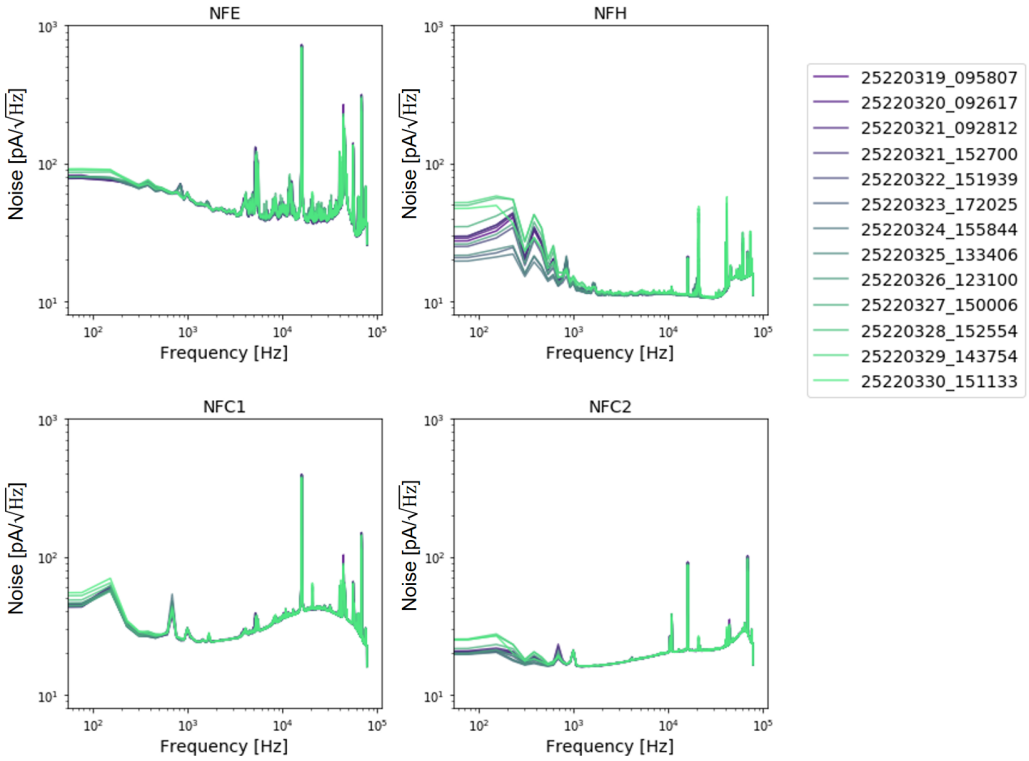

Figure 5.8: Day-by-day variation of noise PSDs throughout the science data. Each curve corresponds to one series of data, whose 5^{th} to 8^{th} digits indicate the month and date when it was taken.

frequency. The number of photons in each pulse follows a Poisson distribution with λ depending on the operating voltage. Sometimes a zero photon pulse is possible for a low voltage operation of the LED source, which leads to no trigger being collected at the corresponding time. However, the exact time of each LED pulse is not provided directly by the source itself. Therefore, to identify the LED pulses from the background or potential dark matter events and interpolate forced triggers at those missing positions due to zero photon pulses, an LED interpolation algorithm is designed and added to the processing package for the Nexus Run 14 LED data.

The interpolation algorithm has three steps in general:

1. Calibrate the LED burst frequency from a rough initial guess (e.g. 10Hz) from the experimental records.

   For each triggered pulse (except the last 15 ones), calculate the distances between its trigger location and those of the next 15 triggered pulses and put them into a histogram. Zooming into the central bin and fitting with a Gaussian function, we will get a more accurate estimation of the true burst frequency.

2. Identify LED pulses by calculating their distances to the neighboring events and apply a selection cut based on how many distances are close enough to our expectation.

   For each triggered pulse, calculate the distances between its trigger location and those of the previous 10 triggered pulses (for the first 10 pulses, using distances to the next 10 pulses instead) and put them into a histogram. Select those with more than two distances (out of 10) falling into the +/- 0.05% range of the calibrated minimum distance from step 1.

3. Interpolate into the missing entries among the locations of LED pulses.

With the background pulses filtered out, we now have a list of triggered LED events locations with missing entries where the LED pulses have 0 photon there and therefore they are not triggered. To find those empty positions, we calculated the distance of neighbouring LED events triggered, which should be N times the minimal distance. If $N > 1$, N-1 events will be uniformly interpolated in between.

After these three steps, we have a list of locations of all LED pulses (triggered and interpolated). Then we will force trigger at those positions and reconstruct the RQs as usual, and the results will be written into a new LED interpolation channel without affecting the original RQ output. For a triggered LED event, it will show up twice in the dictionary, both in its triggering channel (e.g. NFC1) and in the LED interpolation channel, as illustrated in 5.9. The LED interpolation channel will be used for energy calibration as well as other studies in the following sections.

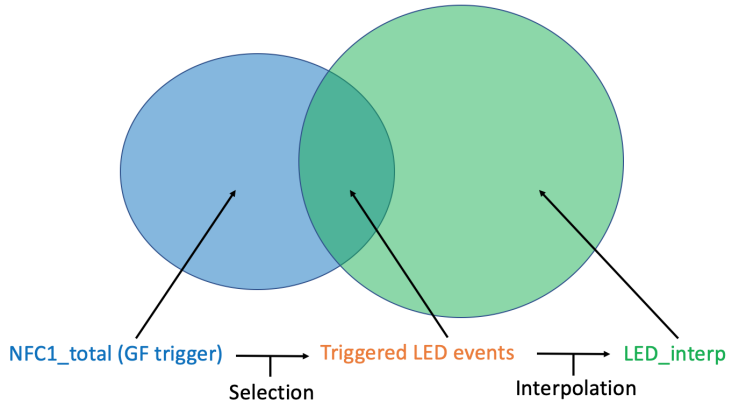

Figure 5.9: Diagram illustrating the relation between different event sets. The blue circle includes all triggered events in the detector, while the green one contains all LED pulses generated periodically. The overlap of the two are the triggered LED events.

5.2.2 Working Point Alignments and Corrections

The parasitic resistances have changed between Nexus Run 13 and Nexus Run 14 due to a connector saver being added to the wiring to accommodate the additional height caused by adding the LED box to the detector tower. They were evaluated through the IV curve measurements as shown in Table 5.3.

Table 5.3: Parasitic resistances in Nexus Run 13 and Nexus Run 14, as illustrated as R_p in Fig. 2.7

Parasitic resistance (mOhm)	PAS1	PBS1	PCS1	PDS1	PES2	PFS2
R13	8.69	8.76	8.81	9.29	9.90	7.92
R14	9.01	8.99	8.90	9.36	10.11	7.87

Consequently, the same bias current (also internally referred to as the *working point* (WP)) will not reproduce the same OF amplitude for each e-h pair peak. Therefore, a working point scan was

conducted during Nexus Run 14 by varying the QET bias until the *current scale* for each channel as defined in Eq. 5.3:

$$\Delta I_{pk} = \begin{cases} OF_{1st} - OF_{0th} & \text{LED data} \\ OF_{1st} & \text{Background data} \end{cases}, \tag{5.3}$$

is close to that of Nexus Run 13. Here, the *Background data* refer to those series with LED source turned off, and the OF amplitude of the zeroth energy peak, defined by the mean value of a local Gaussian fit, was subtracted in the case of LED data for two reasons:

1. There are cross-talks between the TES readout wire and the LED wire.
2. The low-energy LED photons get absorbed promptly ($\sim$2 eV, silicon absorption length of O(1 μm)) and are very likely to be surface events.

The quantitative study of the zeroth peak correction from these two sources will be discussed in the next subsection. Both of them will not appear in the Nexus Run 13 science data.

The detailed information on each working point for all three detectors is summarized in Table 5.4. The working points identified as "NR14 closest WP" give the closest current scale to that of Nexus Run 13 science data. The corresponding Nexus Run 14 background data are compared with the Nexus Run 13 30% unblinded science spectra, and a linear scaling is assumed for the mapping of OF amplitudes between the two runs. Fig. 5.10 compares the spectra of the Nexus Run 14 bg series at the suggested WPs with those of the Nexus Run 13 science data. The linear scaling factors of the WP alignment β_i (where i stands for detector indexes) for the amplitudes are calculated from their 1eh peak positions determined from a local Gaussian fitting. The results of β_i are listed in Table 5.5.

Table 5.4: The working points of 100V LED data of Nexus Run 14. The QET bias column lists the inner and outer bias currents for each work point.

Label	QET Bias [uA]	Detector	Description
WP1	50/51	NFC1	40% of the transition
WP3	49/49	NFC1	NR14 closest WP
WP2	46/46	NFC1	NR13 WP
WP1	55/51	NFC2	40% of transition and NR14 closest WP
WP3	52/51	NFC2	NR13 WP
WP2	43/41	NFH	40% of the transition
WP1	42/40	NFH	NR14 closest WP
WP3	40/40	NFH	NR13 WP

Table 5.5: The WP alignment linear scaling factors β_i for amplitudes from Nexus Run 13 to Nexus Run 14.

	NFC1	NFC2	NFH
β_i (NR14 bg/NR13 science)	0.963	0.998	0.964
$\Delta\beta_i$	0.002	0.002	0.012

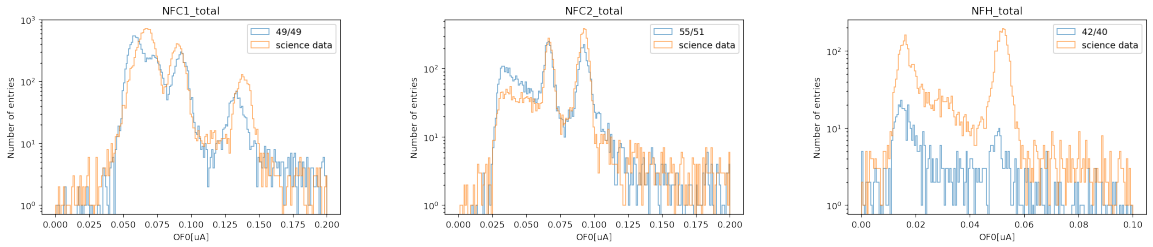

(a) NFC1 (b) NFC2 (c) NFH

Figure 5.10: OF amplitude scaling between the Nexus Run 14 background data taken at suggested working points and the Nexus Run 13 science data. The WP alignment linear scaling factors β_i for amplitudes are calculated from the corresponding 1eh peak positions determined from a local Gaussian fitting.

5.2.3 Zeroth Peak Correction: Cross-Talk Amplitudes and Unamplified Phonons

In Nexus Run 14, a non-zero 0th peak offset in the OF0 spectra was observed, which potentially comes from two sources: (1) unamplified LED photons and (2) cross-talk amplitudes between LED and TES wires. The unamplified LED photons arise from the surface trapping effect, where the photons emitted by the LED source get trapped on the hit surface, producing no NTL phonons. Therefore, their energies are not amplified by the voltage applied through the crystal. The contribution to the 0th peak offset from unamplified photons obviously has a positive dependence on the λ of the LED source, and it is a *real* physical effect that changes our expectation of the peak positions (no longer centered at n$\times$100 eV). However, the other source, the cross-talk amplitudes caused by the induction between LED and TES wires, remain constant for a specific detector for the same LED amplitude, adding a constant shift to the whole OF amplitude spectrum. This part of the extra OF amplitude is *fake*, and needs to be subtracted before the energy calibration.

To calculate λ, the number of expected LED photons of the Poisson distribution given a specific setting of LED offset current, we fit a spectrum with the flat CTII model (as mentioned in Section 4) with a photon source, as illustrated by the red curve in Fig. 5.11. The fit results will provide us the λ information for each series.

Then we inspect the 0th peak offsets in the OF0 spectra for different series, extract their values from a Gaussian fit and plot them against their LED λs, as shown in Fig. 5.12. We approximate the relation between the LED λ and the OF0 amplitude caused by the unamplified photons with a linear function, considering that the uncertainty from higher-order terms is negligible compared to other sources as we will see in Section 5.2.6. The non-zero y-intercept from the linear fit confirms the existence of cross-talk amplitudes, whereas the non-zero slope confirms the existence of the surface trapping effect.

Here, we look at OF0 amplitudes instead of OFLs because OFL does not function as a good energy estimator at extreme low energies of a few eV. In such cases, allowing the trigger point to be adjusted locally in time will usually lead to the reconstruction of a neighboring noise fluctuation, causing the OFL 0th peak to split spontaneously even without the two sources mentioned above.

This linear function extracted from Fig. 5.12 enables us to estimate zeroth peak offsets for high λ series that do not have a visible zeroth peak. Although these high λ series are not in our analysis

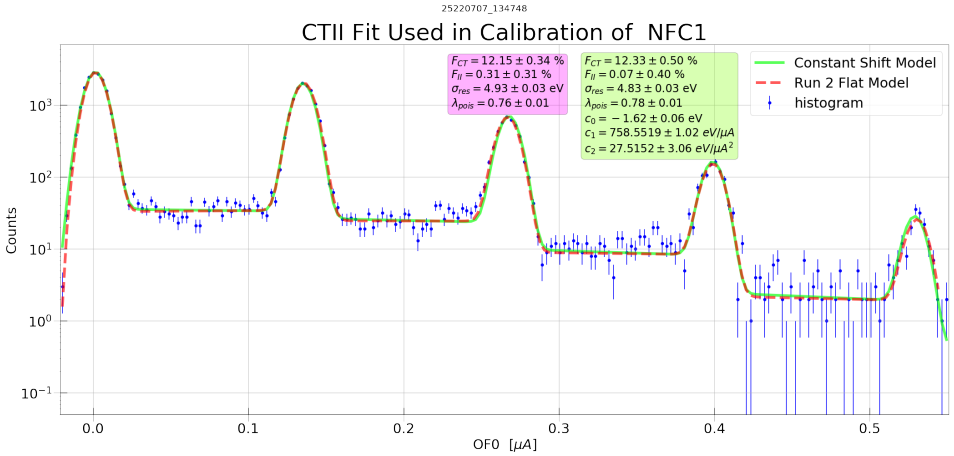

Figure 5.11: OF0 CTII calibration fit for NFC1 detector using the flat model (red) in comparison with using the constant shift model (green). This OF0 preliminary calibration gives us best fit values and uncertainties for CTII parameters, which will be further used in OFL recalibration.

range and therefore not used in the science run calibration, they are important for other analyses such as the Compton step study.

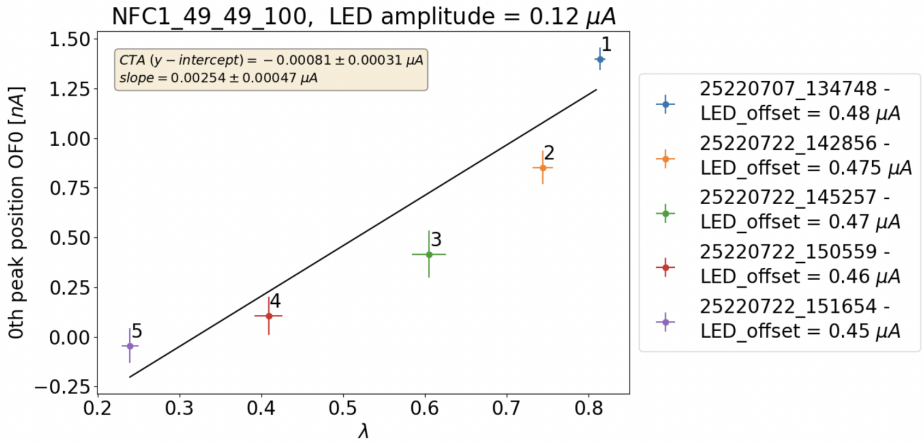

Figure 5.12: 0th peak versus λ plot with linear fit for NFC1 detector at WP3 with an LED amplitude of 0.12 uA. The y-intercept is interpreted as the cross talk amplitude (CTA) while the slope indicates the dependence of the OF0 amplitude caused by un-amplified photons on the LED λ. The points are numbered increasingly in the chronological order that they were taken.

5.2.4 Detector Response Modelling and OFL Recalibration

Generally, the energy calibrated from the OF amplitude can be expressed as a polynomial expansion in the form of Eq. 5.4:

$$E(OF) = c_1 \times OF + c_2 \times OF^2 + ..., \tag{5.4}$$

with the linear term being dominant. In this analysis, we take into account a second-order correction

to the linear mapping from the OF amplitude to the calibrated energy, and ignore the higher-order terms assuming their negligible influences.

After subtracting the crosstalk amplitude from the OF0 spectrum, a constant shift parameter c_0 is included in the calibration to take into account surface trapping effects. The new detector response model we use at this stage is the CTII constant shift model. The differences between the constant shift model and the flat model are listed in Table 5.6, with a detailed discussion in Section 4. Fig. 5.11 shows the OF0 calibration fitting results with the constant shift model in comparison with that of the flat model.

While the OF0 amplitude allows us to subtract the 0th peak offset more accurately, it is still a worse energy estimator compared with the OFL amplitude in our analysis range, since the OFL amplitude is reconstructed in a way allowing local adjustments of the trigger point, compensating for the systematic error caused by discrete sampling. Therefore, an OFL recalibration is performed to achieve higher accuracy, where the detector response parameters are taken from the OF0 calibration fitting, as shown in Fig. 5.13.

Table 5.6: Model parameters for the OF0 spectrum fits.

Parameter	Description	Flat Model	Constant Shift Model
F_{CT}	Charge trapping probability	floating	floating
F_{II}	Impact ionization probability	floating	floating
σ_{res}	Width of the Gaussian kernel	floating	floating
c_1	Linear term calibration constant	not part of the fit	floating
c_2	Quadratic term calibration constant	not part of the fit	floating
λ_{pois}	Photon source λ	floating	floating
c_0	Overall shift constant	not part of the fit	floating

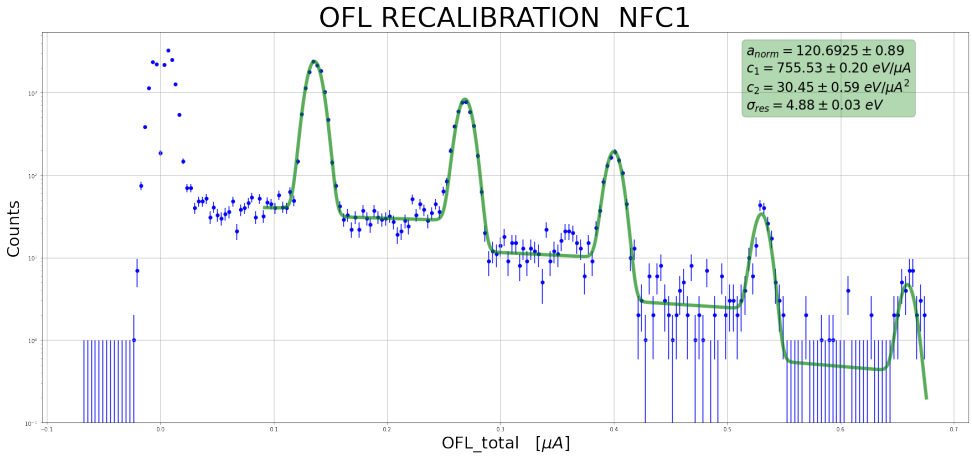

Figure 5.13: OFL recalibration with inputs from OF0 calibration fits. The four parameters shown in the green box are allowed to float, and the remaining parameters to construct the fitting function are taken from the green box in Fig. 5.11. The 0th peak is excluded from the fitting due to the OFL estimator being unreliable in extreme low energies.

The Nexus Run 14 LED data not only help calibrate the energy, but also play significant roles as

subsidiary experiments to provide insights into the prior distributions of nuisance parameters. This information can be achieved from the best-fit values and uncertainties of the CTII parameters from the OF0 calibration and the detector energy resolution from the OFL recalibration. They will be mentioned in more detail in Section 5.5.

Due to the good detector resolution performance and the low noise level, we selected the NFC1 detector as our only limit setting detector for HVeV Run 4. Although the NFC2 detector uses the same design as NFC1, difference experimental performances arouse from factors which are hard to control in fabrication. The exposure loss from not using other detectors is not a real issue for this analysis, since we are not exposure limited in the first and second peaks where we are most likely to be competitive, as pointed out by a previous sensitivity study.

Starting from this section in Chapter 5, we will only show plots of the NFC1 detector, and leave those of other detectors in the Appendix.

5.2.5 Position-Dependent Relative Calibration

Each HVeV detector consists of two channels, referred to as the inner channel OF_in and the outer channel OF_out, as illustrated in Fig. 3.2. Each channel has TESs connected in parallel. The total output signal is the sum of the inner and outer channel output signals. However, the inner and outer channels do not have the same amplified amplitude. With the same input signals received, their output signals are different. This discrepancy can arise for various reasons, such as the different numbers of TESs in each channel, or imperfections in the manufacturing process. Consequently, the detector's sensitivity to the position of energy deposition is affected, causing variations in the total output signal depending on where the energy is deposited within the HVeV detector.

To account for the position dependence effect of the energy deposition, a re-weighting of the inner and outer channels of an HVeV detector is necessary. Here, the unblind science data of Nexus Run 13 are investigated, and we choose to reweight the inner channel as shown in Fig. 5.14. The total output signal OF0_total is the summation of the OF0_out and OF0_in times a relative weighting factor α. The reason for using the OF0 amplitude instead of OFL is to prevent the noise condition changes between OF0 and OFL, since the noise is estimated by the OF0 amplitude.

$$A_{total} = A_{outer} + \alpha A_{inner}$$

total event amplitude (current)

relative weighting factor

Figure 5.14: The expression of re-weighted total amplitude, with the relative channel weighting factor α multiplying at the inner channel.

As illustrated in Fig. 5.15, events plotted on the OF0_in versus OF0_out plane exhibit bifocal centers. This duality in the centering of the 1eh peak arises from the geometric configuration of the detector's inner and outer channels. The core idea of position-dependent relative weighting is that by applying the formula in Fig. 5.14, the new inner and outer channels will have a symmetric event amplitude distribution, as shown in Fig. 5.16. Mathematically, it is equivalent to forcing the

line connecting the two centers of the event clusters to have a slope of -1. The center locations of the two event clusters are not difficult to find, since we only need to fit Gaussian functions in both OF_in and OF_out histograms. The associated value of α is subsequently identified as the final relative channel weighting factor, as presented in Table 5.7. Note that when detector noise levels are significantly high, the fitting results for the two Gaussian functions can exhibit substantial uncertainties, potentially compromising the accuracy of the derived outcomes. This situation is illustrative of the challenges faced with the NFE detector.

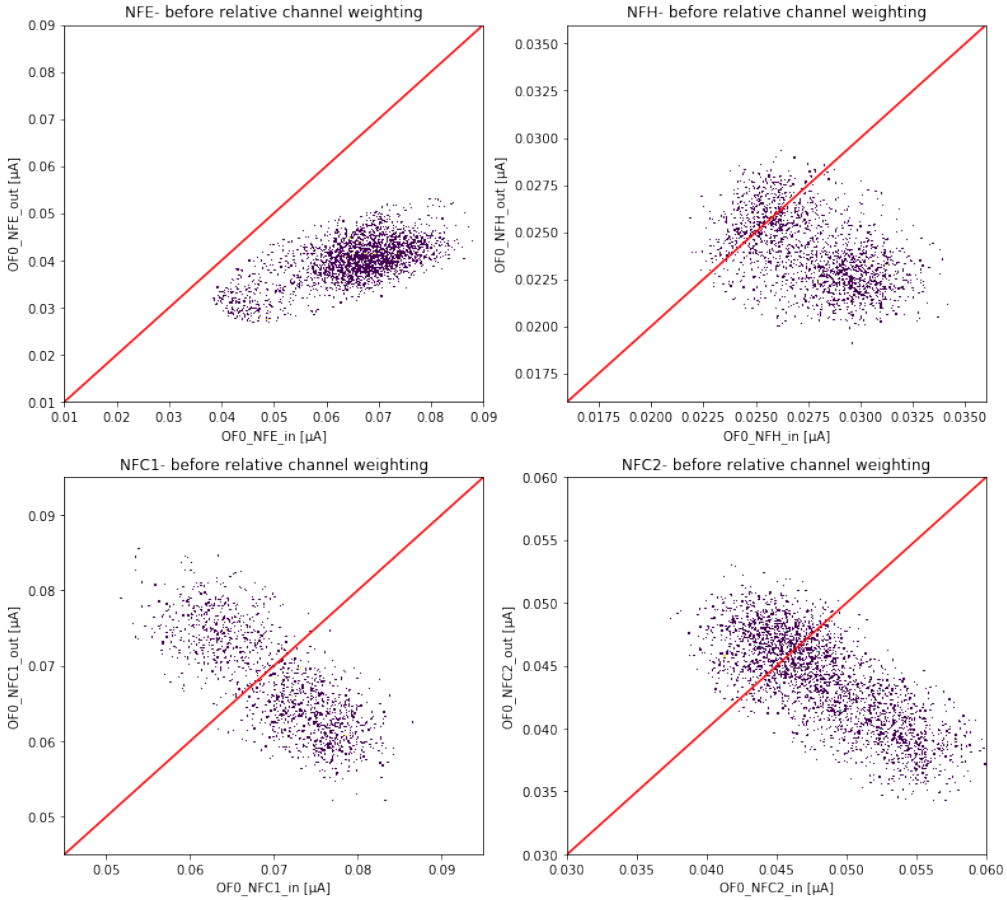

Figure 5.15: 2D histograms of 1eh events in OF0_in and OF0_out plane for different detectors before relative channel weighting.

Table 5.7: Model parameters for the OF0 spectrum fits.

	NFC1	NFC2	NFE	NFH
α	0.99	0.87	0.64	0.87
$\Delta\alpha$	0.01	0.01	0.89	0.01

For the only limit setting detector NFC1, the relative channel weighting factor α is consistent with identity. Therefore, we decide not to implement the reweighting and instead use the direct sum of inner and outer channels.

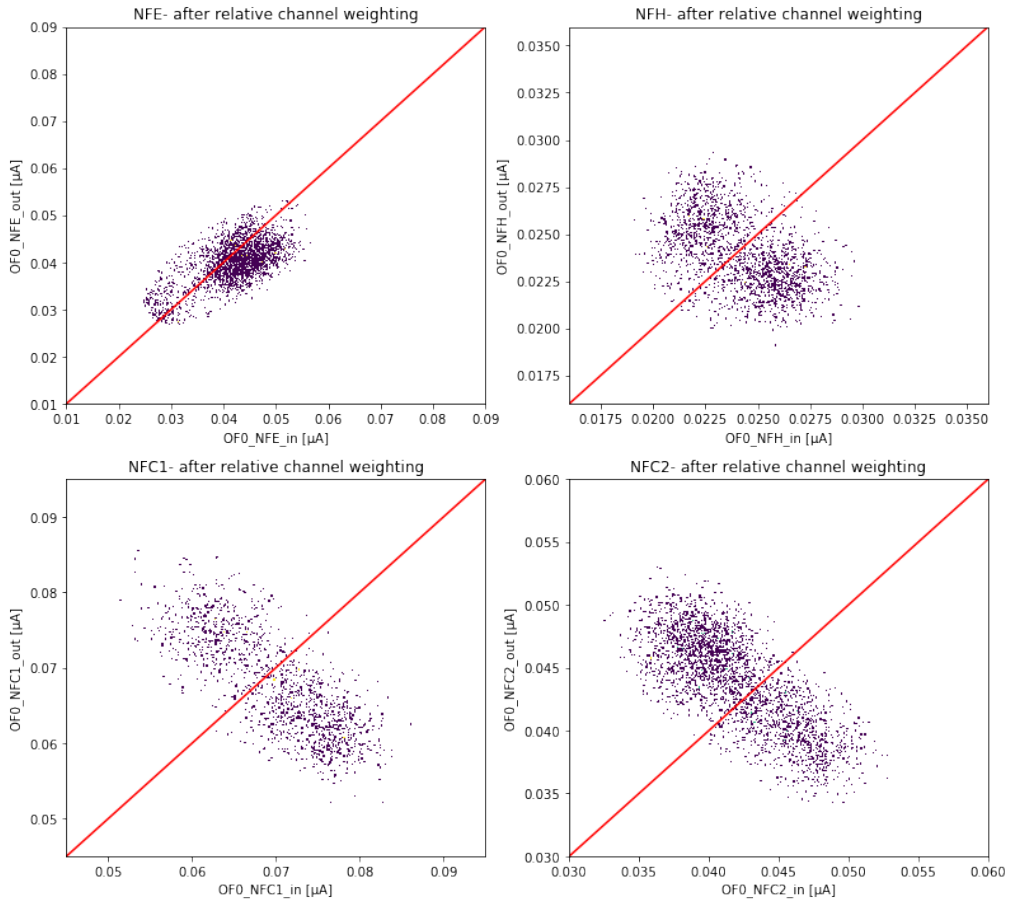

Figure 5.16: 2D histograms of 1eh events in OF0_in and OF0_out plane for different detectors after relative channel weighting.

5.2.6 Calibration Uncertainties

Statistical and systematic uncertainties from different steps are calculated as a function of energy, and are added in quadrature to give the total uncertainty in energy calibration, as shown in Fig. 5.17. This total uncertainty is assumed to be perfectly correlated between different events, and therefore affects as an overall shift to the energy spectrum. The prior distribution of this overall spectrum shift due to the energy calibration uncertainties is a Gaussian distribution centered at zero with a standard deviation equal to the magnitude of the total uncertainty calculated in Fig. 5.17.

As observed in Fig. 5.17, the level of total energy uncertainty is at $\sim 1eV$ level for the first peak and lower, and gradually increases to ~ 3 eV for the third and fourth peak. This increase is mainly caused by the uncertainty from the working point alignment, which was conducted based on the first peak position (as discussed in Section 5.2.2). In the limit setting procedure, we extract the total calibration uncertainty for each peak separately from the plot, and apply them into different prior distributions.

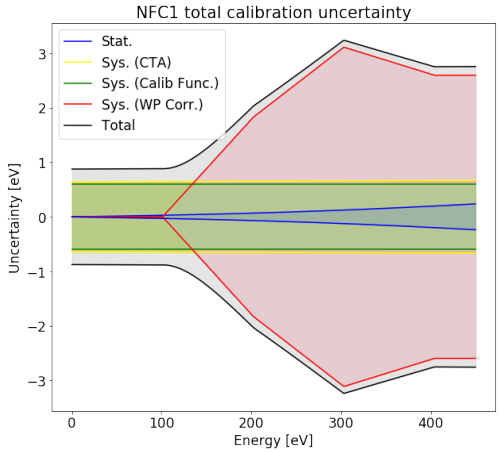

Figure 5.17: Plot of the total uncertainty (sys+stat) as a function of energy for the NFC1 detector. Different components of the systematic uncertainty are shown separately. Uncertainties are added by quadrature.

5.3 Live-Time Data Selections

Four types of live-time cuts are developed and applied in this analysis in order to select periods that are most ideal for the dark matter search:

1. Fridge temperature cut.
2. Baseline Excursion live-time cut.
3. Elevated rate live-time cut.
4. Coincidence-type live-time cuts.

As discussed in the processing section, the pulse analysis window comprises 2048 time samples out of a half-second MIDAS trace, with the trigger point at the center. At the beginning and end of each MIDAS event, there are 1024 samples (out of a total of 78,125) that the trigger is blind to, giving rise to a live time fraction of 97.38% before any live-time cuts. This was already included in calculating the raw live-times and exposures at the beginning of this section.

The following subsections will describe the method and definition of each cut.

5.3.1 Fridge Temperature Cut

The fridge temperature in the mixing chamber, monitored the whole science run at a sampling frequency of 0.025 Hz, remained stable at $(11 \pm 0.1)mK$ during normal operation. However, the fridge temperature can experience fluctuations, especially when the temperature regulation is not working properly. Fig. 5.18 shows the recorded fridge temperature during the Nexus Run 13 science data taking. A fridge temperature cut is developed to ensure that the selected live time always has a temperature below 11.1 mK. It is observed that only one single period on March 29th experienced abnormal temperature due to some unknown reasons. We decided to cut out a 2-hour time from that day, which is conservative but also has a negligible impact on our total exposure.

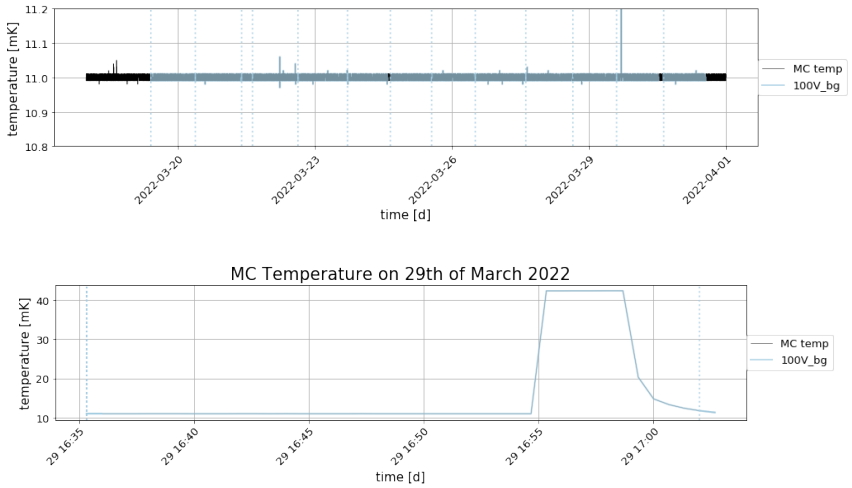

Figure 5.18: Top: Mixing Chamber temperature sampled every 40 seconds. Blue shaded regions of the line are periods when data was being taken. With the exception of a five minute period on the 29th of March 2022, no other temperature excursion above 11.1 mK. Bottom: largest temperature excursion recorded around 16:55 CDT and lasted for five minutes. The fridge temperature cut was defined to cut all MIDAS event traces that occurred starting from 16:00:00 to 18:00:00 CDT.

5.3.2 Baseline Excursion Live-Time Cut

Apart from the fridge temperature, the baseline parameter, represented by the average amplitude in the non-signal region, is also a complementary indicator of the detector stability. In this analysis, we define a parameter called "trace baseline" for each 0.5 s trace, and decide whether a whole trace is removed or not based on its trace baseline level compared with the overall distribution of this quantity throughout the science run.

The steps to calculate a trace baseline are as follows:

1. For each 0.5 s trace from the continuous readout, apply the optimal filter to the raw trace and set threshold triggers.
2. Remove 1024 time samples in both directions around the trigger point. In this way, the signal regions are excluded.
3. Average the remaining sampling points in the entire trace and save it as the "trace baseline".
4. Put all the trace baselines for different traces in the 30% unblinded data in a histogram, fit it with a Gaussian function and find the 3σ upper and lower bounds as the cut thresholds.
5. Apply live-time cut on a trace basis: if the trace baseline for a 0.5 s trace falls outside of the 3σ region, the whole trace become deadtime.

Figure 5.19 shows the trace baseline fluctuation throughout the science run for the NFC1 detector.

5.3.3 Elevated Rate Live-Time Cut

In the models we are examining, the number of dark matter induced events in a constant time range should in general follow a Poisson distribution. However, Fig. 5.20 shows that during our science

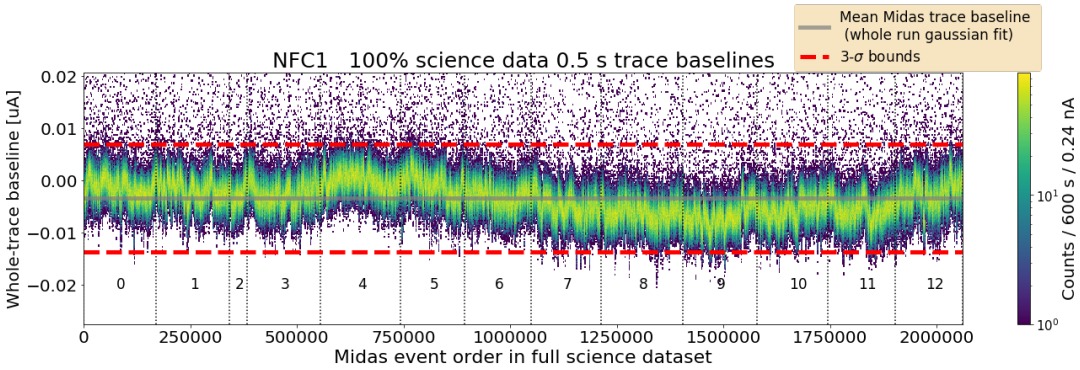

Figure 5.19: A trace-based quantity for the mean baseline was calculated for each 0.5 s Midas event (trace) by applying the Optimal Filter trigger, cutting out the regions with threshold triggered events, and averaging what remains of the trace to obtain the "trace baseline" in current units. Vertical lines indicate series boundaries.

run, there are spikes in the trigger rate and they return slowly to the normal level. Such an effect is highly unlikely related to dark matter (at least for the types in our signal models) and therefore needs to be excluded from our analysis. The exact source of these events still remains mysterious to us. Before we have a clear understanding of the cause of this phenomenon, it is necessary to remove them using an elevated rate live-time cut.

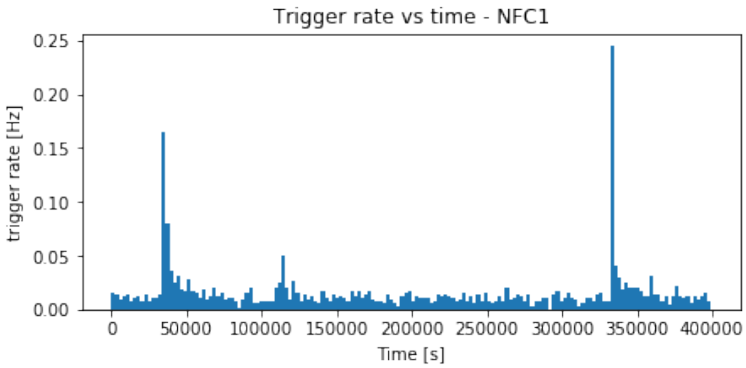

Figure 5.20: A trigger rate plot with respect to time from the 30% unblinded science data of HVeV Run 4 for the NFC1 detector.

Taking advantage of the sharp rising edge and the long tail of such "spike events", the cut is defined in the following way:

1. Divide the data taking time into 2400 second intervals. For each interval, count the number of triggered events during that period.

2. Put the event counts for all periods into a histogram, fit it with a Poisson function as predicted by the statistics, and extract the mean and standard deviation of the fit.

3. Set the threshold of the event count in a 2400-second interval at 9σ level, making it extremely unlikely (less than 0.001% probability) to misidentify potential dark matter events as the "spike events" we are going to remove. This threshold is set in an extremely conservative way since we will cut a long period for each occurrence of the "spike events".

4. Identify the starting point of a cut region by looking for the first interval that passes the event

count threshold. Then we remove 10 hours after each spike.

Figure 5.21 shows the result of applying the elevated rate live-time cut on the NFC1 detector for the 30% unblinded data. Around one-fourth of our exposure is lost due to this cut.

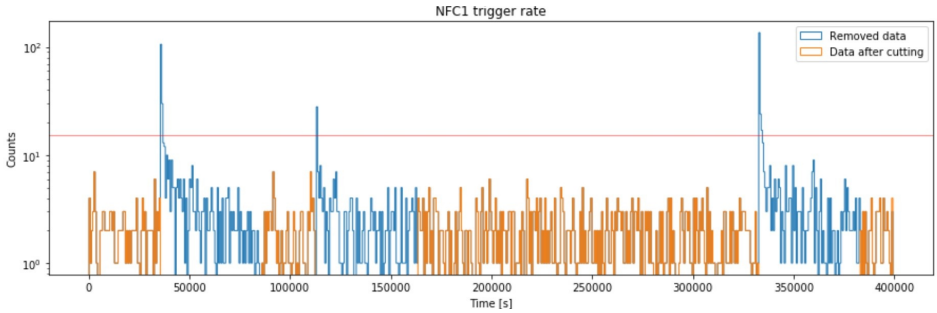

Figure 5.21: Elevated rate live-time cut on detector NFC1. The red line is the cut threshold. Blue bins are data removed by the cut and the orange one are preserved. A total of 23.03% exposure is lost due to this cut.

5.3.4 Coincidence-Type Live-Time Cut

The expected event rate for our dark matter signal models are all extremely low so that two consecutive triggers in a short time period is highly inconsistent with our signal assumptions, both in one detector and across different detectors. Fig. 5.22 shows one example of such events. Two coincidence-type cuts are developed by setting an exclusion time window around each event.

1. Coincidence cut: for any triggered event within any detector, if another event occurs within that window of time in any other detector, the entire 0.5 s trace containing that event is removed from the data.

2. DT cut: for any triggered event within a detector, if another event occurs within that window of time in the same detector, the entire 0.5 s trace containing that event is removed from the data.

Define the neighbouring time interval of each event as in Eq. 5.5:

$$\Delta t = \min(t_{before}, t_{after}), \tag{5.5}$$

where t_{before} is the time interval between the current event and the last one, while t_{after} is the time interval between the current event and the next one. Whether the last or next event is required to be in the same or different detectors depends on the type of cut being applied. We choose the exclusion time window to be the same length as a truncated pulse, i.e. 2048 samples (13ms). For each event with $\Delta t < 13ms$, the entire 0.5 s trace is removed. Fig. 5.23 shows the Δt distribution after each live-time cut consecutively.

5.3.5 Overview of All Live-time Cuts

Table 5.8 shows the fraction of the survived live time after each consecutive live-time cut. Eventually, we get the live-time for the NFC1 detector: 224.47 hours for the full data set and 63.22 hours for

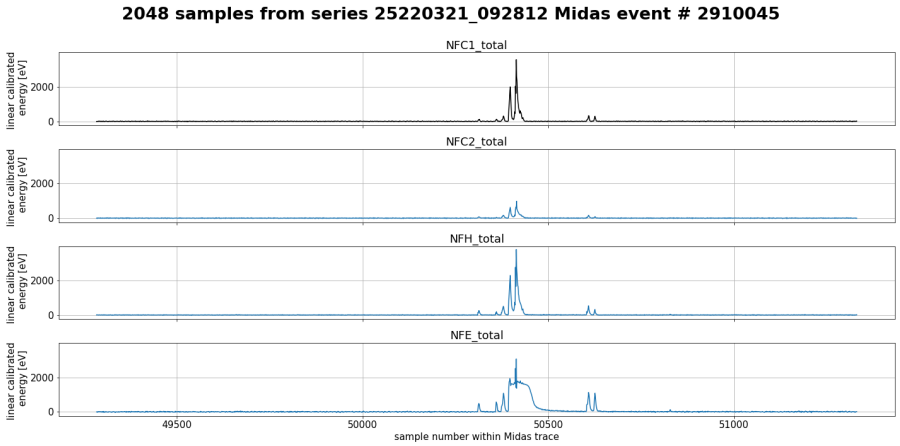

Figure 5.22: Example of a coincident event across all detectors.

30% unblinded data. The difference in the passage fraction of the elevated rate cut comes from the fact that an extra 10 hour period was removed considering only the 30% dataset compared to considering the full dataset. Fig. 5.24 shows the 30% raw spectra overlaid with those after applying each live-time cut one after another. The total exposure after all live-time cuts for the unblinded data is 2.450 gram-days.

Table 5.8: NFC1 live-time passage fraction for all live-time cuts. The combined row indicates the percentage of midas traces that pass all live-time cuts.

Live-time cut	% after cut on 30% data	% after cut on full data
Fridge temperature cut	99.30	99.30
Baseline excursion cut	99.28	99.26
Elevated rate cut	76.97	82.07
Δt cut	99.87	99.87
Coincidence cut	99.63	99.63
Combined	75.53	80.54

5.4 Data Quality Selection: Energy Dependent χ^2 Cut

Data quality cuts are usually designed to discriminate non-signal events (e.g. noises from the electronics, or background events) from signal events at an event-by-event level. The events surviving all data quality cuts are assumed to be signals only. Inevitably, some signal events are falsely removed during this process, but the loss from that will be taken into consideration through the cut efficiency study. In this analysis, only one data quality cut is applied: the energy dependent χ^2 cut.

5.4.1 Cut Definition

As discussed in Section 5.1, the frequency domain χ^2 is by definition a measurement of the inconsistencies between the shape of the signal template and the current pulse. Therefore, we can set a threshold on χ^2_{OFL} and keep only events with a lower value than that. Due to the non-linearity effect shown in our detector, this χ^2 cut could have an energy dependence. To determine the actual

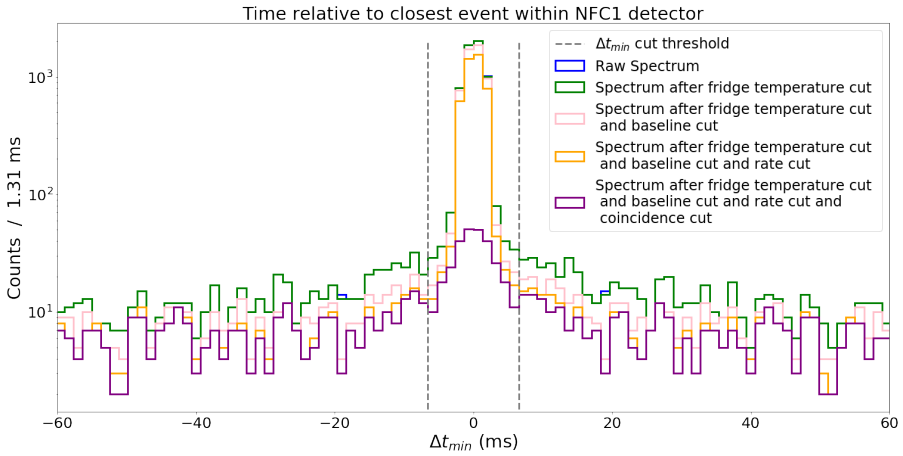

Figure 5.23: A coincidence-type event is defined by two or more triggers less than 6.55 ms away from each other. Coincidence-type live-time cuts include the coincidence cut (cross-detector) and the delta-t cut (same-detector). The Δt spectrum for NFC1 is shown in the histogram. The coincidence cut applied in the plot removes coincidence periods between NFC1 and any other detector. The effect of the coincidence cut is shown by the purple histogram, and the DT cut removes what remains between the dotted lines.

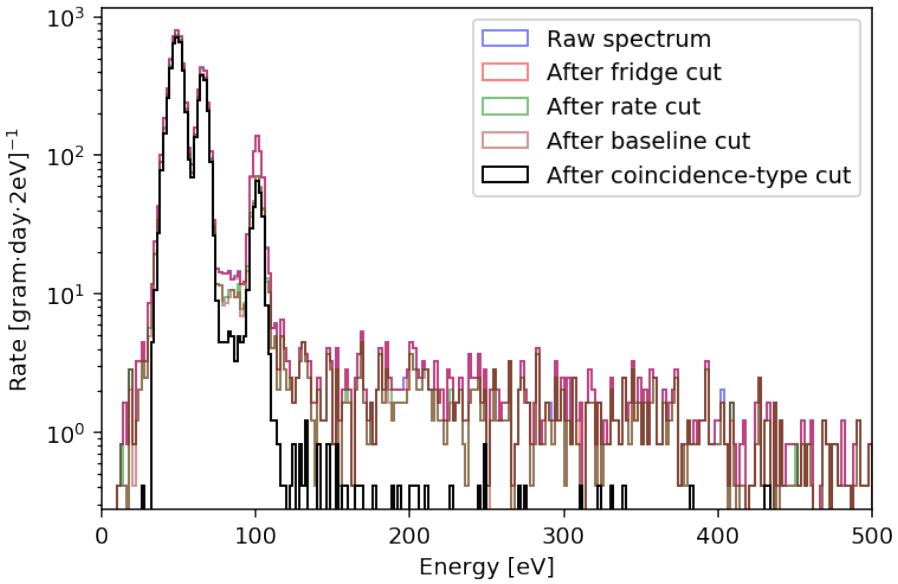

Figure 5.24: 30% unblinded spectra are shown without any cut (blue), after the fridge cut (red), after the rate cut (green), after the basline cut (brown) and after the coincidence-type cut (black). The exposure for the 30% unblinded data after all live-time cuts is 2.450 gram-days.

values of the thresholds, we took advantage of the Caesium calibration data taken in Nexus Run 13, where the gamma source is expected to produce a pulse shape similar to that of the DM signals due to the same electronic response.

The cut is developed between 0 and 500 eV, considering that the fifth electron-hole peak and even higher ones in the energy spectrum would be excluded from our analysis range. As a first step, we split the energy in 20-eV intervals from 30 to 510 eV. Fig. 5.25 shows the events from the 0V

Cs-137 data divided into 20 eV energy intervals.

We evaluated $\chi^2_{\rm OFL}$ distribution in each of the 20 eV intervals. Fig. 5.26 displays one of the energy intervals around the 1eh peak. The other plots for all energy intervals are shown in Appendix A.2. The histogram is fitted with a Gaussian function plus a flat background. The entries with $\chi^2_{\rm OFL}$ close to 1 are assumed to be DM signal-like events, while those with high χ^2 outliers are regarded non-signals. A sensible cut threshold would be at the 3 σ upper edge of the Gaussian distribution, but before that we first compare it with other energy intervals, as shown in Fig. 5.27. We fit all those individual 3 σ upper edges with the following function (Eq. 5.6):

$$\chi^2_{OFL} = P_2 \times E[\text{eV}]^{P_1} + P_0, \tag{5.6}$$

where P_0, P_1 and P_2 are the fitting parameters. In this way, we get an analytically defined energy dependent χ^2 cut that preserves most DM signal events while excluding noises. The values of the parameters for different detectors are shown in Table 5.9.

From the red fitting curve in Fig. 5.27, we can clearly observe an increasing trend in $\chi^2_{\rm OFL}$ as the energy increases. This can be explained by the fact that our signal template is built from 1eh pulses. High energy pulses do not scale perfectly with the low energy ones due to the non-linearity effect in the detector, so that $\chi^2_{\rm OFL}$ cannot be kept at the exact same level.

Table 5.9: Energy dependent χ^2 cut parameters for different detectors determined from the Nexus Run 13 Caesium data.

Parameters	NFC1	NFC2	NFH
p0	1.146	1.472	1.315
p1	3.341	3.659	0.862
p2	6.803e-11	1.182e-11	5.499e-4

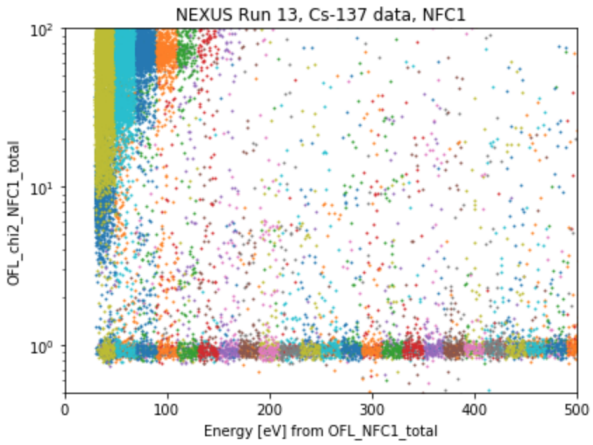

Figure 5.25: Cs-137 data split in 20 eV intervals (each color correspond to a different interval).

The 30% unblinded spectrum before and after the χ^2 cut is shown in Fig. 5.28.

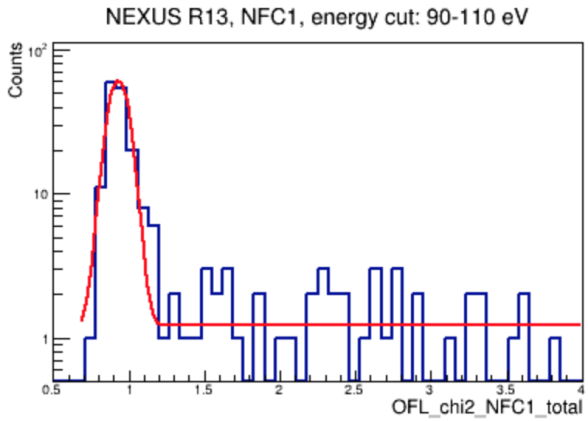

Figure 5.26: χ^2_{OFL} distribution for one energy interval between [90, 110] eV in the Cs-137 data. The histogram is fit with a Gaussian function plus a flat background.

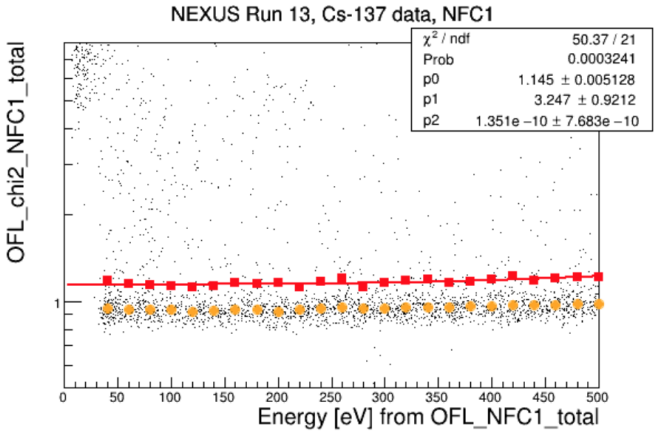

Figure 5.27: χ^2_{OFL} as a function of energy for the Cs-137 data. Each yellow point corresponds to the mean value of the χ^2 distribution in Fig. 5.26. The red points correspond to the mean value (of each 20 eV interval) adding 3 σ of the Gaussian distribution in Fig. 5.26. The red points are fit with Eq. 5.6. p0, p1 and p2 are fitting parameters as in the formula.

5.4.2 Cut Efficiency Calculation: Monte Carlo Simulation Method

The cut efficiency of a specific data quality cut measures the expected ratio of signal events surviving the selection. To get a reasonable estimation of that, one needs to have a set of events which are highly representative for all signals, and then check their performance through the cut.

In HVeV Run 4, the cut efficiency of the energy dependent χ^2 cut has been estimated in two different ways, either through Monte Carlo simulations or through the passage fraction of signal-like Caesium events. Theoretically, the cut efficiency can also be calculated from the LED calibration data in Nexus Run 14, but we choose not to follow that approach due to the sophistication in working-point shifts and the low statistics in regions between e-h peaks. This subsection will focus on the cut efficiency calculation with the Monte Carlo method, while the next one will discuss the method with a pre-selection of Caesium data.

In the MC simulation of signal events, we simulate the signal pulse component and noise compo-

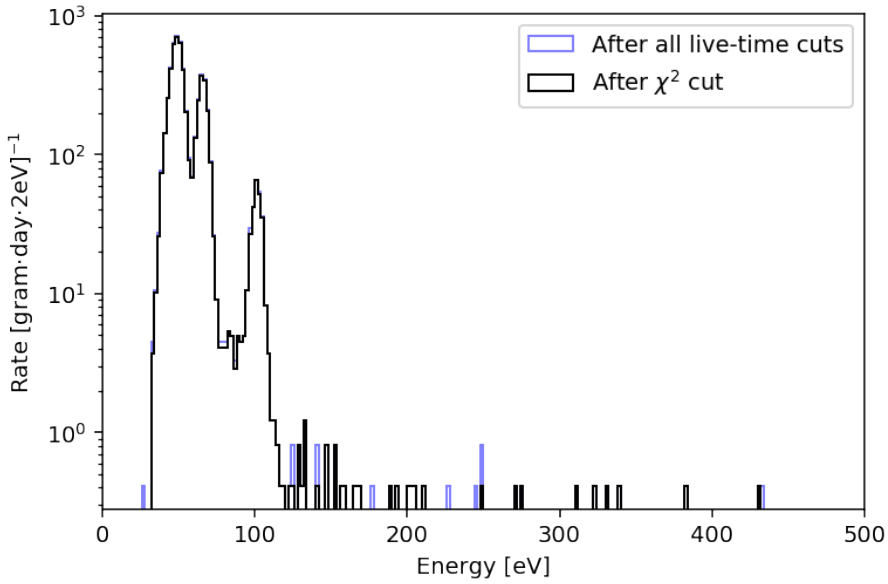

Figure 5.28: 30% unblinded spectra are shown before (blue) and after (black) the χ^2 cut. The exposure for the 30% unblinded data after all live-time cuts is 2.450 gram-days.

nent separately and then add their amplitudes after that. For the noise part, since we already have random trigger events with pulse rejection for each data series, we can directly sample from that pool. Fig. 5.29 shows that the noise levels are comparable during the data taking of 0V Caesium data and the science data, but considering the quality cut is designed for the science data, the random trigger events from the latter are used, with the same baseline live-time cut applied to ensure we are sampling from a stable period.

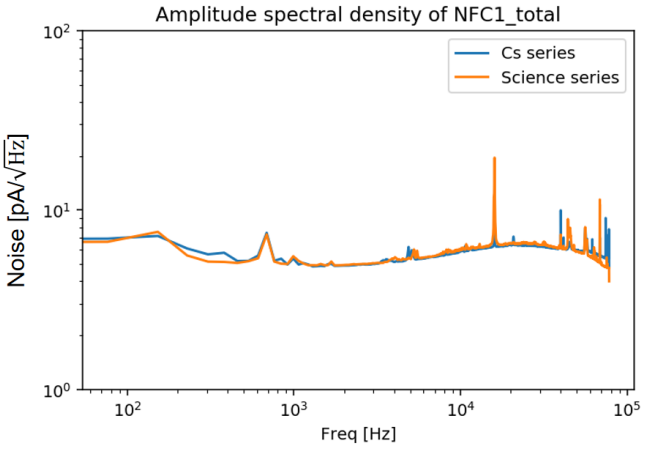

Figure 5.29: Noise PSDs comparison between 0V Caesium data and the science data for the NFC1 detector.

For the signal shape simulation, we follow the same approach of pulse averaging as mentioned in Section 3.1, but apply it to the 0V Caesium data and extend it to higher energies. The reason of switching to the 0V Caesium data instead of using the science data is that the latter does not have enough high energy events to provide the required level of statistics. Templates of $n \times 100eV$ up to

700 eV are built as shown in Fig. 5.30. As a comparison, Fig. 5.31 and Fig. 5.32 demonstrate that the first e-h peak templates from the 0V Caesium data and the science data are generally consistent with each other, except for differences in high frequency due to the relatively low statistic in the former case. For any energy in between, we apply a linear morphing as in Eq. 5.7:

$$s(E) = \frac{E - E_1}{100[\text{eV}]} \times s(E_1) + \frac{E_2 - E}{100[\text{eV}]} \times s(E_2), \tag{5.7}$$

where s(E) is the signal shape at energy E, and E_1, E_2 are the neighbouring $n \times 100eV$ templates.

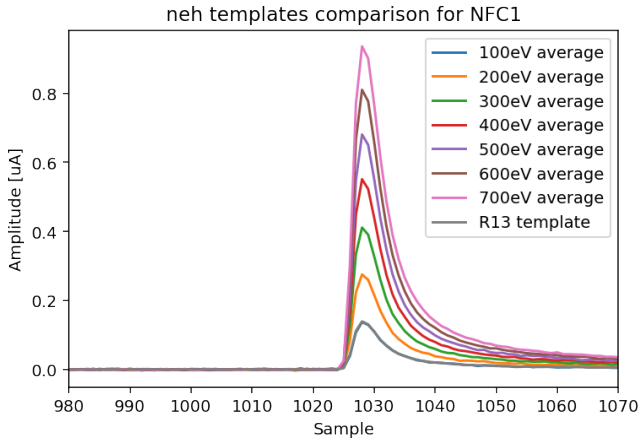

Figure 5.30: Monte Carlo pulse templates generated from pulse averaging of the 0V Caesium data up to the 7^{th} peak. Each template comes from an average of 100 pulses $\pm 20eV$ of the corresponding peak energy and surviving the χ^2 cut.

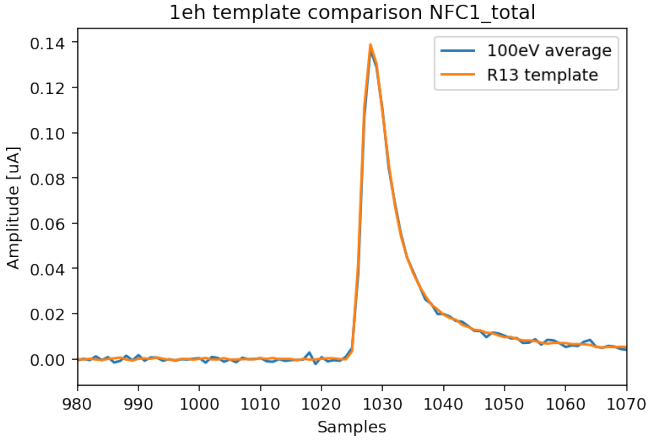

Figure 5.31: First e-h peak template from the 0V Caesium data (blue) in comparison with that from the science data (orange) in the time domain.

When combining the signal pulse with a sample of noise to form a single event and pass it to the continuous readout processing, one subtlety is that the new trigger point might not be at the exact same position as that of the signal pulse. Therefore, we require slightly longer simulated pulses to address such potential trigger point shifts. For the noise part, our solution is to truncate 2058

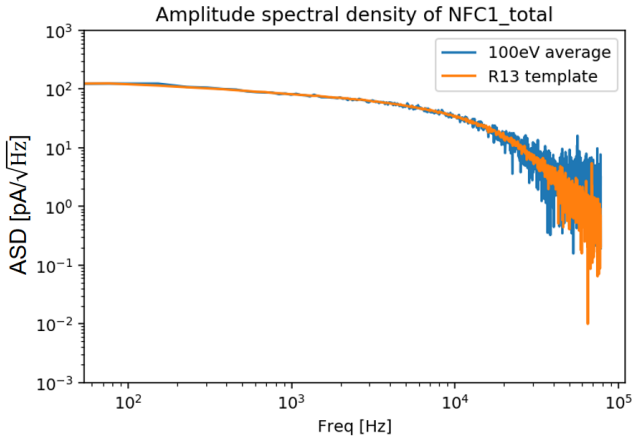

Figure 5.32: First e-h peak template from the 0V Caesium data (blue) in comparison with that from the science data (orange) in the frequency domain.

samples for each random trigger, instead of the original length of 2048 samples, five more each at the beginning and the end. For the signal part, we simply add zeros for corresponding positions, as the signal amplitude expected there is negligible anyway. Now, with this adjustment, after the same threshold triggering procedure, we cut down a 2048-sample trace for each simulated pulse based on its trigger point. Those truncated traces are reconstructed as in normal processing.

A total of 130,000 events are simulated, 100 each for energy from 0 eV to 650 eV every 0.5 eV. Fig. 5.33 shows the 2D histogram of the simulated events in the energy versus χ^2 space, as well as the curve of the energy dependent χ^2 cut. Fig. 5.34 calculated the cut efficiency as a function of energy from the passage fraction of the simulated events. The result gives a slightly increasing dependence on the energy from an efficiency of ∼0.98 in the first e-h peak region to almost 1 at high energies. Further comments and discussions will be addressed in the next subsection, where we have a comparison with the result from the other method.

Apart from the cut efficiency calculation, this MC simulation also helps calculate the trigger efficiency as mentioned in Section 5.1, and helps to tune the non-signal cuts in the pre-selection method as we will introduce next.

5.4.3 Cut Efficiency Calculation: Pre-selection of Caesium Data

Another approach to calculate the cut efficiency is through a direct classification of events in the 0V Caesium data. To identify the subset of signal-like Caesium events among all events in the 0V Caesium data, we designed three non-signal cuts targeting some typical pulse shapes that we would like to exclude. Based on the comparisons with the unblinded science data and the MC simulation results, we argue that the fraction of DM signal-like events excluded by those non-signal cuts is negligible, and assume that the remaining events are a good representation of all DM signal-like events.

1. Coincidence time cut

   The coincidence time cut is designed to rule out pile-up events. The overall event rate of HVeV Run 4 can be estimated through the unblinded science data, which is $\sim 3mHz$ at the 1eh level.

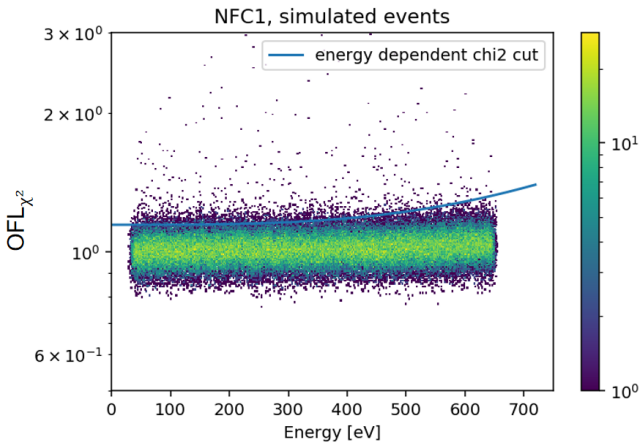

Figure 5.33: 2D histogram of the 130,000 simulated events in the energy versus χ^2 space. X-axis is the total phonon energy calibrated from the OF amplitude through the calibration discussed in Section 5.2. The curve of the energy dependent χ^2 cut is plotted in blue.

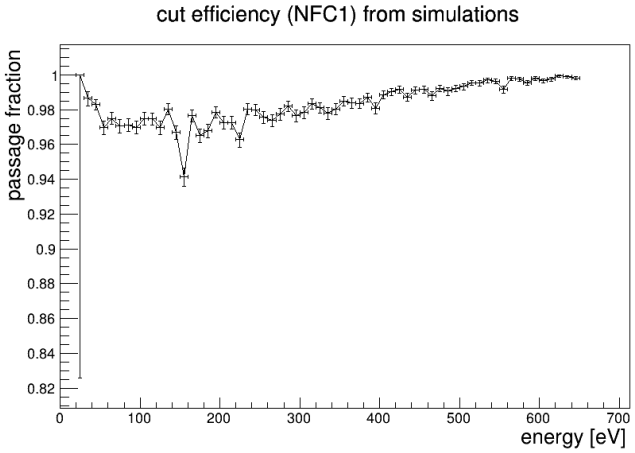

Figure 5.34: The cut efficiency evaluated from the passage fraction of the simulated events. X-axis is the total phonon energy calibrated from the OF amplitude through the calibration discussed in Section 5.2.

We can safely argue that it is highly unlikely to have two DM particles hitting the detector at the same time (more specifically, same truncated pulse window). Defining dt as the triggering time difference between the current event and the closest neighbouring one (either before or after it), we can set a exclusion of $|dt| < 6.554ms$ so that theoretically only 0.073% of the DM events will be removed by coincidence.

2. Baseline slope cut

   The baseline slope of a triggered event is defined to be the slope of linear regression of the first half of the truncated trace. Its distribution in Caesium data, unblinded science data and simulations are shown in Fig. 5.36 separately. Usually it is expected to be close to zero if not for a baseline shift. We choose the threshold from the simulation (which also holds for the unblinded science data) so that less than 0.1 % of the signals are removed by this cut. Events with |BaselineSlope| $> 6 \times 10^{-6}$uA/sample are removed by this cut.

3. Pulse fall time cut

   There are 3 RQs related to the fall time of the pulse: FallTime1 is the fall time from 50% to 30% of the maximal amplitude. FallTime2 is the fall time from 90% to 50%. FallTime3 is the fall time from 100% to 90%. We use the sum of these 3 RQs to check the fall time from 100% to 30%. Again, we chose the range 2 samples $<$ Fall time $<$ 10 samples from the simulation so that less than 0.1% of signals are excluded. Fig. 5.37 shows the distribution of the fall time in the simulation and Caesium data, separately.

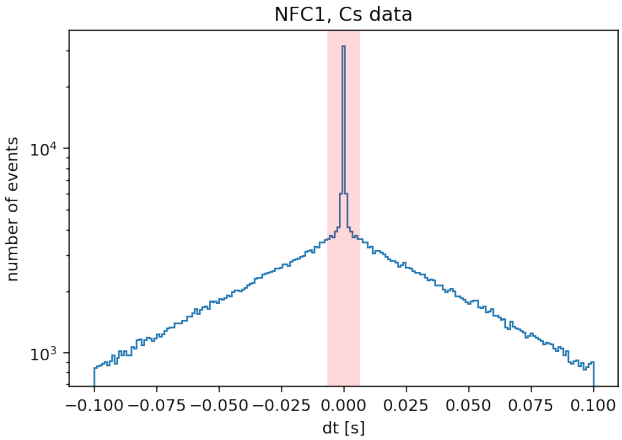

Figure 5.35: Distribution of the neighbouring time intervals for Monte Carlo simulated events. The red band is the exclusion region of the coincidence time cut.

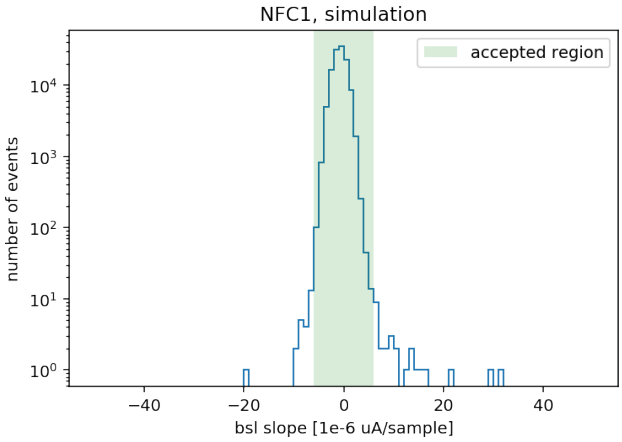

Figure 5.36: Distribution of the baseline slopes for Monte Carlo simulated events. The green band is the accepted region of the baseline slope cut.

After applying the three non-signal cuts defined above, we assume the survived events can represent our dark matter signals, and therefore check their passage fraction to calculate the cut efficiency. Fig. 5.38 shows the 2D histogram of the simulated events in the energy versus χ^2 space, as well as the curve of the energy dependent χ^2 cut. Fig. 5.34 calculated the cut efficiency as a function of energy from the passage fraction of the signal-like events. The cut efficiency is in general flat (with a best fit slope consistent with 0 if doing a linear fit) at a level of $\sim$0.95.

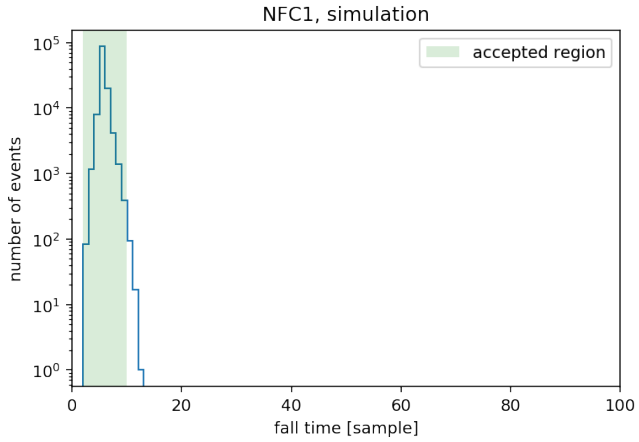

Figure 5.37: Distribution of the fall time for Monte Carlo simulated events. The green band is the accepted region of the fall time cut.

In comparison, the cut efficiencies calculated from the two methods are close to each other in general. However, the simulation result gives a slightly higher value and demonstrates a non-negligible slope with energy, as shown in Fig. 5.34. We believe the reason is that the signal shape variations (event-by-event) are not considered and modeled in our simulation. Two consequences follow: (1) The signal shape variations are expected to slightly increase the χ^2 value, and therefore the χ^2 of the simulated events are underestimated in the simulation. (2) The signal shape variations are expected to increase with energy, which is reflected by the construction of the χ^2 cut (defined at 3 σ upper bound of the Gaussian fit of the main peak in χ^2 distribution), but not included in the simulation. Therefore, the efficiency curve is expected to be flat in energy with the signal shape variations included, which explains the increase of the efficiency curve with energy from the simulation.

Based on the argument above, we decided to take the result of the pre-selection method as an estimation of the cut efficiency, and use the simulation result only for the evaluation of the systematic uncertainty. Consequently, the cut efficiency of the energy dependent χ^2 cut in HVeV Run 4 is finalized as 0.95 ± 0.02.

5.5 Upper Limit Setting

This section describes the limit setting approach adopted in the HVeV Run 4 analysis. Section 5.5.1 introduces the Poisson counting statistics as a starting point. Sections 5.5.2 and 5.5.3 present a likelihood-based limit setting algorithm that incorporates systematic uncertainties. In Sections 5.5.4 and 5.5.5, the low statistic performance of this method is investigated. Finally, Section 5.5.6 describes the peak selection strategy used in this analysis when combining results from different orders of electron-hole pair peaks.

5.5.1 Basic Approach: The Poisson Counting Method

In particle physics, one often faces the task of setting upper limits on the cross-section, flux or other signal parameters that directly related to the expected observed number of events, based on

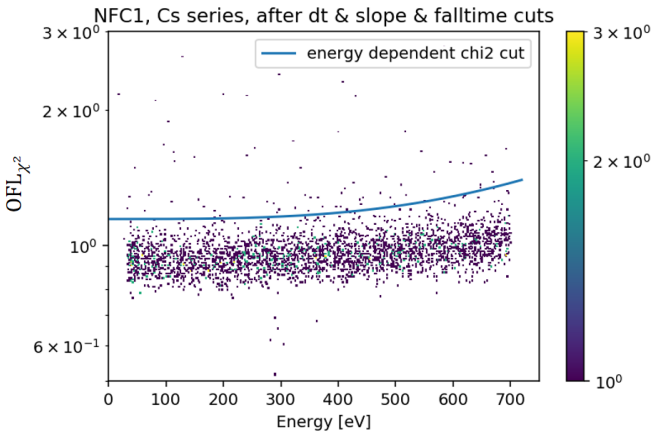

Figure 5.38: 2D histogram of energy vs χ^2 for the Caesium events after non-signal cuts, with the energy dependent χ^2 cut shown in the same plot. X-axis is the total phonon energy calibrated from the OF amplitude through the calibration discussed in Section 5.2.

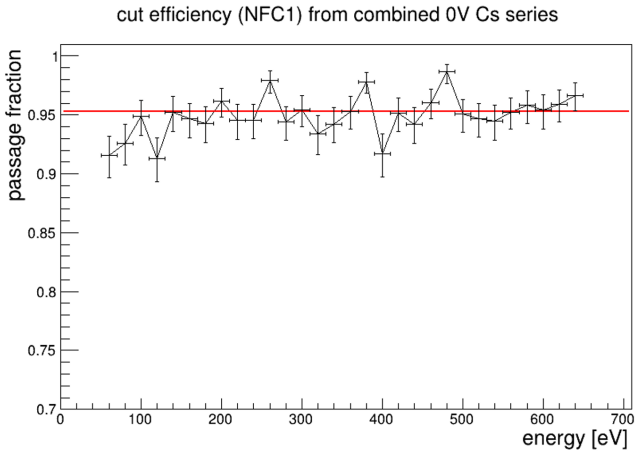

Figure 5.39: Cut efficiency estimation for energy dependent χ^2 cut for NFC1 detector from pre-selection of 0V Caesium data. X-axis is the total phonon energy calibrated from the OF amplitude with the calibration discussed in Section 5.2. The red line is the best-fit overall efficiency of ~ 0.95.

the dataset collected in an experiment. In an ideal case where the signal-only assumption is made, either because the background events are reduced to an extremely low level or the background is highly unknown so that only a conservative limit can be produced, the Poisson counting method becomes a natural choice as it is the most basic approach in this field. In the absence of background events, we no longer care about the measured physical quantity of each event (e.g. energy deposition in the case of HVeV Run 4 experiment) as long as it is in the analysis range, and only count the number of events N taking place. As we know, the observed number of events occurring at some exposure from a probabilistic physical procedure follows a Poisson distribution. Therefore, the upper limit of the expected number of events N_c at a confidence level C can be determined by varying the Poisson λ until there is only 1-C chance of observing less than N events. Correspondingly, the upper limit of the signal model parameter σ_c can be calculated from N_c given the signal model dR/dE, cut efficiencies $\epsilon(E)$, the exposure X, as well as the analysis range [a, b]:

$$N_c = \int_a^b \frac{dR}{dE}(\sigma = \sigma_c)\epsilon(E)XdE. \tag{5.8}$$

Usually, N_c has some scaling relation with σ_c, which further simplifies the calculation and makes the analytical solution possible. For instance, in our dark matter inelastic scattering case, N_c is proportional to the cross-section σ_c, so that Eq. 5.8 can be reduced to Eq. 5.9:

$$\sigma_c = \frac{N_c\sigma_0}{\int_a^b \frac{dR}{dE}(\sigma = \sigma_0)\epsilon(E)XdE}, \tag{5.9}$$

where σ_0 is an arbitrary reference value to generate dR/dE. Similar relations apply to the dark photon absorption and axion-like particles, except that in these two cases N_c is scaled with the square of either ε or g_{ae}, the corresponding parameter of interest.

However, when it comes to more complicated scenarios where one or more nuisance parameters are involved and potentially influence the number of expected events, the Poisson counting method will struggle to handle it since the measured physical quantity (energy E in our case) of each event is no longer irrelevant. They will determine the probability of the nuisance parameters picking certain values, which further affects the scaling between N_c and σ_c.

In HVeV Run 3 where the Poisson counting method is adopted, this problem is handled with a frequentist approach [83]. The limit calculations of Eq. 5.9 were repeated thousands of times with different nuisance parameter values which follow their prior distributions from subsidiary experiments. Then they find the median value of these thousands of upper limits, as well as the 1σ fluctuation (68% and 32% percentage values), and publish both of them in the 90% confidence level upper limit curve. The disadvantage of this approach is that the systematic uncertainties from nuisance parameters are not absorbed into a single limit curve, making comparisons with other experiments less straightforward as this is not the common practice in the field.

To address this issue, in HVeV Run 4, we look for a more general approach that includes the handling of nuisance parameters, while keeping the Poisson counting method as a validation or comparison, especially in the low statistic cases where the nuisance parameters are not as important.

5.5.2 Likelihood-Based Limit setting

Likelihood-based limit setting is one of the most widely used approaches in particle physics that enables dealing with nuisance parameters. The likelihood function L(μ, θ |E) is the joint probability density of the observed data E as a function of the parameter of interest μ and the nuisance parameters θ of a statistical model. In the most general form, it is a product of three terms: (1) the Poisson term accounting for the variation of total number of events (Eq. 5.10), (2) the discrimination term separating signals from background events (Eq. 5.11), and (3) the constraint term including the prior knowledge of the nuisance parameters achieved from subsidiary experiments assuming the uncertainties are Gaussian distributed (Eq. 5.12).

$$L_{Poisson} = (\nu_\chi + \sum_b \nu_b)^N e^{-(\nu_\chi + \sum_b \nu_b)}/N!, \tag{5.10}$$

$$L_{Disc} = \prod_{i=1}^{N} [f_\chi(E_i) + \sum_b f_b(E_i)], \tag{5.11}$$

$$L_{Constr} = \prod_k \frac{1}{\sqrt{2\pi\sigma_k^2}} e^{-(\theta_k - \mu_k)^2/2\sigma_k^2}. \tag{5.12}$$

In the equations above, ν_χ is the expected number of signal events, ν_b is the expected number of background events from the source b, N is the total number of events observed in the dataset, E_i is the measured energy of the i^{th} event, $f_\chi(E)$ is the signal probability density function (PDF), $f_b(E)$ is the PDF of background source b, and θ_k is the k^{th} nuisance parameter with an expected mean of μ_k and a standard deviation of σ_k.

In the specific case of HVeV Run 4, one major background could be the leakage events from electrodes to the crystal due to the applied high voltage. However, our knowledge about either the rate or the energy distribution of those leakage events are highly insufficient to build a convincing background model. Therefore, we decide to make the signal-only assumption and only set conservative upper limits on the dark matter elastic scattering cross-section, the mixing parameter of dark photon absorption, and the coupling constant of axion-like particles.

With this assumption, the background component $\sum_b f_b(E_i)$ in the discrimination term in Eq. 5.11 vanishes, as well as the number of background events ν_b in Eq. 5.10. If we denote the signal model parameter (which is our parameter of interest) as μ, the nuisance parameters as θ_k, and notice that the expected number of signal events ν_χ depends on μ and θ_k through the signal model, the likelihood function will be simplified in the form of Eq. 5.13 and Eq. 5.14:

$$L(\mu, \theta) = \frac{\nu_\chi^N e^{-\nu_\chi}}{N!} \prod_{i=1}^{N} f_\chi(\mu, \theta | E_i) \prod_k \frac{1}{\sqrt{2\pi\sigma_k^2}} e^{-(\theta_k - \mu_k)^2/2\sigma_k^2}, \tag{5.13}$$

$$\nu_\chi = \int_a^b \frac{dR}{dE}(\mu, \theta)\epsilon(E)X dE. \tag{5.14}$$

Note that the cut efficiency $\epsilon(E)$ is also one of the nuisance parameters, but here we separate it from other signal model nuisance parameters.

5.5.3 Test Statistic and Wilk's Theorem

To establish an upper limit, the common approach is to define the test statistic as in Eq. 5.15:

$$t(\mu) = \begin{cases} -2 \ln \frac{L(\mu, \hat{\hat{\theta}})}{L(\hat{\mu}, \hat{\theta})} & \mu \geq \hat{\mu} \\ 0 & \mu < \hat{\mu} \end{cases}, \tag{5.15}$$

where $\hat{\mu}$ and $\hat{\theta}$ represent the best fit-values corresponding to the global maximized likelihood, and $\hat{\hat{\theta}}$ is the best-fit values for a specific value of μ. The likelihood in the numerator is called the profiled likelihood since the nuisance parameters are profiled out and the likelihood is a function of parameter of interest only. The ratio between the profiled likelihood and the globally maximized likelihood is usually referred to as the profile likelihood ratio, and the test statistic is simply -2 times the logarithm

of the profile likelihood ratio. By definition, a higher value of $t(\mu)$ indicates larger incompatibility between the hypothesized μ value and the experimental dataset. The reason for defining it to be zero when μ is smaller than its best-fit value is that we are setting a one-side confidence interval (upper limit), and therefore one would not regard data with $\mu < \hat{\mu}$ as representing less compatibility with μ than the data obtained, and therefore this is not taken as part of the rejection region of the test [97].

The Wald approximation [97] claims that for a single parameter of interest, the profile likelihood ratio follows Eq. 5.16:

$$-2\ln\frac{L(\mu,\hat{\hat{\theta}})}{L(\hat{\mu},\hat{\theta})} = \frac{(\mu-\hat{\mu})^2}{\sigma^2} + \mathcal{O}(1/\sqrt{N}), \tag{5.16}$$

where $\hat{\mu}$ follows a Gaussian distribution with mean value μ' and standard deviation σ. This approximation stays true at the large N limit, with an inaccuracy to the order of $1/\sqrt{N}$. It is easy to show that with the approximation in Eq. 5.16, the probability density distribution $f(t_\mu)$ of the test statistic will converge to a non-central chi-square distribution with one degree of freedom, as shown in Eq. 5.17:

$$f(t(\mu),\Lambda) = \frac{1}{2\sqrt{t(\mu)}}\frac{1}{\sqrt{2\pi}}[e^{-(\sqrt{t(\mu)}+\sqrt{\Lambda})^2/2} + e^{-(\sqrt{t(\mu)}-\sqrt{\Lambda})^2/2}], \tag{5.17}$$

where Λ is a function of μ, μ' and σ, as shown in Eq. 5.18:

$$\Lambda = \frac{(\mu-\mu')^2}{\sigma^2}. \tag{5.18}$$

The Wilk's theorem [97] states that when we evaluate the test statistic $t(\mu)$ at the true value of μ, i.e. $\mu = \mu'$, we will have $\Lambda = 0$ and $f(t_{\mu=\mu'})$ will asymptotically approaches a χ^2 distribution with one degree of freedom. Here, the number of degrees of freedom of the χ^2 distribution depends on the difference in the number of degrees of freedom between the null hypothesis and the alternative hypothesis, which is equivalent to the number of parameters of interest. In the case of HVeV Run 4, it is always one.

The Wilk's theorem provides huge convenience for the mapping of a confidence level to the corresponding test statistic value through the χ^2 distribution which is known analytically, as shown in Fig. 5.40. However, as an approximation, it requires the condition of a large number of events, which makes its accuracy unreliable in rare event scenarios. In practice, the Wilk's theorem approximation usually only works well given more than a few tens of events, and a coverage test is necessary for its validation.

5.5.4 Coverage Test of the Wilk's Theorem Approximation

Statistically, the *coverage probability*, often referred to simply as *coverage*, is the probability that a confidence interval or confidence region will contain the true value of the parameter of interest. It is defined as the proportion of instances as it approaches infinity where the interval includes the true value.

The coverage test of the Wilk's theorem approximation is conducted with one of our signal models

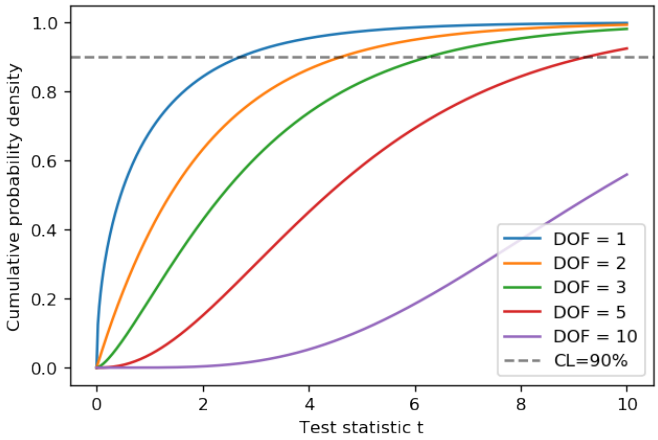

Figure 5.40: Cumulative density function of χ^2 distributions with different degrees of freedoms (DOFs). In the case of DOF=1, t=2.71 will give a 90% CL exclusion region with two sides. For upper limit setting (one-side exclusion region), $t_{90\%}$=1.64.

(as shown in Fig. 5.41) using Monte Carlo datasets. The detailed steps to implement the coverage test at the level of $N_{expected,true}$ with the number of MC datasets = $N_{dataset}$ are listed as follows:

1. Pick a true value of $\epsilon = \epsilon_{true}$, and calculate the corresponding the expected number of events $N_{expected,true}$ using the median values of the nuisance parameters.

2. For each dataset, the nuisance parameters θ are randomly generated from their prior distributions.

3. The number of events N_i generated for different datasets are based on ϵ_{true} and θ_i with a Poisson fluctuation allowed. The event energies in each dataset follow the corresponding signal PDF determined by ϵ_{true} and θ_i.

4. Calculate upper limits with each dataset with the Wilk's Theorem approximation ($t_{90\%}$ = 1.64).

5. Put all those $N_{dataset}$ number of upper limits in a histogram of ϵ, find the coverage equal to the fraction of entries with $\epsilon > \epsilon_{true}$, or equivalently $n_{sig} > N_{expected,true}$.

6. Change ϵ_{true} ($N_{expected,true}$) and repeat steps 1-5 to get the coverage as a function of ϵ_{true} ($N_{expected,true}$).

Figure 5.42 gives the results of the coverage test as a function of the expected number of events from the test signal model. We noticed that the upper limits from Wilk's theorem approximation is in general under coverage at low statistics, with some oscillating pattern which will be discussed later. Consequently, the limit we set with Wilk's theorem approximation would be over-confident in such circumstances. An alternative approach to decide on the 90% CL threshold of the test statistic for low statistic limit setting is required.

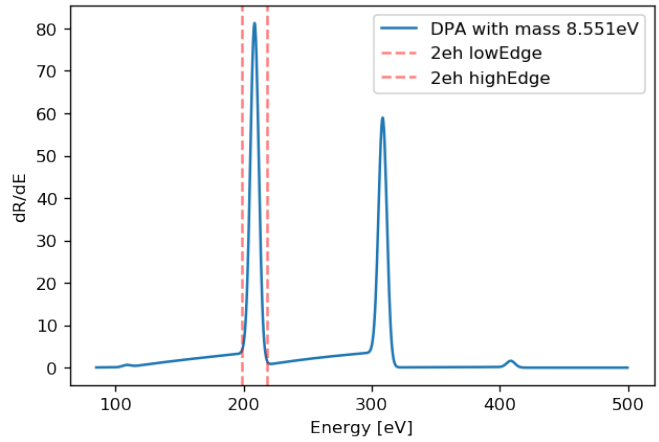

Figure 5.41: DPA model of mass 8.551 eV at 2^{nd} peak is used for the coverage test of Wilk's theorem approximation, as well as the test statistic distribution study in low statistics with Monte Carlo simulations. The red dashed lines show the analysis region for this specific model.

5.5.5 Monte Carlo Simulations for Test Statistic Distributions at Low Statistics

A more general way to find the test statistic distribution $f(t_\mu)$ as a function of μ is through Monte Carlo toy experiments, where a specific true value of μ is chosen, and all nuisance parameters are randomly generated from their prior distributions. For each MC dataset, the actual observed number of events is allowed to fluctuate following the Poisson distribution around its expectation determined from the chosen μ_{true} and θ_j (j is the index of the MC dataset). Once the dataset is generated, the test statistic evaluated at $\mu = \mu_{true}$ can be calculated from Eq. 5.15. All these t_μ values gathered from MC datasets form a distribution, which represents $f(t_\mu)$ given enough statistics. From this distribution, one can find the test statistic threshold t_c corresponding to a specific confidence level C. In the case of our dark photon absorption model, the parameter of interest μ is the kinetic mixing parameter ϵ, and the steps for this Monte Carlo algorithm are listed as following:

1. Pick a true value of $\epsilon = \epsilon_{\text{true}}$, and calculate the corresponding expected number of events $N_{\text{expected,true}}$ using the median values of the nuisance parameters.
2. For each dataset, the nuisance parameters θ are randomly generated from their prior distributions.
3. The number of events N_i generated for different datasets are based on ϵ_{true} and θ_i with a Poisson fluctuation allowed. The event energies in each dataset follow the corresponding signal PDF determined by ϵ_{true} and θ_i.
4. Evaluate the test statistic at $\epsilon = \epsilon_{\text{true}}$.
5. Put all those $t(\epsilon_{\text{true}})$ in a histogram, find $t_{90\%}$ from the 90% quantile of the distribution.
6. Change ϵ_{true} ($N_{\text{expected,true}}$) and repeat step 1-5 to find the curve $t_{90\%}$ as a function of ϵ_{true}.

We know that when the number of expected signal events is low, the variation of nuisance parameters will in general have less influence compared with that in the high statistic scenario,

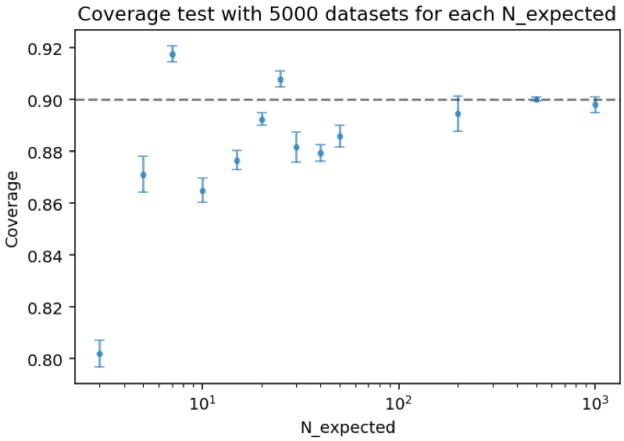

Figure 5.42: Coverage test results for different expected number of events. Each $N_{expected}$ point contains 5 repeated calculations with 5000 datasets each. The coverage asymptotically approaches 90% as the number of expected events approach infinity, but stays under coverage ($< 90\%$) in general when the statistic is low. Furthermore, an oscillation feature has been observed in this region.

and the likelihood function will be dominated by the Poisson fluctuation. Therefore, it is worth getting started from the most trivial case where nuisance parameters are fixed at median values. In a pure Poisson counting experiment, the possible values of the test statistic and their corresponding probabilities can be analytically calculated through Eq. 5.19 and Eq. 5.20:

$$P = \text{Poisson}(n, N), \tag{5.19}$$

$$t = -2 \log \frac{\text{Poisson}(n, N)}{\text{Poisson}(N, N)}, \tag{5.20}$$

where n is the expected number of events (or the true value of the signal rate, can be non-integer values) and N is the observed number of events in one dataset. For instance, in the case of $n = 5$, the Poisson counting experiment will have a distribution as shown in Fig. 5.43, with each discrete t value and its probability listed in Table 5.10. Note that the discreteness of the distribution in Fig. 5.43 comes from the fact that only an integer number of events can be observed in each toy experiment. Therefore, the 90% confidence level test statistic threshold $t_{90\%}$ is by definition always over coverage.

Table 5.10: Theoretical prediction of test statistic values and corresponding probabilities for a Poisson counting experiment with an expected number of events $n = 5$.

N	0	1	2	3	4	5	≥ 5
t/2	5.000	2.391	1.167	0.468	0.107	0	0
P	0.0067	0.0337	0.0842	0.1404	0.1755	0.1755	0.3840

When nuisance parameters are involved, each discrete value of t allowed in Table 5.10 will expand to a local cluster depending on the strictness of the prior constraints on these nuisance parameters. Fig. 5.44 overlaps the MC simulation results for the DPA model with the theoretical predication of Poisson counting without nuisance parameters. Five repeated calculations each with 1000 datasets

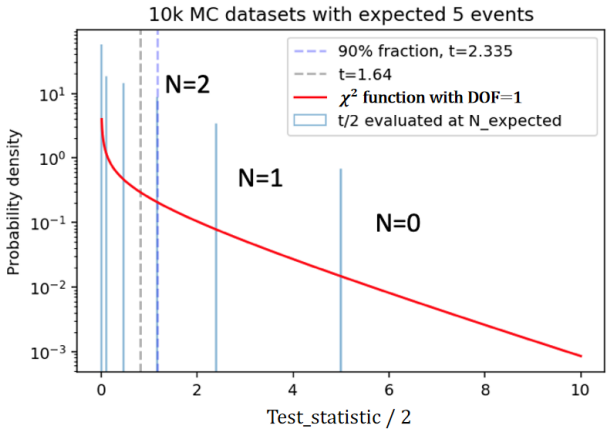

Figure 5.43: Test statistic distribution of a Poisson counting experiment with an expected number of events $n = 5$ from 10,000 Monte Carlo toy experiments. The y-axis is the probability density of the histogram. The red curve is the high statistic asymptotic distribution from the Wilk's Theorem. The 90% confidence level test statistic threshold $t_{90\%}$ (blue dashed line) is found at the 90% quantile of the distribution.

have been done for the MC simulations. The MC results are consistent with the Poisson counting predictions due to the relatively strong constraint on our nuisance parameters. Therefore, for practical (computational) considerations, we decided to approximate the true test statistic distributions of our models with the Poisson theoretical predictions. The oscillation pattern in Fig. 5.44, as we also observed in the coverage test, originates from the discreteness of the Poisson counting.

Once we have the 90% test statistic threshold as a function of the number of events, or equivalently as a function of the parameter of interest if we scale these two by choosing the median nuisance parameter values, then the corresponding upper limit is determined by looking for the intersection between the test statistic function of our experimental data and the 90% CL curve, both as a function of the parameter of interest, as shown in Fig. 5.45. To further simplify the root searching procedure, the green curve is replaced in a conservative way by the red one, which is the top envelope achieved by fitting the local maximum points with an exponential decay function. Its analytical expression in N_{expected} frame is as follows:

$$t = 5.80 \times \exp\left(-0.38 \times N\right) + 2.01. \tag{5.21}$$

Finally, we need to decide on the condition to switch from Wilk's theorem approximation (where the gray dashed line of $t = 1.64$ in Fig. 5.44 is used instead of the red curve) to the low statistic theoretical predication. Fig. 5.46 shows the ratio between the Poisson counting upper limits assuming median values for all nuisance parameters, over the upper limits calculated under the Wilk's Theorem approximation averaged over 1k Monte Carlo simulations. We notice that above 20 events, the difference between the two methods is below 3%, so we decide to apply the Wilk's theorem approximation whenever the observed number of events in the analysis range is more than 20.

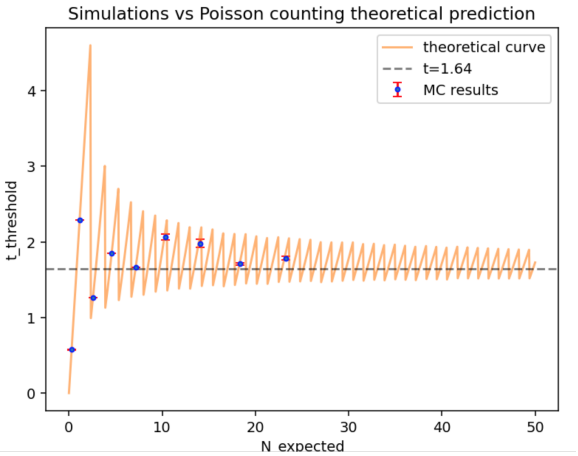

Figure 5.44: MC simulation results for DPA model vs theoretical predication of Poisson counting without nuisance parameters.

5.5.6 Peak Selection

The analysis range of HVeV Run 4 covers the first four peaks of the spectrum. The likelihood-based limit setting approach introduced above is applied to each individual peak separately. A peak selection scheme is required to determine the final limit for a specific signal model at certain masses from the upper limits of all four peaks.

In HVeV Run 4, the lowest peak selection is adopted, where we pre-determine from the 30% unblinded data the selected peak which gives the lowest limit among all four peaks at a certain mass. The same peaks are chosen for the remaining 70% blinded data.

5.5.7 Overview of Limit Setting Parameters

Limits are calculated for each individual electron-hole peak up to the fourth peak. The analysis ranges are $[E_c - 3\sigma, E_c + 3\sigma]$, where E_c is the expected energy deposition based on the signal model and the order of the peak, and σ is the median value of the detector resolution. In the absorption case with dark matter mass m and order of peak n, $E_c = 100 \times n + m$, while in the DM-electron scattering case the peak center is calculated from the weighted average of the recoil energies $\times$ rate $\times$ ionization probability.

Five nuisance parameters are involved in the likelihood limit setting: detector resolution, overall energy shift caused by calibration uncertainties, quality cut efficiency, charge trapping and impact ionization fractions.

By fitting the first-order peak in the 30% spectrum using a Gaussian function from 90 to 110 eV after all cuts as shown in Fig. 5.28, we get an estimation of the NFC1 detector resolution of (3.24 $\pm$ 0.12) eV. Comparing this value with the resolution (4.88 $\pm$ 0.03) eV achieved in Fig. 5.13 from the CTII fitting, we noticed that there is a systematic difference, which can be explained by the fact that the LED source produces non-DM-signal-like effects (such as surface trapping events) that further contribute to the resolution we observe from the CTII fitting. Therefore, the resolution from the first peak of unblinded science data is used in limit setting.

The calibration uncertainties of events are taken into consideration as an overall shift of the

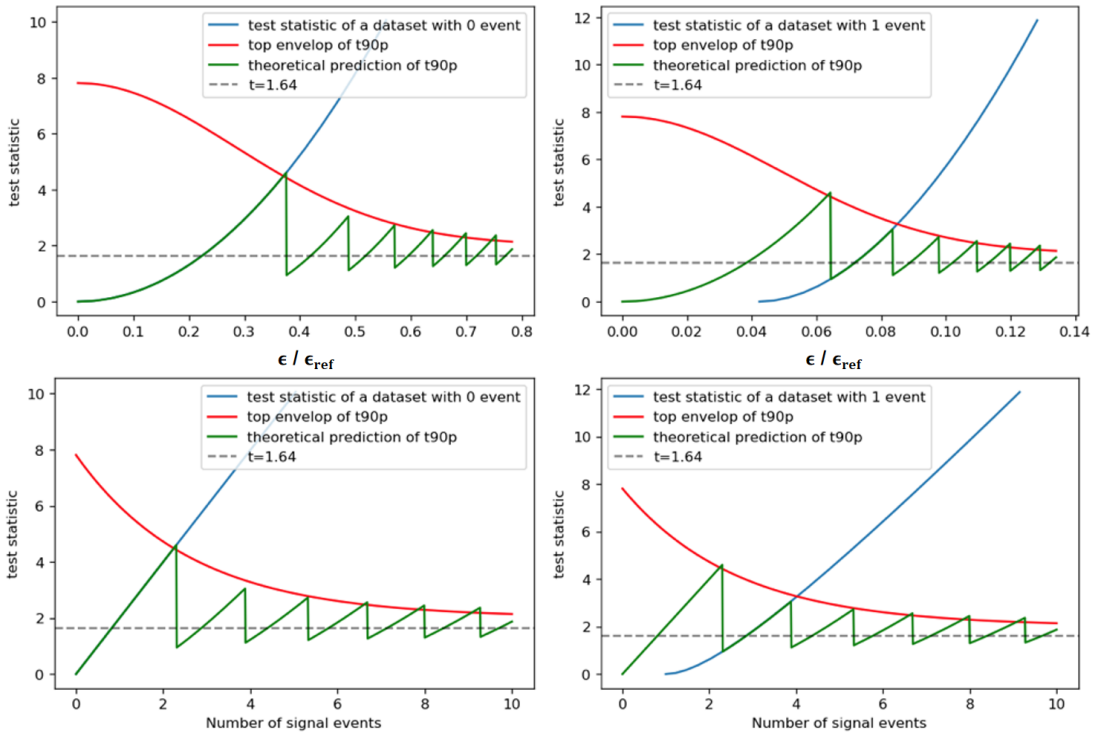

Figure 5.45: Upper limit setting by searching for the intersection between the test statistic curve of the experimental data and the 90% CL curve. The bottom plots are in the space of number of events converted by choosing the median nuisance parameter values. The green curves in the bottom plots are identical to the orange curve shown in Fig. 5.44, while the red curves are the top envelops of them using exponential decay fittings.

energy spectrum with perfect correlation. This shift has a mean value of zero, and peak-dependent standard deviation equal to the calibration uncertainty estimated at the current peak, as shown in Fig. 5.17.

The quality cut efficiency is flat at around 95%, as shown in Fig. 5.39. A 2% standard deviation fluctuation is allowed based on the comparison with the efficiency calculated from the simulation method.

The prior distribution of the CTII fraction parameters is taken from Fig. 5.13. All prior distributions are assumed Gaussian around the corresponding median values, and truncated at 0 for CTII fractions and at 1 for cut efficiency. The total exposure of the 30% unblinded data is 2.45 gram-days.

Table 5.11 shows the Gaussian prior distributions of all five nuisance parameters.

Table 5.11: Gaussian prior distributions of nuisance parameters in HVeV Run 4 limit setting.

	Median value	Standard deviation
Detector resolution [eV]	3.24	0.12
Calibration uncertainty shift [eV]	0	[0.67, 1.99, 3.31, 3.18] (at each peak)
Quality cut flat efficiency	0.95	0.02
Charge trapping fraction (%)	12.3	0.50
Impact ionization fraction (%)	0.07	0.40

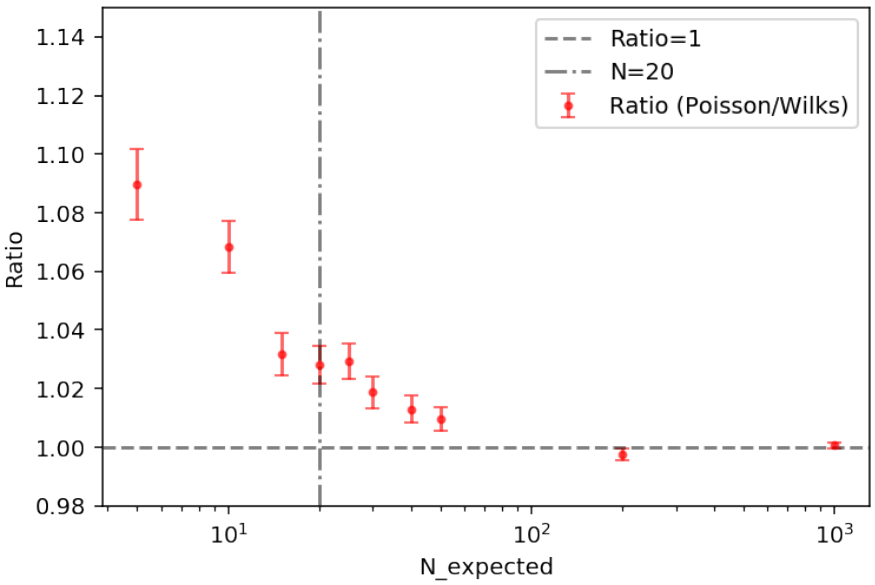

Figure 5.46: Ratio of the Poisson counting theoretical upper limit over the upper limits calculated under the Wilk's Theorem approximation averaged over 1k Monte Carlo simulations. Above 20 events, the difference between the two methods is below 3%.

5.6 Overburden Attenuation

Before reaching the detector, local dark matter halo particles must pass through the Earth's atmosphere and the rocks of the crust (overburden), or sometimes even through the entire Earth. Depending on the type of dark matter, it may be absorbed or scatter multiple times before reaching the detector, requiring calculations to account for this attenuation. For direct boson absorption models (dark photons and axion-like particles), a simple exponential attenuation model can be used, as the interaction results in the complete loss of the particle. However, for electron-recoiling dark matter, the detailed kinematics of interactions with the overburden constituents must be taken into consideration. In this section, we provide order-of-magnitude estimations for the upper bound of the exclusion region for each model due to potential dark matter attenuation effects in the overburden.

5.6.1 Attenuation for Dark Matter Electron Recoils

To calculate the earth shielding for dark matter electron recoil, one can input the original local velocity distribution and estimates the dark matter velocity distribution near the detector based on assumptions about the interaction type. Similar work has been done in the analysis of inelastic dark matter scattering in CDMSlite R3 [98], where a significant amount of effort was taken to study the composition of the Soudan Overburden, as well as including the angular distribution of the attenuation. However, the justification of using the simple continuous stopping model in that analysis only holds true for the search of GeV-scale dark matter, where a package called *verne* [99] was used for the implementation. For the sub-GeV dark matter that we are interested in for HVeV Run 4, deflections become significant and therefore need to be modeled.

While an analytic modeling tool named *EarthShadow* [100] valid for the low-mass dark matter exists, it utilizes the effective field theory (EFT) approach which does not include the light mediator

case as well as multiple scattering. Semi-analytic models have been explored, such as the one implemented in *DMprop* [101], which uses a probabilistic approach that recursively calculates probabilities of particle survival after an arbitrary number of scatterings, under the crucial simplifying assumption of isotropic scattering. While isotropic scattering with heavy nuclei is approximately true in the case of light dark matter with masses above 100 MeV and through a point-like interaction (heavy mediator), it barely covers the requirement of HVeV Run 4 which includes dark matter masses down to 1 MeV, as well as the light mediator signal model.

A Monte Carlo tool *DaMaSCUS-CRUST* [102] is used in HVeV Run 4 for the study of limit setting with earth shielding. The same package was also used in HVeV Run 3 [83]. It includes both the light mediator case and point-like interactions, as well as the modeling of multiple scattering. It does so by simulating and tracking individual particles as many as necessary for a given cross-section. This procedure is time consuming, so the authors of the software implemented geometric-importance sampling (similar to what is implemented in Geant4 [103]) which requires tuning of parameters, especially for the light mediator case at dark matter masses near 1 GeV. In that case forward scattering is highly favored so that higher statistics are required to find the attenuation. The ideal parameters could also vary for each dark matter mass tested.

Once we include the effect of overburden attenuation on the dark matter, the spectrum no longer scales with the interaction dark matter cross-section due to the change of its shape, as demonstrated in Fig. 5.48 and 5.49. Therefore, to produce a double-sided exclusion region, one may have to test each (σ_e, m_{DM}) combination in the parameter space as a separate hypothesis if the profile likelihood-based limit setting approach is used. However, the calculation is significantly simplified if we use the Poisson counting method to set a limit with nuisance parameters fixed at their median values. One can simply find the roots of the difference between the upper bound on the number of observed counts in a certain e-h peak and the expected number of events given a cross-section. The roots will define the boundaries of the excluded cross-section region. For this reason, we decide to keep the likelihood approach for the calculation of the lower boundary of the exclusion region (upper limit setting), which is more accurate and will be compared with results from other experiments, while using the Poisson counting method in this rough estimation of the upper boundary of the exclusion region due to the overburden attenuation.

In this analysis, we request from *DaMaSCUS-CRUST* the velocity distributions on a grid of points in the parameter space (constant step size in log space), generate the signal models only on those pre-defined grid points, and then interpolate the *significance function* as defined in Eq. 5.22:

$$f(\sigma, CL) = C_{DMe}(\sigma) - C_P(CL), \tag{5.22}$$

to set exclusion limits linearly on the log scale. $C_{DMe}(\sigma)$ is the expected number of dark matter electron recoil events considering overburden attenuation and given a cross-section σ, while $C_P(CL)$ is the upper limit of number of events based on the experimental observation and at a confidence level of CL. The positive region of $f(\sigma, CL)$ is then the excluded space of the cross-section σ, as shown in Fig. 5.47 .Due to the discrete sampling, cross-section exclusion limits calculated through this method will have an intrinsic systematic uncertainty of at least $10^{\Delta \log \sigma} - 1$ which is $\sim 26\%$, where $\Delta \log \sigma = 0.1$ is the step size between the simulated cross-sections.

The final exclusion regions for the cross section corresponding to light and heavy mediators

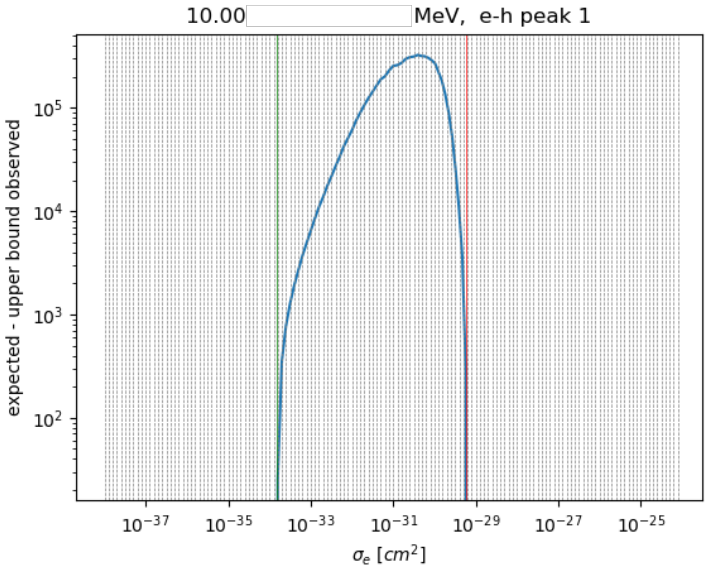

Figure 5.47: Example of a Poisson counting significance function using DaMaSCUS velocities. Green vertical line is the first root of the function, red line is the second root indicating the critical cross section beyond which no exclusion is possible at 90% confidence level.

separately are shown in Fig. 5.50 and Fig. 5.51, above which we no longer have the ability to exclude the parameter space due to a significant effect of earth shielding.

5.6.2 Attenuation for Dark Matter Absorption Models

For absorption models, we applied the same method developed in HVeV Run 3 earth shielding [83] to estimate the attenuation for dark photon absorption and axion-like particles. Note that this method only serves as an order-of-magnitude level estimation for the upper bound, instead of a precise calculation. The idea is to assume the dark matter velocity distributions remain unchanged, but the overall dark matter flux is attenuated depending on the density and depth of the overburden, as shown in Eq. 5.23:

$$\Phi = \Phi_0 e^{-\rho L \sigma}, \tag{5.23}$$

where σ is the DP-electron or ALP-electron absorption cross-section measured in (cm^2/g) (in some sources it is referred to as the mass attenuation factor which is related to the actual cross-section σ_{cs} measured in cm^2 as $\sigma_\rho = \sigma_{cs} n_e$, with n_e being the number density), ρ being the density of the overburden and L being the length that dark matter particles traverse in the overburden.

The final expressions of the maximum level of the kinetic mixing parameter/coupling constant above which the earth shielding effect becomes significant are given in Eq. 5.24 and Eq. 5.25:

$$\varepsilon_{max} = \left(\frac{\sigma_1 L m^2 c^4}{v_{DM} \hbar (m^2 c^4 - 2mc^2\sigma_2 + \sigma_1^2 + \sigma_2^2)}\right)^{-1/2}, \tag{5.24}$$

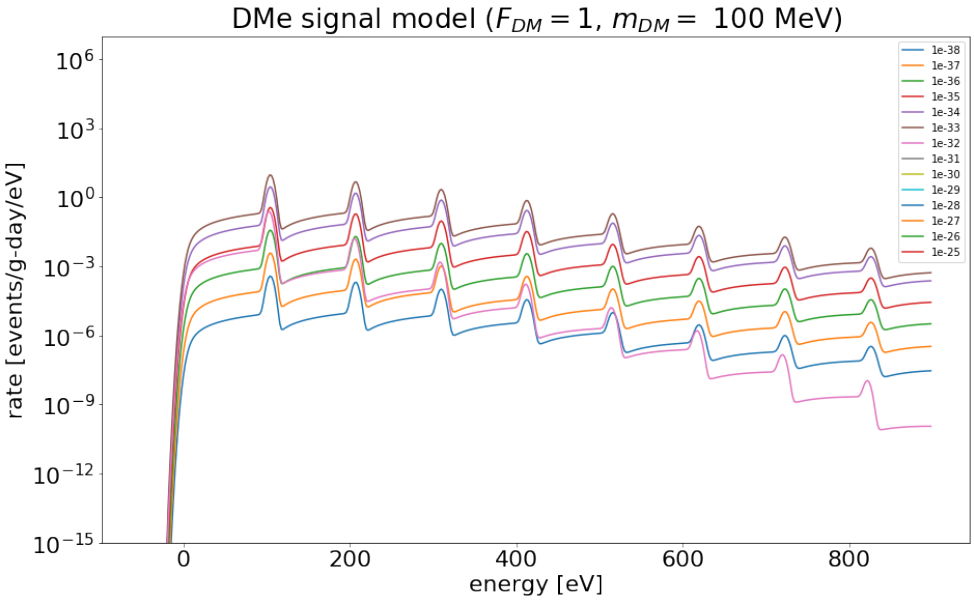

Figure 5.48: DaMaSCUS signal modeling for F_{DM}=1, 100 MeV and 107m depth. Legend shows cross-sections in cm^2. As the cross-section increases, the signal rate first increase following the scaling relation, but then drops quickly due to overburden attenuation which has a significant effect on large cross-section signals.

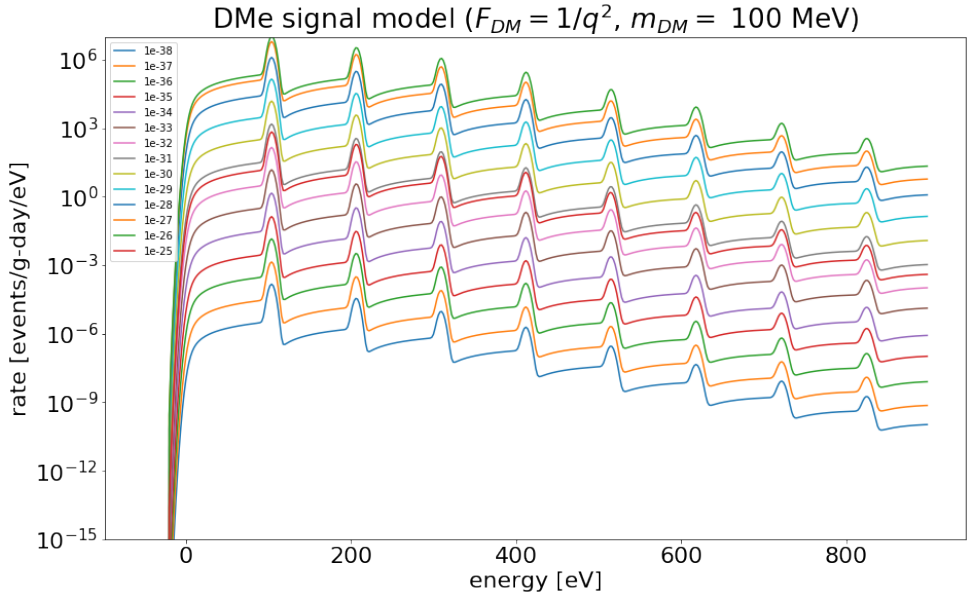

Figure 5.49: DaMaSCUS signal modeling for F_{DM}=$1/q^2$, 100 MeV and 107m depth. Legend shows cross-sections in cm^2. Similar trend occurs as above.

$$g_{ae,max} = (\sigma_1 \frac{3mL^2}{16\pi\alpha m_e^2 v_{DM}\hbar})^{-1/2}, \tag{5.25}$$

where σ_1 and σ_2 are the real and imaginary parts of the complex conductivity, m is the mass of the

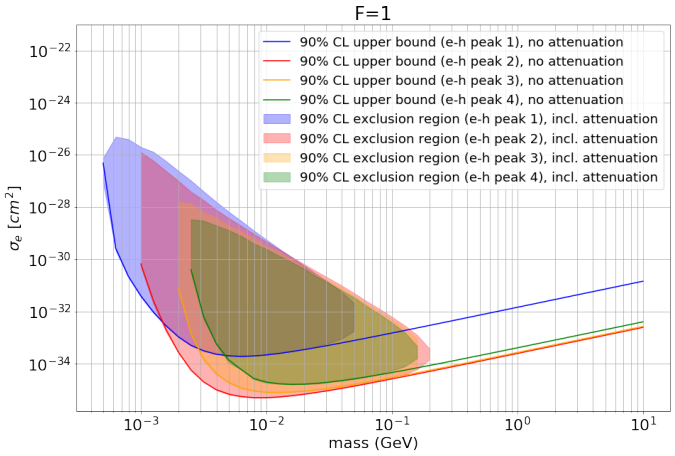

Figure 5.50: Exclusion region for DMe (shaded region) with F_{DM}=1. Lines indicate upper bound on DMe cross-section assuming no DM attenuation. The nominal values for resolution, charge trapping, impact ionization, cut efficiency, as well as the same 3-sigma counting windows for each peak are used to produce these exclusion regions.

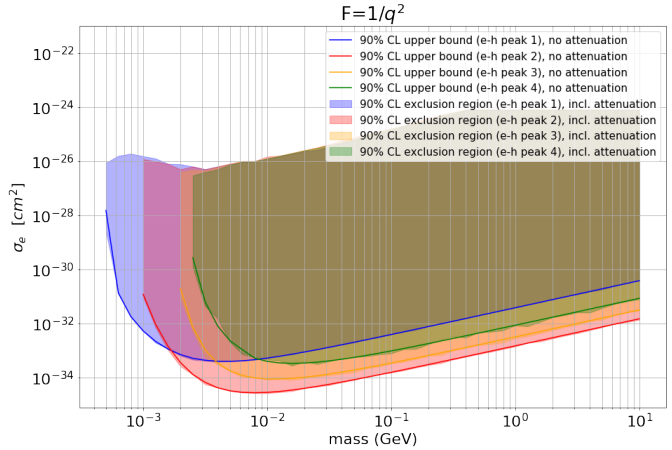

Figure 5.51: Exclusion region for DMe (shaded region) with $F_{DM}=1/q^2$. Lines indicate upper bound on DMe cross-section assuming no DM attenuation. The nominal values for resolution, charge trapping, impact ionization, signal efficiency, as well as the same 3-sigma counting windows for each peak are used to produce these exclusion regions.

vector bosons, c is the speed of light, $\hbar$ is the reduced Planck constant and v_{DM} is the velocity of dark matter.

Figure 5.52 and Fig. 5.53 show the estimations obtained along with the 30% DPA/ALP limits. When the mixing/coupling parameter is higher than a certain value as indicated in the hashed region in the plots, the attenuation becomes significant so that we can no longer rule out the parameter space there from the upper limit setting.

5.7 Results for the 30 % Unblinded Data

Figure 5.54 and Fig. 5.55 show the limits calculated for individual peaks of all four signal models using 30% unblinded data. The R3 90% exposure combined limits are shown on the same plots.

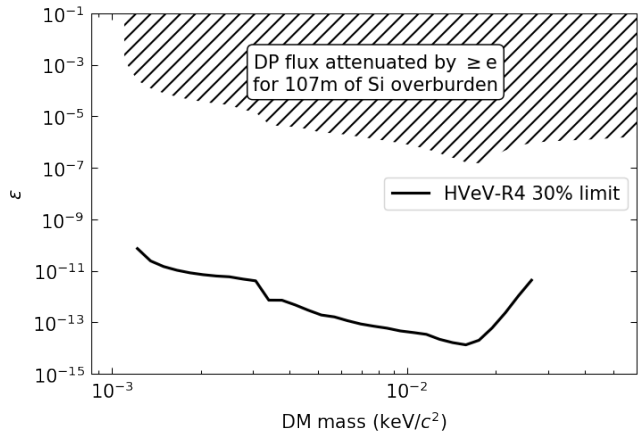

Figure 5.52: Estimation of the level above which the attenuation in earth shielding becomes significant, compared to the HVeV-R4 30% exclusion limits of the DPA kinetic mixing parameter. The hashed region is where 107 meters (the NEXUS depth) of silicon overburden would attenuate the DM flux by at least a factor of e. Silicon is used to approximate the overburden because its complex conductivity is known down to the required energy.

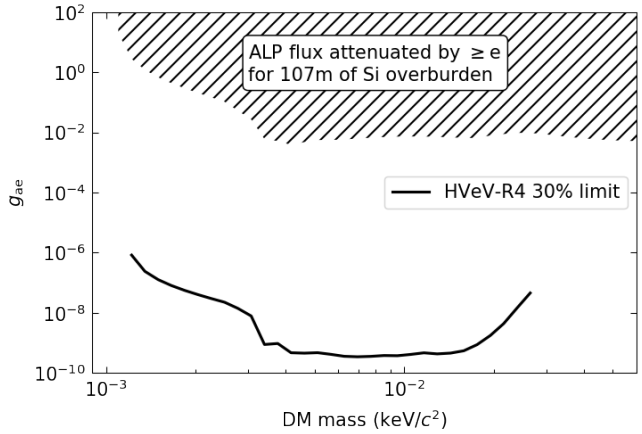

Figure 5.53: Estimation of the level above which the attenuation in earth shielding becomes significant, compared to the HVeV-R4 30% exclusion limits of the ALP-e mixing parameter. The hashed region is where 107 meters (the NEXUS depth) of silicon overburden would attenuate the DM flux by at least a factor of e. Silicon is used to approximate the overburden because its complex conductivity is known down to the required energy.

Fig. 5.56 and Fig. 5.57 show the corresponding peak choices with the lowest peak selection scheme. The same choices of peaks will be applied for the remaining 70% data limit setting.

5.8 Results for the 70 % Blinded Data

The 70% blinded spectrum can be seen in Fig. 5.58, including a comparison with the 30% spectrum that we discussed in Section 6.5. The corresponding exposure is 6.085 gram-days after live-time cuts.

A two-sample Kolmogorov–Smirnov (K-S) test [104] has been conducted for the 30% unblinded

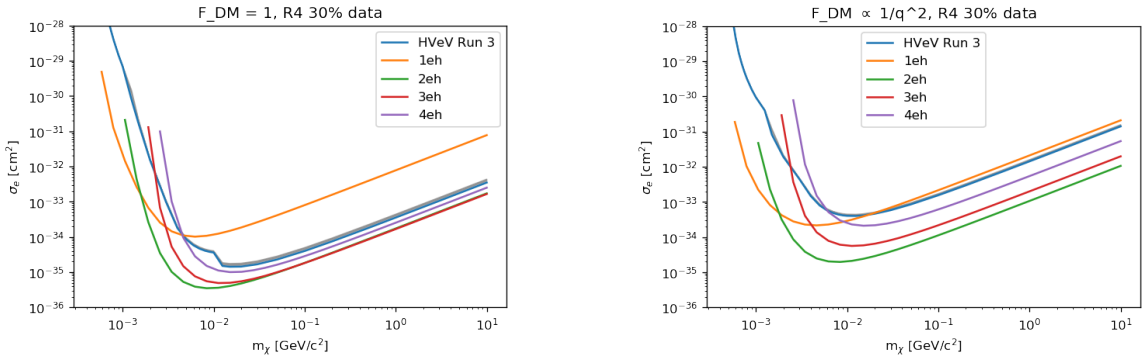

(a) DM-electron with form factor = 1

(b) DM-electron with form factor $\propto q^2$

Figure 5.54: DM-electron scattering limits calculated for individual peaks using 30% unblinded data. The corresponding exposure for the 30% unblinded data is 2.450 gram-days after live-time cuts.

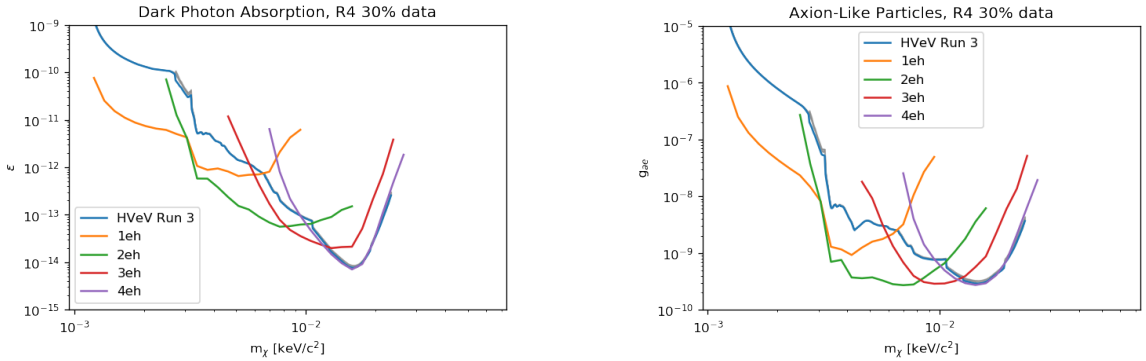

(a) Dark photon absorption

(b) Axion-like particles

Figure 5.55: Absorption limits calculated for individual peaks using 30% unblinded data. The corresponding exposure for the 30% unblinded data is 2.450 gram-days after live-time cuts.

data and the 70% blinded data after all live-time cuts. In the K-S test, the test statistic is a measure of the maximum absolute difference between the empirical cumulative distribution functions (ECDFs) of the two datasets. The significance of the difference between the two datasets is typically assessed by the associated p-value, under the null hypothesis that the two datasets are drawn from the same distribution. The test gives a K-S statistic of 0.010 and a p-value of $0.262 > 0.05$, indicating their distributions are not significantly different from each other.

Figure 5.59 and Fig. 5.60 show the final limits calculated with HVeV Run 4 70% blinded data with a peak selection pre-determined from the 30% unblinded data (Section 6.5). The comparison with results from other experiments is shown in Fig. 5.61, Fig. 5.62, Fig. 5.63 and Fig. 5.64. For DMe signal with DM form factor 1, the peak selection from 30% data (3rd peak) does not match the actual lowest peak of the 70% data (2nd peak). This is due to the low statistics in the region of higher order peaks, which cause (1) the statistical fluctuation to be significant, and (2) the 90% CL upper limit does not scale linearly with the exposure. Considering this, the final results for higher order peaks could be improved given more exposure.

HVeV Run 4 pushes the upper limits further down compared with the results achieved in Run

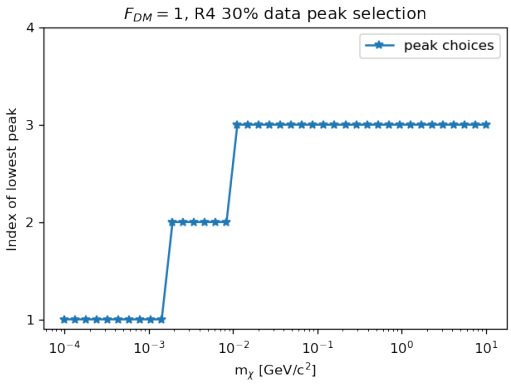

(a) DM-electron with form factor = 1

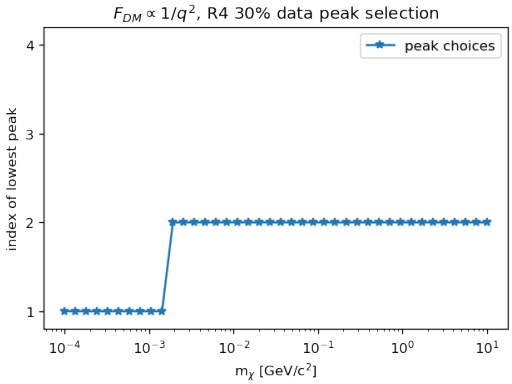

(b) DM-electron with form factor $\propto q^2$

Figure 5.56: Peak selection for DM-electron scattering determined from 30% unblinded data. The same peaks determined here for each mass will be used when calculating limits from the blinded data.

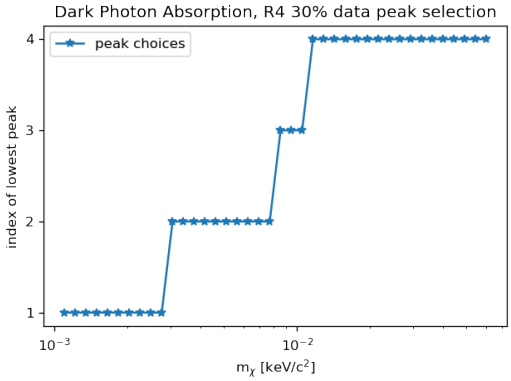

(a) Dark photon absorption

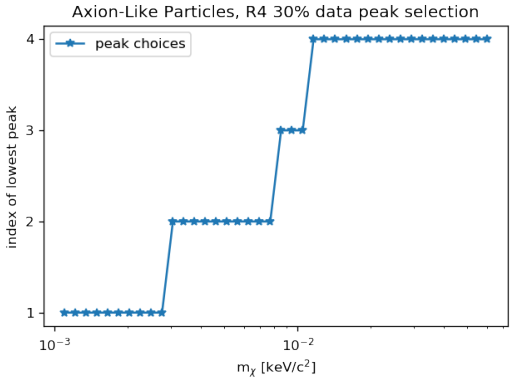

(b) Axion-like particles

Figure 5.57: Peak selection for absorption models determined from 30% unblinded data. The same peaks determined here for each mass will be used when calculating limits from the blinded data.

3, and becomes competitive or world leading in some of the mass regions, especially in the low mass parameter space where the 1st or 2nd peak is dominant.

The overburden exclusion results overlaid with the 90% CL limits from 70% blinded data for all four signal models are shown in Fig. 5.65 and Fig. 5.66. Same approaches of calculations are conducted as described in Section 5.6.

In this chapter, we presented the full analysis of HVeV Run 4 DM search data. We first discussed continuous readout processing and event reconstruction based on the OF method. Then we talked about energy calibration using the Nexus Run 14 LED data, so that the reconstructed OF amplitudes can be converted to the total energy deposited in the detector. Four live-time selections and an energy dependent χ^2 cut are developed to filter the DM search data. The cut efficiencies of the χ^2 cut are estimated with the 0V Caesium data taken in Nexus Run 13, which turn out to be energy independent in our analysis range. A likelihood-based limit setting approach is adopted under the signal-only conservative assumption. Only 30 % of the DM search data was unblinded at the beginning to study

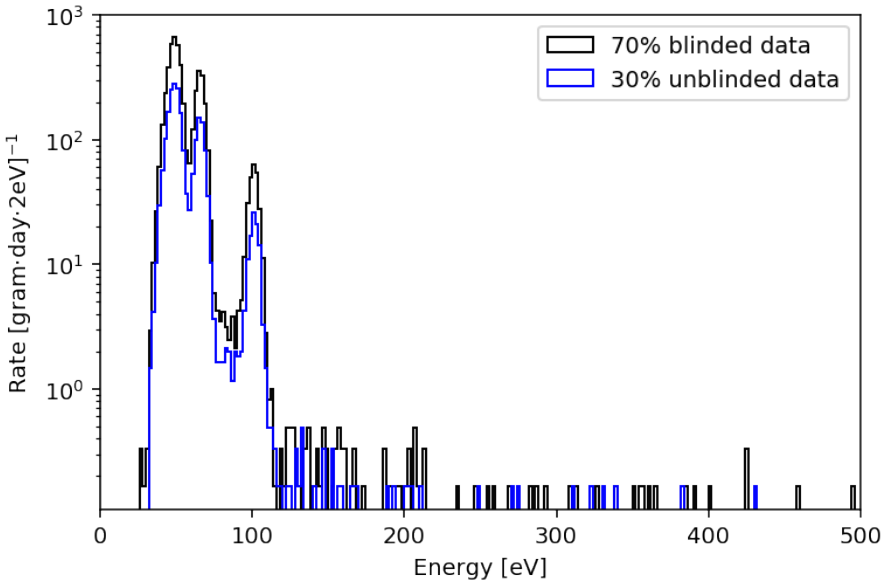

Figure 5.58: 70% blinded spectrum after all cuts (black) in comparison with 30% unblinded spectrum (blue). The exposure for the 70% blinded data is 6.085 gram-days after live-time cuts.

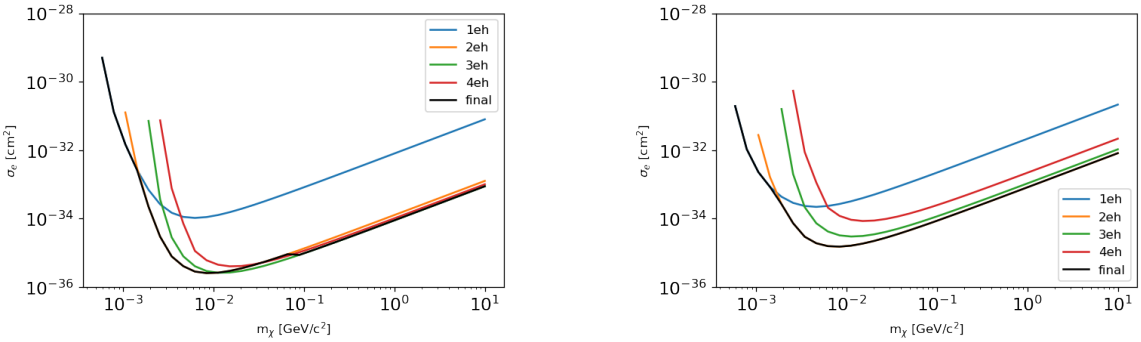

(a) DM-electron with form factor = 1

(b) DM-electron with form factor $\propto 1/q^2$

Figure 5.59: DM-electron scattering limits calculated for individual peaks using 70% unblinded data. The corresponding exposure for the 70% unblinded data is 6.085 gram-days after live-time cuts.

the energy calibration, live-time and event selections, and the limit setting approach. The remaining 70 % blinded data were analyzed after the unblinded final limits are produced and peak choices are determined. Finally, an overburden attenuation study gives order-of-magnitude estimations of the parameter space boundaries where the upper limits are no longer valid due to the earth shielding.

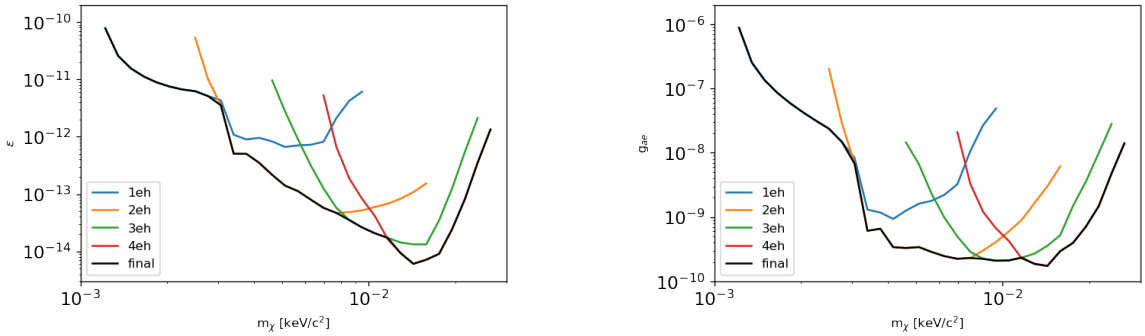

(a) Dark photon absorption

(b) Axion-like particles

Figure 5.60: Absorption limits calculated for individual peaks using 70% unblinded data. The corresponding exposure for the 70% unblinded data is 6.085 gram-days after live-time cuts.

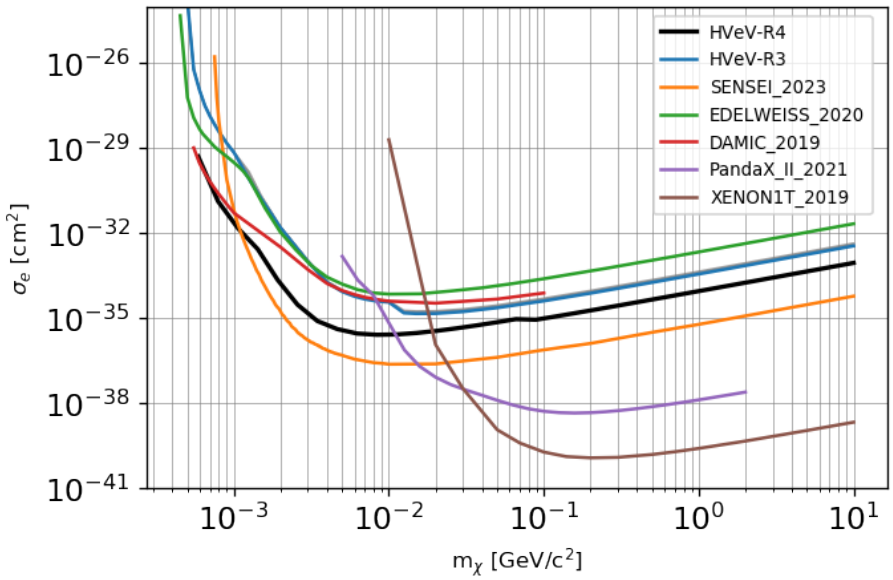

Figure 5.61: The combined limit of DM-electron scattering cross-section with form factor 1 (black line) in comparison with results from other experiments (colored lines) [83][50][51].

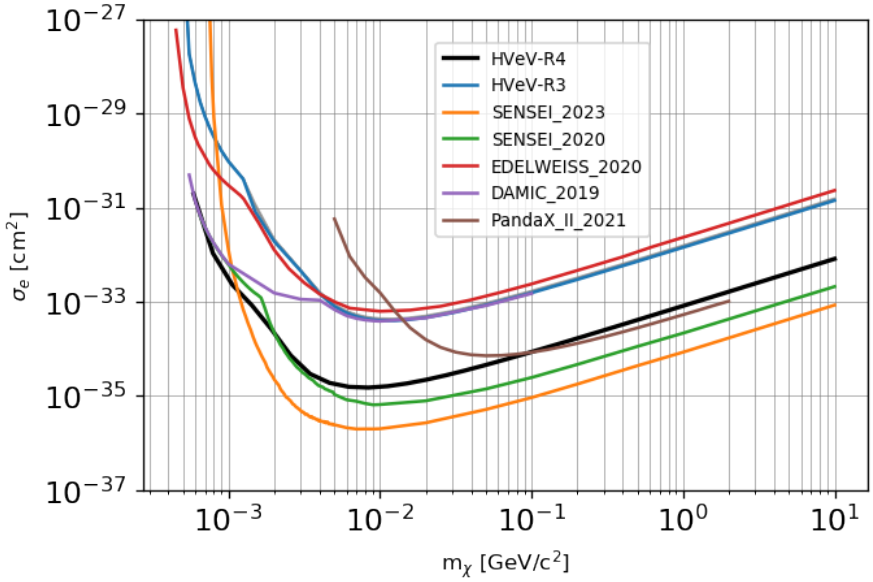

Figure 5.62: The combined limit of DM-electron scattering cross-section with form factor $\propto 1/q^2$ (black line) in comparison with results from other experiments (colored lines) [83][50][51].

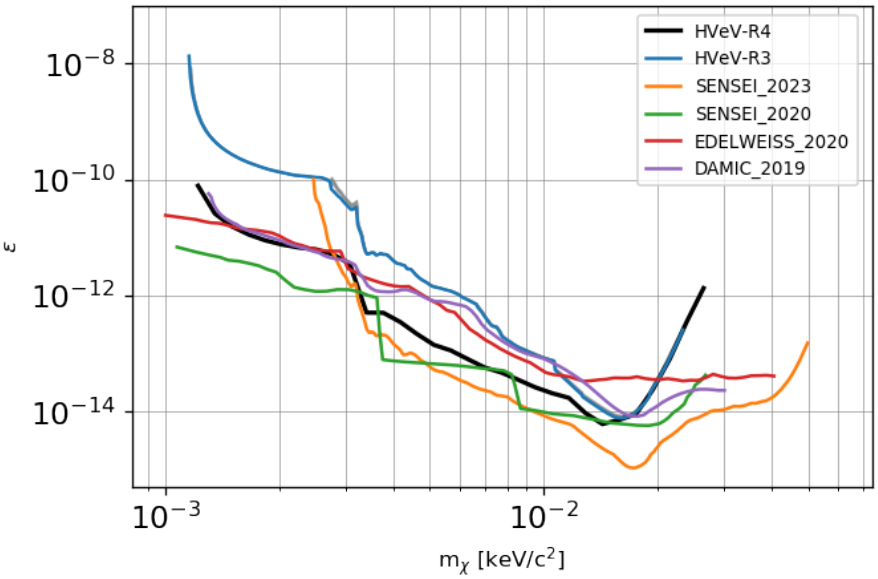

Figure 5.63: The combined limit of dark photon absorption mixing parameter (black line) in comparison with results from other experiments (colored lines) [83][50][51].

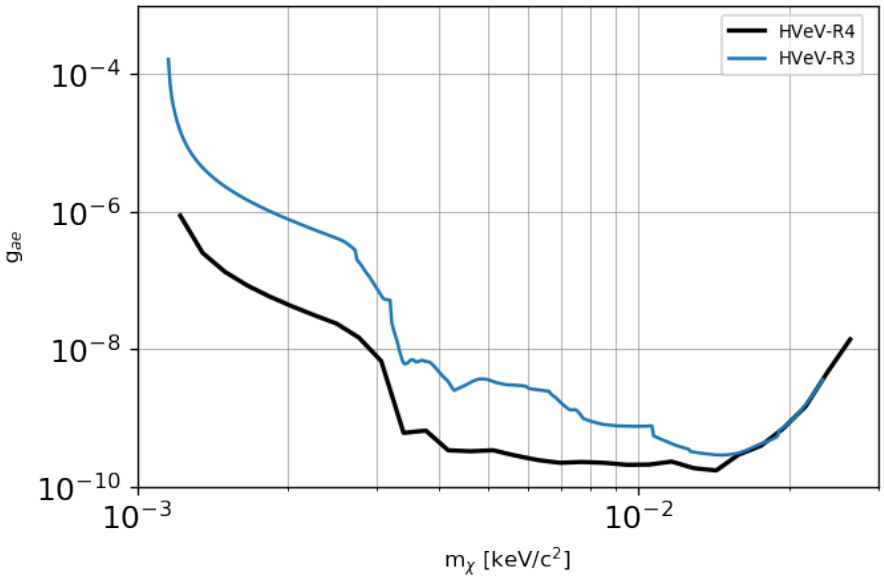

Figure 5.64: The combined limit of axion-like particles coupling constant in comparison with results from the previous HVeV run [83].

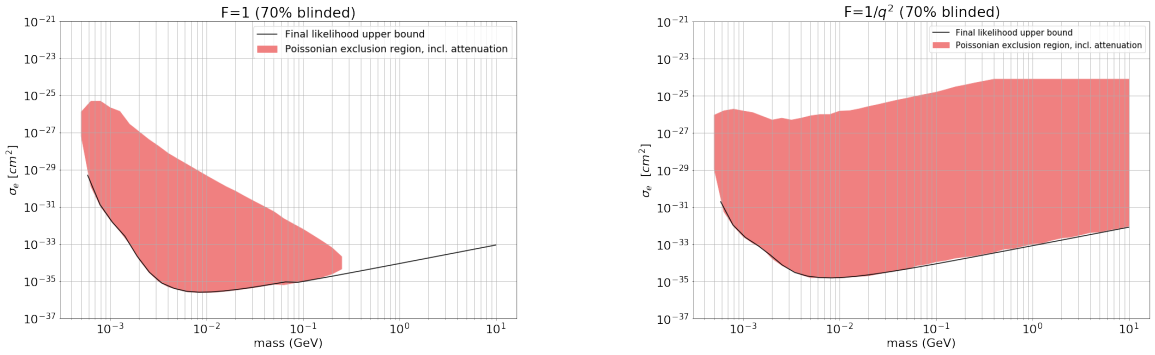

(a) DM-electron with form factor = 1

(b) DM-electron with form factor $\propto 1/q^2$

Figure 5.65: HVeV Run 4 (left: $F_{DM} = 1$, right: $F_{DM} \propto 1/q^2$) 90% CL Limit with overlay of estimated region of 90% CL exclusion including dark matter attenuation effects. Calculations are based on 70% blinded science data.

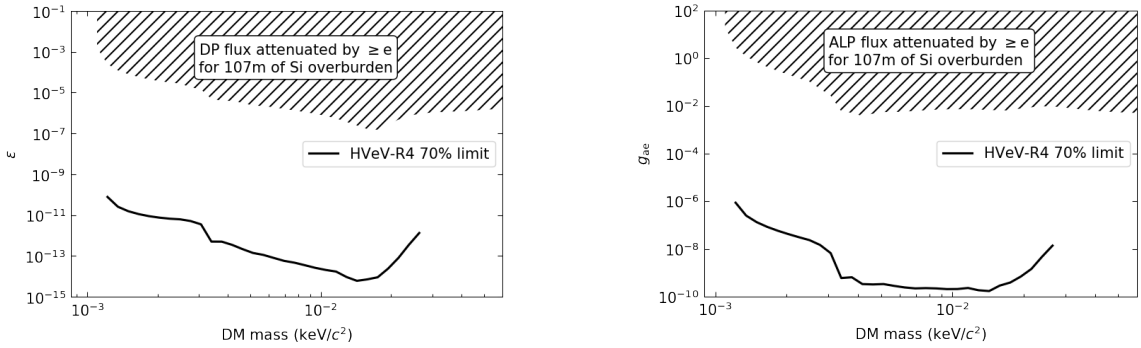

(a) Dark photon absorption

(b) Axion-like particles

Figure 5.66: Estimation of (left: dark photon absorption kinetic mixing parameter, right: axion-like particles coupling constant) above which the attenuation in shielding becomes significant, compared to the HVeV-R4 70% exclusion limits. The hashed region is where 107 meters (the NEXUS depth) of silicon overburden would attenuate the DM flux by the factor e (or more). Silicon is used to approximate the overburden because its complex conductivity is known down to the required energy.

Chapter 6

Summary and Outlook

Dark matter, as motivated by the inconsistency between the gravitational theory and astronomical observations, has still remained mysterious. For decades, WIMPs have been the most popular dark matter candidate in the science community, with a favored mass of 10 GeV to 10 TeV scale. However, the absence of a discovery forces physicists to explore other possibilities, including searching in lower mass parameter spaces as well as seeking other candidates. SuperCDMS SNOLAB is a next-generation dark matter direct detection experiment, with the main science goal to improve the sensitivity for dark matter particles with mass less than 10 GeV by at least one order of magnitude over existing sensitivities. Cryogenically-cooled kilogram-scale germanium and silicon crystal detectors are employed for their capability of detecting very small recoil energies between dark matter particles and nuclei/electrons. HVeV detectors, similar to CDMS-HV detectors but with a gram-scale crystal mass and single charge sensitivity, were initially designed for a prototype study, but later proved to be able to produce world-leading exclusion results for low mass dark matter candidates. HVeV Run 4 is the fourth generation of HVeV experiments, optimized to have improved channel layout designs, which has removed one of the major background source from its predecessor. 13 days of data have been taken in HVeV Run 4, with 70% used for a blinded analysis corresponding to 10.80 gram-days exposure. The final exclusion limits achieved for DM-electron scattering in the mass range of MeV to GeV, dark photon absorption and axion-like particle absorption in the mass range of eV to tens of eV, turn out to be competitive compared with other world leading experimental results. The work will result in a publication in 2025.

The major limitation of this analysis is the lack of a background model. As a consequence, we have to make the conservative assumption and treat all observed events as signals when setting exclusion limits. The reason for the absence of a background model is that we still have little understanding of some background sources, especially those in the low energy region which we call "low energy excess events". In HVeV Run 3, it was identified that the interaction of muons with SiO_2 in the printed circuit boards surrounding the detector excite electrons, leading to fluorescence and phosphorescence which may cause a signal in the detector and become a major source of background events. Once it was removed as in HVeV Run 4, we observed a significant reduction in the event rate. Similarly, if we could understand the source of these low energy excess events, we can either eliminate them in future experiments, or at least establish a background model for them. Based on this idea, a new HVeV run has already taken place in 2024 at a cryogenic underground test facility

(CUTE) in SNOLAB, with the main science goal of investigating the nature of the low energy excess events under the low background environment at CUTE.

Another potential improvement of the analysis is the modeling of CTII effects. The exponential CTII model used in HVeV Run 4 provides no description of the underlying mechanisms of CT or II processes, and simply assumes that there is some probability that these processes occur due to impurities throughout the crystal bulk [93]. The characteristic lengths of these processes could depend not only on the density of impurities, but also on the strength of the electric field, prebiasing history, "baking" history (impurity neutralization by detector irradiation) and temperature [105][106]. Future plans include investigations of detector response using HVeV detectors. For instance, conducting CT and II measurements with crystals of varying impurity levels, while adjusting the voltage bias or prebiasing applied to the crystals, will enhance our understanding of the factors influencing CT and II [93].

While the thesis has focused on the dark matter search efforts with HVeV detectors in multiple runs, it is important to emphasize that HVeV detectors also serve as a research and development (R&D) effort to facilitate the SuperCDMS SNOLAB experiment coming in the near future. As similar electron-hole pair quantization in the energy spectrum is expected to be observed in SuperCDMS HV detectors, the characteristic study of HVeV detectors could provide valuable insights for the SNOLAB experiment.

Appendix A

Plots of NFC2 and NFH Detectors in the Analysis

For most sections of Chapter 5, only NFC1 plots are shown since it is the detector for limit setting. In this appendix, the analysis plots are presented for the energy calibration, energy dependent χ^2 cut definitions, and cut efficiency calculations of the NFC2 and NFH detectors. In addition, in Section A.2, the energy interval plots for the NFC1 detector are also presented. For the NFE detector, due to insufficient calibration data taken in Nexus Run 14 (at that time we already analyzed Nexus Run 13 unblinded data and decided to use only the NFC1 detector for limit setting), we skip it for the following plots.

A.1 Energy Calibrations

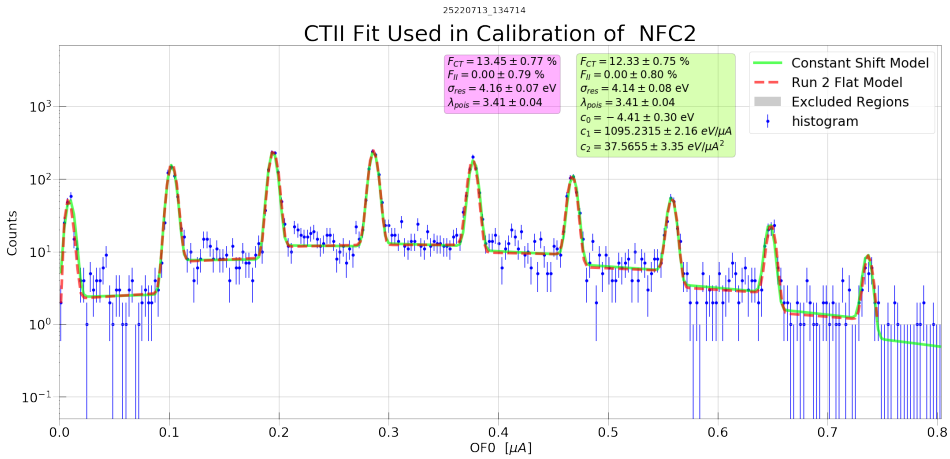

Figure A.1: OF0 CTII calibration fit for NFC2 detector using the flat model (red) in comparison with using the constant shift model (green). This OF0 preliminary calibration gives us best fit values and uncertainties for CTII parameters, which will be further used in OFL recalibration.

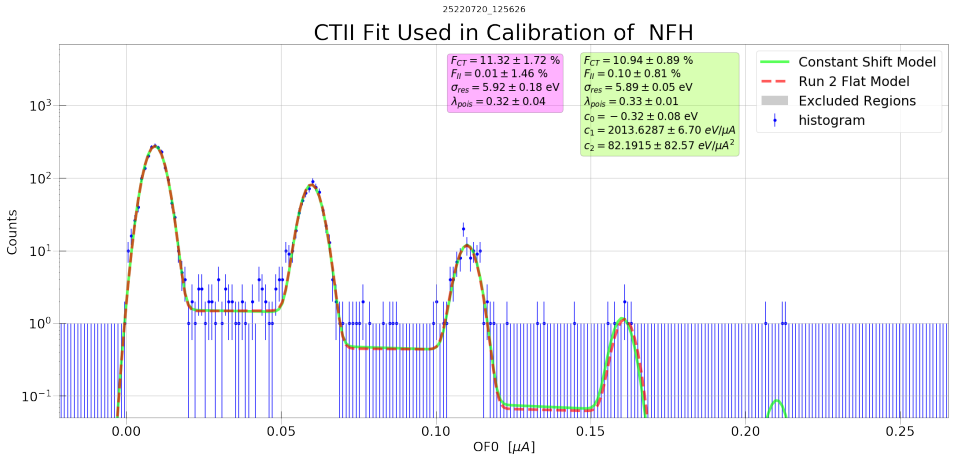

Figure A.2: OF0 CTII calibration fit for NFH detector using the flat model (red) in comparison with using the constant shift model (green). This OF0 preliminary calibration gives us best fit values and uncertainties for CTII parameters, which will be further used in OFL recalibration.

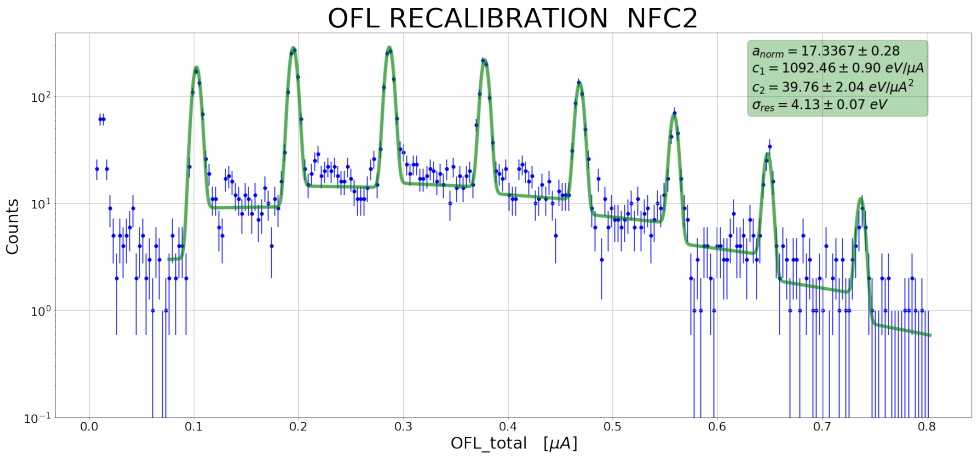

Figure A.3: OFL recalibration for NFC2 with inputs from OF0 calibration fits. The four parameters shown in the green box are allowed to float, and the remaining parameters to construct the fitting function are taken from the green box in Fig. A.1. The 0th peak is excluded from the fitting due to the OFL estimator being unreliable in extreme low energies.

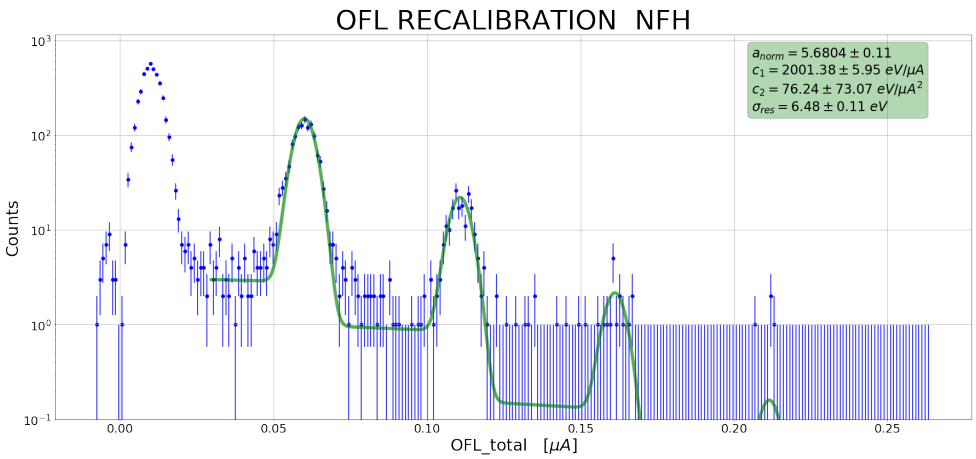

Figure A.4: OFL recalibration for NFH with inputs from OF0 calibration fits. The four parameters shown in the green box are allowed to float, and the remaining parameters to construct the fitting function are taken from the green box in Fig. A.2. The 0th peak is excluded from the fitting due to the OFL estimator being unreliable in extreme low energies.

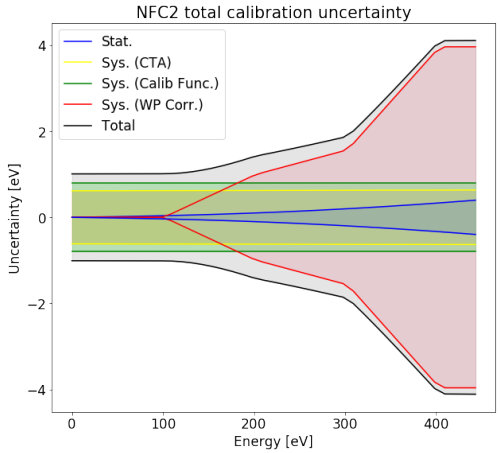

Figure A.5: Plot of the NFC2 total uncertainty (sys+stat) as a function of energy. Different components of the systematic uncertainty are shown separately. Uncertainties are added by quadrature.

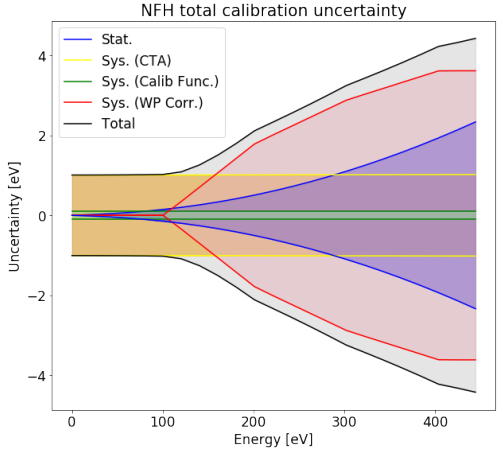

Figure A.6: Plot of the NFH total uncertainty (sys+stat) as a function of energy. Different components of the systematic uncertainty are shown separately. Uncertainties are added by quadrature.

A.2 Energy Dependent χ^2 Cut Definitions

A.2.1 Gaussian Fits to the χ^2 Distributions of Caesium Events in Different Energy Intervals

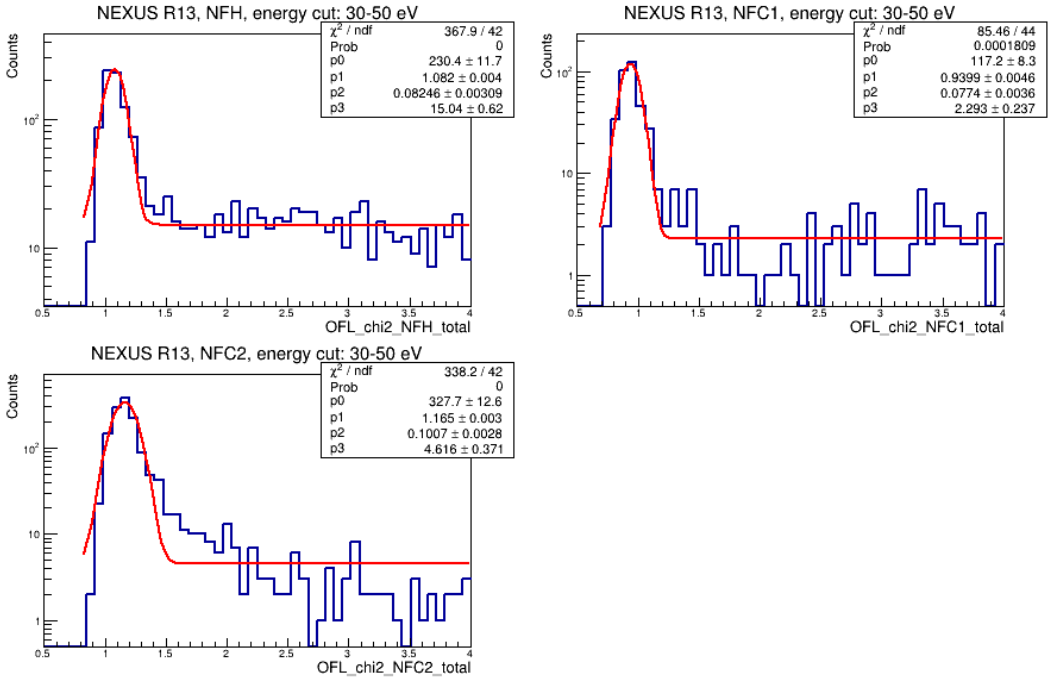

Figure A.7: Frequency-domain χ^2 distribution in the 30 to 50 eV energy interval from Caesium events. The distribution is fit with a Gaussian function plus a flat background.

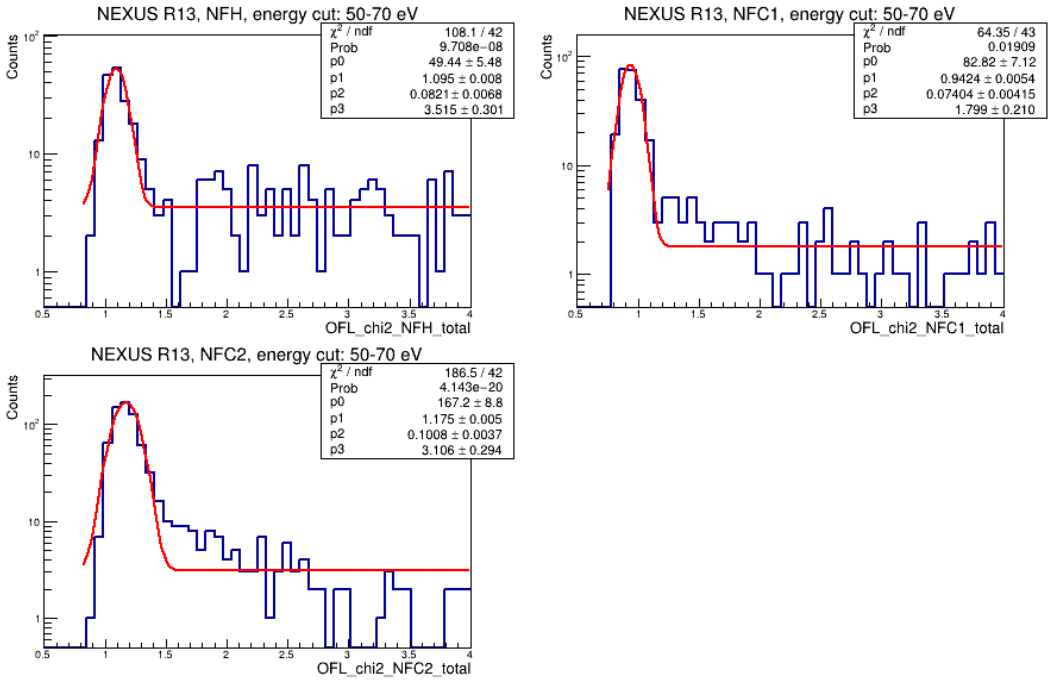

Figure A.8: Frequency-domain χ^2 distribution in the 50 to 70 eV energy interval from Caesium events. The distribution is fit with a Gaussian function plus a flat background.

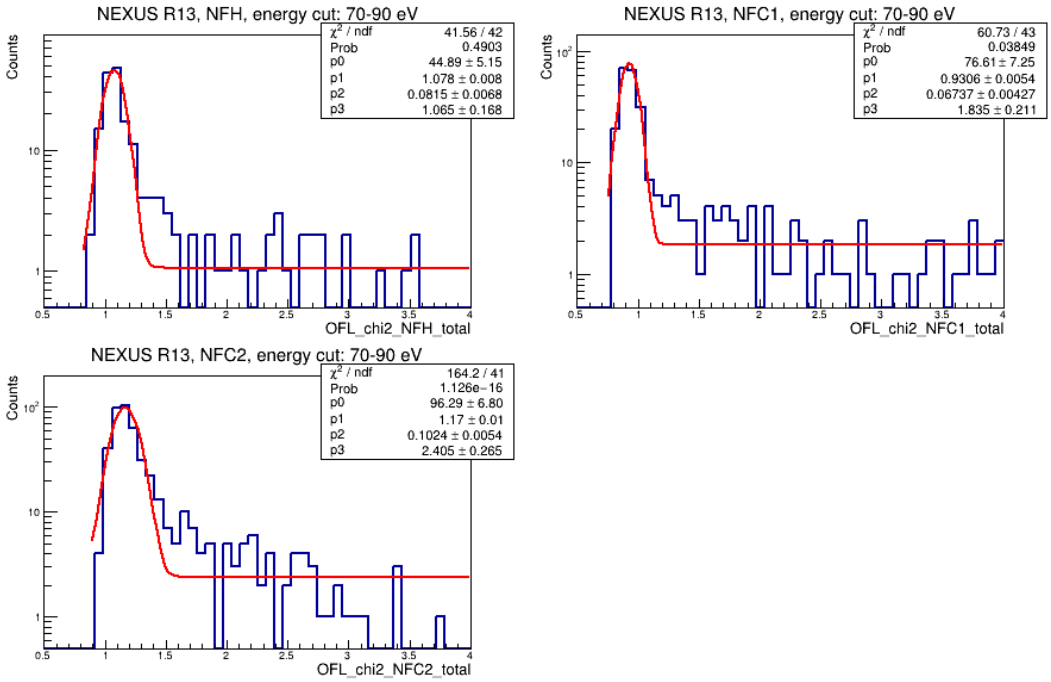

Figure A.9: Frequency-domain χ^2 distribution in the 70 to 90 eV energy interval from Caesium events. The distribution is fit with a Gaussian function plus a flat background.

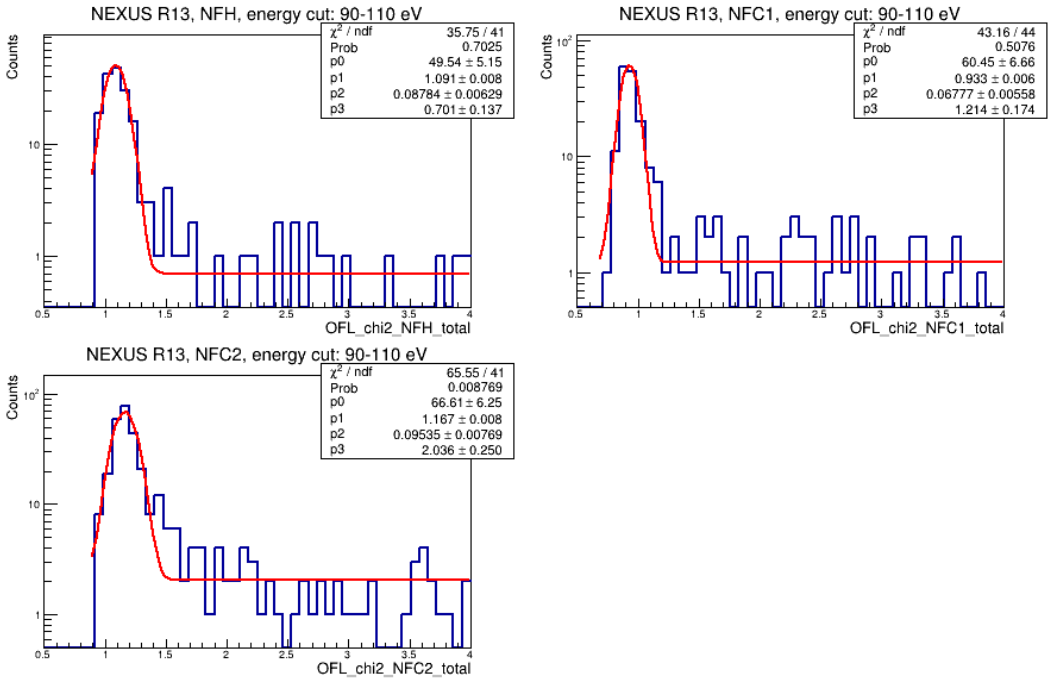

Figure A.10: Frequency-domain χ^2 distribution in the 90 to 110 eV energy interval from Caesium events. The distribution is fit with a Gaussian function plus a flat background.

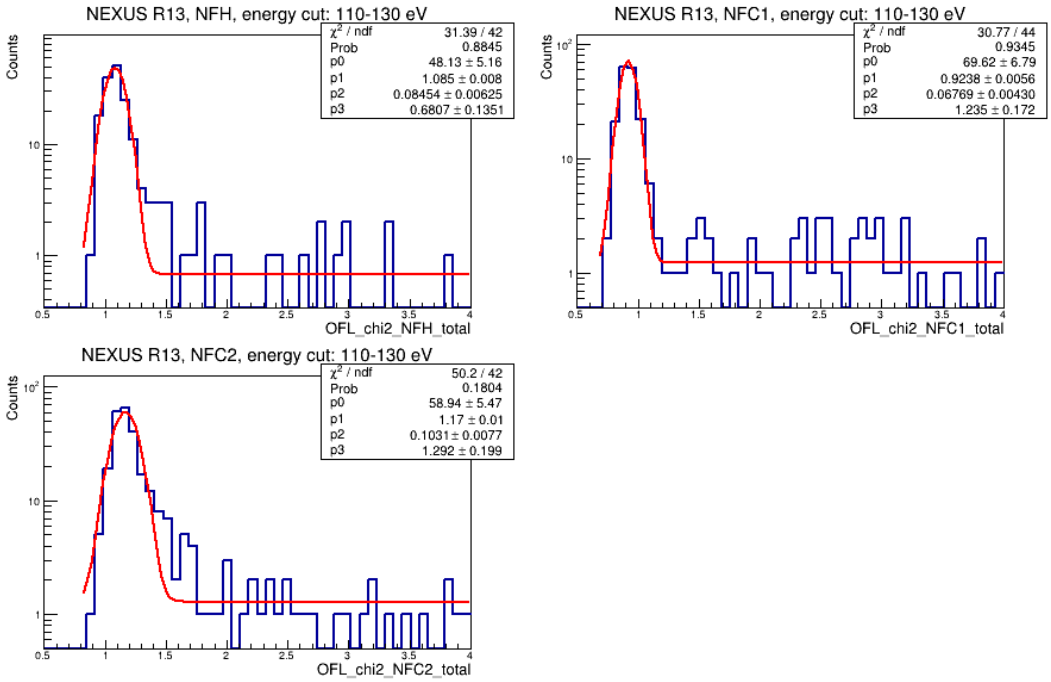

Figure A.11: Frequency-domain χ^2 distribution in the 110 to 130 eV energy interval from Caesium events. The distribution is fit with a Gaussian function plus a flat background.

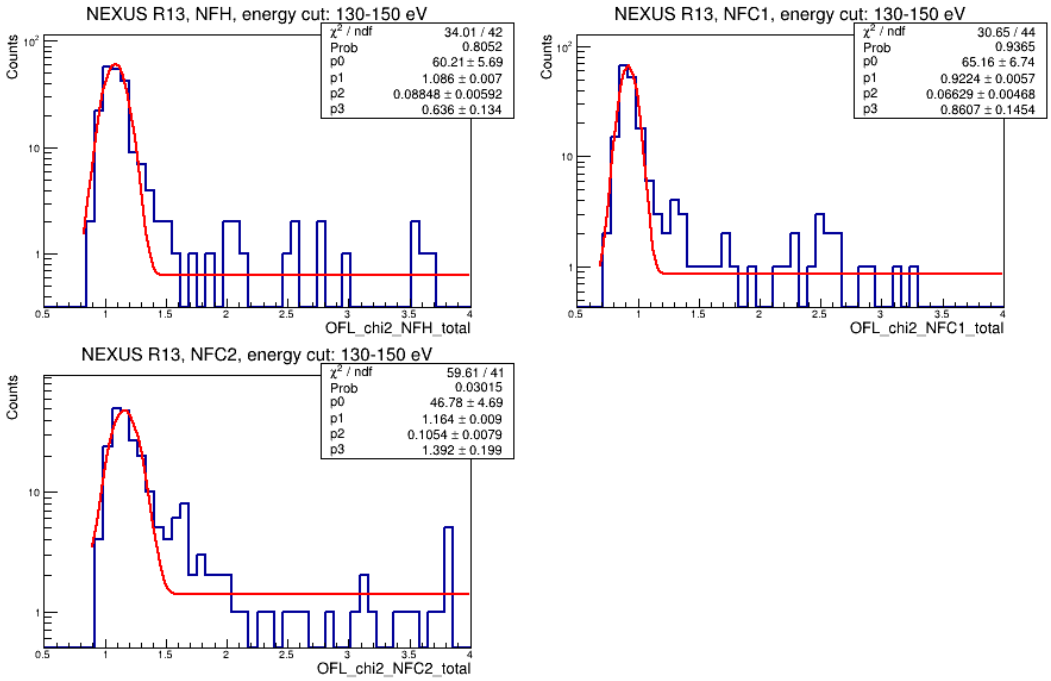

Figure A.12: Frequency-domain χ^2 distribution in the 130 to 150 eV energy interval from Caesium events. The distribution is fit with a Gaussian function plus a flat background.

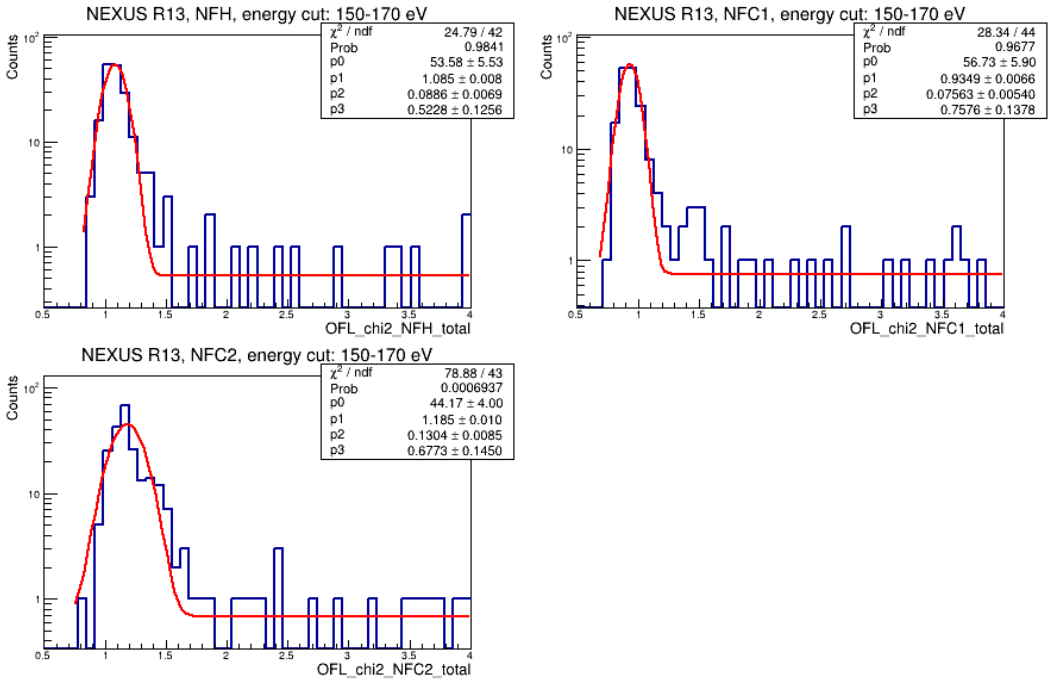

Figure A.13: Frequency-domain χ^2 distribution in the 150 to 170 eV energy interval from Caesium events. The distribution is fit with a Gaussian function plus a flat background.

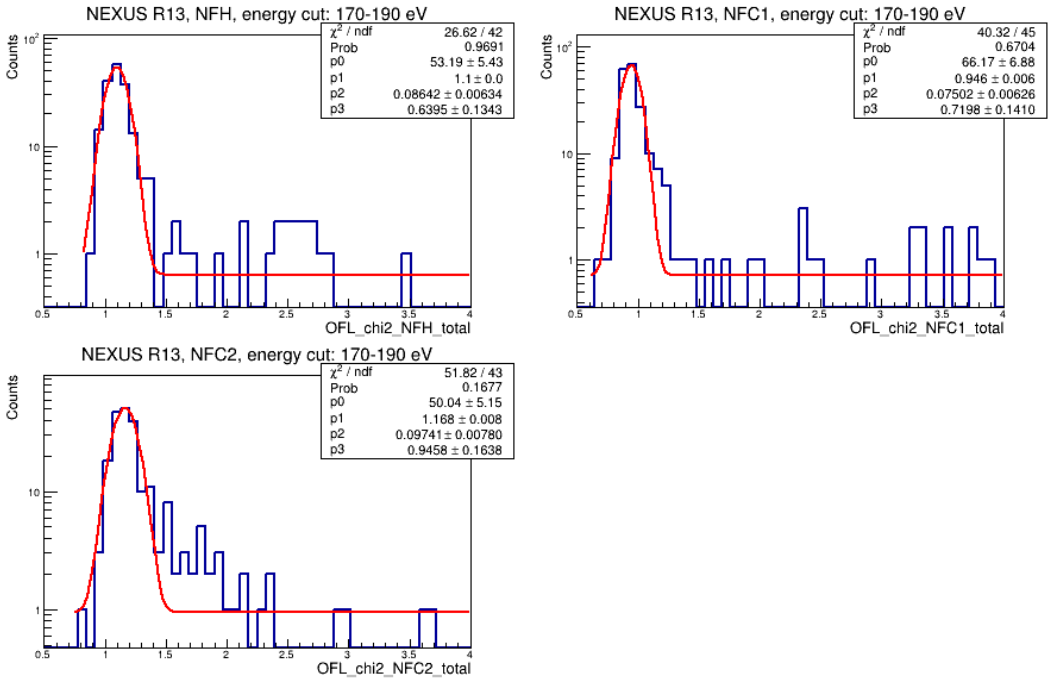

Figure A.14: Frequency-domain χ^2 distribution in the 170 to 190 eV energy interval from Caesium events. The distribution is fit with a Gaussian function plus a flat background.

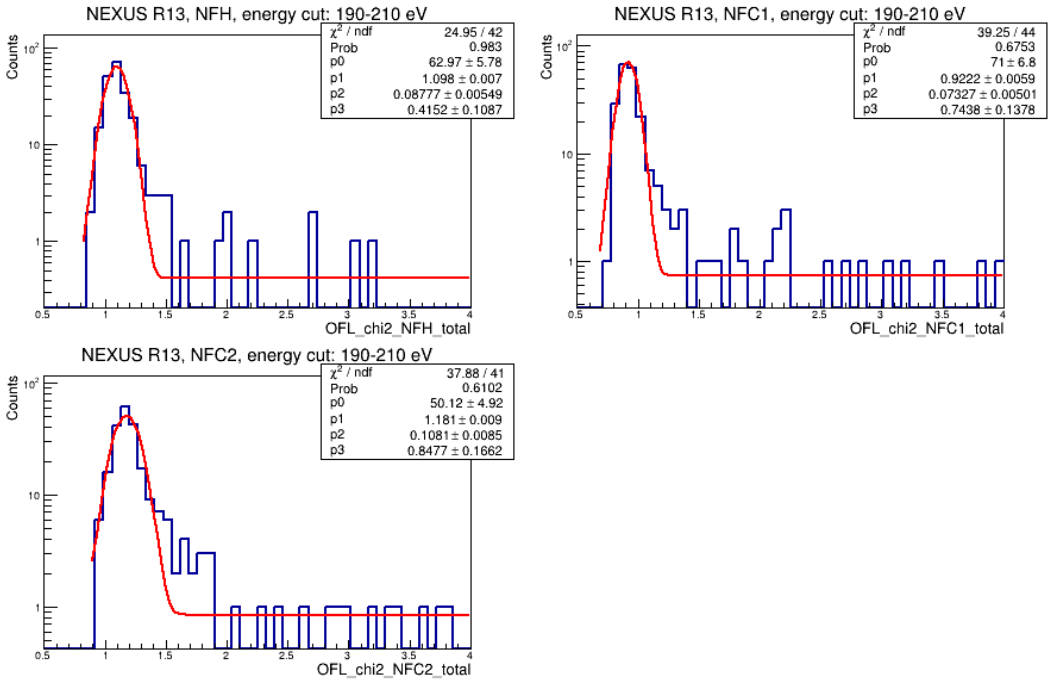

Figure A.15: Frequency-domain χ^2 distribution in the 190 to 210 eV energy interval from Caesium events. The distribution is fit with a Gaussian function plus a flat background.

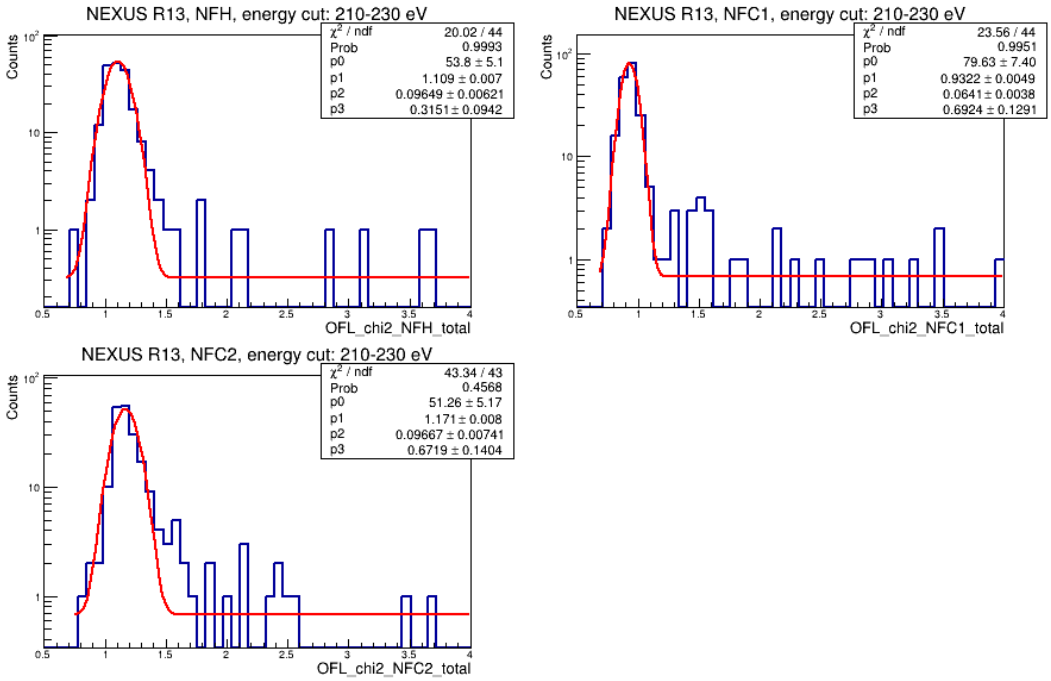

Figure A.16: Frequency-domain χ^2 distribution in the 210 to 230 eV energy interval from Caesium events. The distribution is fit with a Gaussian function plus a flat background.

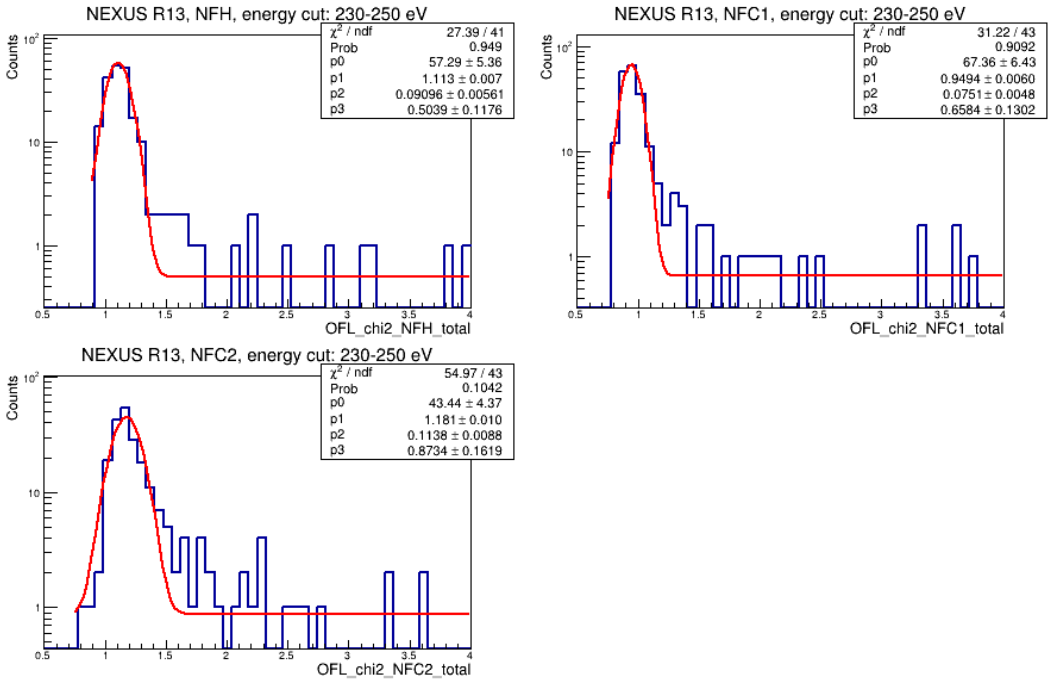

Figure A.17: Frequency-domain χ^2 distribution in the 230 to 250 eV energy interval from Caesium events. The distribution is fit with a Gaussian function plus a flat background.

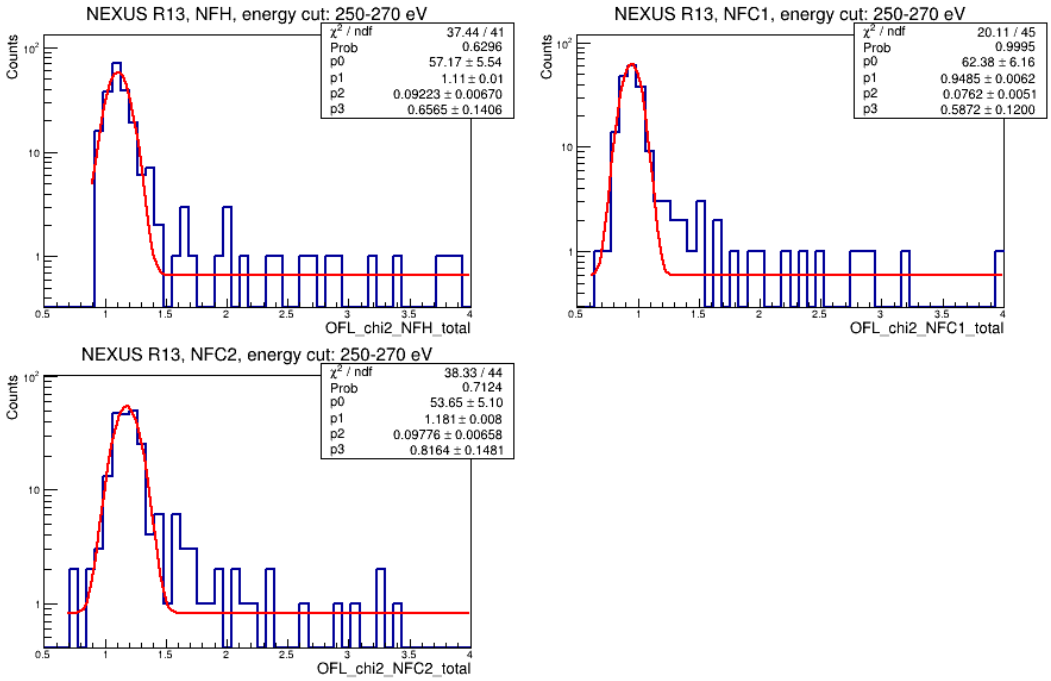

Figure A.18: Frequency-domain χ^2 distribution in the 250 to 270 eV energy interval from Caesium events. The distribution is fit with a Gaussian function plus a flat background.

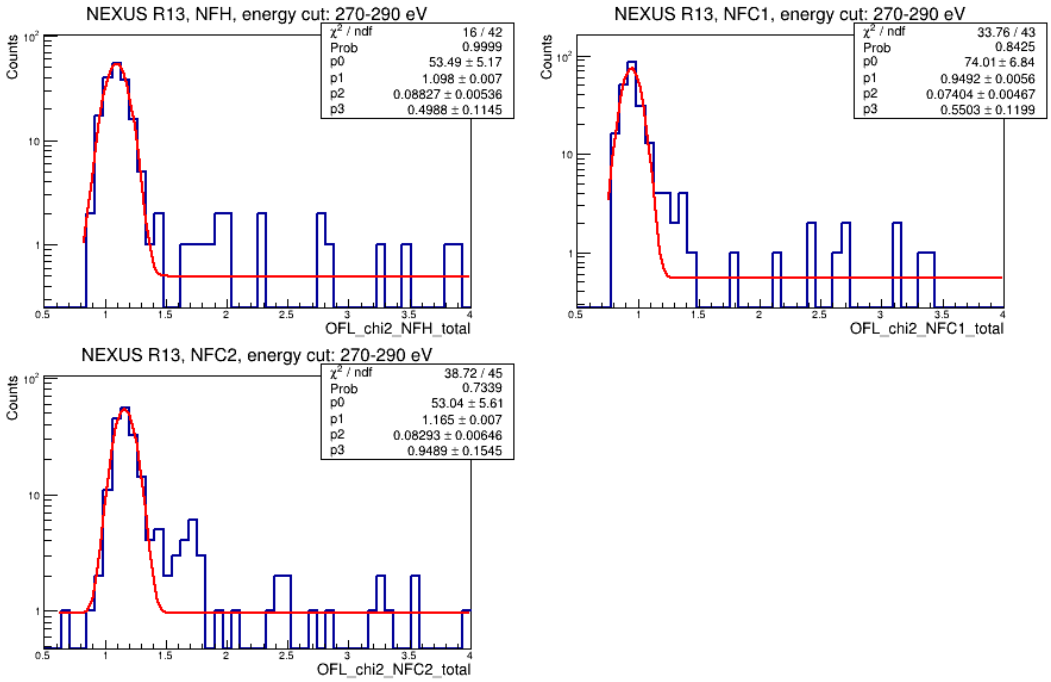

Figure A.19: Frequency-domain χ^2 distribution in the 270 to 290 eV energy interval from Caesium events. The distribution is fit with a Gaussian function plus a flat background.

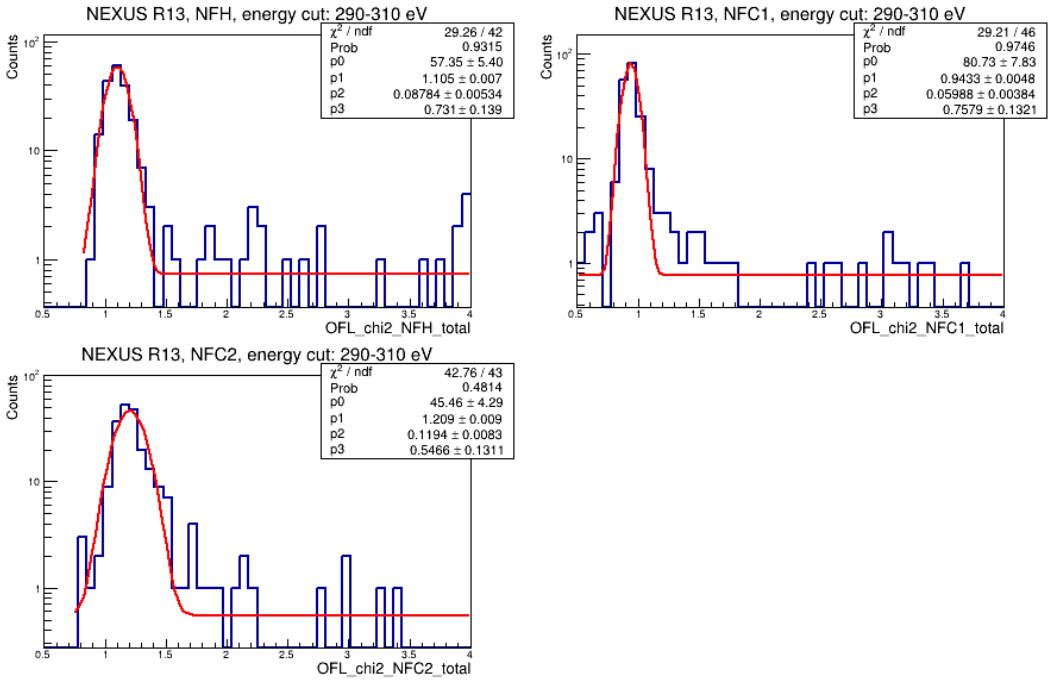

Figure A.20: Frequency-domain χ^2 distribution in the 290 to 310 eV energy interval from Caesium events. The distribution is fit with a Gaussian function plus a flat background.

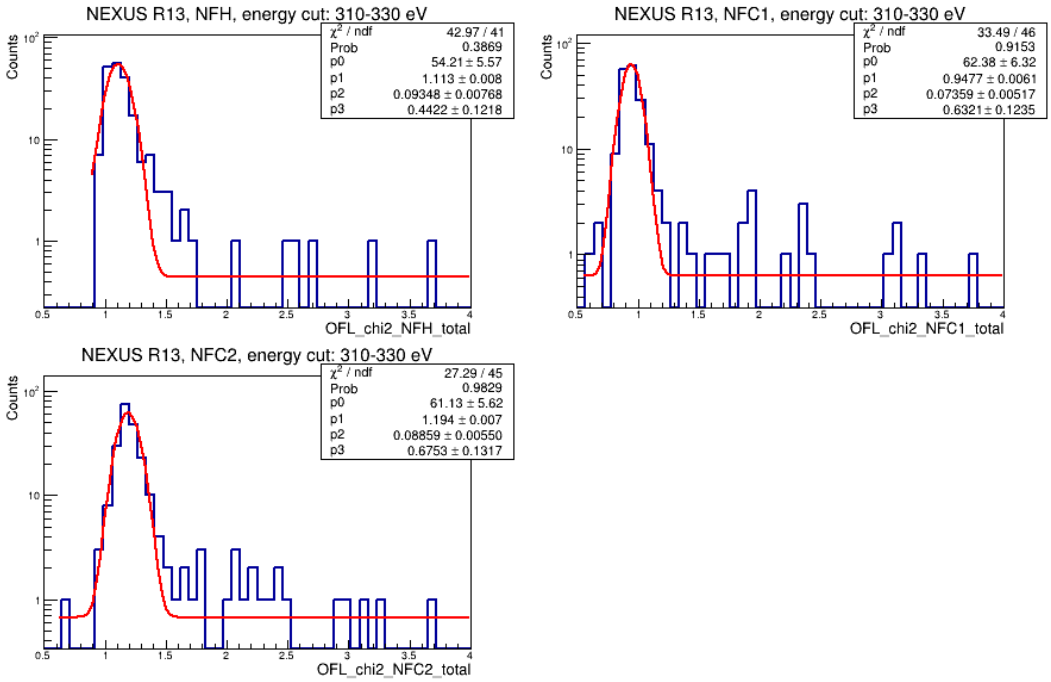

Figure A.21: Frequency-domain χ^2 distribution in the 310 to 330 eV energy interval from Caesium events. The distribution is fit with a Gaussian function plus a flat background.

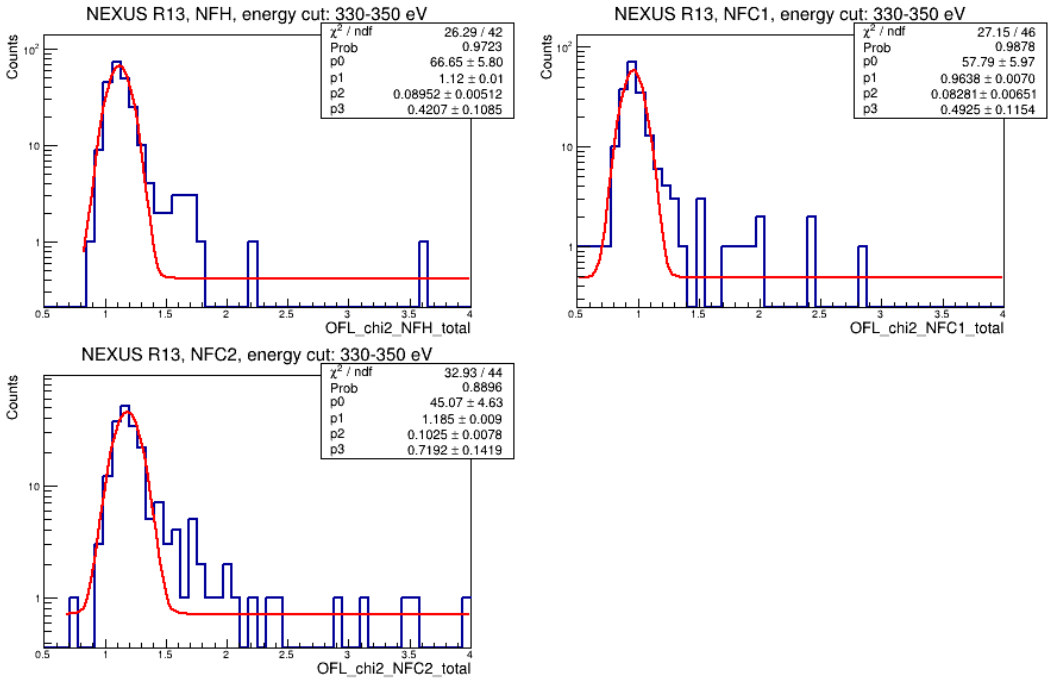

Figure A.22: Frequency-domain χ^2 distribution in the 330 to 350 eV energy interval from Caesium events. The distribution is fit with a Gaussian function plus a flat background.

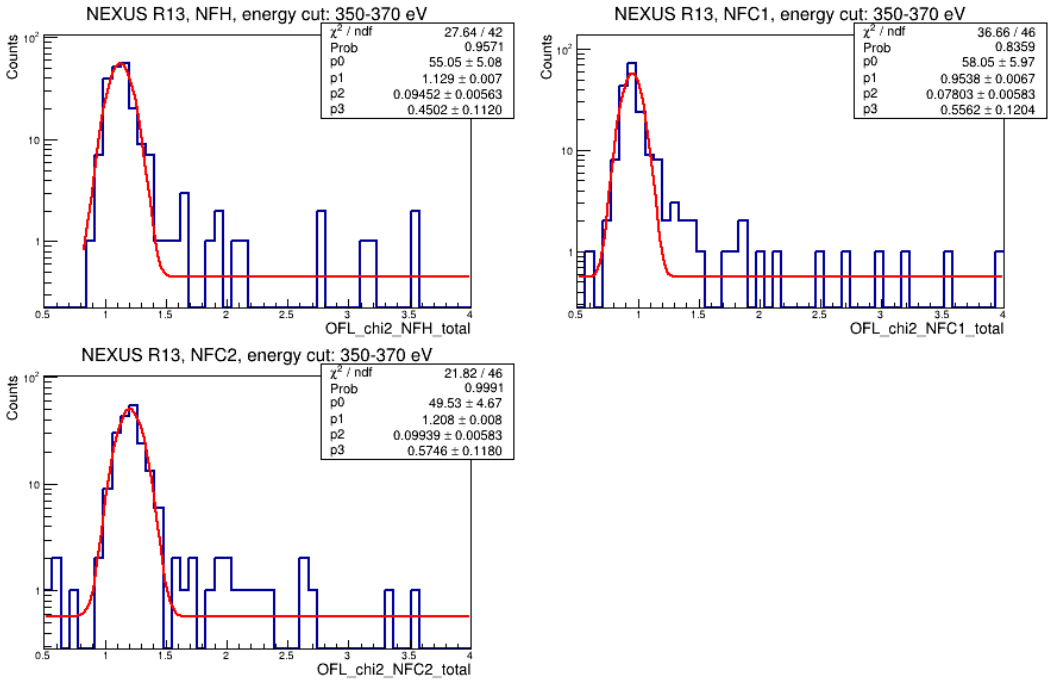

Figure A.23: Frequency-domain χ^2 distribution in the 350 to 370 eV energy interval from Caesium events. The distribution is fit with a Gaussian function plus a flat background.

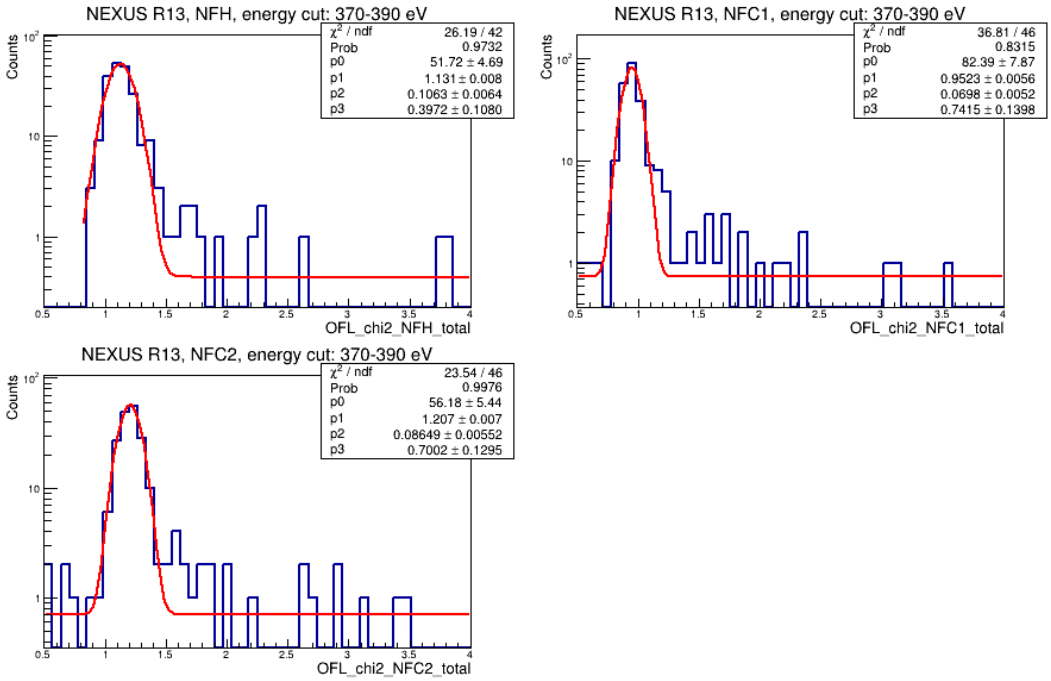

Figure A.24: Frequency-domain χ^2 distribution in the 370 to 390 eV energy interval from Caesium events. The distribution is fit with a Gaussian function plus a flat background.

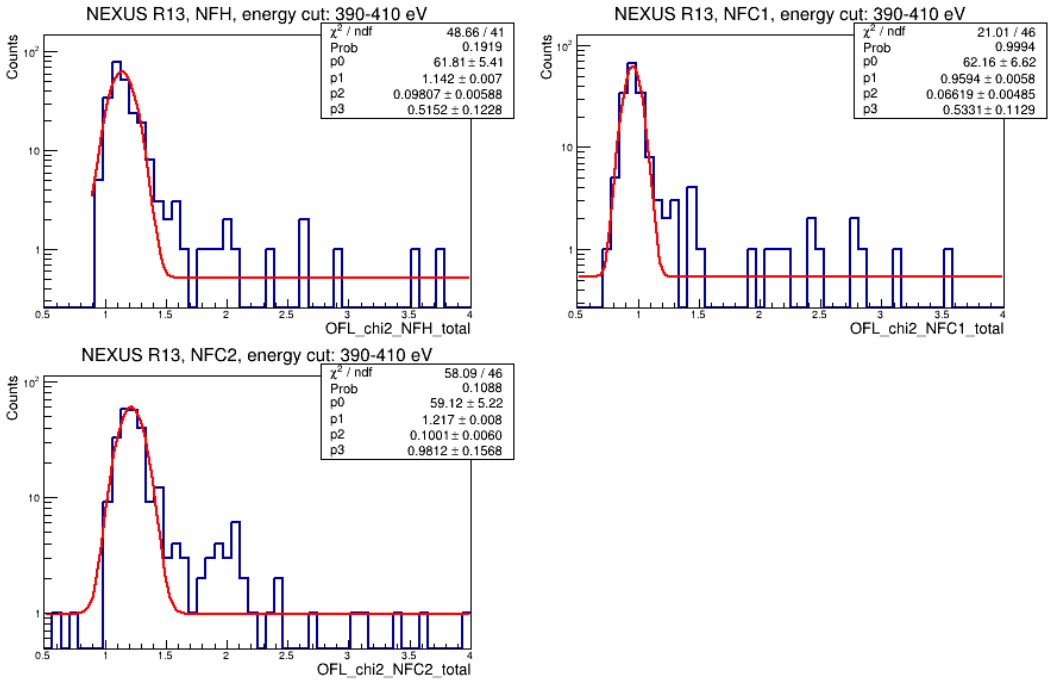

Figure A.25: Frequency-domain χ^2 distribution in the 390 to 410 eV energy interval from Caesium events. The distribution is fit with a Gaussian function plus a flat background.

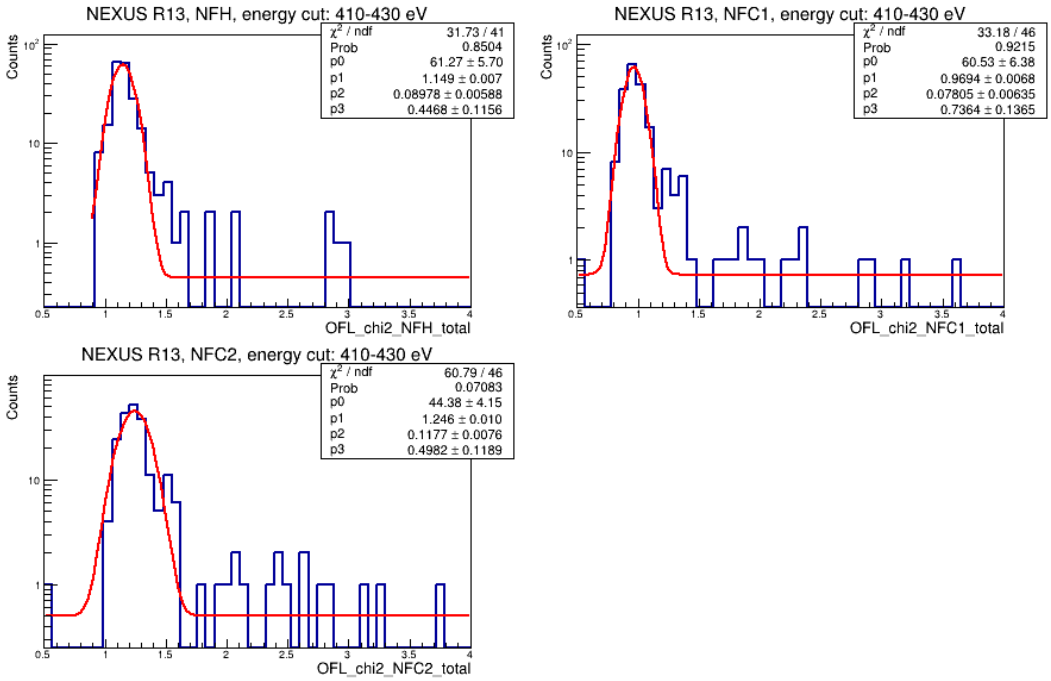

Figure A.26: Frequency-domain χ^2 distribution in the 410 to 430 eV energy interval from Caesium events. The distribution is fit with a Gaussian function plus a flat background.

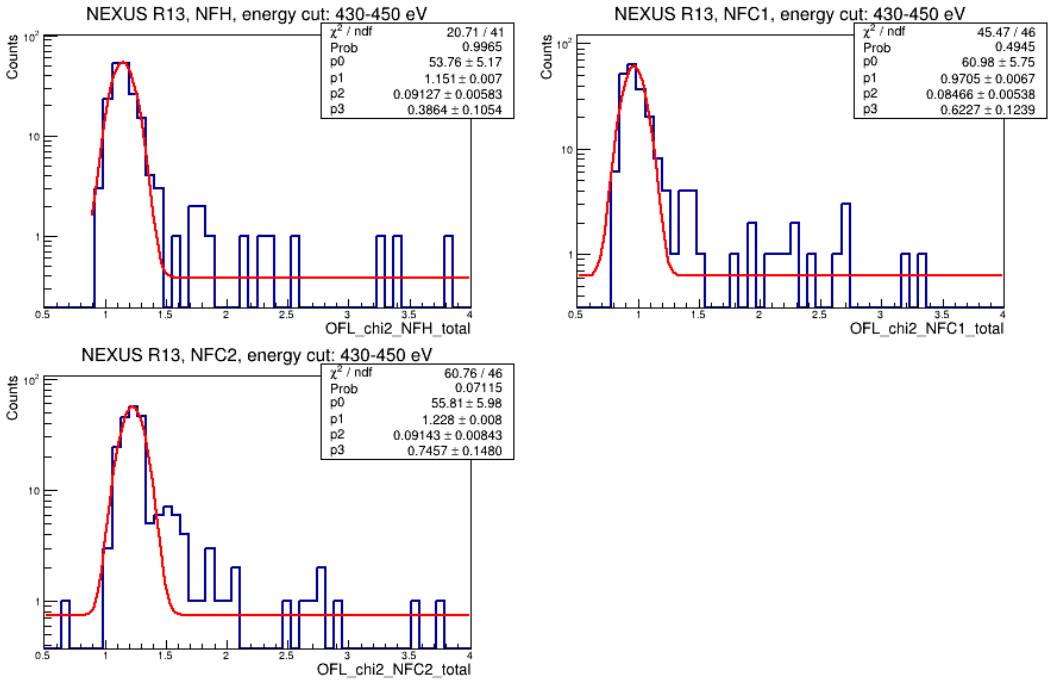

Figure A.27: Frequency-domain χ^2 distribution in the 430 to 450 eV energy interval from Caesium events. The distribution is fit with a Gaussian function plus a flat background.

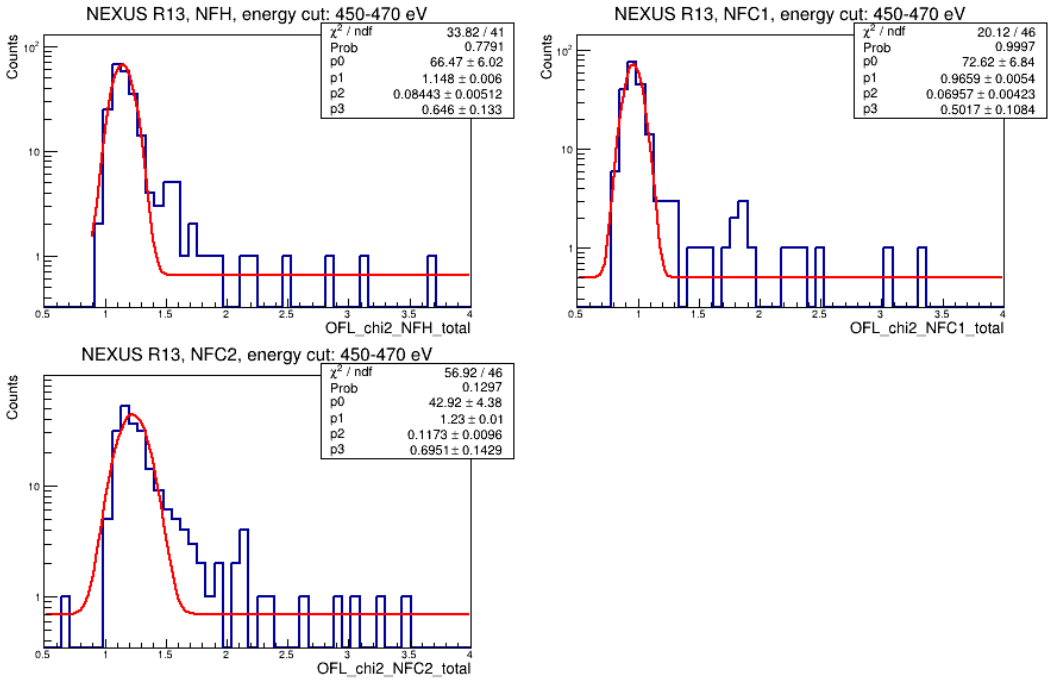

Figure A.28: Frequency-domain χ^2 distribution in the 450 to 470 eV energy interval from Caesium events. The distribution is fit with a Gaussian function plus a flat background.

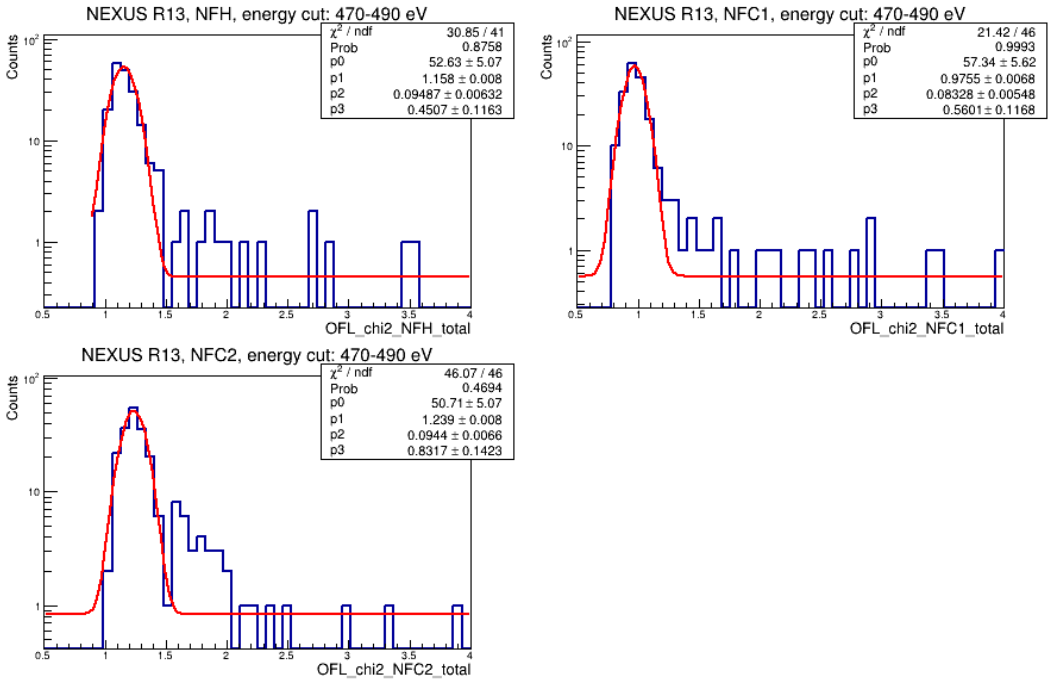

Figure A.29: Frequency-domain χ^2 distribution in the 470 to 490 eV energy interval from Caesium events. The distribution is fit with a Gaussian function plus a flat background.

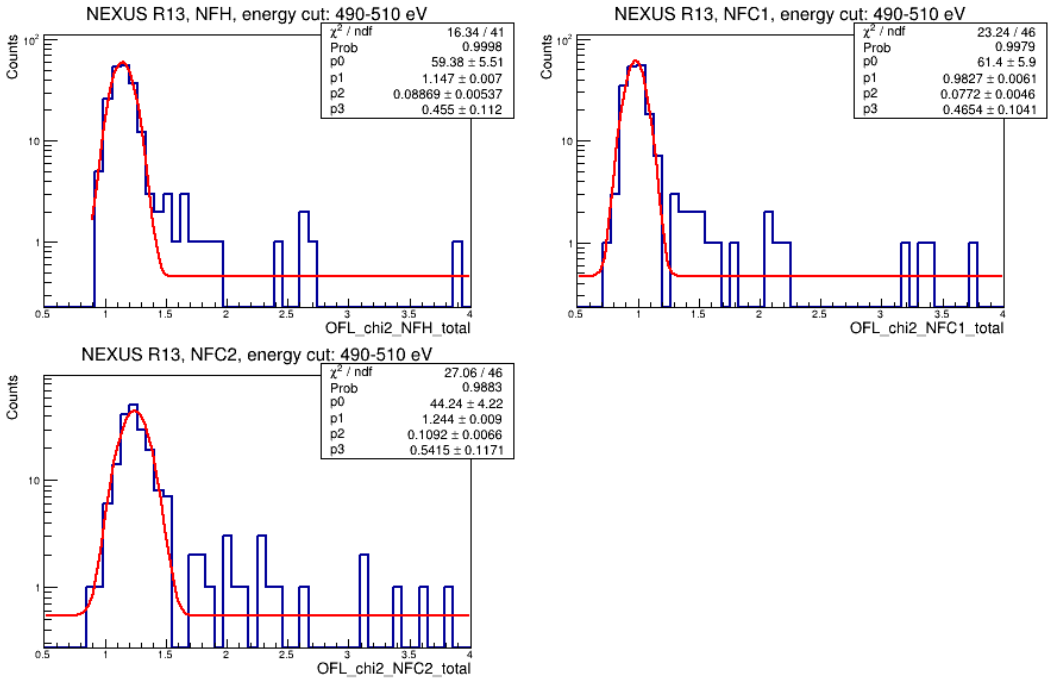

Figure A.30: Frequency-domain χ^2 distribution in the 490 to 510 eV energy interval from Caesium events. The distribution is fit with a Gaussian function plus a flat background.

A.2.2 Cut Threshold as a Function of Energy

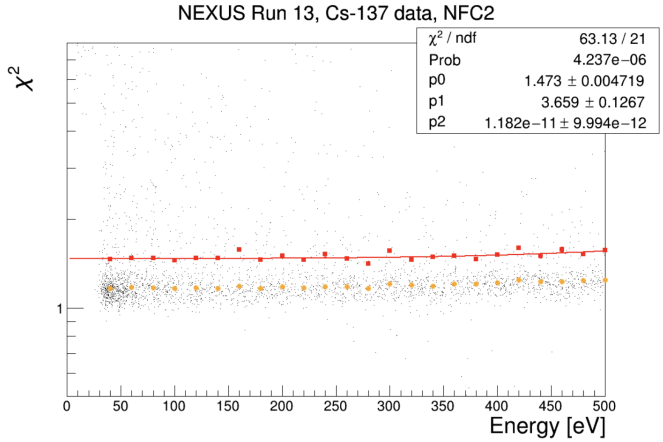

Figure A.31: χ^2_{OFL} as a function of energy for the Cs-137 data of the NFC2 detector. Each yellow point corresponds to the mean value of the χ^2 distribution in the corresponding plot of Section A.2.1. The red points correspond to the mean value (of each 20 eV interval) adding 3 σ of the Gaussian distribution. The red points are fit with Eq. 5.6. p0, p1 and p2 are fitting parameters as in the formula.

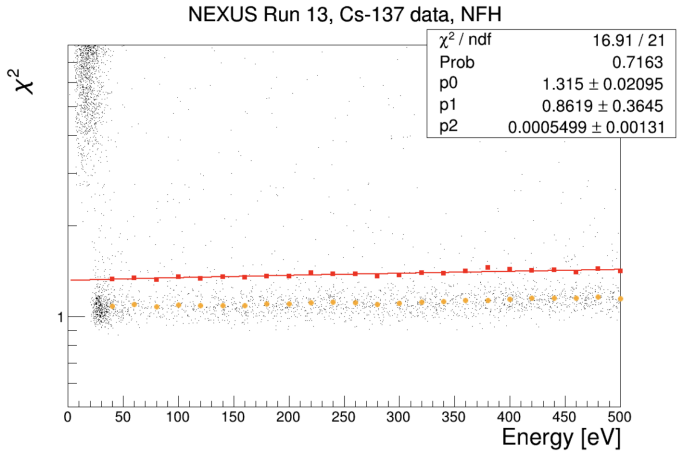

Figure A.32: χ^2_{OFL} as a function of energy for the Cs-137 data of the NFH detector. Each yellow point corresponds to the mean value of the χ^2 distribution in the corresponding plot of Section A.2.1. The red points correspond to the mean value (of each 20 eV interval) adding 3 σ of the Gaussian distribution. The red points are fit with Eq. 5.6. p0, p1 and p2 are fitting parameters as in the formula.

A.3 Cut Efficiency Calculations from Pre-selection of Caesium Data

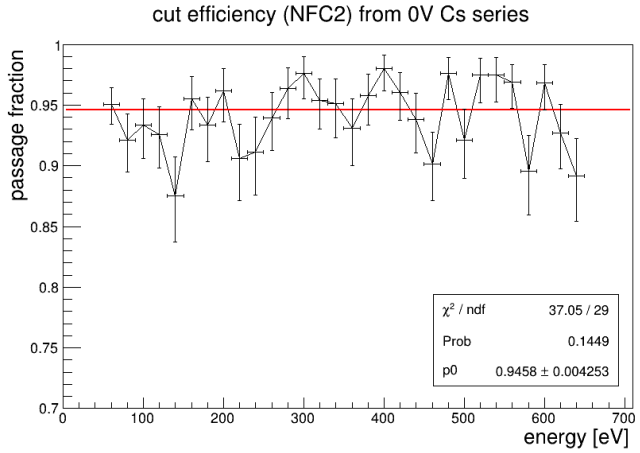

Figure A.33: Cut efficiency estimation for energy dependent χ^2 cut for NFC2 detector from pre-selection of 0V Caesium data. X-axis is the total phonon energy calibrated from the OF amplitude through the calibration discussed in Section 5.2. The red line is the overall constant fit.

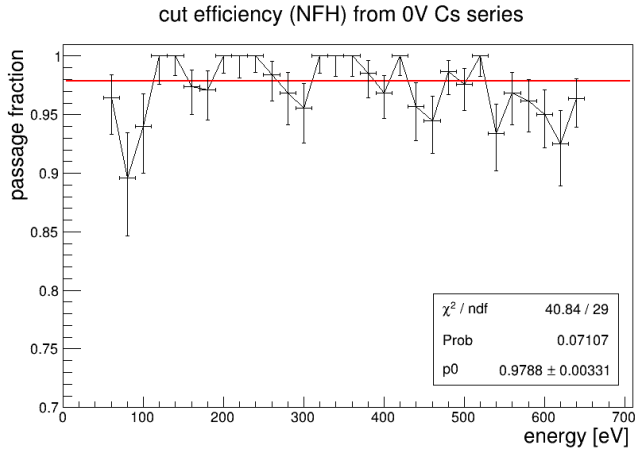

Figure A.34: Cut efficiency estimation for energy dependent χ^2 cut for NFH detector from pre-selection of 0V Caesium data. X-axis is the total phonon energy calibrated from the OF amplitude through the calibration discussed in Section 5.2. The red line is the overall constant fit.

Bibliography

[1] Musaab F Albakry, I Alkhatib, DWP Amaral, T Aralis, T Aramaki, IJ Arnquist, I Ataee Langroudy, E Azadbakht, S Banik, C Bathurst, et al. A strategy for low-mass dark matter searches with cryogenic detectors in the supercdms snolab facility. *arXiv preprint arXiv:2203.08463*, 2022.

[2] R Agnese, AJ Anderson, T Aramaki, I Arnquist, W Baker, D Barker, R Basu Thakur, DA Bauer, A Borgland, MA Bowles, et al. Projected sensitivity of the supercdms snolab experiment. *Physical Review D*, 95(8):082002, 2017.

[3] William Thomson and Baron Kelvin. *Baltimore lectures on molecular dynamics and the wave theory of light*. Cambridge University Press, 2010.

[4] Henri Poincaré. The Milky Way and the theory of gases. *Popular Astronomy, vol. 14, pp. 475-488*, 14:475–488, 1906.

[5] Gianfranco Bertone and Dan Hooper. History of dark matter. *Reviews of Modern Physics*, 90(4):045002, 2018.

[6] Jan H Oort. The force exerted by the stellar system in the direction perpendicular to the galactic plane and some related problems. *Bulletin of the Astronomical Institutes of the Netherlands, Vol. 6, p. 249*, 6:249, 1932.

[7] Fritz Zwicky. Die rotverschiebung von extragalaktischen nebeln. *Helvetica Physica Acta, Vol. 6, p. 110-127*, 6:110–127, 1933.

[8] SIDNEY VAN DEN BERGH. Collapsed objects in clusters of galaxies. *Nature*, 224(5222):891–891, 1969.

[9] PJE Peebles. Princeton series in physics. *Princeton, NJ: Princeton Univer*, 1993.

[10] J Tarter and J Silk. Current constraints on hidden mass in the coma cluster. *Quarterly Journal of the Royal Astronomical Society, Vol. 15, p. 122*, 15:122, 1974.

[11] Mark W Goodman and Edward Witten. Detectability of certain dark-matter candidates. *Physical Review D*, 31(12):3059, 1985.

[12] Horace W Babcock. The rotation of the andromeda nebula. *Lick Observatory bulletin; no. 498; Lick Observatory bulletins; no. 498., Berkeley: University of California Press,[1939], p. 41-51,[2] leaves of plates; 31 cm.*, 19:41–51, 1939.

[13] Vera C Rubin and W Kent Ford Jr. Rotation of the andromeda nebula from a spectroscopic survey of emission regions. *Astrophysical Journal, vol. 159, p. 379*, 159:379, 1970.

[14] Morton S Roberts and Robert N Whitehurst. The rotation curve and geometry of m31 at large galactocentric distances. *Astrophysical Journal, Vol. 201, p. 327-346*, 201:327–346, 1975.

[15] Claude Carignan, Laurent Chemin, Walter K Huchtmeier, and Felix J Lockman. The extended hi rotation curve and mass distribution of m31. *The Astrophysical Journal*, 641(2):L109, 2006.

[16] Kenneth C Freeman. On the disks of spiral and s0 galaxies. *Astrophysical Journal, vol. 160, p. 811*, 160:811, 1970.

[17] MS Roberts and AH Rots. Comparison of rotation curves of different galaxy types. *Astronomy and Astrophysics, Vol. 26, p. 483-485 (1973)*, 26:483–485, 1973.

[18] Planck Collaboration. Planck 2015 results. X. Diffuse component separation: Foreground maps. *Astronomy & Astrophysics*, 594:A10, 2016.

[19] Donald H Perkins. *Particle astrophysics*. Number 10. OUP Oxford, 2009.

[20] Masaharu Tanabashi, Particle Data Grp, K Hagiwara, K Hikasa, Katsumasa Nakamura, Y Sumino, F Takahashi, J Tanaka, K Agashe, Giulio Aielli, et al. Review of particle physics. *Physical Review D*, 98(3), 2018.

[21] P J E Peebles. Large-scale background temperature and mass fluctuations due to scale-invariant primeval perturbations. *The Astrophysical Journal*, 263, 1982.

[22] R Adam, Peter AR Ade, N Aghanim, MIR Alves, M Arnaud, M Ashdown, J Aumont, C Baccigalupi, AJ Banday, RB Barreiro, et al. Planck 2015 results-x. diffuse component separation: Foreground maps. *Astronomy & Astrophysics*, 594:A10, 2016.

[23] Douglas Clowe, Maruša Bradač, Anthony H Gonzalez, Maxim Markevitch, Scott W Randall, Christine Jones, and Dennis Zaritsky. A direct empirical proof of the existence of dark matter. *The Astrophysical Journal*, 648(2):L109, 2006.

[24] Gianfranco Gentile, Paolo Salucci, U Klein, D Vergani, and P Kalberla. The cored distribution of dark matter in spiral galaxies. *Monthly Notices of the Royal Astronomical Society*, 351(3):903–922, 2004.

[25] Justin I Read. The local dark matter density. *Journal of Physics G: Nuclear and Particle Physics*, 41(6):063101, 2014.

[26] Marika Asgari and Catherine Heymans. The halo model for cosmology: a pedagogical review. *arXiv preprint*, 2023. arXiv:2303.08752.

[27] Gonzalo Herrera and Alejandro Ibarra. Direct detection of non-galactic light dark matter. *Physics Letters B*, 820:136551, 2021.

[28] Matthew James Wilson. *A new search for low-mass dark matter and an examination and reduction of the uncertainty due to the photoelectric absorption cross section using a cryogenic Silicon detector with single-charge sensitivity*. PhD thesis, University of Toronto (Canada), 2022.

[29] Gerard Jungman, Marc Kamionkowski, and Kim Griest. Supersymmetric dark matter. *Physics Reports*, 267(5-6):195–373, 1996.

[30] David G Cerdeno and Anne M Green. Direct detection of wimps. *arXiv preprint arXiv:1002.1912*, 2010.

[31] F Mayet, Anne M Green, James BR Battat, J Billard, N Bozorgnia, GB Gelmini, P Gondolo, BJ Kavanagh, SK Lee, D Loomba, et al. A review of the discovery reach of directional dark matter detection. *Physics Reports*, 627:1–49, 2016.

[32] Elena Aprile, Jelle Aalbers, F Agostini, M Alfonsi, L Althueser, FD Amaro, Vasile C Antochi, E Angelino, F Arneodo, Derek Barge, et al. Light dark matter search with ionization signals in xenon1t. *Physical Review Letters*, 123(25):251801, 2019.

[33] Xiangyi Cui, Abdusalam Abdukerim, Wei Chen, Xun Chen, Yunhua Chen, Binbin Dong, Deqing Fang, Changbo Fu, Karl Giboni, Franco Giuliani, et al. Dark matter results from 54-ton-day exposure of pandax-ii experiment. *Physical review letters*, 119(18):181302, 2017.

[34] F Ruppin, J Billard, E Figueroa-Feliciano, and L Strigari. Complementarity of dark matter detectors in light of the neutrino background. *Physical Review D*, 90(8):083510, 2014.

[35] Julien Baur, Nathalie Palanque-Delabrouille, Christophe Yèche, Christophe Magneville, and Matteo Viel. Lyman-alpha forests cool warm dark matter. *Journal of Cosmology and Astroparticle Physics*, 2016(08):012, 2016.

[36] Marco Battaglieri, Alberto Belloni, Aaron Chou, Priscilla Cushman, Bertrand Echenard, Rouven Essig, Juan Estrada, Jonathan L Feng, Brenna Flaugher, Patrick J Fox, et al. Us cosmic visions: new ideas in dark matter 2017: community report. *arXiv preprint arXiv:1707.04591*, 2017.

[37] Xiao-Gang Wen and Edward Witten. Electric and magnetic charges in superstring models. *Nuclear Physics B*, 261:651–677, 1985.

[38] Steven A Abel, Mark D Goodsell, Joerg Jaeckel, VV Khoze, and Andreas Ringwald. Kinetic mixing of the photon with hidden u (1) s in string phenomenology. *Journal of High Energy Physics*, 2008(07):124, 2008.

[39] R Agnese, AJ Anderson, D Balakishiyeva, R Basu Thakur, DA Bauer, J Billard, A Borgland, MA Bowles, D Brandt, PL Brink, et al. First direct limits on lightly ionizing particles with electric charge less than e/6. *Physical review letters*, 114(11):111302, 2015.

[40] Michelangelo Ambrosio, R Antolini, Giulio Auriemma, D Bakari, A Baldini, GC Barbarino, BC Barish, G Battistoni, Roberto Bellotti, C Bemporad, et al. Search for lightly ionizing particles with the macro detector. *Physical Review D*, 62(5):052003, 2000.

[41] R Agnese, AJ Anderson, D Balakishiyeva, R Basu Thakur, DA Bauer, J Billard, A Borgland, MA Bowles, D Brandt, PL Brink, et al. First direct limits on lightly ionizing particles with electric charge less than e/6. *Physical review letters*, 114(11):111302, 2015.

[42] M Mori, Y Oyama, A Suzuki, K Takahashi, M Yamada, K Miyano, H Miyata, H Takei, KS Hirata, T Kajita, et al. Search for fractionally charged particles in kamiokande ii. *Physical Review D*, 43(9):2843, 1991.

[43] M Aglietta, P Antonioli, G Badino, C Castagnoli, A Castellina, VL Dadykin, W Fulgione, P Galeotti, FF Khalchukov, EV Korolkova, et al. Search for fractionally charged particles in the mont blanc lsd scintillation detector. *Astroparticle Physics*, 2(1):29–34, 1994.

[44] Michelangelo Ambrosio, R Antolini, Giulio Auriemma, D Bakari, A Baldini, GC Barbarino, BC Barish, G Battistoni, Roberto Bellotti, C Bemporad, et al. Search for lightly ionizing particles with the macro detector. *Physical Review D*, 62(5):052003, 2000.

[45] Morad Aaboud, Georges Aad, Brad Abbott, B Abeloos, SH Abidi, OS AbouZeid, Nadine L Abraham, Halina Abramowicz, Henso Abreu, R Abreu, et al. Search for dark matter and other new phenomena in events with an energetic jet and large missing transverse momentum using the atlas detector. *Journal of High Energy Physics*, 2018(1):1–53, 2018.

[46] Georges Aad, Brad Abbott, Jalal Abdallah, Samah Abdel Khalek, Ovsat Abdinov, Rosemarie Aben, Babak Abi, Maris Abolins, OS AbouZeid, Halina Abramowicz, et al. Search for new phenomena in events with a photon and missing transverse momentum in pp collisions at s= 8 TeV with the atlas detector. *Physical Review D*, 91(1):012008, 2015.

[47] CMS collaboration et al. Search for dark matter produced with an energetic jet or a hadronically decaying w or z boson at $\sqrt{s} = 13$ TeV. *arXiv preprint arXiv:1703.01651*, 2017.

[48] R Agnese, T Aralis, T Aramaki, Isaac J Arnquist, Elham Azadbakht, W Baker, Samir Banik, D Barker, DA Bauer, T Binder, et al. Search for low-mass dark matter with cdmslite using a profile likelihood fit. *Physical Review D*, 99(6):062001, 2019.

[49] DS Akerib, S Alsum, HM Araújo, X Bai, AJ Bailey, J Balajthy, P Beltrame, EP Bernard, A Bernstein, TP Biesiadzinski, et al. Results from a search for dark matter in the complete lux exposure. *Physical review letters*, 118(2):021303, 2017.

[50] E Aprile, K Abe, F Agostini, S Ahmed Maouloud, L Althueser, B Andrieu, E Angelino, JR Angevaare, VC Antochi, D Antón Martin, et al. First dark matter search with nuclear recoils from the xenonnt experiment. *Physical review letters*, 131(4):041003, 2023.

[51] Michelangelo Traina. Results on low-mass weakly interacting massive particles from a 11 kg d target exposure of damic at snolab (icrc2021 proceedings). *arXiv preprint arXiv:2108.05983*, 2021.

[52] P Agnes, Ivone Freire da Mota Albuquerque, T Alexander, AK Alton, M Ave, HO Back, G Batignani, K Biery, V Bocci, WM Bonivento, et al. Search for dark-matter–nucleon interactions via migdal effect with darkside-50. *Physical review letters*, 130(10):101001, 2023.

[53] F Petricca, G Angloher, P Bauer, A Bento, C Bucci, L Canonica, X Defay, A Erb, F v Feilitzsch, N Ferreiro Iachellini, et al. First results on low-mass dark matter from the cresst-iii experiment. In *Journal of Physics: Conference Series*, volume 1342, page 012076. IOP Publishing, 2020.

[54] F Ruppin, J Billard, E Figueroa-Feliciano, and L Strigari. Complementarity of dark matter detectors in light of the neutrino background. *Physical Review D*, 90(8):083510, 2014.

[55] Zachary H Levine and Douglas C Allan. Linear optical response in silicon and germanium including self-energy effects. *Physical review letters*, 63(16):1719, 1989.

[56] Zachary H Levine and Douglas C Allan. Quasiparticle calculation of the dielectric response of silicon and germanium. *Physical Review B*, 43(5):4187, 1991.

[57] Paolo Giannozzi, Stefano Baroni, Nicola Bonini, Matteo Calandra, Roberto Car, Carlo Cavazzoni, Davide Ceresoli, Guido L Chiarotti, Matteo Cococcioni, Ismaila Dabo, et al. Quantum espresso: a modular and open-source software project for quantum simulations of materials. *Journal of physics: Condensed matter*, 21(39):395502, 2009.

[58] Rouven Essig, Marivi Fernandez-Serra, Jeremy Mardon, Adrian Soto, Tomer Volansky, and Tien-Tien Yu. Direct detection of sub-gev dark matter with semiconductor targets. *Journal of High Energy Physics*, 2016(5):1–54, 2016.

[59] YU Peter and Manuel Cardona. *Fundamentals of semiconductors: physics and materials properties*. Springer Science & Business Media, 2010.

[60] BS Neganov and VN Trofimov. Colorimetric method measuring ionizing radiation. *Otkryt. Izobret*, 146(215):53, 1985.

[61] PN Luke. Voltage-assisted calorimetric ionization detector. *Journal of Applied Physics*, 64(12):6858–6860, 1988.

[62] R Ren, Corey Bathurst, YY Chang, R Chen, CW Fink, Z Hong, NA Kurinsky, N Mast, N Mishra, Valentina Novati, et al. Design and characterization of a phonon-mediated cryogenic particle detector with an ev-scale threshold and 100 kev-scale dynamic range. *Physical Review D*, 104(3):032010, 2021.

[63] Viktor S Vavilov. Radiation ionization processes in germanium and silicon crystals. *Soviet Physics Uspekhi*, 4(5):761, 1962.

[64] Godehard Angloher, M Bauer, I Bavykina, A Bento, C Bucci, C Ciemniak, G Deuter, F von Feilitzsch, D Hauff, P Huff, et al. Results from 730 kg days of the cresst-ii dark matter search. *The European Physical Journal C*, 72:1–22, 2012.

[65] G Angloher, A Bento, C Bucci, L Canonica, A Erb, F von Feilitzsch, N Ferreiro Iachellini, P Gorla, Achim Gütlein, D Hauff, et al. Results on low mass wimps using an upgraded cresst-ii detector. *The European Physical Journal C*, 74(12):1–6, 2014.

[66] G Angloher, A Bento, C Bucci, L Canonica, X Defay, A Erb, F von Feilitzsch, N Ferreiro Iachellini, P Gorla, A Gütlein, et al. Results on light dark matter particles with a low-threshold cresst-ii detector. *The European Physical Journal C*, 76:1–8, 2016.

[67] Kent D Irwin, Sae Woo Nam, Blas Cabrera, B Chugg, and Betty A Young. A quasiparticle-trap-assisted transition-edge sensor for phonon-mediated particle detection. *Review of Scientific Instruments*, 66(11):5322–5326, 1995.

[68] Matt Christopher Pyle. *Optimizing the design and analysis of cryogenic semiconductor dark matter detectors for maximum sensitivity*. Stanford University, 2012.

[69] Jens Lindhard, V Nielsen, M Scharff, and PV Thomsen. Integral equations governing radiation effects. *Mat. Fys. Medd. Dan. Vid. Selsk*, 33(10):1–42, 1963.

[70] M. F. Albakry et al. First measurement of the nuclear-recoil ionization yield in silicon at 100 ev. *Physical Review Letters*, 131(9):091801, 2023.

[71] G Gerbier, E Lesquoy, J Rich, M Spiro, C Tao, D Yvon, S Zylberajch, P Delbourgo, G Haouat, C Humeau, et al. Measurement of the ionization of slow silicon nuclei in silicon for the calibration of a silicon dark-matter detector. *Physical Review D*, 42(9):3211, 1990.

[72] Brian L Dougherty. Measurements of ionization produced in silicon crystals by low-energy silicon atoms. *Physical Review A*, 45(3):2104, 1992.

[73] AE Chavarria, JI Collar, JR Pena, P Privitera, AE Robinson, B Scholz, C Sengul, J Zhou, J Estrada, F Izraelevitch, et al. Measurement of the ionization produced by sub-kev silicon nuclear recoils in a ccd dark matter detector. *Physical Review D*, 94(8):082007, 2016.

[74] F Izraelevitch, D Amidei, A Aprahamian, R Arcos-Olalla, G Cancelo, C Casarella, AE Chavarria, P Collon, Juan Estrada, G Fernández Moroni, et al. A measurement of the ionization efficiency of nuclear recoils in silicon. *Journal of Instrumentation*, 12(06):P06014, 2017.

[75] AN Villano, M Fritts, N Mast, S Brown, P Cushman, K Harris, and V Mandic. First observation of isolated nuclear recoils following neutron capture for dark matter calibration. *Physical Review D*, 105(8):083014, 2022.

[76] R Agnese, AJ Anderson, T Aramaki, W Baker, D Balakishiyeva, S Banik, D Barker, R Basu Thakur, DA Bauer, T Binder, et al. Nuclear-recoil energy scale in cdms ii silicon dark-matter detectors. *Nuclear Instruments and Methods in Physics Research Section A: Accelerators, Spectrometers, Detectors and Associated Equipment*, 905:71–81, 2018.

[77] JD Lewin and PF Smith. Review of mathematics, numerical factors, and corrections for dark matter experiments based on elastic nuclear recoil. *Astroparticle Physics*, 6(1):87–112, 1996.

[78] Karthik Ramanathan and Noah Kurinsky. Ionization yield in silicon for ev-scale electron-recoil processes. *Physical Review D*, 102(6):063026, 2020.

[79] R. K. Romani, P. L. Brink, B. Cabrera, M. Cherry, T. Howarth, N. Kurinsky, R. A. Moffatt, R. Partridge, F. Ponce, M. Pyle, A. Tomada, S. Yellin, J. J. Yen, and B. A. Young. Thermal detection of single e-h pairs in a biased silicon crystal detector. *Applied Physics Letters*, 112(4), January 2018.

[80] R Agnese, T Aralis, T Aramaki, IJ Arnquist, E Azadbakht, W Baker, S Banik, D Barker, DA Bauer, T Binder, et al. First dark matter constraints from a supercdms single-charge sensitive detector. *Physical review letters*, 121(5):051301, 2018.

[81] DW Amaral, T Aralis, T Aramaki, IJ Arnquist, E Azadbakht, S Banik, D Barker, C Bathurst, DA Bauer, LVS Bezerra, et al. Constraints on low-mass, relic dark matter candidates from a surface-operated supercdms single-charge sensitive detector. *Physical Review D*, 102(9):091101, 2020.

[82] MF Albakry, I Alkhatib, DWP Amaral, T Aralis, T Aramaki, IJ Arnquist, I Ataee Langroudy, E Azadbakht, S Banik, C Bathurst, et al. Investigating the sources of low-energy events in a supercdms-hvev detector. *Physical Review D*, 105(11):112006, 2022.

[83] MF Albakry, I Alkhatib, D Alonso-González, DWP Amaral, J Anczarski, T Aralis, T Aramaki, IJ Arnquist, I Ataee Langroudy, E Azadbakht, et al. Light dark matter constraints from supercdms hvev detectors operated underground with an anticoincidence event selection. *arXiv preprint arXiv:2407.08085*, 2024.

[84] Noah Kurinsky, To Chin Yu, Yonit Hochberg, and Blas Cabrera. Diamond detectors for direct detection of sub-gev dark matter. *Physical Review D*, 99(12):123005, 2019.

[85] Rouven Essig, Marivi Fernandez-Serra, Jeremy Mardon, Adrian Soto, Tomer Volansky, and Tien-Tien Yu. Direct detection of sub-gev dark matter with semiconductor targets, 2016.

[86] Itay M Bloch, Rouven Essig, Kohsaku Tobioka, Tomer Volansky, and Tien-Tien Yu. Searching for dark absorption with direct detection experiments. *Journal of High Energy Physics*, 2017(6):1–21, 2017.

[87] Yonit Hochberg, Tongyan Lin, and Kathryn M Zurek. Absorption of light dark matter in semiconductors. *Physical Review D*, 95(2):023013, 2017.

[88] T. Mannel. Theory and phenomenology of cp violation. In *Proceedings of the 7th International Conference on Hyperons, Charm and Beauty Hadrons*, volume 167, pages 170–174, 2007.

[89] Roberto D Peccei. The strong cp problem and axions. In *Axions: Theory, Cosmology, and Experimental Searches*, pages 3–17. Springer, 2008.

[90] A Derevianko, VA Dzuba, VV Flambaum, and M Pospelov. Axio-electric effect. *Physical Review D—Particles, Fields, Gravitation, and Cosmology*, 82(6):065006, 2010.

[91] Changbo Fu, Xiaopeng Zhou, Xun Chen, Yunhua Chen, Xiangyi Cui, Deqing Fang, Karl Giboni, Franco Giuliani, Ke Han, Xingtao Huang, et al. Limits on axion couplings from the first 80 days of data of the pandax-ii experiment. *Physical review letters*, 119(18):181806, 2017.

[92] F Ponce, W Page, PL Brink, B Cabrera, M Cherry, C Fink, N Kurinsky, R Partridge, M Pyle, B Sadoulet, et al. Modeling of impact ionization and charge trapping in supercdms hvev detectors. *Journal of Low Temperature Physics*, 199:598–605, 2020.

[93] MJ Wilson, A Zaytsev, B Von Krosigk, I Alkhatib, M Buchanan, R Chen, MD Diamond, E Figueroa-Feliciano, SAS Harms, Z Hong, et al. Improved modeling of detector response effects in phonon-based crystal detectors used for dark matter searches. *Physical Review D*, 109(11):112018, 2024.

[94] Michael H Kelsey, Robert Agnese, Yasin F Alam, I Ataee Langroudy, Elham Azadbakht, D Brandt, Raymond Bunker, Blas Cabrera, Y-Y Chang, Harrison Coombes, et al. G4cmp: Condensed matter physics simulation using the geant4 toolkit. *Nuclear Instruments and Methods in Physics Research Section A: Accelerators, Spectrometers, Detectors and Associated Equipment*, 1055:168473, 2023.

[95] Noah Kurinsky. *The low-mass limit: Dark matter detectors with eV-scale energy resolution*. Stanford University, 2018.

[96] Emilio Gatti and Pier Francesco Manfredi. Processing the signals from solid-state detectors in elementary-particle physics. *La Rivista del Nuovo Cimento (1978-1999)*, 9:1–146, 1986.

[97] Glen Cowan. Use of the profile likelihood function in searches for new physics. 2011.

[98] R Agnese, AJ Anderson, T Aralis, T Aramaki, IJ Arnquist, W Baker, D Balakishiyeva, D Barker, R Basu Thakur, DA Bauer, et al. Low-mass dark matter search with cdmslite. *Physical Review D*, 97(2):022002, 2018.

[99] Bradley J Kavanagh. Earth scattering of superheavy dark matter: Updated constraints from detectors old and new. *Physical Review D*, 97(12):123013, 2018.

[100] Bradley J Kavanagh, Riccardo Catena, and Chris Kouvaris. Signatures of earth-scattering in the direct detection of dark matter. *Journal of Cosmology and Astroparticle Physics*, 2017(01):012, 2017.

[101] Christopher V Cappiello. Analytic approach to light dark matter propagation. *Physical Review Letters*, 130(22):221001, 2023.

[102] Timon Emken and Chris Kouvaris. How blind are underground and surface detectors to strongly interacting dark matter? *Physical Review D*, 97(11):115047, 2018.

[103] Michael Dressel. Geometrical importance sampling in geant4: from design to verification. Technical report, 2003.

[104] AA Makarov and GI Simonova. Some properties of two-sample kolmogorov–smirnov test in the case of contamination of one of the samples. *Journal of Mathematical Sciences*, 6(220):718–723, 2016.

[105] Kyle Michael Sundqvist. *Carrier transport and related effects in detectors of the cryogenic dark matter search*. University of California, Berkeley, 2012.

[106] Arran Thomas James Phipps. *Ionization collection in detectors of the cryogenic dark matter search*. University of California, Berkeley, 2016.